16 July 2010 | $10

Science

AAAS

EDITORIAL

257 A Volunteer Army for Science
Donald G. Rea and Katherine M. Nielsen

NEWS OF THE WEEK

262 Familial DNA Testing Scores a Win in Serial Killer Case

263 Kidney Disease Is Parasite-Slaying Protein's Downside
>> Science *Express Report by G. Genovese* et al.

264 New Biosecurity Rules to Target the Riskiest Pathogens

264 U.S. Panel Weighs Guidelines for Synthetic Biology

265 Scientists Eulogize Center—And Prepare for Stiff Competition

266 Probing Culture's Secrets, From Capuchins to Children

267 From the *Science* Policy Blog

268 How a Little Fish Keeps Overfished Ecosystem Productive
>> *Report p. 333*

269 From *Science*'s Online Daily News Site

NEWS FOCUS

270 From the Outside Looking In
>> Science *Podcast*

274 Confronting Anatomy's Nazi Past
The Dilemma of Pernkopf's Atlas

LETTERS

276 Funding Should Come to Those Who Wait
R. R. Swaisgood et al.

Brazilian Law: Full Speed in Reverse?
J. P. Metzger et al.

Sponsors of Traumatic Brain Injury Project
G. Manley

Warming, Photoperiods, and Tree Phenology
I. Chuine et al.

Response
C. Körner and D. Basler

277 TECHNICAL COMMENT ABSTRACTS

277 CORRECTIONS AND CLARIFICATIONS

BOOKS *ET AL.*

279 The Price of Altruism
O. Harman, reviewed by S. A. Frank

280 Image and Reality
A. J. Rocke, reviewed by P. J. Ramberg

EDUCATION FORUM

282 Performance-Based Data in the Study of STEM Ph.D. Education
D. F. Feldon et al.

PERSPECTIVES

284 Hiding in Plain Sight
M. I. Rosenberg and C. Desplan
>> *Report p. 336*

285 Reengineering Enzymes
S. Lutz
>> *Reports pp. 305 and 309*

287 Consumers Who Care
S. DellaVigna
>> *Report p. 325*

288 The Ongoing Mystery of Sea-Floor Methane
M. Alperin and T. Hoehler

290 When Still Waters Ran Deep
T. Kiefer

291 Sickle Cell Disease at 100 Years
S. H. Orkin and D. R. Higgs

BREVIA

293 Chromosome Size Differences May Affect Meiosis and Genome Size
J. Wang et al.
Deletions and insertions affect chromosome segregation in the worm *Caenorhabditis elegans*.

CONTENTS continued >>

page 270

page 279

COVER

A seedling carpet dominated by *Dipteryx oleifera* (almendro) in the forest understory of Barro Colorado Island, Panama. Seedlings here have a lower probability of surviving when surrounded by neighbors of their own species. However, rare species suffer more from the presence of like neighbors than do common species, suggesting a mechanism that shapes species abundances in diverse tropical forest communities. See page 330.

Photo: Christian Ziegler

DEPARTMENTS

254 This Week in *Science*
258 Editors' Choice
260 *Science* Staff
261 Random Samples
346 New Products
347 *Science* Careers

RESEARCH ARTICLE

294 *Staphylococcus aureus* Nonribosomal Peptide Secondary Metabolites Regulate Virulence
M. A. Wyatt et al.
Dipeptides produced by a major bacterial pathogen are essential for successful infection.

REPORTS

297 Observation of the Magnon Hall Effect
Y. Onose et al.
Spin excitations in an insulating ferromagnet exhibit an anomalous thermal Hall effect.

299 Single-Crystal X-ray Structure of 1,3-Dimethylcyclobutadiene by Confinement in a Crystalline Matrix
Y.-M. Legrand et al.
A normally unstable hydrocarbon has been trapped and structurally characterized within a host crystal.

303 Disordering of an Organic Overlayer on a Metal Surface Upon Cooling
A. Schöll et al.
Strengthening a surface bond of an organic molecule upon cooling leads to disordering between molecules.

305 Biocatalytic Asymmetric Synthesis of Chiral Amines from Ketones Applied to Sitagliptin Manufacture
C. K. Savile et al.
Strengthening of the bond of an organic molecule to a silver surface upon cooling disrupts intermolecular ordering.
>> *Perspective p. 285*

309 Computational Design of an Enzyme Catalyst for a Stereoselective Bimolecular Diels-Alder Reaction
J. B. Siegel et al.
Synthetic enzymes catalyze a carbon-carbon bond-forming reaction with high stereoselectivity and substrate specificity.
>> *Perspective p. 285*

313 Meniscus-Confined Three-Dimensional Electrodeposition for Direct Writing of Wire Bonds
J. Hu and M.-F. Yu
A micropipette helps guide the electrodeposition of copper and platinum wires for electronics connections.

316 Cenozoic Tectonics of Western North America Controlled by Evolving Width of Farallon Slab
W. P. Schellart et al.
The width of a descending slab is the primary control on the dynamics of subduction.

319 Simulated Rapid Warming of Abyssal North Pacific Waters
S. Masuda et al.
Computer simulations suggest a possible reason for the warming of North Pacific bottom water during the past four decades.

322 Ocean Warming Slows Coral Growth in the Central Red Sea
N. E. Cantin et al.
Rising summertime sea surface temperatures are slowing the rate of growth of healthy corals in the Red Sea.

325 Shared Social Responsibility: A Field Experiment in Pay-What-You-Want Pricing and Charitable Giving
A. Gneezy et al.
Exchanging goods for money ends up benefiting buyers, sellers, and charities.
>> *Perspective p. 287;* Science *Podcast*

327 The Structure of cbb_3 Cytochrome Oxidase Provides Insights into Proton Pumping
S. Buschmann et al.
The third class of heme-copper oxidases reveals new structural solutions to achieve redox-driven proton translocation.

330 Asymmetric Density Dependence Shapes Species Abundances in a Tropical Tree Community
L. S. Comita et al.
Seedling survival in a tropical forest shows that species abundance is related to a species' sensitivity to conspecific neighbors.

333 Trophic Structure and Community Stability in an Overfished Ecosystem
A. C. Utne-Palm et al.
An endemic goby exploits jellyfish and microbial biomass, partially restoring the food chain in the Benguela ecosystem.
>> *News story p. 268*

336 Small Peptides Switch the Transcriptional Activity of Shavenbaby During *Drosophila* Embryogenesis
T. Kondo et al.
A conserved locus in insects encodes four small peptides that shift a transcription factor from repressor into activator.
>> *Perspective p. 284*

339 Hedgehog Signaling Regulates Segment Formation in the Annelid *Platynereis*
N. Dray et al.
The processes that pattern body segmentation in annelids and arthropods both require the same signaling mechanism.

342 Chemoattraction to Dimethylsulfoniopropionate Throughout the Marine Microbial Food Web
J. R. Seymour et al.
A microfluidics device reveals a common response of bacterial plankton to sulfur compounds emitted by marine algae.

CONTENTS continued >>

pages 287 & 325

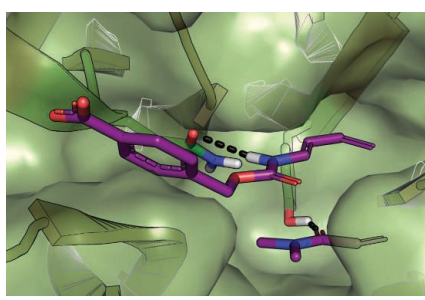

page 309

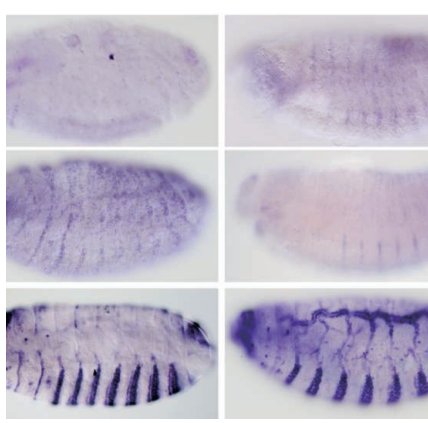

page 336

SCIENCEONLINE

SCIENCEXPRESS
www.sciencexpress.org

MESSENGER Observations of Extreme Loading and Unloading of Mercury's Magnetic Tail
J. A. Slavin et al.
Relative to Earth, Mercury's magnetospheric substorms are more intense and occur on shorter time scales.
10.1126/science.1188067

Evidence for Young Volcanism on Mercury from the Third MESSENGER Flyby
L. M. Prockter et al.
Volcanism and associated deformation on Mercury may have lasted well into the last half of the history of the solar system.
10.1126/science.1188186

Mercury's Complex Exosphere: Results from MESSENGER's Third Flyby
R. J. Vervack Jr. et al.
Mercury's exosphere is more varied and more intertwined with its magnetospheric environment than previously thought.
10.1126/science.1188572

Association of Trypanolytic ApoL1 Variants with Kidney Disease in African-Americans
G. Genovese et al.
Genetic variants associated with kidney disease in African-Americans may confer protection against trypanosomes.
10.1126/science.1193032
>> *News story p. 263;* Science *Podcast*

Astrocytes Control Breathing Through pH-dependent Release of ATP
A. V. Gourine et al.
Central nervous system glial cells are key players in the chemo-reflex essential for breathing.
10.1126/science.1190721

Induction of Broadly Neutralizing H1N1 Influenza Antibodies by Vaccination
C.-J. Wei et al.
An influenza virus vaccine elicits a broadly neutralizing, cross-protective antibody response in mice, ferrets, and nonhuman primates.
10.1126/science.1192517

Substrate Elasticity Regulates Skeletal Muscle Stem Cell Self-Renewal in Culture
P. M. Gilbert et al.
Muscle stem cells prefer a soft substrate.
10.1126/science.1191035

Signaling Kinase AMPK Activates Stress-Promoted Transcription via Histone H2B Phosphorylation
D. Bungard et al.
The energy sensor AMPK facilitates gene transcription by localizing to chromatin and phosphorylating histone H2B.
10.1126/science.1191241

TECHNICALCOMMENTS

Comment on "Observational and Model Evidence for Positive Low-Level Cloud Feedback"
A. J. Broccoli and S. A. Klein
Full text at www.sciencemag.org/cgi/content/full/329/5989/277-a

Response to Comment on "Observational and Model Evidence for Positive Low-Level Cloud Feedback"
A. C. Clement et al.
Full text at www.sciencemag.org/cgi/content/full/329/5989/277-b

SCIENCENOW
www.sciencenow.org
Highlights From Our Daily News Coverage

Amazon Hit by Its Own Katrina
Severe storm mowed down vast swaths of rainforest.

The Vaccine That Came In From the Cold
Genes from Arctic bacteria turn mammalian pathogens into vaccines.

Keeping Insulin Hanging Around
Long-lasting insulin shot shows promise in animals.

SCIENCESIGNALING
www.sciencesignaling.org
The Signal Transduction Knowledge Environment

RESEARCH ARTICLE: Regulation of Notch1 Signaling by Nrf2—Implications for Tissue Regeneration
N. Wakabayashi et al.
The cell survival pathway mediated by the transcription factor Nrf2 facilitates tissue regeneration by promoting Notch1 signaling.

RESEARCH ARTICLE: Signaling to Transcription Networks in the Neuronal Retrograde Injury Response
I. Michaelevski et al.
Robustness in nerve injury responses results from control of axon-to-soma signaling networks by multiple regulatory components.

NETWATCH: MolecularMovies.org
Learn how to make 3D animations illustrating molecular and cellular events; in Educator Sites.

NETWATCH: Nuclear Receptor Resource (NRR)
Explore the nuclear hormone receptor superfamily through a collection of databases, interactive pathways, and graphics; in Protein Databases.

SCIENCECAREERS
www.sciencecareers.org/career_magazine
Free Career Resources for Scientists

Veterinarian Scientists Bring Unique Perspectives to Translational Research
L. Chiu
D.V.M.-Ph.D.s are uniquely qualified to do research in animal models and translate findings across species, including humans.

Tooling Up: Integrate Yourself
D. Jensen
Being viewed as an outsider can happen to anyone, and it can have devastating career consequences.

SCIENCETRANSLATIONAL MEDICINE
www.sciencetranslationalmedicine.org
Integrating Medicine and Science

EDITORIAL: Something in Common
S. H. Friend
The first Sage Commons Congress took steps toward open sharing of data to drive therapeutic development.

COMMENTARY: The Demographic and Biomedical Case for Late-Life Interventions in Aging
M. J. Rae et al.
A global research agenda on aging has the potential to avert enormous economic, social, and human costs.

RESEARCH ARTICLE: Natural Immunization Against Malaria—Causal Prophylaxis with Antibiotics
J. Friesen et al.
Malaria-infected mice treated with antibiotics remain healthy and are protected against subsequent malaria infection.

RESEARCH ARTICLE: Quinone Oxidoreductase-2–Mediated Prodrug Cancer Therapy
M. R. Middleton et al.
An oxidoreductase enzyme, abundant in tumors, can be catalytically activated to a cytotoxic DNA binding species in human subjects.

SCIENCEPODCAST
www.sciencemag.org/multimedia/podcast
Free Weekly Show
Download the 16 July *Science* Podcast to hear about sharing social responsibility with companies, genetic variants associated with kidney disease, bringing science to Washington D.C. schools, and more.

SCIENCEINSIDER
news.sciencemag.org/scienceinsider
Science Policy News and Analysis

SCIENCE (ISSN 0036-8075) is published weekly on Friday, except the last week in December, by the American Association for the Advancement of Science, 1200 New York Avenue, NW, Washington, DC 20005. Periodicals Mail postage (publication No. 484460) paid at Washington, DC, and additional mailing offices. Copyright © 2010 by the American Association for the Advancement of Science. The title SCIENCE is a registered trademark of the AAAS. Domestic individual membership and subscription (51 issues): $146 ($74 allocated to subscription). Domestic institutional subscription (51 issues): $910; Foreign postage extra: Mexico, Caribbean (surface mail) $55; other countries (air assist delivery) $85. First class, airmail, student, and emeritus rates on request. Canadian rates with GST available upon request, GST #1254 88122. Publications Mail Agreement Number 1069624. **Printed in the U.S.A.**

Change of address: Allow 4 weeks, giving old and new addresses and 8-digit account number. **Postmaster:** Send change of address to AAAS, P.O. Box 96178, Washington, DC 20090–6178. **Single-copy sales:** $10.00 current issue, $15.00 back issue prepaid includes surface postage; bulk rates on request. **Authorization to photocopy** material for internal or personal use under circumstances not falling within the fair use provisions of the Copyright Act is granted by AAAS to libraries and other users registered with the Copyright Clearance Center (CCC) Transactional Reporting Service, provided that $20.00 per article is paid directly to CCC, 222 Rosewood Drive, Danvers, MA 01923. The identification code for *Science* is 0036-8075. *Science* is indexed in the *Reader's Guide to Periodical Literature* and in several specialized indexes.

AAAS
ADVANCING SCIENCE, SERVING SOCIETY

Donald G. Rea is chairman of SSE/AAAS. E-mail: donaldrea@aol.com.

Katherine M. Nielsen is codirector of the SEP/UCSF program. E-mail: katherine.nielsen@ucsf.edu.

A Volunteer Army for Science

LATE LAST YEAR, PRESIDENT OBAMA ANNOUNCED AN "EDUCATE TO INNOVATE" CAMPAIGN TO INCREASE the engagement and performance of America's students in science, technology, engineering, and mathematics (STEM). The United States has more than a million scientists and engineers over 60 years of age with bachelor's degrees or higher, and nearly 600,000 doctoral students and 50,000 postdoctoral trainees in STEM fields. Existing volunteer programs prove that if the government were to dedicate new federal resources, tens of thousands of volunteers could be recruited from these groups and trained to help the United States achieve its national goals.

There are several successful models of programs that bring STEM volunteers into U.S. schools, from early to pre-college stages [kindergarten through grade 12 (K-12)]. In the early 1990s, government funds were used to help form two programs that allow senior scientists and engineers to assist teachers. Retirees Enhancing Science Education through Experiments and Demonstrations (RE-SEED), centered at Northeastern University, operates a middle-school program in the Boston area in addition to training volunteers in other locations. Teaching Opportunities for Partners in Science (TOPS) is led by the San Joaquin County Office of Education in California and targets elementary schools in five northern California counties. Both programs require volunteers to participate for an entire school year and commit a few hours a week. TOPS and RE-SEED have served as examples for more recent programs: the Senior Scientists and Engineers Volunteer Program of the American Association for the Advancement of Science (SSE/AAAS); the Maine School Science Volunteers; and RE-SEED of Silicon Valley, California. Other volunteer programs utilize seniors at different levels of commitment.*

Volunteer programs based in universities recruit younger STEM volunteers: graduate students, postdoctoral fellows, researchers, and students from science-based professional schools. The Science and Health Education Partnership (SEP) at the University of California, San Francisco (UCSF), which began in 1987, works with the San Francisco Unified School District and involves about 100 of its 115 schools. A major component of the program is classroom support, with more than 250 graduate students contributing over 8000 hours annually. Similar programs exist at many other U.S. universities.* In addition, the U.S. National Science Foundation's GK-12 Fellowship Program has, for the past 11 years, provided financial support to nearly 6000 graduate students in science and engineering, each of whom spends up to 15 hours a week in local science classrooms as part of their fellowship obligation.

A key element of all these programs is dedicated leadership. A successful program requires a leader who recruits volunteers and teachers, delineates program expectations, provides support and training for volunteers, and assists partnerships when challenges arise. The training of volunteers is critical. An unprepared scientist who engages with students may do more harm than good, talking over the heads of the students and intimidating them. As an example, in the SEP/UCSF program, volunteers take a course that introduces inquiry-based science teaching, classroom and materials management, research-based teaching strategies, and lesson planning.†

Current volunteer programs rely on a mix of resources. To grow this effort, it is critical that the Educate to Innovate initiative include competitively awarded federal funding for such volunteer programs. A cost of $100,000 per year is a rough estimate for a program with 100 volunteers. For every $1 million spent on these programs, about 100,000 hours of classroom support could be provided, thereby harnessing a vastly underutilized resource for the benefit of K-12 science students. The White House has inspired volunteer scientists and engineers with its Educate to Innovate initiative. Now the Administration must provide the resources needed to help them succeed.

– Donald G. Rea and Katherine M. Nielsen

10.1126/science.1194900

*www.seniorscientist.org. †http://biochemistry.ucsf.edu/programs/sep/workshops-and-classes-teaching-workshops.html.

CREDITS: (TOP LEFT) TERRI REA; (BOTTOM LEFT) LAKISHA WITZEL; (RIGHT) GK-12 PROGRAM/DAVE MORISHIGE

Downloaded from www.sciencemag.org on July 15, 2010

Published by AAAS

Capuchin culture
266

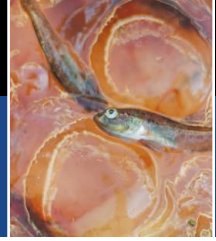

Linchpin of an overfished ecosystem
268

FORENSICS

Familial DNA Testing Scores A Win in Serial Killer Case

A quarter-century of conventional detective work failed to track down the killer responsible for the deaths of at least 10 young women in south Los Angeles dating back to the mid-1980s. But a discarded piece of pizza and a relatively new method of DNA testing has finally cracked the case, police announced last week. On 7 July, L.A. police arrested Lonnie Franklin Jr., 57, a former garage attendant and sanitation worker they suspect is the serial killer nicknamed the "Grim Sleeper."

Since 2008, California has allowed so-called familial DNA searches, in which investigators look for close but not exact matches between DNA evidence collected at crime scenes and the state's data bank of DNA collected from 1.3 million convicted felons. The method has a longer history in the United Kingdom, where it led to a conviction in a murder case in 2004. In Colorado, the method led to a guilty plea in a car-theft case in Denver last year.

The high-profile Grim Sleeper case may encourage other states to adopt familial DNA searches, but the method raises concerns about privacy and ethics, say some legal scholars. "It's hard not to celebrate when an alleged serial killer is caught, but getting carried away based on glamorous cases like this one is a real mistake," says Erin Murphy of the University of California, Berkeley, School of Law.

Last week, *Science* spoke with two scientists involved with the DNA search, senior criminalist Steven Myers and case-work laboratory manager Gary Sims, both based at the Jan Bashinski DNA Laboratory in Richmond, California. They explained that the searches initially focus on 15 regions of DNA on 13 chromosomes. These regions contain genetic stutters called short tandem repeats, in which a pattern of base pairs repeats itself over and over. The number of repeats varies from person to person, and two people who are related are likely to have the same number of repeats at more of these sites. The lab's analysis also considers how frequently a given variation occurs in the general population: two people who share a rare variation are more likely to be related than are two people who share a common one.

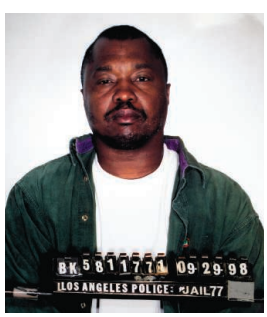

Proud of their work. A familial DNA search by forensic scientists in California led to the arrest of Lonnie Franklin, the suspected Grim Sleeper killer.

Sims and Myers explained that the lab's software uses this information to generate a ranked list of the convicted felons in the DNA database who are most likely to be first-order relatives—parents, children, or full siblings—of the person a DNA sample came from. (They say the statistics aren't strong enough to identify more distant relatives, who share a quarter or less of their DNA.) When both individuals in question are male, the lab also looks at a similar number of short tandem repeats on the Y chromosome, which should be an exact match between fathers and sons and between full brothers.

A 2008 search with DNA evidence from the Grim Sleeper crime scene came up empty. But a second search in April 2010 did turn up a potential match: a young man named Christopher Franklin who was convicted last year on a felony weapons charge. The DNA search along with the dates of the murders cast suspicion on Christopher Franklin's father. After an internal review of the overall case, investigators at the Bashinski lab notified the L.A. police, who followed the elder Franklin and eventually got a DNA sample from a discarded piece of pizza. Lonnie Franklin's DNA matched DNA from the crime scenes, and police arrested him at his home last week. Sims says the lab is proud of its work. "To put this whole thing together … and see it pay off is very gratifying," he says. "Nobody popped champagne bottles or anything like that, but we all feel like we earned our pay."

"I think it's great that this tool was used to catch this defendant," says Hank Greely of Stanford Law School. But he cautions that the method does have downsides. His research suggests that in a database with DNA from a million individuals, hundreds or even thousands of people might have a close enough match to suggest a blood relationship, depending on the strictness of the test and the rarity of the genotypes being tested. If those matches cast suspicion on innocent people, the burden would fall disproportionately on African Americans, who are overrepresented in the U.S. prison population. "It does raise some concerns about discrimination," he says.

For Murphy, these and other costs outweigh the benefits. "We in a free society work on the premise that you have a right to go about your business without answering questions from the government unless they have reason to suspect you of an offense," she says. In her view, familial DNA testing upends that assumption because people can become the target of an investigation solely by virtue of sharing DNA with someone in the database.

Privacy and fairness are also concerns, she says. "It's sending a message to the relatives of convicted people that their privacy is less valuable somehow than that of other law-abiding citizens," Murphy says. "That, to me, is not worth the price." **–GREG MILLER**

CREDITS (LEFT TO RIGHT): COPYRIGHT © 2010 *LOS ANGELES TIMES*/GENARO MOLINA; LOS ANGELES POLICE DEPARTMENT/AP PHOTO

Downloaded from www.sciencemag.org on July 15, 2010

Published by AAAS

BIOSECURITY

New Biosecurity Rules to Target The Riskiest Pathogens

Grading by risk. The government will require tougher security measures for a select group of bioagents.

Ever since the Federal Bureau of Investigation (FBI) implicated U.S. Army researcher Bruce Ivins in the 2001 anthrax letter attacks, U.S. scientists have been nervously anticipating tighter regulations for research involving dangerous pathogens and toxins. But an executive order issued by President Barack Obama earlier this month indicates that the regulations on these so-called select agents may actually end up more streamlined and less burdensome.

The 2 July order from the White House says that the government will put the most dangerous of the 82 items currently on the select-agent list into a high-risk category and consider reducing the number of agents on the overall list. The high-risk category, Tier 1, would potentially be subject to tougher security standards than before, including greater physical security and more rigorous screening of researchers. The remaining select agents could require lesser security measures than now. The government will also harmonize rules across funding agencies.

The move is "the result of an effort to strike a balance between security and science," says Peter Emanuel, who helped draft the order as assistant director of chemical and biological countermeasures at the White House Office of Science and Technology Policy. "The order is consistent with what the scientific community has been calling for all along," says Kavita Berger of the AAAS Center for Science, Technology and Security Policy.

The two departments responsible for oversight of the select-agent program—Health and Human Services and Agriculture—will decide over the next 18 months which items end up in Tier 1. "Right now, for something to be considered a select agent, its impact on public health is the primary determinant," says Emanuel. Several additional factors will now be taken into account, he says, such as the ease with which an agent could be turned into a weapon, how quickly medical countermeasures could be implemented, and available intelligence on whether terrorist organizations might be actively pursuing that particular pathogen or toxin. For example, the lack of effective countermeasures against the Marburg virus would make it a higher security risk than unmodified anthrax, for which vaccines and treatments are available, according to a government report that helped inform the executive order.

As for enhancing physical security for Tier 1 agents, "many labs already have very

BIOETHICS

U.S. Panel Weighs Guidelines for Synthetic Biology

Last week, the United States began the highest review to date—in the president's bioethics commission—of problems that could come out of the young field of synthetic biology. Some scientists who spoke at the meeting in Washington, D.C., on 8 to 9 July warned that the growing ease of manipulating DNA in living organisms could spawn new pathogens and ramp up the risks of bioterrorism. Close oversight is needed, they said; others worried that new rules could stifle research. The commission will take a "deep dive" into the subject before coming back with advice by the end of this year, said University of Pennsylvania President Amy Gutmann, who co-chairs the panel with Emory University President James Wagner.

The impetus for the meeting was a May report in *Science* in which researchers from the J. Craig Venter Institute added a synthetic genome to a bacterial cell and got the cell to replicate using the new DNA (*Science*, 21 May, p. 958; 2 July, p. 52). The day the paper was published, President Barack Obama asked his new bioethics commission to spend 6 months examining the implications of this and other kinds of synthetic biology. The decade-old field includes less controversial efforts, for example, tinkering with combinations of genes in cells to create biological circuits (*Science*, 9 January 2004, p. 158).

The 13 panelists struggled to grasp what is new about synthetic biology. Witness Bonnie Bassler, a molecular biologist at Princeton University, claimed to see only a "slight" novelty compared with what researchers have been doing for 50 years. She decried the hype, especially Venter's "misleading title claiming creation of a bacterial cell," which she said has "unnecessarily alarmed people."

Total immersion. Bioethics panel co-chairs Amy Gutmann and James Wagner are leading a 6-month review of potential future biohazards.

But Venter himself told the commission that synthetic biology is "very different from what's happened before" because it is now relatively easy to build large pieces of DNA from digital code and a DNA synthesizer. This changes the rules, Venter and other witnesses said, because it puts the ability to make the DNA of dangerous (but not replicating) microbes within the reach of students and amateurs.

The discussion was murky on whether synthetic biology requires a new oversight framework. As many noted, existing guidelines cover federally funded research on recombinant DNA, and strict laws control research on select agents, or pathogens that could potentially be used as bioweapons. These rules are being extended to synthetic biology. But Venter and others advocate at least one major change—to make mandatory a voluntary program in which companies now screen DNA orders for sequences of select agents to spot potential bioterrorists.

There is a gap in the system, however:

Downloaded from www.sciencemag.org on July 15, 2010

CREDITS (TOP TO BOTTOM): JAMES GATHANY/CDC; PROVIDED BY PRESIDENTIAL COMMISSION FOR THE STUDY OF BIOETHICAL ISSUES

Published by AAAS

sophisticated security systems like biometric devices for allowing access," says Carol Linden, principal deputy director of the Biomedical Advanced Research and Development Authority and co-chair of the report that the executive order is based on. What's needed now are uniform standards, she says.

The screening and monitoring of researchers working with Tier 1 agents may be a trickier issue. The report issued by Linden's panel recommends enhancing the vetting process for all researchers who work with select agents, including a security check every 3 years instead of the current five. Another recommendation is to do a better job of checking the criminal histories of foreign nationals through cooperation with police agencies overseas. Yet another is to clarify how to identify mental health problems that could lead to potentially criminal or unsafe behavior in the lab.

Researchers have long noted that the select-agent rules have proved a barrier in certain key sectors of public health research such as vaccine development; if the list is shortened, as the executive order suggests, more talent may be attracted to these fields, says David Relman, a biologist at Stanford University in Palo Alto, California.

–YUDHIJIT BHATTACHARJEE

Researchers with no federal funding, called "garage" biologists or "do-it-yourselfers" by several witnesses, aren't necessarily covered. Stanford University engineer Drew Endy proposed a citizen biosafety review process, comparing the situation to self-regulation by amateur radio operators. Harvard University synthetic biologist George Church argued for "licensing and surveillance" of synthetic biology labs.

At several points, Harvard Medical School geneticist and panel member Raju Kucherlapati noted the "déjà vu" tenor of concerns, similar to those first aired about recombinant DNA technology 35 years ago. Indeed, the ground seemed very well-worn in discussions of the ecological risks of releasing a synthetic organism into the environment.

The panelists heard a variety of recommendations: for a moratorium on deliberate releases, for a White House–level office to oversee synthetic biology, and for more funding for the field.

The commission will hold two more meetings in September and November, said Gutmann. She told *Science* that any suggestion that the panel favors new regulations is "totally unfounded." **–JOCELYN KAISER**

CREDIT: DREW TITMARSH/AUSTRALIAN INSTITUTE FOR BIOENGINEERING & NANOTECHNOLOGY

STEM CELL RESEARCH

Scientists Eulogize Center—And Prepare for Stiff Competition

MELBOURNE, AUSTRALIA—The death knell has rung for the Australian Stem Cell Centre (ASCC). Without fanfare, the Australian government has omitted the embattled outfit from its 2011 budget, which will force ASCC to close next June. The center's federally-funded budget of $9.7 million per year will be replaced with two programs that together will spend about $3 million a year on stem cell projects.

The moves will hamper Australia's ability to compete in a hot research field, some scientists claim. "It's a step backwards. Internationally, we're falling further behind," says Melissa Little, a former ASCC chief scientific officer now at the University of Queensland, St. Lucia.

A consortium led by Alan Trounson, now president of the California Institute for Regenerative Medicine, founded ASCC in 2002. Trounson left ASCC the next year amid disagreements over the center's emphasis on commercialization. Tensions culminated in 2008 with the dismissal of CEO Stephen Livesey and the resignation of the entire governing board (*Science*, 24 October 2008, p. 524). In July 2009, ASCC released a new business plan with a more academic bent and last month showcased fresh results at a conference in New South Wales. "Some really great research programs have emerged," says Martin Pera, a former chief of embryonic stem cell research at ASCC who is now director of the Eli and Edythe Broad Center for Regenerative Medicine and Stem Cell Research at the University of Southern California in Los Angeles.

The turnaround was not enough to repair ASCC's tarnished image in the government's eyes. Government funding "was always intended to conclude in June 2011," science minister Kim Carr told *Science*. With ASCC's funding slated to run out in June 2011, the government has unveiled two programs intended to throw researchers a lifeline. The Australian Research Council will offer a 7-year stem cell research initiative funded at $2.6 million a year. And the National Health and Medical Research Council will kick in $400,000 a year for 5 years for a regenerative medicine program that will target translational research.

One big criticism of the new programs is that only university scientists are eligible to apply. That cuts out of the action two leading stem cell centers: the Walter and Eliza Hall Institute (WEHI) of Medical Research here and the Victor Chang Cardiac Research Institute in Sydney. "We're not likely to get all the skills we need if half the people are disenfranchised," laments WEHI Director Douglas Hilton. Another concern is that there may be little left over from the new funds to support ASCC-style patient outreach. It would be a "tragedy" to let ASCC "die on the vine," says Humphrey Firkins, a Queensland-based patients' advocate who suffers from inclusion body myositis, a rare muscle disorder. ASCC's outreach, he says, enabled patients to avoid expensive trips abroad.

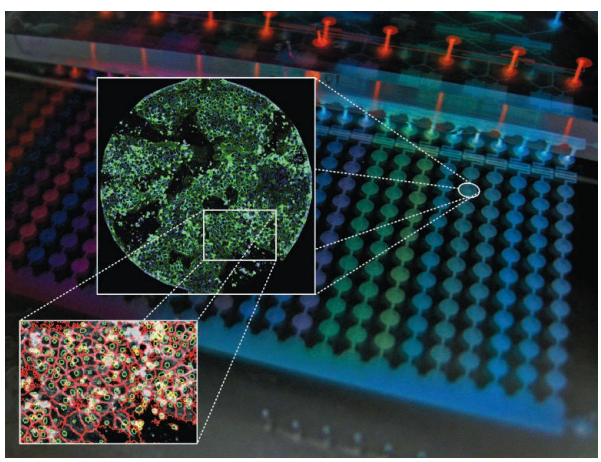

Scientific legacy. Collaborations forged by ASCC produced this tiny stem cell bioreactor.

Scientists are hoping that state governments, universities, and CSIRO, Australia's national science agency, will ride to the rescue with additional stem cell funds. In the meantime, researchers have begun assembling grant proposals—and eulogizing ASCC. "The ASCC brought engineers and biologists together," says Peter Gray, director of the Australian Institute for Bioengineering and Nanotechnology at the University of Queensland. His group teamed up with ASCC's Susie Nilsson and David Haylock, now at CSIRO, to create miniature stem cell bioreactors. This kind of collaboration, says Haylock, "is the legacy of the ASCC."

–ELIZABETH FINKEL

Elizabeth Finkel is a writer in Melbourne.

Downloaded from www.sciencemag.org on July 15, 2010

Published by AAAS

Love hurts. Some capuchin monkeys may test their social bonds by poking each other in the eye.

CREDIT: SUSAN PERRY

ANTHROPOLOGY

Probing Culture's Secrets, From Capuchins to Children

LONDON—Scientists once designated culture as the exclusive province of humans. But that elitist attitude is long gone, as evidenced by a recent meeting* here on how culture, usually defined as the passing on of traditions by learning from others, arises and changes. The 700 attendees, a mixture of researchers and members of the public, heard talks on cultural transmission in fish, meerkats, birds, and monkeys, as well as in extinct and living humans. Researchers probed questions such as what sparks cultural trends and how complex traditions are transmitted, and most agreed that studies of both animals and children will provide important clues. "The field of cultural evolution ranges from fish to humans and includes child development," says meeting co-organizer Andrew Whiten, a psychologist at the University of St. Andrews in the United Kingdom.

But why do certain cultural trends, such as fashions, begin and catch on? Even science finds it hard to answer that question. At the meeting, anthropologist Susan Perry of the University of California (UC), Los Angeles, described her team's work observing white-faced capuchin monkeys since the early 1990s at several sites in Costa Rica. The monkeys have adopted a number of local traditions, some directly related to foraging for food, such as either cracking or rubbing woody capsules of *Luehea* fruits to get out their seeds. But other traditions have no clear survival purpose, such as sniffing each other's fingers and inserting them into a companion's nose, or biting off a big chunk of another monkey's fur and holding it in the mouth while he or she playfully tries to get it back. Although foraging traditions tend to be long-lasting, Perry has found that, perhaps like some human fashions, these more mysterious capuchin trends tend to last only about 10 years or so before fading.

In one group of capuchins, the team's long-term observations have allowed them to witness a rare event: the emergence of a new tradition. In what Perry calls a "bizarre" and "high-risk" ritual, the monkeys poke each other's eyeballs. One monkey will insert his or her long, sharp, dirty fingernail deep into the eye socket of another animal, between the eyelid and the eyeball, up to the first knuckle. In videos Perry played for the meeting, the monkeys on the receiving end of the fingernail, typically social allies, could be seen to grimace and bat their eyelids furiously (as did many members of the audience) but did not attempt to remove the finger or otherwise object to the treatment. Indeed, during these eye-poking sessions, which last up to an hour, monkeys insisted on the finger being reinserted if it popped out of the eye socket.

Why would the monkeys do something potentially dangerous? Perry suggests that capuchins, which, like humans, are highly cooperative and live in large groups, use this apparently pain-inflicting behavior to test the strength of their social bonds. Back in the 1970s, evolutionary biologist Amotz Zahavi of Tel Aviv University in Israel suggested that some animals engage in certain behaviors to solidify alliances, and researchers have observed some examples. For example, some male baboons will hold each other's testicles before teaming up to fight higher-ranking individuals, apparently to establish trust before going into battle.

When it comes to the capuchins, "this is a plausible hypothesis," Whiten says, especially because more functional explanations do not seem to explain the eye poking. Nevertheless, Whiten adds, "it is difficult to test directly."

Perry notes that capuchin behaviors such as eye poking and cracking fruit capsules are true traditions, but they don't ratchet up into the kinds of complex culture prevalent in every human society, from language to literature to sophisticated technology. Animal traditions lack this cumulative cultural evolution.

How do humans wind up the cultural ratchet? At the meeting, Derek Lyons, a developmental psychologist at UC Irvine, presented new data on a phenomenon in young children that he and others think may be key to humans' faithful transmission of complex culture: "overimitation," or the tendency to copy the actions of an adult even when they are unnecessary for achieving a goal. No other animal has been shown to copy in this way, Lyons and others say.

Lyons's work builds on a landmark 2005 study by Whiten and primatologist Victoria Horner, now at Emory University in Atlanta. They demonstrated that when young chimpanzees and children are shown how to retrieve a reward from a box using a series of both relevant and irrelevant steps, the chimps skipped the unnecessary steps, whereas children tended to imitate everything. Recent work by another team

*Culture Evolves, 28–30 June, London, sponsored by the Royal Society and the British Academy. See www.cultureevolves.org.

Downloaded from www.sciencemag.org on July 15, 2010

Published by AAAS

suggests that overimitation is universal in human children (http://news.sciencemag.org/sciencenow/2010/05/kids-overimitate-adults-regardle.html). Lyons and his coworkers reported further work in 3- to 5-year-old children in 2007 in the *Proceedings of the National Academy of Sciences*. For example, children were shown how to retrieve toy turtles from transparent plastic containers using irrelevant steps such as tapping the container with a feather and relevant steps such as opening the container's door. The children continued to overimitate even when they were led to believe that the experiment was over or when they were explicitly told to avoid "silly" extra steps.

Why do children do this? In London, Lyons played a new series of videotaped experiments with children of the same ages in which he attempted to, as he put it, "snap them out of" their overimitative tendencies. In one experiment, a puppet orangutan named Felix, stationed at an opening on the other end of the box, competed with the children to see who could get the toy turtle out of the box first. Again, Lyons showed each child how to get the turtle while mixing in irrelevant actions such as tapping the box and pushing unnecessary levers. The children, who could not see what Felix was doing, continued to perform most of Lyons's irrelevant actions, even when Felix kept winning and getting the turtle.

The only way to avoid overimitation, Lyons found, was to convey that one of his actions was unintentional. When he pretended to get a call from his mother on his cell phone and "accidentally" flipped a useless lever while gesturing during the supposed conversation, the children did not flip that lever.

These findings are inconsistent with earlier hypotheses that children overimitate to please adults, Lyons said. Rather, he concluded, they support something he called "automatic causal encoding" (ACE), in which a child assumes that the adult knows what he or she is doing and that each step in the procedure is necessary. "ACE is an important mechanism kids use to bootstrap their knowledge of complex artifacts," he says. Archaeologist Dietrich Stout of Emory University, who studies prehistoric toolmaking, says ACE may have been important for the cultural transmission of stone-tool technologies in early hominins. "Certain things, like the internal workings of the plastic box or the precise force with which to hit a stone core, are not directly available to the observer," Stout says. He agrees with Lyons that such a strategy is "a logical approach when confronted with a complicated, unfamiliar artifact."

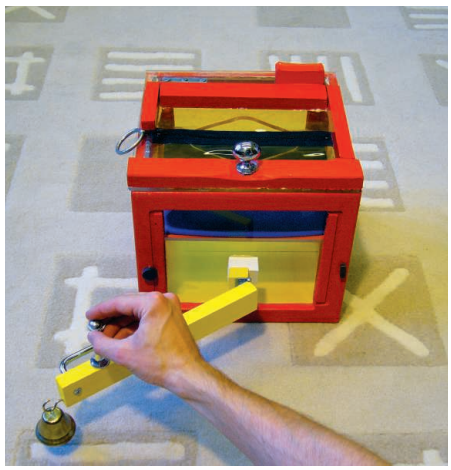

False moves. Young children trying to get a toy out of this box will "overimitate" adults.

Uta Frith, a cognitive neuroscientist at University College London, concurs. "This is an example of actions for which we cannot see rhyme or reason but which we believe are important and relevant to us," Frith says. "I am persuaded that this is the secret of the evolution of human culture."

–MICHAEL BALTER

ScienceInsider

From the *Science* Policy Blog

In one of the final chapters of the controversy over the **stolen e-mails from climate scientists**, an independent panel has mostly cleared researchers at the U.K.'s University of East Anglia (UEA) of scientific malfeasance. The panel, led by Muir Russell (right), declared their "rigour and honesty as scientists … not in doubt." http://bit.ly/UEAclimate

Even so, the panel criticized the climate scientists for **failing to show sufficient openness** in their dealings with outside critics. The researchers had complained that it took too much time to respond to requests for information, official or otherwise, and that the results, in most cases, were used to misrepresent their work. But one scientist told *Science*Insider that researchers should have regular, "built-in transparency" to their data, which could "actually save time" by making responding to requests easier. "That comes with the added benefit of retaining [public] trust in the science of climate change," he said. http://bit.ly/climateopen

Meanwhile, the report came under fire by scientists on both ends of the ideological spectrum. Respected climate scientist John Christy, who questions humanity's role in climate change, said the panel erred by not interviewing leading **skeptic blogger Steven McIntyre**. And Kevin Trenberth, a stalwart among the climate mainstream, said the report, ordered by UEA, should have had a broader mandate to criticize how quotes from the e-mails were taken out of context. http://bit.ly/christymerit and http://bit.ly/trenberthreview

The European Union's 27 member states were poised to decline a request from the European Commission, the union's executive body, to provide extra money to cover **cost overruns for the €16 billion ITER fusion reactor project.** The commission must now figure out how to find the extra money, a tall order in a region already reeling from the global financial crisis. http://bit.ly/iter-funding

After getting spurned in its controversial effort to offer a science prize, the regime controlling Equatorial Guinea has inked a deal to host an African Union "**science observatory**." http://bit.ly/eguineaobserve

In an effort to boost **climate science**, the Chinese government has announced funding for 19 major projects to develop China's earth system models, an investment of roughly $82 million. http://bit.ly/chinaclimate

For more science policy news, visit **news.sciencemag.org/scienceinsider**.

CREDITS (TOP TO BOTTOM): DEREK EUGEN LYONS; SANG TAN/AP PHOTO

Downloaded from www.sciencemag.org on July 15, 2010

Published by AAAS

ECOLOGY

How a Little Fish Keeps Overfished Ecosystem Productive

From a food-web perspective, jellyfish are typically considered a dead end. Few organisms are thought to eat them, so they tend to sink to the ocean bottom, where they slowly decay, their carbon and energy wasted. But off the coast of southwest Africa, researchers have discovered that a small fish called the bearded goby feasts on jellies, and in doing so, helps to sustain seabirds, mammals, and larger fish in that ecosystem. On page 333, they describe this fish's unusual lifestyle, which includes hiding out on the muddy sea floor in water toxic to other fish. "An interesting and counterintuitive new food web [was] created by the [recent] jellyfish bloom," says Roberto Danovaro of the Polytechnic University of Marche in Ancona, Italy. "Certainly similar mechanisms are happening in many places, likely as a result of the ecosystem shift[s] related to global change and direct anthropogenic impacts."

Caught together. Most fish avoid jellyfish, but not the bearded goby, which hides in and eats them.

Until the 1970s, this 9000-square-kilometer region off the coast of Namibia was a rich fishery, particularly for sardines. It's the site of the northern Benguela upwelling, where deeper, nutrient-rich water periodically flows coastward, promoting the growth of plankton. Filter-feeding sardines kept the plankton under control, but as overfishing depleted the sardine stocks, dying plankton sank to the bottom and decayed, using up almost all of the oxygen in the water and creating a so-called dead zone. Jellyfish gorged on the now-abundant plankton, and their numbers exploded.

At the same time, the numbers of bearded goby, *Sufflogobius bibarbatus*, a big-headed fish that grows to about 13 centimeters, increased. With sardines gone, the goby became the main prey of the hake and horse mackerel, as well as food for seabirds, penguins, and seals. Mark Gibbons of the University of the Western Cape in Cape Town, South Africa, and his colleagues were curious about how the goby is able to thrive in such an inhospitable ecosystem. They recruited two goby experts, Anne Utne-Palm and Anne G. V. Salvanes of the University of Bergen in Norway, to help make sense of this little fish.

Gibbons, Utne-Palm, Salvanes, and a cadre of students did a series of field and lab studies of the goby's habits and habitat. They also characterized the water column, assessing the oxygen content and amount of hydrogen sulfide at various depths. "The various elements combine to tell a compelling story," says Andrew Brierley, a marine ecologist at the University of St. Andrews in the United Kingdom.

Most of the region's sea bottom is covered by a thick mud rich in hydrogen sulfide and the bacteria that utilize this toxic gas. Little life exists in the bottom 20 to 60 meters of water, where oxygen levels are less than 10% of the expected level. The goby's predators, for example, can't survive there.

But echo soundings and trawling over a 24-hour period indicated that's where the gobies hang out during the day, Gibbons, Utne-Palm, Salvanes, and their colleagues report. Tests in aquaria with low levels of oxygen showed that these fish stop pumping water and oxygen over their gills in this hostile environment, in a sense holding their breath. Then at night, they ascend to where oxygen levels are higher, catch up on their breathing, and spend time with jellyfish and other organisms.

Many fish, including one of the goby's predators, the horse mackerel, avoid jellyfish. But fishers find jellyfish associated with bearded goby six times more frequently than other fish, says Utne-Palm, and in the lab, gobies frequently hang out among a jellyfish's tentacles or on its bell. She thinks by swimming among the jellyfish, the goby shields itself from potential predators. Its thick, slimy skin may protect it against jellyfish stings.

The jellyfish apparently provide more than shelter: When the researchers examined the stomach contents of gobies and the stable isotope ratios of their tissue—which mimics that of the food they consume—they found that jellyfish represent up to 60% of the goby's diet. Up to a third of the rest comes from sulfur-containing bacterial mats on the sea floor or other components of the mud: The stomachs were often full of diatoms and worms called polychaetes. "It's feeding on things that usually fish don't feed on," says Utne-Palm. "They are bringing dead-end products back into the ecosystem, making the ecosystem more productive than it would be otherwise."

What gets eaten on the bottom gets digested later on, when fish then reoxygenate their tissues. Fish caught at the bottom had undigested stomach contents, whereas those caught at night had begun to process what they had eaten.

Lab experiments also showed that a low oxygen level doesn't impair gobies' behavior or damage their heart the way it does their predators. These fish can also survive what for other organisms are intolerable concentrations of hydrogen sulfide, perhaps by not breathing at all in its presence. "This goby can deal with both low oxygen and with jellies and hence loves the new environment we have created for it, by fishing the heck out of everything else," says Daniel Pauly, a fisheries biologist at the University of British Columbia, Vancouver, in Canada.

Utne-Palm thinks this new food web is fairly stable and that sardines will not make a comeback anytime soon. But at least the goby is helping to keep the new ecosystem productive. "Nobody could have predicted," says Gibbons, "that an insignificant little fish could have turned out to save the day—or at least stabilized the day for us."

–ELIZABETH PENNISI

CREDIT: KIM ANDREASSEN

Downloaded from www.sciencemag.org on July 15, 2010

Published by AAAS

ScienceNOW

From *Science*'s Online Daily News Site

Face to Face With Human Mobility Research

The 2009 H1N1 flu pandemic kept scores of virologists busy, but it also attracted interest from the growing number of scientists studying how people move and interact with one another.

At a session last week at the Eurosciences Open Forum (ESOF) in Turin, Italy, Alain Barrat of the Center of Theoretical Physics in Marseille, France, presented his work using radio-frequency identification tags to monitor interactions in schools, hospitals, museums, and academic conferences. The tags register when another RFID tag is within 1 or 2 meters, thus recording face-to-face contact. (The tag's radio signal can't travel through a person's body.)

Barrat and colleagues monitored how long contacts last and documented networks of contacts for each venue. (A paper will soon appear in *PLoS ONE*, he says.) In the hospital setting, for example, patients rarely meet other patients, which is good, he says, as that should stymie the spread of communicable diseases. http://bit.ly/humans-move

Read more coverage of this year's ESOF at http://news.sciencemag.org/esof.

Can a Stimulating Life Ward Off Cancer?

A provocative new study suggests that leading slightly stressful lives makes mice more resistant to cancer.

Neuroscientists Matthew During and Lei Cao, both of Ohio State University and Cornell University, injected melanoma cells into two sets of young male mice—groups of five animals that had been housed in a bread box–size standard cage with food but nothing else, and groups of 18 to 20 mice that had been raised in a crib-size cage with food, toys, a maze, running wheels, and places to hide.

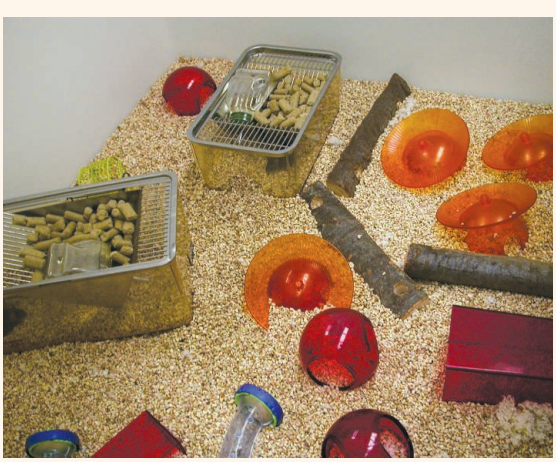

Mice that had spent 3 weeks in the enriched cage developed tumors that were 43% smaller in volume than the tumors of those raised in standard cages. The difference in tumor mass was 77% when the mice had spent 6 weeks in the special cages. And unlike mice raised in standard cages, a few of those in the enriched cages developed no tumors at all, the researchers reported in *Cell*.

Exercise alone didn't explain the effect. Mice raised in a typical cage connected to a running wheel developed tumors just as massive as those of the mice that did no cardio. But the enriched-cage mice had much lower blood levels of leptin, a hormone linked to obesity and cancer. And their hypothalamuses had higher levels of brain-derived neurotrophic factor (BDNF), a growth factor that the researchers suggest inhibits leptin production. The mild stress of living in a larger space with more fellows signals the brain to produce more BDNF, During speculates. http://bit.ly/cages-cancer

Meerkats Have Their Own Traditions

In January, the height of summer in the Kalahari Desert, some meerkats poke their noses out of their burrows as early as 5 a.m. Other groups sleep up to an hour later. Over 11 years of observations, researchers found that each group stuck to its schedule, even when the original members of the population had all died. Meerkats move between groups, so the differences aren't genetic, the researchers reported in the *Proceedings of the Royal Society B*. Instead, the immigrants adapt to the group's customs, and pups learn wake-up time from adults—further evidence, the team says, that nonhumans can have traditions, too. http://bit.ly/meerkat-customs

The Vaccine That Came In From the Cold

Scientists say they have discovered a way to develop cool new vaccines—and they mean that literally. Francis Nano of the University of Victoria, Canada, and colleagues studied a bacterium called *Francisella novicida*, an innocuous cousin of a dangerous human pathogen called *F. tularensis*, which is high up on the list of potential bioterror agents. One at a time, the team swapped out nine essential genes in *F. novicida* for genes from Arctic bacteria, such as *Colwellia psychrerythraea*, a marine microbe that only survives at low temperatures. *Francisella* normally dies at 45°C, but introducing the temperature-sensitive genes lowered that threshold by up to 12°C.

When the team injected these altered strains into the tails of rats, they found that the microbes reproduced locally but didn't spread to the warmer spleen and lungs, as they would normally do. When the researchers injected them into mice, the animals didn't get sick—and they were protected from an otherwise fatal dose of the unaltered *F. novicida* given 3 weeks later. The method, described in the *Proceedings of the National Academy of Sciences*, might be used to develop a better vaccine for TB, Nano says. http://bit.ly/cool-vaccine

Read the full postings, comments, and more at **news.sciencemag.org/sciencenow**.

CREDITS (TOP TO BOTTOM): ALEX THORNTON; ADAM MARTIN

Downloaded from www.sciencemag.org on July 15, 2010

Published by AAAS

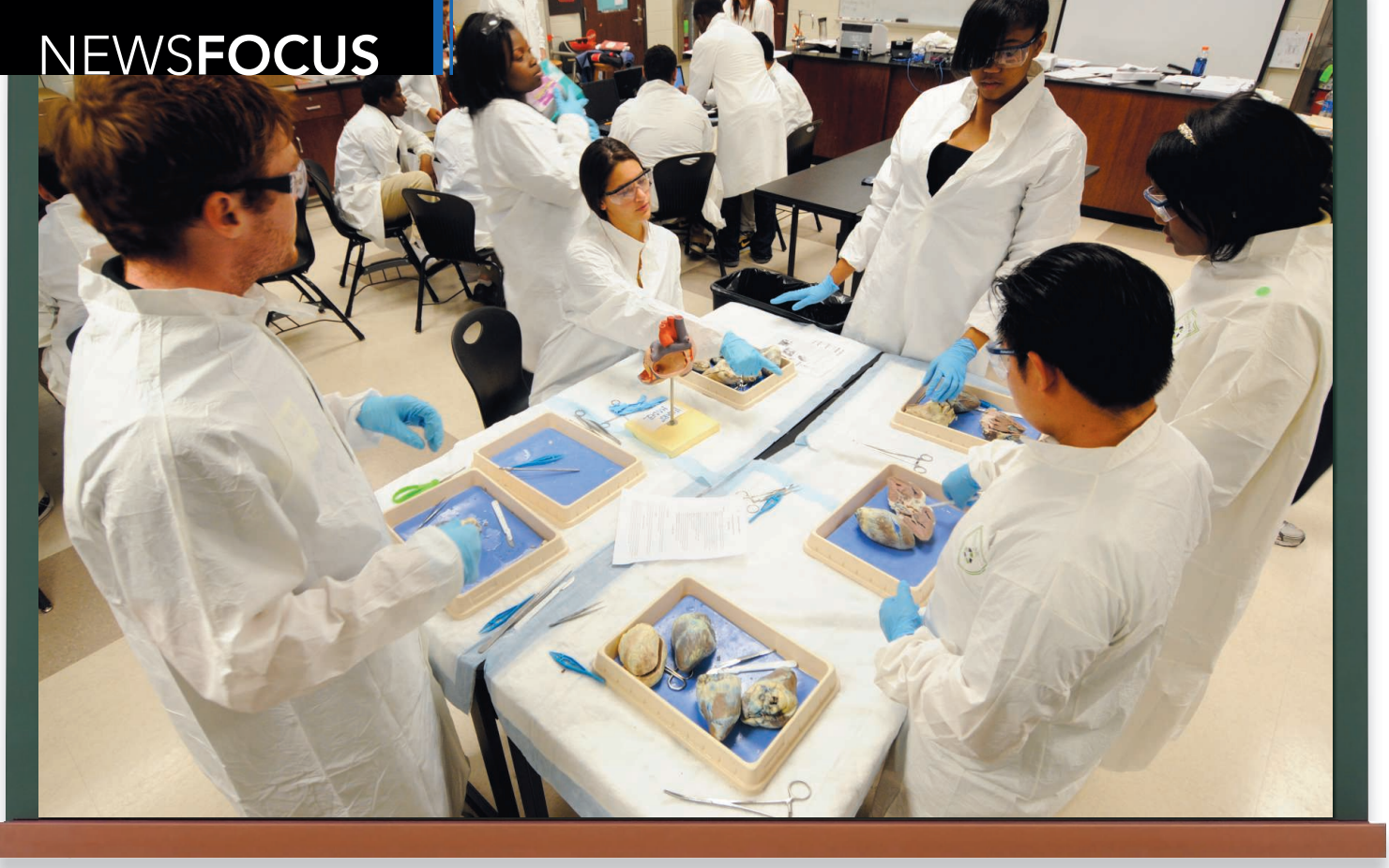

CREDIT: STEVE BARRETT

From the Outside Looking In

A new push to get scientists into the classroom begins with the best of intentions. But that's not always enough, say those involved with the D.C. public schools

MICHAEL KASPAR THOUGHT HE HAD EVERYthing lined up for a special "Celebration of Science" this spring in Washington, D.C. The 6 May event would combine the annual citywide elementary school science fair with the official launch of National Lab Day, an awkward name for an ongoing nationwide effort to link teachers with science professionals in their area via an interactive Web site (nationallabday.org). Officials at the National Science Foundation (NSF), based in nearby suburban Virginia, saw the event as another way to promote STEM (science, technology, engineering, and mathematics) education. The Smithsonian's National Museum of Natural History had agreed to host the affair, and Kaspar's organization, the DC STEM Alliance, would supply the judges and provide logistical support.

The event was meant to funnel some of the thousands of area scientists working at government agencies, professional organizations, and other scientific institutions into the District of Columbia Public Schools (DCPS), a beleaguered urban system with low student test scores and chronic management problems. Teaching science in the public schools is a hard and lonely job under the best of circumstances. Tapping the skills of outside scientists and engineers can be one way to reduce that isolation—and improve the quality of instruction.

But D.C. school administrators were not ready to take on National Lab Day (*Science*, 4 December 2009, p. 1332), and they said they needed more time to organize the citywide science fair. Smithsonian officials didn't want to proceed without a commitment from DCPS. And NSF had its hands full scheduling visits by federal officials to local schools. So the May event was scrapped.

Initiatives such as National Lab Day assume that school systems are eager and able to make use of offers of outside help. Kaspar's experience suggests it's not that simple. To find out, *Science* examined some of those collaborative activities within the D.C. public school system.

Without exception, the outsiders say they welcome the chance to support their local schools. But effective partnerships require a lot more than good intentions and eager volunteers. They also hinge on how much time teachers spend on science, their knowledge of the subject, and the institutional support they receive. What the volunteers bring to the table matters, too. Here are some of their stories.

Does anybody care?

Scientists hoping to partner with D.C. public schools will find a system in the midst of sweeping changes instigated by Michelle Rhee, hired as chancellor by D.C. Mayor Adrian Fenty after the mayor gained control of the system. A national advocate for school reform, Rhee has pushed to improve the quality of the DCPS teaching staff and strengthen its curriculum. Rhee likes to cite gains in student test scores in reading and math, especially in the lower grades, as an early validation of her efforts. There are no comparable results for science, however, and some observers say her impact on science to date has not been so positive.

Downloaded from www.sciencemag.org on July 15, 2010

Published by AAAS

Hearty science. National Lab Day at Bell Multicultural High School brought together scientists from Walter Reed Army Institute for Research and students in Kristy Sundberg's (*above*) physiology and anatomy classes.

CREDITS: STEVE BARRETT

It's certainly disrupted Kaspar's life. Trained as a plant biologist with a Ph.D. in science education, Kaspar was DCPS's director of science for 3 years until he lost his job in July 2009 as part of a downsizing of administrative staff and a reshuffling of responsibilities. His office was eliminated, and the responsibility for science was parceled out to school principals. (Kaspar has remained active in science education through the nonprofit DC STEM Alliance, which he founded.) "I came to DCPS to get a bird's-eye view of what science education was like in an urban district," says James Rountree, a former high school science teacher in a neighboring district whom Kaspar hired. "I had that chance for a few months under Mike. But we don't have a science department anymore," adds Rountree, now a curriculum specialist with no formal responsibilities for science.

Kaspar was responsible for the care and feeding of science teachers throughout the district. His duties included facilitating outside collaborations on citywide science fairs, supplementing the regular curriculum, and helping classroom teachers improve their skills. The elimination of the science department, says one D.C. science teacher, sends a message that "there's no one looking out for science, which means that it's not important and that nobody cares." Not so, says Jennifer Calloway, a DCPS spokesperson. The move was part of a broader effort "to serve teachers in a more coherent way," she says. "General education teachers now coordinate daily science instruction with support from knowledgeable staff in the central office."

Elementary school teachers are in dire need of such support, say science educators. For starters, science plays second fiddle to reading and mathematics, which are the chief metrics for student achievement under the existing federal education laws. Its place on the daily schedule is determined by the school principal, who also decides whether to designate a staff position for a science teacher. As a result, science may be taught for 45 minutes once or twice a week—or not at all.

"We don't do any science because we don't have room for it in the schedule," says Nina Fernandez, a rookie second-grade teacher at Malcolm X Elementary School in Southeast D.C., which last year was designated a STEM catalyst school as part of an attempt to use science to lift some of the district's lowest-performing schools. At best, she adds, "we try to squeeze science and social studies into reading and math lessons."

On a hot Saturday in early May, Fernandez is making bird feeders as part of a series of workshops run by the Carnegie Academy for Science Education (CASE), which has a contract to train teachers at the six STEM catalyst schools. CASE's parent organization—the Washington, D.C.–based Carnegie Institution for Science—began working with D.C. schools on a voluntary basis in 1989. Instead of sending its scientists into the regular classroom, the institution invited students to a Saturday science program called First Light. CASE was created 5 years later to improve the skills of their teachers. "First Light made a huge difference in how the kids did in school," says Toby Horn, who co-directs CASE. "So the teachers and principals asked us to help them, too."

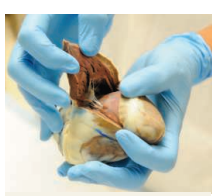

Online
sciencemag.org
Additional anecdotes and photographs of STEM activities.

One of the goals of the CASE training is to give Fernandez and her colleagues at the STEM catalyst schools the content knowledge they need to feel comfortable teaching the subject. "I didn't take any science courses in college," Fernandez admits. "I was prelaw, and the closest thing, I guess, was an environmental law class."

Until then, the burden for teaching science rests on teachers like Melvina Jones, who for the past dozen years has been a science specialist at Burroughs Elementary, a K–8 school near Catholic University in Northeast Washington. "Students could get science from their classroom teachers," Jones says, "but a lot of them shy away from it." She enjoys the challenge: Despite holding an undergraduate degree in biology and a master's in education, Jones says she is now pursuing a second master's degree in physics education "because I wanted to learn more content." And that's notwithstanding a presidential award for science teaching she received in 2004.

But Jones is part of a vanishing breed. There are only about 10 such specialists across the school system's 88 public elementary schools. Their number has shrunk by almost half in the past few years as principals have chosen to put resources elsewhere. And even designated science teachers don't always teach science full-time. Daniel Markus, a science teacher at John W. Ross Elementary in Northwest D.C., taught 10 science classes in 2008–09, allowing him to see most students twice a week. This past academic year, however, the number shrank to seven so that he could help out with math. "I could teach more science," he says, "but my principal decides how much I'll do."

Lighting a fire

For all those reasons, elementary school teachers could use outside help. As head of science, Kaspar organized monthly meetings so that science teachers could swap information about potential partnerships and other ways to improve instruction. But those meetings stopped after he was let go, and his departure has left a void.

"If the teachers aren't plugged in," says Mary Lord, a member of the D.C. state school board and a strong advocate for STEM education, "then how do they find out about opportunities that may arise? It's hard for outsiders to hook up with the school system." With regard to National Lab Day, for example, Lord says one of the organizers told her that, at one point this spring, more teachers from Alaska than from D.C. had signed up for lab day events.

A leading figure in bringing the event into D.C. schools is Netosh Jones, a third-grade teacher at Martin Luther King Elementary School in Southeast D.C. Three years ago, after a decade in the classroom, Jones responded to Kaspar's suggestion and applied for a new teaching fellowship program at NASA to earn a master's degree in

Downloaded from www.sciencemag.org on July 15, 2010

Published by AAAS

science education. Winning it lit a fire under her that continues to burn brightly. "I'm not really a science teacher," she confesses, "but I know that science is important. And after I became an Endeavor fellow, my principal made me the science coach."

Jones has embraced her new role. She has helped Kaspar revive a state chapter of the National Science Teachers Association and has been active in the DC STEM Alliance. And it was no accident that Education Secretary Arne Duncan chose to visit her classroom on 12 May as part of the school's all-day celebration of National Lab Day, a festive event that included dozens of educators, environmentalists, and even a trio of 20-something Hollywood entertainers.

"She's a force of nature," says Horn about Jones. "Even in suburban schools with a lot more resources, you don't see teachers like Netosh." Jones's enthusiasm, backed by a willing principal, has attracted a flood of scientific and engineering talent to the school on an ongoing basis.

Bringing together classroom teachers and scientists is only the first step in improving STEM education. What happens next depends on many factors, including the commitment of the volunteers and the type of encouragement they receive.

Race to the top? Education Secretary Arne Duncan inspects battery-powered cars built by third-grade students at Martin Luther King Elementary School as their teacher, Netosh Jones, looks on.

Two years ago, for example, Kaspar helped arrange a meeting between the new principal of Stanton Elementary School, who Kaspar had heard was interested in strengthening STEM instruction at the low-performing school, and Donald Messer, a former aerospace engineer and business executive. Now retired from the federal government, Messer had recruited a half-dozen or so fellow Rotary Club members to volunteer at a school located in a violence-prone neighborhood of Southeast D.C. far removed from where they live and where tourists visit.

Messer, who holds a Ph.D. in applied mathematics and physics, believes that the twice-a-week math tutoring is making a difference. He points to higher scores on the citywide standardized test administered in spring 2009, and he's anxiously awaiting this year's results. But he acknowledges that the attrition rate among Rotarians has been high. "Some volunteers came once and refused to go back because they were afraid of the neighborhood," he says. He understands their concern but sees no alternative. "There's no point doing this in the nicer parts of town," he says. "Those kids are already doing well, and they have everything they need. Giving money is easy. Volunteering is not easy."

In addition to tutoring math, Messer this year worked with three students on their science-fair projects. One of them even managed to measure the force of gravity by throwing a golf ball in the school gym, timing its ascent and descent with a stopwatch, and then plugging the numbers into an equation Messer provided. "We were pretty close," Messer says about the student's answer, "although I don't think he understood the concept of acceleration."

But the fair itself left a bitter taste in his mouth. Absent any grand "celebration," the citywide fair, hastily organized and barely publicized, was held last month in the basement of an elementary school. It drew students from only 12 of D.C.'s 88 public schools (one-quarter the usual number), and there were so few volunteers that many students had to wait hours to explain their project to a judge. "We made do, but it would have been nice to see more support," says Rountree. Messer was particularly incensed by the school system's decision to shrink the winner's circle for each grade from four in each of 15 categories to three grand-prize winners. The Stanton students were shut out. To compensate for what he calls "their disappointment over total nonrecognition," Messer gave each student a "certificate of achievement"—and a $40 cash prize that came from his own pocket.

A GEM of an idea

What happens at science fairs may seem like small potatoes, but science educators say that fairs, when done properly, give students a rare opportunity to get their hands dirty doing real science. For scientists like Marti Jett, chief of molecular pathology at the Walter Reed Army Institute of Research in Silver Spring, Maryland, the fairs can also serve as a recruiting tool for her ever-expanding outreach program.

Jett leads a team at Walter Reed that for 2 decades has handled the judging for the annual D.C. secondary school science fair—"We started doing it because everybody else seemed to have abandoned them," she explains. She's also involved in the annual Intel Science Talent Search, arguably the country's most prestigious science fair.

But a science fair is not a static, 1-day event for Jett. For the past few years, she and her colleagues have been helping D.C. students conceive and carry out science-rich projects that they will present at the fair. "We tell them, 'Think of something that interests you, research it on the Web, come up with a hypothesis, and then design an experiment to test it.' I refuse to judge a project comparing Tide and Era [laundry detergents]," she says.

That effort is part of a larger internship program that Jett began as a way to diversity the pool of summer students working at Walter Reed. Subsidized initially from her own research funds, the program is called Gains in the Education of Mathematics and Science (GEMS). It has grown beyond her wildest dreams, with support from the U.S. National Institutes of Health and other organizations. GEMS provides "a different perspective" from what students usually get in the classroom, Jett says: "We don't talk about teaching science or math or engineering. Instead, we say, 'Here's the problem. And here's what you need to know to solve it."

Most of the GEMS instructors are undergraduate or graduate students; some are themselves former interns. Jett says these "near peers" are not only more approachable than senior scientists like herself but also role models for students who may have never seen a scientist "who looks like them" and who have lots of questions about what it's like to attend college and major in a STEM field.

To celebrate National Lab Day in May, Jett sent part of her team to Bell Multicultural High School on the Columbia Heights Educational Campus in Northwest D.C. Bell is one of the schools participating in the GEMS program, and the teacher

CREDIT: PHOTOGRAPHY BY PAUL GRAVES @ WWW.PHOTOSRUSSTUDIO.COM

Downloaded from www.sciencemag.org on July 15, 2010

Published by AAAS

Poster children. This spring's citywide elementary school science fair drew many fewer participants and judges than in past years.

CREDITS: J. MERVIS/*SCIENCE*

whose class they visited, Kristy Sundberg, is someone who knows from personal experience how outside scientists can improve classroom instruction.

Sundberg earned a Ph.D. in neuroscience from the University of California, San Diego (UCSD), and completed a postdoctoral fellowship at Yale University before deciding last year to become a high school science teacher. At UCSD she so enjoyed teaching a Saturday neuroscience course to preteen students—"It was definitely not for superbright kids trying to accelerate"—that she tapped into the university's outreach program to help start a student group, then won a $1500 grant from the Dana Foundation to buy supplies, including animal brains. In 2007, she took the idea with her to New Haven, Connecticut, planting a seed that has grown into an even larger enterprise. "Now I'm on the other side," she laughs about her decision to become a high school teacher.

Despite being a rookie, Sandberg has designed her own curriculum. "Each unit is a disease," she explains, "and I cover what students need to know to understand the basic physiology of cancer, diabetes, heart disease, AIDS, and so on." Accordingly, the National Lab Day activity in her classroom focused on the cardiovascular system. Rotating from station to station, Bell students hooked themselves up to blood pressure cuffs and electrocardiogram kits that the GEMS instructors had brought and carved up the sheep hearts that the mentors fished out of buckets. It was the first time that most of her students had seen such equipment, much less had the chance to use it. Students also worked out with a personal trainer and then measured the effect of exercise on their heart rates.

Jett acknowledges what she calls the "wowie" factor of such 1-day visits. But her team also hoped to recruit some students to its summer internships. "We're trying to establish a true mentoring experience," she says, "in which kids come back year after year."

Building bridges

Outsiders can also help teachers add a fresh twist to the regular curriculum. But it's difficult to know how much students actually retain.

William Stafford wanted to give his 10th-grade geometry students at Theodore Roosevelt High School in Northwest D.C. a reward for completing the citywide testing regimen in late April. A second-year teacher who majored in math and is now completing his master's degree in education as a Teach for America fellow, Stafford thought that building a 30-centimeter-long model bridge would give students a chance to apply what they had just learned about angles, proportions, and ratios. And he knew they'd get a kick out of testing its strength.

Stafford teamed up with Sheri Wallach, another Roosevelt math teacher. With $600 from Donorschoose.org, a Web site to help urban teachers, they were able to buy a 2-year supply of kits first developed 30 years ago by physicists at the Illinois Institute of Technology. The kits come with background information on bridge design and the rules for what has grown into an international competition (bridgecontest.phys.iit.edu). For technical expertise, he turned to the National Lab Day site and found Andrew Heier, a 25-year-old engineer who worked at SAIC, a large defense contractor with an office in nearby Arlington, Virginia.

Heier visited Roosevelt a half-dozen times during the 2-week unit and even gave a 15-minute PowerPoint presentation, titled "Sensor Boresight Optimization," on the geometry of tracking a missile launched from Florida at a target in Texas. "I practiced it ahead of time," he confessed. Even so, his talk may have been a bit hard for most of the students to follow. One student, after choosing a bridge type that would divide the span into thirds, couldn't figure out the correct length of each segment, even with a calculator. A reminder from Stafford about the Pythagorean theorem evoked little recognition. The characteristics of isosceles and equilateral triangles seemed a mystery to much of the class.

On "breaking day," students watched intently as Stafford and Wallach piled weights, books, and other objects into the cardboard box dangling from a hook on the underside of each bridge. As each model creaked toward its demise, the teachers would point out what the student might have done to make it sturdier. The project was so popular that two teachers even sacrificed a subsequent lunch period to accommodate students who hadn't finished on time. But there were limits to their generosity. "They get to do it, but they won't get credit," says Stafford, munching on his sandwich. "They need to learn to meet deadlines."

Stafford's rules for the bridge-building unit are a reminder that whatever contribution scientists make to improving STEM education must fit within the parameters of the regular classroom. In the end, it's the classroom teachers who will ultimately determine the success or failure of efforts aimed at bringing scientists into the schools.

–JEFFREY MERVIS

Downloaded from www.sciencemag.org on July 15, 2010

Published by AAAS

ANATOMY

Confronting Anatomy's Nazi Past

Studies uncover a symbiosis between the Nazi regime, which needed to dispose of executed prisoners, and anatomical institutes, which sought bodies for study

In 1938, senior anatomists at the University of Vienna began an unusual arrangement: They worked closely with local Nazi officials to obtain corpses for teaching and research, receiving the bodies of prisoners shot in the Gestapo rifle range or guillotined in Vienna's assize court building. So many corpses were transferred that Viennese authorities ran a special streetcar, dubbed the "Death Transport," between the court and the medical school in the early morning. If the medical school morgue was full, court officials postponed the executions. Viennese physicians secured at least 1337 bodies of Nazi victims this way, according to a report issued by the University of Vienna in 1998.

The Viennese tram is just one example of the systemic relationship that arose between medical schools and executioners across Nazi-controlled Europe. Although other aspects of Nazi science have been explored previously, such as the role of psychiatrists in selecting mentally ill patients for euthanasia, anatomists' broad complicity in Nazi injustices has emerged mostly in papers published in the past year or so.

These studies document the grim symbiosis that arose between anatomists who wanted human bodies for teaching and research and a criminal regime that wanted to dispose quietly of the corpses of large numbers of executed prisoners. Medical schools were assigned particular prisons from which to receive corpses and accepted extra bodies for incineration. One leading Berlin anatomist manipulated the timing of executions and used the terror that female prisoners experienced as they waited to die as a scientific variable in a study, according to research published in *Clinical Anatomy* last year. "The picture is one of a very gradual slippage in moral values among anatomists," says Christoph Redies, a professor of anatomy at the Jena University Hospital in Germany, "to clear outrages and injustices."

The research is prompting German anatomists to acknowledge publicly for the first time the extent of their field's involvement in Nazi abuses. And it raises ethical questions about the continuing use of research and illustrations based on dissections of Nazi victims (see sidebar). Spurred by the new findings, Germany's Anatomical Society is holding its first symposium on "Anatomy in the Third Reich" on 29 September at the University of Würzburg. "We hope that this will contribute to a global debate on ethical standards for the use of human cadavers in research and teaching," says Andreas Winkelmann, an anatomist at Charité Medical University in Berlin.

The symposium is likely to spark intense discussion, for anatomists continue to grapple with the ethics of using bodies from state-sanctioned executions. In 2008, New York state's Attorney General Andrew Cuomo investigated allegations that a touring museum show of plastinated bodies put on by Premier Exhibitions Inc. had displayed the bodies of executed Chinese prisoners who may not have consented to the display. Cuomo could not confirm the allegations, although the company admitted that some remains came from the Chinese Bureau of Police. The company's current show displays only "individuals known to have died of natural causes," says the chief medical director of the show, Roy Glover.

The abundance of new historical data from the Third Reich is bound to fuel a fresh round of debate on such issues. A series of three studies published last fall in *Clinical Anatomy* by anatomist Sabine Hildebrandt of the University of Michigan, Ann Arbor, traces the evolution of practices of German anatomists before and during the Third Reich.

Before the Third Reich, German anatomists used unclaimed corpses from hospitals, psychiatric facilities, and prisons, but the latter was a minor source because Germany executed fewer than 20 civilians a year between 1907 and 1932. After 1933, notes Hildebrandt, the Nazi government meted out death sentences for even minor infractions, such as telling political jokes. So between 1933 and 1945, German prisons executed at least 16,000 civilians. (Only a few of these were

CREDIT: E. PERNKOPF, *ATLAS DER TOPOGRAPHISCHEN UND ANGEWANDTEN ANATOMIE DES MENSCHEN / BD. 1+* 22ND EDITION 1980 ©URBAN & SCHWARZENBERG

Downloaded from www.sciencemag.org on July 15, 2010

The Dilemma of Pernkopf's Atlas

For more than 2 decades beginning in 1933, University of Vienna anatomist Eduard Pernkopf labored on his anatomical atlas, which he published as the *Topographical Anatomy of Man*. He put in 18-hour days dissecting human bodies and supervising a team of artists who painted what he revealed in intricate detail. The resulting four-volume anatomical atlas was described by *The New England Journal of Medicine* in 1990 as "an outstanding book of great value to anatomists and surgeons," and its anatomical illustrations remain unsurpassed even today.

But Pernkopf and several of his artists were avid Nazis, as revealed in a 1988 study by David Williams of Purdue University in West Lafayette, Indiana. A University of Vienna investigation determined in 1998 that Pernkopf's anatomy department received bodies of executed prisoners from the Gestapo and from Vienna's assize court (see main text). "Some of these bodies were certainly used for Pernkopf's atlas," says Williams.

What should anatomists in 2010 do with an atlas that is both scientifically valuable and morally tainted? Researchers remain deeply divided.

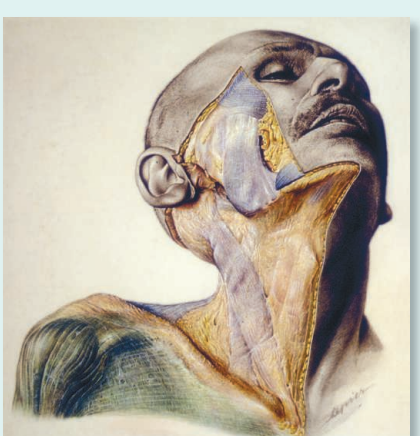

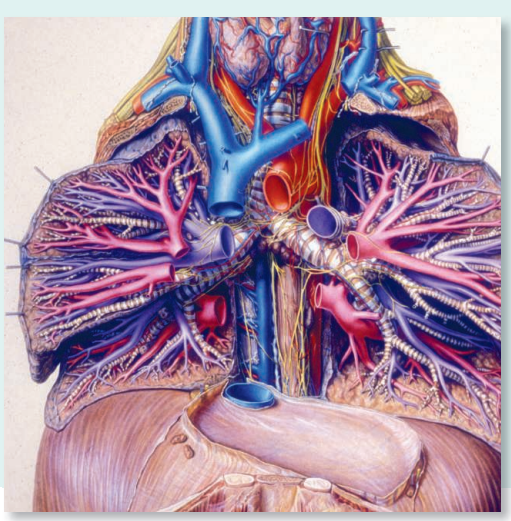

Published by AAAS

members of minorities such as Jews, who were usually transported to concentration or death camps.) By 1942, the corpses of all prisoners convicted of high treason were automatically handed over to anatomists.

Thus, as Hildebrandt's research shows, anatomists became an integral part of the system of capital punishment. Each anatomical institute was assigned to a prison facility that possessed an execution chamber, and anatomists received advance notice of executions. What was then the Berlin Institute of Anatomy, for example, was assigned to Plötzensee Prison, 6 kilometers away, and on an execution day the institute sent an assistant there in a van. "He arrived there before the execution started. Then he waited for the bodies," says Winkelmann. In her study, Hildebrandt determined that 10 German anatomical institutes received a minimum of 3228 such cadavers; data were missing for the remaining 21 institutes. Many anatomists believed that they were doing nothing wrong. "It was all legal," Hildebrandt says.

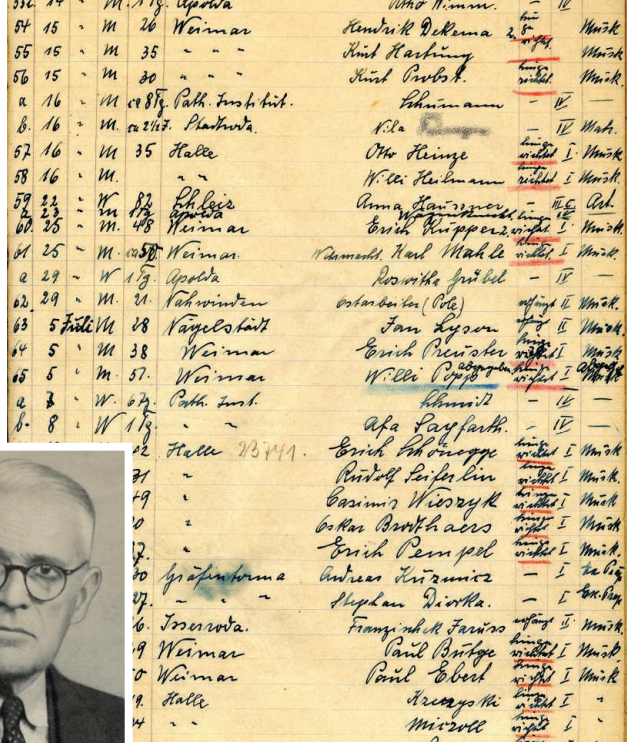

Grim records. A 1943 register from Jena shows cadavers' cause of death, including execution (underlined in red); in Berlin, anatomist Hermann Stieve gathered data on women facing execution.

CREDITS (TOP TO BOTTOM): UNIVERSITY ARCHIVES JENA (UAJ-S XXXVIII, NO. 70/1); CENTER FOR ANATOMY/CHARITÉ - UNIVERSITÄTSMEDIZIN BERLIN, GERMANY

Studying cadavers that were beheaded or bore clear signs of other abuse may have traumatized some students, says Hildebrandt: "There was no way that [the students] couldn't have seen where the bodies came from." In one case traced by Winkelmann and Udo Schagen, a historian at Charité Medical University, a young Berlin Institute of Anatomy researcher named Charlotte Pommer abandoned anatomy after witnessing the dissection of an executed political prisoner whom Pommer had known personally.

In 1999, William Seidelman, now a professor emeritus of family medicine at the University of Toronto in Canada, raised serious questions about the activities of a respected German researcher, Hermann Stieve, director of the Berlin Institute of Anatomy from 1935 to 1952. Over the next decade, Winkelmann and Schagen explored Stieve's work, publishing their findings last year.

By poring over old scientific papers and other records, they found that Stieve was interested in the effects of stress on reproductive systems. In the 1920s, he dissected chickens stressed by the presence of a caged fox. After the Nazis came to power, Stieve examined the effects of stress on the timing of human ovulation. He collected data on 200 female prisoners who were stressed by learning the date of their execution, and he dissected them after their deaths.

Stieve worked closely with prison authorities, Winkelmann and Schagen found. He sent an assistant to Plötzensee to obtain from prison doctors the women's medical histories, as well as data on their menstrual cycles and reactions to the announcement of their execution date. He also persuaded Plötzensee's director to continue conducting executions in the morning, despite the daylight air attacks in Berlin, so tissue samples could be processed the day of the execution. Moreover, Stieve agreed to take the corpses of all the prison's 2915 executed inmates, far more than the institute needed, and burned the excess bodies in the crematory.

Stieve suspended his personal feelings to such a degree, says Winkelmann, that he saw little difference between designing a study on caged chickens and women on death row. Today, some scientists still quote results from Stieve's human studies in their papers, he notes. "What the best and brightest did was see the imprisonment and beheading of human beings as opportunities," Seidelman says.

In 2003, the German Medical Council recommended that German universities remove from their anatomical collections all specimens, including histological slides and human bones, originating from Nazi victims. After investigating their collections, many German universities buried all the Nazi-era human remains in places of honor. But Hildebrandt and other researchers believe that this is only a first step in righting a major historical wrong. They would like to see researchers identify the Nazi victims used by anatomists so that a modern generation can honor their memory today.

–HEATHER PRINGLE

Heather Pringle is the author of *The Master Plan: Himmler's Scholars and the Holocaust* (2005).

Williams, a professor of medical illustration, thinks the injustices recorded in the paintings far outweigh their scientific value and refuses to use the illustrations he once held up as a standard of excellence to his students.

Others, however, think that the atlas can be used if researchers approach the illustrations' subjects in a respectful manner. "As long as you talk about the history of the atlas and the people involved, I think you can keep it and use it as a teaching tool for anatomy as well as for medical ethics," says anatomist Sabine Hildebrandt of the University of Michigan, Ann Arbor, who has also investigated abuses of Nazi-era anatomists.

Pernkopf's sullied masterpiece is not the only troubling scientific legacy of Nazi injustices. For example, the Clara cell, a structure in the human airway, honors Max Clara, an anatomist at the University of Leipzig during the Nazi era. Clara described the cell in 1937 after working on the bodies of executed prisoners, as anatomist Andreas Winkelmann of Charité Medical University in Berlin and medical historian Thorsten Noack of Heinrich Heine University in Dusseldorf revealed in the *European Respiratory Journal Express* in March. "A different term would be preferable," says Winkelmann.

But such eponyms serve an important purpose as testaments to a time when medicine crossed an ethical line, says William Seidelman, professor emeritus of family medicine at the University of Toronto in Canada: "I don't think we should revise history." **–H.P.**

Nazi victims? Eduard Pernkopf's anatomy atlas was a triumph of illustration but included images from the bodies of executed Nazi prisoners.

Downloaded from www.sciencemag.org on July 15, 2010

Published by AAAS

LETTERS

edited by Jennifer Sills

Funding Should Come to Those Who Wait

Long-term studies. Studies spanning decades have yielded insights into red deer and other species.

WE APPLAUD THE PERSPECTIVE BY T. CLUTTON-BROCK AND B. C. Sheldon ("The Seven Ages of *Pan*," 5 March, p. 1207) on the value of long-term behavior and ecological research. We pick up where they left off: funding.

Long-term research has cumulative value that far exceeds its annual rate of return. Sadly, quick empirical studies trump long-term research in the reward system for academic promotion in ecology and behavior. If long-term research is to flourish, we must build a reward system for studies characterized by deferred gratification. A sea change in these values must precede attempts to address funding.

To secure the future of long-term field projects, we must act on three fronts:

(i) We must devise funding mechanisms for "legacy" projects deemed too valuable to falter. Whereas the National Science Foundation's (NSF's) National Ecological Observatory Network and Long-Term Ecological Research programs support long-term collaborative, site-based research, there is a compelling need to support the diversity of long-term investigator-initiated programs. As implemented, NSF's Long-Term Research in Environmental Biology program is a first step, but has insufficient support to maintain many valuable projects.

(ii) We must develop mechanisms to fund the establishment of new programs with long-term potential. Such potential may not be initially appreciated, but with vision and support, new systems studied over the long run will produce novel insights.

(iii) Support for ecological research must be increased. We do not advocate robbing Peter (short-term research) to pay Paul (long-term research). However, we maintain that Paul has already been robbed and some balance needs to be restored.

Most of us involved in long-term research have a story to share, in which time-limited funding shortages took our programs to the edge of a precipice. Investigators that succeed and become known for long-term research, almost by definition, have found a way to adapt to funding shortfalls, usually at great personal sacrifice. A recent case at the Los Amigos Biological Station in the Peruvian Amazon speaks to the value of funding continuity (*1*). During a 4-year period of programmatic support, the scientific productivity of the station surged, producing many valuable findings and building substantial scientific capacity for the region. Since the funding evaporated, the station has failed to return to its former glory, at great loss to our ability to make scientific inroads into understanding the ecology of this area, characterized by unrivaled biodiversity.

Of course, long-term programs must remain intellectually vibrant and methodologically rigorous if they are to be supported. In the end, the onus is on ecologists to convince ourselves, society, and funding agencies that long-term research has unique and irreplaceable value.

RONALD R. SWAISGOOD,[1]* JOHN W. TERBORGH,[2] DANIEL T. BLUMSTEIN[3]

[1]Applied Animal Ecology, San Diego Zoo's Institute for Conservation Research, San Diego, CA 92027, USA. [2]Center for Tropical Conservation, Duke University, Durham, NC 27705, USA. [3]Department of Ecology and Evolutionary Biology, University of California, Los Angeles, CA 90095, USA.

*To whom correspondence should be addressed. E-mail: rswaisgood@sandiegozoo.org

Reference

1. N. C. A. Pitman, *Trends Ecol. Evol.* **25**, 381 (2010).

Brazilian Law: Full Speed in Reverse?

IS IT POSSIBLE TO COMBINE MODERN TROPICAL agriculture with environmental conservation? Brazilian agriculture offers encouraging examples that achieve high production together with adequate environmental protection (*1*, *2*). However, these effective practices may soon lose ground to the conventional custom of resource overexploitation and environmental degradation.

A revision to the Forest Act, the main Brazilian environmental legislation on private land, has just been submitted to Congress, and there is a strong chance that it will be approved. The proposed revision raises serious concerns in the Brazilian scientific community, which was largely ignored during its elaboration. The new rules will benefit sectors that depend on expanding frontiers by clear-cutting forests and savannas and will reduce mandatory restoration of native vegetation illegally cleared since 1965. If approved, CO_2 emissions may increase substantially, instead of being reduced as was recently pledged in Copenhagen. Simple species-area relationship analyses also project the extinction of more than 100,000 species, a massive loss that will invalidate any commitment to biodiversity conservation. Proponents of the new law, with well-known ties to specific agribusiness groups, claim an alleged shortage of land for agricultural expansion, and accuse the current legislation of being overprotective of

Letters to the Editor

Letters (~300 words) discuss material published in *Science* in the previous 3 months or issues of general interest. They can be submitted through the Web (www.submit2science.org) or by regular mail (1200 New York Ave., NW, Washington, DC 20005, USA). Letters are not acknowledged upon receipt, nor are authors generally consulted before publication. Whether published in full or in part, letters are subject to editing for clarity and space.

CREDIT: MEHMET KARATAY/WIKIMEDIA COMMONS

Downloaded from www.sciencemag.org on July 15, 2010

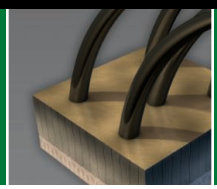

Not noncoding
284

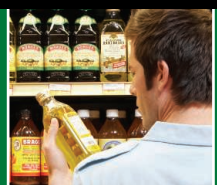

Consumer concerns
287

the environment in response to foreign interests fronted by green nongovernmental organizations. However, recent studies (*3*) show that, without further conversion of natural vegetation, crop production can be increased by converting suitable pastures to agriculture and intensifying livestock production on the remaining pasture. Brazil has a high potential for achieving sustainable development and thereby conserving its unique biological heritage. Although opposed by the Ministry of the Environment and most scientists, the combination of traditional politicians, opportunistic economic groups, and powerful landowners may be hard to resist. The situation is delicate and serious. Under the new Forest Act, Brazil risks suffering its worst environmental setback in half a century, with critical and irreversible consequences beyond its borders.

JEAN PAUL METZGER,[1]* THOMAS M. LEWINSOHN,[2] CARLOS A. JOLY,[3] LUCIANO M. VERDADE,[4] LUIZ ANTONIO MARTINELLI,[5] RICARDO R. RODRIGUES[6]

[1]Department of Ecology, Institute of Bioscience, University of São Paulo, 05508-900, São Paulo, SP, Brazil. [2]Department of Animal Biology, State University of Campinas, Campinas, SP, Brazil. [3]Department of Plant Biology, Biology Institute, State University of Campinas, Campinas, SP, Brazil. [4]Center of Nuclear Energy in Agriculture, University of São Paulo, Piracicaba, Brazil. [5]Program on Food Security and the Environment, Stanford University, Stanford, CA 94305, USA. [6]Department of Biological Sciences, "Luiz de Queiroz" College of Agriculture, University of São Paulo, Piracicaba, Brazil.

*To whom correspondence should be addressed. E-mail: jpm@ib.usp.br

References

1. D. Nepstad *et al.*, *Science* **326**, 1350 (2009).
2. C. R. Fonseca *et al.*, *Biol. Conserv.* **142**, 1209 (2009).
3. G. Sparovek *et al.*, *Considerações sobre o Código Florestal brasileiro* ("Luiz de Queiroz" College of Agriculture, University of São Paulo, Piracicaba, Brazil, 2010); http://eco.ib.usp.br/lepac/codigo_florestal/Sparovek_etal_2010.pdf.

TECHNICAL COMMENT ABSTRACTS

Comment on "Observational and Model Evidence for Positive Low-Level Cloud Feedback"

Anthony J. Broccoli and Stephen A. Klein

Clement *et al.* (Reports, 24 July 2009, p. 460) provided observational evidence for systematic relationships between variations in marine low cloudiness and other climatic variables and found that most current-generation climate models were deficient in reproducing such relationships. Our analysis of one of these models (GFDL CM2.1), using more complete model output, indicates better agreement with observations, suggesting that more detailed analysis of climate model simulations is necessary.

Full text at www.sciencemag.org/cgi/content/full/329/5989/277-a

Response to Comment on "Observational and Model Evidence for Positive Low-Level Cloud Feedback"

Amy C. Clement, Robert Burgman, Joel R. Norris

Broccoli and Klein argue for additional diagnostics to better assess the simulation of cloud feedbacks in climate models. We agree, and here provide additional analysis of two climate models that reveals where model deficiencies in cloud simulation in the Northeast Pacific may occur. Cloud diagnostics from the forthcoming Climate Model Intercomparison Project 5 should make such additional analyses possible for a large number of climate models.

Full text at www.sciencemag.org/cgi/content/full/329/5989/277-b

CORRECTIONS AND CLARIFICATIONS

News of the Week: "Invisibility cloaks for visible light must remain tiny, theorists predict" by A. Cho (25 June, p. 1621). The size limit on a cloak for infrared or visible light was misstated. It is a few hundred micrometers, not a few micrometers.

News Focus: "Putting light's light touch to work as optics meets mechanics" by A. Cho (14 May, p. 812). In the third paragraph, "pitchfork" should have been "tuning fork."

Reports: "Community structure in time-dependent, multiscale, and multiplex networks" by P. J. Mucha *et al.* (14 May, p. 876). Equation 3 contained a typographical error that was not caught during the editing process: The δ_{sr} term should have been outside of the parentheses within the square brackets. The correct equation, which also appears in the supporting online material as equation 9, is to the right. See the revised supporting online material (www.sciencemag.org/cgi/content/full/sci;328/5980/876/DC2), which also includes a correction to equation 11. The computations supporting the examples described in the Report were all performed with the correct formula for $Q_{\text{multislice}}$. The authors thank Giuseppe Mangioni for pointing out the error.

$$Q_{\text{multislice}} = \frac{1}{2\mu}\sum_{ijsr}\left[\left(A_{ijs} - \gamma_s \frac{k_{is}k_{js}}{2m_s}\right)\delta_{sr} + \delta_{ij}C_{jsr}\right]\delta(g_{is}, g_{jr})$$

Sponsors of Traumatic Brain Injury Project

I'M DELIGHTED THAT *SCIENCE* TOOK THE TIME to highlight the ongoing efforts of the Common Data Elements Project for research in psychological health and traumatic brain injury ("New guidelines aim to improve studies of traumatic brain injury," G. Miller, News of the Week, 16 April, p. 297). The level of interagency collaboration that made the project possible is exactly the type of leadership that Americans should expect from the federal government.

As noted in the story, the project is cosponsored by four federal agencies—three of whom were mentioned. The other agency is the National Institute on Disability and Rehabilitation Research (NIDRR) within the Department of Education. NIDRR has leadership, resources, and subject matter experts without which this project would not have been nearly as successful. Together, all four agencies will continue to develop recommendations and support ongoing efforts to improve and refine the Common Data Elements.

GEOFFREY MANLEY

Department of Neurosurgery, Brain and Spinal Injury Center, University of California, San Francisco, CA 94110, USA. E-mail: manleyg@neurosurg.ucsf.edu

Warming, Photoperiods, and Tree Phenology

C. KÖRNER AND D. BASLER ("PHENOLOGY under global warming," Perspectives, 19 March, p. 1461) suggest that because of photoperiodic constraints, observed effects of temperature on spring life-cycle events cannot be extrapolated to future temperature conditions.

However, no study has demonstrated that photoperiod is more dominant than temperature when predicting leaf senescence (*1*), leafing, or flowering, even in beech—one of the species most sensitive to photoperiod (*2*, *3*). On the contrary, the literature [e.g., (*4*, *5*)] supports the idea that spring phenology is highly dependent on temperature during both the endodormancy phase (the period during which the plant remains dormant due

Downloaded from www.sciencemag.org on July 15, 2010

Published by AAAS

to internal factors) and the ecodormancy phase (the period during which the plant remains dormant due to external, environmental conditions). Warming temperatures have a negative impact on endodormancy (the chilling requirement is unfulfilled, delaying dormancy break) and a positive impact on ecodormancy (bud cell growth accelerates). Therefore, tree phenology does not respond linearly to increasing temperature (*6*, *7*). The key concern should be quantitatively assessing the net balance between these antagonistic warming effects on spring phenology.

ISABELLE CHUINE,[1]* XAVIER MORIN,[2] HARALD BUGMANN[2]

[1]Centre d'Ecologie Fonctionnelle et Evolutive, 34293 Montpellier cedex 5, France. [2]Forest Ecology, Institute of Terrestrial Ecosystems, Department of Environmental Sciences, ETH Zürich, Universitätstrasse 22, 8092 Zürich, Switzerland.

*To whom correspondence should be addressed. E-mail: isabelle.chuine@cefe.cnrs.fr

References and Notes

1. N. Delpierre *et al.*, *Agric. For. Meteorol*. **149**, 938 (2009).
2. K. Kramer, *J. Appl. Ecol*. **31**, 172 (1994).
3. Y. Vitasse, S. Delzon, J.-M. Louvet, A. Kremer, R. Michalet, *Agric. For. Meteorol*. **149**, 735 (2009).
4. I. Chuine, K. Kramer, H. Hänninen, in *Phenology: An Integrative Environmental Science*, M. D. Schwarz, Ed. (Kluwer, Dordrecht, Netherlands, 2003), vol. 39, pp. 217–235.
5. H. Hänninen, K. Kramer, *Silva Fenn.* **41**, 167 (2007).
6. X. Morin *et al.*, *Glob. Change Biol.* **15**, 961 (2009).
7. X. Morin, J. Roy, L. Sonié, I. Chuine, *New Phytol.* **186**, 900 (2010).
8. Funded by the European Community's FP7 (BACCARA project number 226299), CNRS and ETH.

Response

IN OUR PERSPECTIVE, WE CONCLUDED NEITHER that temperature is an irrelevant environmental driver for phenology nor that photoperiodism in trees is dominant in all cases. Our Perspective was merely a reminder of the classical research on the influence of photoperiod on phenology in late successional trees. Dormancy release is driven by a finely tuned interplay between chilling requirement, photoperiod, and warm temperatures.

For example, during winter, the transition from endodormancy to ecodormancy is mediated by chilling temperatures. Insufficient chilling during a mild winter is likely to delay the development toward sprouting in spring (*1*). However, a long photoperiod may partially compensate for a lack of chilling. In this way, photoperiodism helps to stabilize the time of dormancy release (*2*–*4*). In photoperiod-sensitive species, sprouting may be considerably delayed in short photoperiods (*4*, *5*), even in fully chilled buds (e.g., after cold winters) (*6*). Warm temperatures are most effective in promoting bud burst only after the photoperiod requirement of adequately chilled buds is met (*3*, *6*). This process prevents trees from sprouting before the risk of freezing damage is over.

Photoperiodism in trees has been known for almost 100 years (*7*, *8*), but is an often-ignored environmental cue when predicting the effects of a future climate.

CHRISTIAN KÖRNER* AND DAVID BASLER

Institute of Botany, University of Basel, 4056 Basel, Switzerland.

*To whom correspondence should be addressed. E-mail: ch.koerner@unibas.ch

References and Notes

1. X. Morin *et al.*, *Glob. Change Biol.* **15**, 961 (2009).
2. O. M. Heide, *Physiolog. Plant.* **88**, 531 (1993).
3. R. Häkkinen, T. Linkosalo, P. Hari, *Tree Physiol.* **18**, 707 (1998).
4. V. Sanz-Perez, P. Castro-Diez, F. Valladares, *Plant Biol.* **11**, 142 (2009).
5. P. F. Wareing, *Physiol. Plant.* **6**, 692 (1953).
6. O. M. Heide, *Physiol. Plant.* **89**, 187 (1993).
7. P. J. Kramer, *Plant Physiol.* **11**, 127 (1936).
8. G. Klebs, *Abh. Heidelb. Akad. Wiss.* **3** (1914).
9. Funded by Velux-Foundation and NCCR-climate of the Swiss Science Foundation.

Call for Papers

Science Signaling

Science Signaling, from the publisher of ***Science***, AAAS, features top-notch, peer-reviewed, original research weekly. Submit your manuscripts in the following areas of cellular regulation:

- Biochemistry
- Bioinformatics
- Cell Biology
- Development
- Immunology
- Microbiology
- Molecular Biology
- Neuroscience
- Pharmacology
- Physiology and Medicine
- Systems Biology

Science Signaling is indexed in CrossRef and MEDLINE

Subscribing to ***Science Signaling*** ensures that you and your lab have the latest cell signaling resources. For more information visit **www.ScienceSignaling.org**

Submit your research at: www.sciencesignaling.org/about/help/research.dtl

Science Signaling
AAAS

Downloaded from www.sciencemag.org on July 15, 2010

Published by AAAS

HISTORY OF SCIENCE

Belief, Reason, and Insight

Steven A. Frank

The way a scientist chooses problems and interprets nature can be deeply influenced by political views or religious beliefs. At the same time, the scientific truths that last the centuries have a coldly inhuman, rational purity beyond the motivations and beliefs of their human authors. George Price's story brings us up against these alternative traces of history.

The Price of Altruism
George Price and the Search for the Origins of Kindness
by Oren Harman
Norton, New York, 2010. 461 pp. $27.95, C$35. ISBN 9780393067781. Bodley Head, London. £20. ISBN 9781847920621.

Price made three profound contributions to evolutionary theory. First, the Price equation for the effect of selection on a trait (*1*) provided the foundation for the modern analysis of social evolution. W. D. Hamilton completely reworked his famous theory of kin selection after Price explained to him the severe limitations of his original formulation and the need to use Price's equation. The equation also gives the most general understanding of natural selection, transcending genetics to include cultural change, learning, and all forms of dynamical change arising from transmission and biased success. Second, John Maynard Smith's interest in the application of game theory to evolution came directly from Price's original formulation of ritualized combat in animals. In Price's work, mutually armed détente in animal combat arises from the Nash equilibrium of game theory. The first general expression and application of the widely used evolutionarily stable strategy concept in evolutionary games came from Price's work. Third, Price's analysis of R. A. Fisher's fundamental theorem of natural selection cleared up four decades of confusion. Establishing the generality of Fisher's theorem, Price's insight opened the way for a fully realized understanding of natural selection as a central process in all types of evolutionary change.

Each insight was so different from the common thought of its time. How did Price do it? Who was he, and where did he come from? Pieces of the story have been known among evolutionary biologists, just enough to make clear that the history was very strange and in the end very sad. We now welcome Oren Harman's deeply researched life of Price. Harman, a historian of science at Bar Ilan University, tells Price's story well.

Price was born in New York in 1923. His father died early, and the family fortunes crashed with the stock market in 1929, leading to much stress in family life. Price's personality developed early: vain, brilliant, difficulty relating to others, but somehow always secure in his own independent ability to see problems clearly. He obtained a Ph.D. in chemistry at the University of Chicago, working as part of the Manhattan Project. His secret research won a competition for the best method to detect radiation exposure by fluorescent analysis of urine samples. He moved from one science job to another—always recognized for his outstanding ability to solve problems but never staying long with any particular work. He was married, had two daughters, became restless, and was bitterly divorced. Moving, studying, and seeking, he published articles in leading journals and magazines about extrasensory perception, methods for the rapid design of new machines, and the arms race. He had ideas and often real insight on seemingly everything. But after his initial success, he rarely finished anything. Usually alone, he took lower-status jobs or did not work at all.

Price had health problems; a botched surgery caused partial paralysis. He obtained some insurance money in a settlement and, at 44, set off for England to begin again, to focus his mind, to make his reputation. Ambitious, certain of his ability, painfully aware of his failure, he increasingly felt the need to do good the only way he knew how—by his belief in clarity of analysis above all else. Day after lonely day in London libraries, Price slowly moved toward problems of evolution, altruism, and game theory. Maybe he could understand the biological roots of kindness, and do so more deeply than others ever had. By some internal story, he perhaps felt that a success in such studies would assuage his prior failings, make his mark in life, and turn things around.

Just as Price succeeds against all odds, making his three great contributions and touching on other topics, he starts on a series of religious conversions. Having scored, by pure reason alone, a triumph on biological altruism and the most abstract theories of natural selection, he loses faith in science and begins to study scripture with a zeal and analytical power that scares his religious mentors. Then even the scriptural analysis wanes, and he turns to help the downtrodden. Not just to help but to give all he has of his time, possessions, and love—to the point that he becomes as downtrodden as those he sought to help. Struggles and depression follow; at last, suicide.

Harman takes us through all of this. But the book is much more ambitious than just a story of Price's life and work: "Our tale teaches that the people doing science, their backgrounds, historical context, family histories, education, political views, religious affiliations, temperament—all play a role." Harman supports this view by providing vignettes of Thomas Huxley's atheism, Fisher's Anglicanism, Prince Peter Kropotkin's anarchism, and numerous other sketches of the faiths and world views of scientists who touched on problems of altruism and human morality in relation to biology. Each scientist's accomplishments are seen in relation to wider aspects of personal faith and moral outlook. The book's first part jumps between Price's early life and an often dizzying patchwork of disparate scientific and personal biographies. Always interesting, these sketches often leave one off balance as the narrative spins

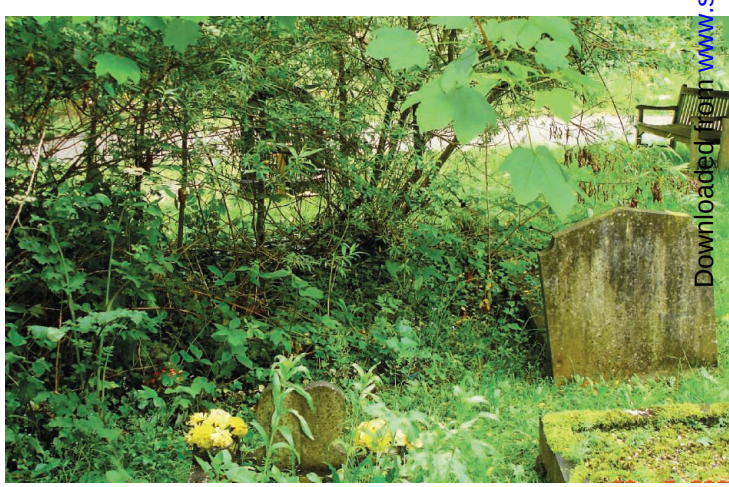

Unmarked grave. Price's burial site, covered by brush to the left of the tombstone, Saint Pancras Cemetery, London.

CREDIT: OREN HARMAN

The reviewer is at the Department of Ecology and Evolutionary Biology, University of California at Irvine, Irvine, CA 92697–2525, USA. E-mail: safrank@uci.edu

Downloaded from www.sciencemag.org on July 15, 2010

Published by AAAS

in another direction or back to Price's emerging story. The thesis does not come until the epilogue: "[O]ur story holds a deeper moral that may not be so easy to fathom: One of the pressing challenges of our times is defining the boundary between questions that can be addressed meaningfully by science and those that are outside its purview." I do not find that moral hard to fathom. Personal meaning and scientific insight are distinct.

Perhaps more interesting, Harman's telling of Price's life implicitly but very strongly takes a stand on the origin of scientific insight. In Harman's view, Price's fundamental scientific work followed from his deep humanistic desires to contribute to the greater good. Similarly, Harman views Fisher's great contributions to evolutionary theory through his reactionary Anglican social views. There can be no question that personal outlook can strongly influence a scientist's work. But that humanistic perspective fundamentally misses an important component of scientific insight and accomplishment. To consider the complementary humanistic and coldly scientific perspectives, let us turn to Newton, perhaps the greatest of all scientists.

John Maynard Keynes, who collected many of Newton's manuscripts on alchemy and religion, saw Newton as "the last of the magicians" rather than "the first of the age of reason":

> [Newton] looked on the whole universe and all that is in it as a riddle, as a secret which could be read by applying pure thought to certain evidence, certain mystic clues which God had laid about the world to allow a sort of philosopher's treasure hunt to the esoteric brotherhood. He believed that these clues were to be found partly in the evidence of the heavens and in the constitution of elements … but also partly in certain papers and traditions handed down by the brethren in an unbroken chain back to the original cryptic revelation in Babylonia. He regarded the universe as a cryptogram set by the Almighty …. By pure thought, by concentration of mind, the riddle, he believed, would be revealed to the initiate. (*2*)

One could say that Newton's mad, lonely pursuit was all about his dreams of the glory of his Christian god. But how much does that matter? In the personal history, in understanding motivation, it matters a lot. But whatever Newton thought he was doing, that has no bearing on the truth of force equals mass times acceleration, the bending of light, the calculus, or the foundations of modern science. Anyone who has suffered the hard work of science knows of the duality of mind required. Motivation, personal belief, whatever it may be, is ephemeral and ultimately independent from the impersonal hard evidence and critical testing that determine lasting scientific truths. It is a fine part of history to reconstruct researchers' personal dreams of glory or god. Scientists may need such dreams to keep them going through the long, hard hours. But after the discovery, it is only the outed secret of nature that matters. Or so the scientist may feel. Whereas the historian, the humanist, will perhaps care more for the faith, the loneliness, the personal story of pain and ultimate victory against all odds. In those very human aspects of science, one may choose to see a mirror that reflects back meaning to one's own personal story. Nonetheless, all great scientists have a second, independent core of rationality that dominates in the long run. Despite the complexities of the tormented life that Harman recounts in *The Price of Altruism*, Price's scientific contributions had that purity of complete and rational order—an austerity and abstractness from all humanistic consideration so complete that it stands alone in the history of evolutionary theory.

References

1. G. R. Price, *Nature* **227**, 520 (1970).
2. J. M. Keynes, *The Collected Writings of John Maynard Keynes*, vol. 2 (Macmillan, London, 1972), pp. 363–364; www-groups.dcs.st-and.ac.uk/~history/Extras/Keynes_Newton.html

10.1126/science.1193026

HISTORY OF SCIENCE

Imagination in Chemistry

Peter J. Ramberg

Modern chemists routinely shuttle between the immediate empirical, sensual characteristics of substances in the laboratory and the invisibly small world of atoms and molecules. Like mathematicians, chemists do much of their thinking on paper, doodling chemical formulas or tinkering with hand-held molecular models. They think in a highly visual, nonverbal way. The origin of this way of thinking lies in the middle of the 19th century, when an extraordinary group of chemists, most of them in Great Britain and Germany, developed productive techniques for revealing the invisible world of the molecule. By 1890, nearly all chemists could "see" what molecules looked like at the microscopic level, meaning they had access to the explicit connections between atoms in the molecule and how those atoms are arranged in space. The ability to elucidate the structure of molecules down to the atomic level by purely macroscopic manipulation of chemicals is arguably one of the greatest intellectual accomplishments of 19th-century science. Yet in crafting their generalized accounts of past science, historians of science have largely ignored this achievement—equal in its importance to Darwin's theory of natural selection. For example, two recent and prominent surveys of the history of modern science do not discuss chemistry after the introduction of John Dalton's atomic theory in the very early 19th century (*1*, *2*). Reading such histories, uninformed readers would get the impression that the science of chemistry was completed by 1810, when in fact, it was just getting started in visualizing the microstructure of our world.

Image and Reality
Kekulé, Kopp, and the Scientific Imagination
by Alan J. Rocke
University of Chicago Press, Chicago, 2010. 401 pp. $45, £29. ISBN 9780226723327. Synthesis.

In *Image and Reality*, Alan Rocke (a historian of science at Case Western Reserve University and the author of several previous works on 19th-century organic chemistry) offers a masterful account of how chemists crafted a unique visual language of the microworld. The book spans the 50 years from 1840 to 1890 but concentrates on the period between roughly 1855 and 1865, when chemists developed the structural theory of organic chemistry. Rocke has previously described that period as a "quiet revolution," because the change happened relatively quickly and without much controversy (*3*). *Image and Reality* highlights another extremely important dimension of the quiet revolution, demonstrating that it was during the development of the theory of chemi-

The reviewer is at the Department of Chemistry, Magruder Hall, Truman State University, 100 East Normal Street, Kirksville, MO 63501, USA. E-mail: ramberg@truman.edu

Downloaded from www.sciencemag.org on July 15, 2010

Published by AAAS

MOLECULAR BIOLOGY

Hiding in Plain Sight

Small peptides encoded by a so-called long noncoding RNA play an active role in regulating gene expression.

Miriam I. Rosenberg and Claude Desplan

The roles of RNA in protein synthesis are well known—as a template for translation of cellular proteins and as ribosomal and transfer RNA (tRNA). However, more recent studies have elucidated the intricate functions of other abundant types of RNAs, such as microRNAs (miRNAs) and small inhibitory RNAs (siRNAs), which control the expression of target messenger RNAs (mRNAs) (*1*). Despite this extensive catalog of functional RNAs, many transcribed RNAs still lack an obvious protein product or the characteristic structure of known functional RNAs. Except for a few examples involved in gene silencing and imprinting (*2*, *3*), the importance of so-called long noncoding RNAs (lncRNA) remains controversial (*4*, *5*). On page 336 of this issue, Kondo *et al*. (*6*) show that an RNA called *polished-rice* (*pri*) has features of a lncRNA, but encodes tiny peptides that control gene expression during development in the fruit fly *Drosophila melanogaster*.

The *pri* gene was first identified as *millepattes* (*mlpt*) in the flour beetle, *Tribolium*, by virtue of its developmental role in body patterning (*7*). The same gene is responsible for the defects in leg, embryonic epidermis, and respiratory system of *pri* mutants [(also called *tarsal-less* (*tal*) in *Drosophila* (*8*, *9*)]. Surprisingly, the gene underlying these important functions does not encode a single large protein or functional RNA, but rather four or five small peptides of 11 to 32 amino acids that are highly conserved among insects (*10*). Unlike many bioactive peptides, Pri peptides are not processed from a longer precursor protein. Instead, the *pri* RNA is polycistronic and encodes several redundant units that are independently translated.

Kondo *et al*. used the epidermal phenotype of the *pri* gene to investigate the function of its peptide products in the *Drosophila* embryo. Specialized epidermal cells build apical projections (bristles) known as trichomes. A master gene, *shavenbaby* (*svb*), controls trichome formation: *svb* mutants lack trichomes, and *svb* expression determines where trichomes form. Indeed, most evolutionary changes in insect trichome patterning are due to modifications of *svb* cis-regulatory elements (*11*). *svb* encodes a multidomain transcription factor that activates expression of trichome-promoting genes (*12*). *pri* mutants also lack trichomes and exhibit altered expression of *svb* transcriptional targets. They do not, however, affect *svb* expression.

How does *pri* work with *svb* to differentiate trichomes in the epidermis? The critical interaction requires *pri* as a temporal switch during trichome formation. Pri peptides direct removal of a large amino-terminal fragment of the Svb protein that contains a transcriptional repression domain. This removal switches Svb from a repressor to an activator of transcription (see the figure). In the absence of *pri*, Svb retains its repression domain, and thus prevents trichome formation. The ability of Pri peptides to direct proteolytic cleavage of a transcription factor within the same cell is a new function for bioactive peptides. How these peptides impart specificity to a protease (and to which protease) is still not clear.

Because the *pri/tal/mlpt* gene is highly conserved and is found in all insects, it is not merely a derived character of *Drosophila*. Furthermore, *pri* mutant flies have additional phenotypes that do not require *svb*, so Pri peptides likely act on other proteins as well. Remarkably, despite the sequence conservation of Pri peptides, their function in insects appears to have evolved rapidly: *pri/tal* does not seem to play a role in embryo segmentation in flies as *mlpt* does in beetles. This highlights the exciting possibility of a new class of regulatory molecules with diverse and dynamic func-

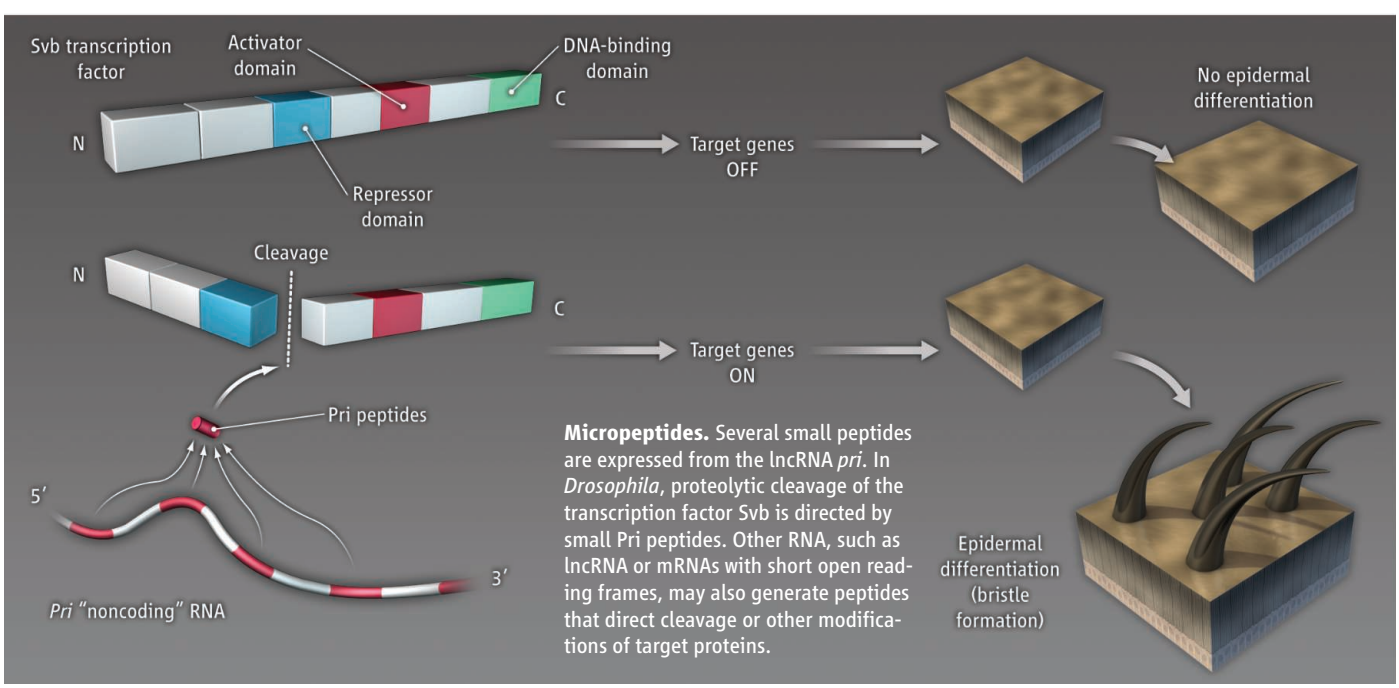

Micropeptides. Several small peptides are expressed from the lncRNA *pri*. In *Drosophila*, proteolytic cleavage of the transcription factor Svb is directed by small Pri peptides. Other RNA, such as lncRNA or mRNAs with short open reading frames, may also generate peptides that direct cleavage or other modifications of target proteins.

CREDIT: C. BICKEL/*SCIENCE*

Center for Developmental Genetics, Department of Biology, New York University, New York, NY 10003, USA. E-mail: cd38@nyu.edu

Downloaded from www.sciencemag.org on July 15, 2010

Published by AAAS

tions that may be hiding in plain sight.

Because of their small size, Pri peptides cannot be identified by genome annotation or by protein prediction algorithms whose threshold of detection is about 100 amino acids. Like the miRNA genes *lin-4*, *let-7*, or *bantam*, the *pri/tal/mlpt* gene was identified by classical forward genetics (starting with a mutant phenotype and then identifying the underlying gene). One exciting question that remains unanswered is how many functional peptides might be hidden among RNAs. Some might be encoded by short open reading frames found in 5′-untranslated regions of mRNAs. An estimated 40% of *Drosophila* mRNAs contain such uORFs and some show signs of evolutionary conservation, suggesting that they are translated (*13*). Ribosome profiling, which sequences ribosome-bound mRNAs, has validated the translation of a number of uORFs in yeast (*14*), and vertebrate genomes have similar percentages of uORF-containing transcripts, which await similar analysis (*15*). When added to the lncRNAs of unknown function, there are many places to look for additional regulatory peptides like Pri. If only some of these transcripts encode active peptides that possess multiple protein substrates, then the scope of posttranslational regulation could quickly expand.

Small functional peptides could evolve rapidly. Random mutations that introduce start codons in existing lncRNAs (or within untranslated regions of coding mRNAs) could generate small peptides that are easily selected to perform a specific function. Many proteins (like Svb) have multiple functional domains, and proteolytic cleavage of one of these domains directed by small peptides may alter protein specificity, stability, localization, or function. A simple recognition code whereby small peptides act as adaptors to direct proteolytic machinery to different protein targets would make a small collection of peptides highly serviceable. Adapting such small peptides to target proteins might open the way to new therapeutic approaches (such as antivirals).

Why does nature need yet another mode of gene regulation? The same question was raised for miRNAs and their modulatory role. The ability of small peptides to quickly alter activities of target proteins without elaborate and time-consuming translation of large proteins suggests a niche for these tiny players as temporal switches. Thus, the discovery of a regulatory mechanism for small peptides highlights how a different reading of the same genomes could reveal additional surprises.

References

1. P. P. Amaral *et al.*, *Science* **319**, 1787 (2008).
2. J. E. Wilusz *et al.*, *Genes Dev.* **23**, 1494 (2009).
3. C. P. Ponting *et al.*, *Cell* **136**, 629 (2009).
4. M. Guttman *et al.*, *Nature* **458**, 223 (2009).
5. J. L. Tupy *et al.*, *Proc. Natl. Acad. Sci. U.S.A.* **102**, 5495 (2005).
6. T. Kondo *et al.*, *Science* **329**, 336 (2010).
7. J. Savard *et al.*, *Cell* **126**, 559 (2006).
8. M. I. Galindo *et al.*, *PLoS Biol.* **5**, e106 (2007).
9. T. Kondo *et al.*, *Nat. Cell Biol.* **9**, 660 (2007).
10. J. I. Pueyo, J. P. Couso, *Dev. Biol.* **324**, 192 (2008).
11. A. P. McGregor *et al.*, *Nature* **448**, 587 (2007).
12. H. Chanut-Delalande *et al.*, *PLoS Biol.* **4**, e290 (2006).
13. C. A. Hayden, G. Bosco, *BMC Genomics* **9**, 61 (2008).
14. N. T. Ingolia *et al.*, *Science* **324**, 218 (2009).
15. S. E. Calvo *et al.*, *Proc. Natl. Acad. Sci. U.S.A.* **106**, 7507 (2009).

10.1126/science.1192769

BIOCHEMISTRY

Reengineering Enzymes

First-principles design and directed evolution expand the role of enzymes in chemical synthesis.

Stefan Lutz

The versatility and proficiency of enzymes makes them promising catalysts for the laboratory and for industrial synthesis of organic molecules, yet natural biocatalysts often do not meet the scientists and engineers' expectations in regards to stability, selectivity, and specificity. On pages 309 and 305 of this issue, two different approaches show how enzymes can be engineered to make them part of the organic chemist's toolkit. Using a first-principles approach, Siegel *et al*. (*1*) applied the Rosetta design software to create an enzyme that performs the stereoselective, intermolecular Diels-Alder cycloaddition, a reaction of great value to organic synthetic chemistry. In contrast, Savile *et al*. (*2*) used structure-based rational design and directed evolution to reprogram the substrate specificity and stability of a native transaminase to replace a rhodium-based hydrogenation catalyst in the production of an antidiabetes compound, sitagliptin.

The enzyme design reported by Siegel *et al*. is the latest example of synthetic biocatalysts for Diels-Alder cycloadditions (*3*–*5*). In this reaction, a conjugated diene (a molecule with two adjacent double bonds) and a dienophile (that donates one double bond) form a cyclic product by the simultaneous formation of two new chemical bonds. The Diels-Alder reaction enjoys great popularity among chemists for the rapid and stereoselective assembly of complex molecules and natural products (*6*, *7*), yet there are only two confirmed examples of naturally occurring Diels-Alderases (DAs), and both catalyze only intramolecular cycloadditions (*8*, *9*).

Tackling the challenge to create a synthetic DA for intermolecular cycloaddition, Siegel *et al*. began with a computational model of the transition state, which sets the geometrical arrangement of the two substrates in the enzyme active site. The substrates' electronic properties were modulated by placing hydrogen-donating and accepting amino acid side chains near the dienophile and diene, respectively, to lower the energy barrier to reaction (see the figure, panel A). Based on this core design, quantum-mechanical simulations then generated an ensemble of ~10^{19} so-called theozymes, which varied the two assisting amino acid side chains and their orientation relative to the model of the transition state.

In a massive computational undertaking, the RosettaMatch algorithm next matched all of the theozyme conformers against a library of 207 protein scaffolds (known protein folds) to identify ~10^6 theozymes that fit into one or more of the scaffolds. The authors subsequently used a combination of RosettaDesign software and scientific intuition to optimize the active site geometry of selected candidates and to eliminate questionable designs. Of the remaining 84 candidates that they synthesized by protein expression, two designs, DA_20_10 and DA_42_04, showed small but significant increases in DA activity relative to the uncatalyzed reaction. After additional fine-tuning of selected residues in the active sites by site-specific mutagenesis, these enzymes matched the performance of catalytic antibodies for this reaction, and did so with excellent stereoselectivity and for multiple reaction cycles.

Built on first principles, these enzyme designs not only test our understanding of protein structure and function but also allow

Chemistry Department, Emory University, Atlanta, GA 30322, USA. E-mail: sal2@emory.edu

Downloaded from www.sciencemag.org on July 15, 2010

Published by AAAS

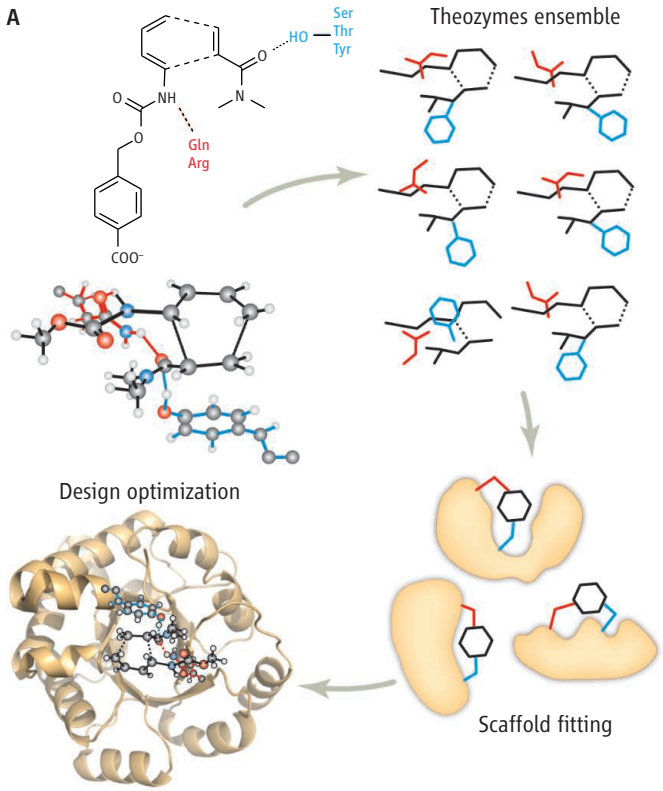

Tailoring enzymes to specific reactions. (**A**) Siegel *et al*. designed an enzyme to perform the Diels-Alder reaction between two molecules based on first principles. They computer-generated a large ensemble of structures in which two key amino acids in the active site (depicted in red and blue) are bound to the transition state. These structures were fitted to a protein scaffold, and target enzymes were then designed and synthesized. (**B**) Savile *et al*. reprogrammed the substrate specificity of a transaminase to perform a reaction in the industrial production of an antidiabetes drug, sitagliptin. Mutational hot spots shown in red are in the active site, and those shown in yellow stabilize binding of the dimeric form of the active enzyme.

prediction and exploration of individual mutations on the overall performance of the biocatalyst. In DA_20_10, each of 15 amino acid changes contributed to the new catalytic function, and the effects of intricate design differences, such as the choice of a glutamine over a glutamate as hydrogen acceptor, were predicted accurately.

The work by Siegel *et al*. is a milestone in enzyme design, extending the application of the Rosetta algorithm for de novo biocatalyst design beyond reactions that break bonds in a single substrate, such as the Kemp elimination and retro-aldolase reaction (*10*, *11*). Nevertheless, the rates of these DAs are still slow compared with most native enzymes. The discrepancies in catalytic performance between native and synthetic biocatalysts suggest that there are major contributing factors to enzymatic activity that have not been considered in our current designs. For example, protein dynamics and the functional contribution of correlated motion to catalysis in enzymes remain an intriguing but controversial factor yet to be explored in design approaches (*12*, *13*).

Savile *et al*. describe a more pragmatic approach to the tailoring of a biocatalyst. Undesirable process conditions and problems with product quality during the asymmetric rhodium-catalyzed hydrogenation step in the production of the antidiabetes compound, sitagliptin, spurred their exploration of a transaminase substitute. Transaminases are enzymes that catalyze the enantioselective transfer of an amino group from a donor substrate via a pyridoxamine intermediate onto the carbonyl group of an acceptor substrate. Savile *et al*. envisioned a direct transamination of prositagliptin ketone (see the figure, panel B). This approach would shorten the process by one step and improve product quality by taking advantage of the high stereo and enantioselectivity of the enzyme.

However, initial screening of native transaminases quickly established the absence of any detectable enzymatic activity for bulky substrates such as prositagliptin ketone (the immediate precursor to the final product). Furthermore, process conditions demand high substrate concentrations, which can be achieved with the poorly water-soluble prositagliptin ketone only by adding organic solvent and raising temperatures, either of which diminishes enzyme lifetime.

Savile *et al*. used structure-based rational design followed by directed evolution to alter the substrate specificity and improve the stability of ATA-117, a transaminase from *Arthrobacter* sp. (*14*). They first used docking studies between a homology model of ATA-117 and prositagliptin ketone to identify potential steric conflicts and unfavorable interactions in the enzyme active site that prevent substrate binding in native enzymes. Guided by the computational model, the binding pocket for the substrate's triazolo piperazine moiety could be optimized by site-saturation mutagenesis of a single position while substitutions in three positions expanded the binding pocket for the trifluorophenyl group. Although the catalytic activity of the resulting ATA-117 variant for prositagliptin ketone was rather low, the establishment of detectable transaminase activity for the target substrate at this stage was critical to the subsequent directed evolution protocol (*15*, *16*).

They next applied 10 rounds of directed evolution, using a combination of site-saturation and random mutagenesis, as well as DNA shuffling, to select transaminase variants with the highest catalytic activity while raising the fraction of organic solvent to 50%, the reaction temperature to 40°C, and the prositagliptin ketone concentrations to 200 g/l. The best enzyme variant not only met these selection criteria but performed the desired transamination with >99.9% enantiomeric excess. Its 27 amino acid substitutions were found not only in the enzyme active site but also in a second hot spot at the protein-protein interface of the ATA-117 homodimer, where they likely help to stabilize the protein. Overall, the work by Savile *et al*. is an impressive demonstration of tailoring enzymes to specific requirements and the potential of biocatalysis to revolutionize chemical processes in industry.

The reports by Siegel *et al*. and Savile *et al*. are a testimony to our current under-

Downloaded from www.sciencemag.org on July 15, 2010

Published by AAAS

standing of enzymes. While the successful design of DAs illustrates the advances (and limitations) in our knowledge of biocatalysis fundamentals, the customized transaminase shows our technical capabilities to effectively manipulate existing enzymes. Together, our current design and directed evolution methods offer the possibility to create new enzymes to meet specific reaction requirements for a wide range of synthetic, industrial, and therapeutic applications.

References and Notes

1. J. B. Siegel *et al.*, *Science* **329**, 309 (2010).
2. C. K. Savile *et al.*, *Science* **329**, 305 (2010).
3. D. Hilvert *et al.*, *J. Am. Chem. Soc.* **111**, 9261 (1989).
4. B. Seelig, A. Jäschke, *Chem. Biol.* **6**, 167 (1999).
5. T. M. Tarasow *et al.*, *Nature* **389**, 54 (1997).
6. K. C. Nicolaou, S. A. Snyder, T. Montagnon, G. Vassilikogiannakis, *Angew. Chem. Int. Ed. Engl.* **41**, 1668 (2002).
7. E. M. Stocking, R. M. Williams, *Angew. Chem. Int. Ed. Engl.* **42**, 3078 (2003).
8. K. Auclair *et al.*, *J. Am. Chem. Soc.* **122**, 11519 (2000).
9. H. Oikawa, K. Katayama, Y. Suzuki, A. Ichihara, *J. Chem. Soc. Chem. Commun.* **1995**, 1321 (1995).
10. L. Jiang *et al.*, *Science* **319**, 1387 (2008).
11. D. Röthlisberger *et al.*, *Nature* **453**, 190 (2008).
12. S. Hammes-Schiffer, S. J. Benkovic, *Annu. Rev. Biochem.* **75**, 519 (2006).
13. K. A. Henzler-Wildman *et al.*, *Nature* **450**, 838 (2007).
14. D. Koszelewski *et al.*, *Adv. Synth. Catal.* **350**, 2761 (2008).
15. N. J. Turner, *Nat. Chem. Biol.* **5**, 567 (2009).
16. R. J. Kazlauskas *et al.*, *Nat. Chem. Biol.* **5**, 526 (2009).

17. Supported by NIH GM69958.

10.1126/science.1192224

ECONOMICS

Consumers Who Care

Can consumers and businesses benefit from socially responsible pricing?

Stefano DellaVigna

People care about others and have concerns for fairness. In a nutshell, this was the finding of early laboratory experiments in economics (*1*, *2*). That people parted with their own money either to benefit anonymous others or to punish unfair subjects, rocked the economic model of selfish decision-makers. But how exactly do people care? Although economists have made great progress in parsing the exact nature of this concern in laboratory experiments, little is known about how concern for others plays out in consumer markets and in corporate decision-making (*3*). On page 325 of this issue, Gneezy *et al*. present some interesting evidence in this regard (*4*). Their results indicate that the impact of consumer concerns about fairness can be at once powerful and subtle.

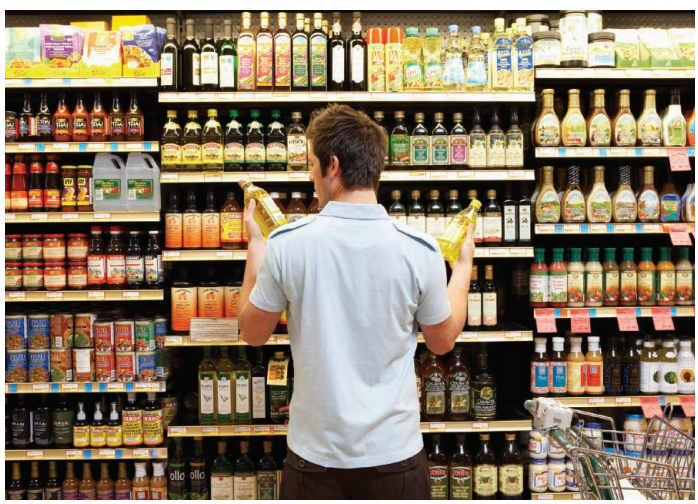

CREDIT: NOEL HENDRICKSON/GETTY IMAGES

Making the sale. Consumer concern for fairness can influence markets and business decisions.

Gneezy *et al*. investigated the extent to which social preferences—such as a taste for fairness and concern for the public good—can increase the sale of a product. Their focus was not on a fair-trade product such as coffee, in which concern for the welfare of farmers readily translates into higher willingness to pay for a product. Rather, the question the authors addressed was whether a company can benefit from appearing altruistic even when the product is as pedestrian as a souvenir photo taken at an entertainment park. In brief, the answer is yes, but the devil is in the details.

Gneezy *et al*. investigated consumer behavior in four situations. In one case, a company selling photos charged consumers a standard price with no charitable contribution announced. In another scenario, photos were sold at whatever price the consumer named—a "pay-what-you-want" condition. The latter was extremely successful in raising sales by a factor of 16 relative to the standard price situation. However, the average price offered by consumers was so low that the company barely recovered the costs of printing and selling a photo. Even though the pay-what-you-want offering presumably showed generosity or at least fairness by the company, and sales skyrocketed, profits tanked. This option thus makes no sense businesswise.

In another condition, the company retained standard pricing but stated that it would give half of the proceeds to charity. This scenario did indeed raise sales, but only by 18%. The revenue gains are small, or even negative, if one subtracts from the revenue the amount given to charity. This result is similar to observed patterns for sellers on eBay. When a seller on eBay advertises that 10% of the proceeds will be devoted to a charity, the sale price of an item (which is determined by consumers) increases, but only by 2% (*5*).

In another treatment, the company upped the ante on the appearance of generosity and altruism, offering pay-what-you-want, of which 50% would go to charity. This treatment raised sales by a factor of 10 relative to the standard pricing with charity, and the average sale price was sufficiently high to guarantee a generous profit margin. The combination worked for the company. But why was this option not as successful in raising sales as the straight pay-what-you-want strategy? Certainly, a generous offer by the company can trigger additional sales. But many of the additional sales are likely to be "cheapskates" (so-called free-riders) who purchase at very low prices. Hence, offers such as pay-what-you-want have the potential to ruin a business if consumers purchasing at very low prices are sufficiently common. When the photo company coupled pay-what-you-want with offering money to charity, these cheapskates abstained from buying rather than paying more for a photo and engaging in altruistic behavior.

This result has interesting implications for understanding social preferences. One possibility is that charitable giving by a company triggers a generous, altruistic response, such that cheapskates restrain and "reciprocal" customers (those that act mutually in return with generous actions) buy at moderate or high prices. This impulse is strong enough to generate purchases of high enough prices in the condition that links pay-what-you-want

Department of Economics, University of California, Berkeley, CA 94720, USA. E-mail: sdellavi@econ.berkeley.edu

Downloaded from www.sciencemag.org on July 15, 2010

Published by AAAS

with charitable giving, but not strong enough such that costumers would spend as much as the standard price (which is higher) when coupled with charity. An alternative interpretation is that the charitable giving by the company does not trigger additional generosity by the consumer, but rather creates additional social pressure. Thus, in the presence of the charitable-giving offer, a consumer may feel bad about not making a purchase or about paying a very low price.

The two explanations are not equivalent. If consumers give because of social pressure, they will dislike being offered the photo with the charity option because this raises the social pressure to give. Instead, genuine altruists are happy to be offered the charity option because they feel good about giving. This distinction dictates the welfare consequences of the corporate strategies studied by Gneezy *et al*.: If giving is due to social pressure, the socially responsible pricing by the company can make the consumers worse off by raising the social pressure costs of not buying.

Recent work separates the two explanations in the context of a door-to-door fund-raising campaign (*6*). A standard fund-raiser was compared to one in which a flyer was placed on doorknobs to notify households 1 day in advance of an upcoming fund-raising visit. The flyer condition lowered the number of households who contributed money, particularly the ones giving small amounts. Thus, when caught at home, households gave (small) amounts because of social pressure, but when notified, did not participate at all in giving by avoiding the solicitor.

To test for the two interpretations in the context of the Gneezy *et al*. study, it would be interesting to run the following additional experimental sessions: For two parallel events in the entertainment park, offer the pay-what-you-want with charity option in one, and the standard price payment in the other. If consumers make purchases as a result of social pressure, they should opt for going to the event with the standard price offer so as to avoid paying the social-pressure cost. If, however, giving is driven by genuine reciprocity, the consumers should be happy to choose the pay-what-you-want with charity option.

Another question that the Gneezy *et al*. study raises is the extent to which the company could have done even better if they had offered a lower fixed price coupled with the charity option. In this case, one could have avoided altogether the free-riders, while taking advantage of the positive social preferences triggered by the charity option. One could therefore test whether the pay-what-you-want condition is by itself perceived as generous.

What is obvious from the study by Gneezy *et al*. is that incorporating social preferences into consumer pricing is an interesting but tricky business. The key advantage of a field experiment like that by Gneezy *et al*. is the possibility to easily study variations. And like laboratory experiments, field experiments that are run in corporations and organizations (*6*) should allow the design of conditions to provide new evidence and test models of social preferences.

References

1. W. Güth, R. Schmittberger, B. Schwarze, *J. Econ. Behav. Organ.* **3**, 367 (1982).
2. R. Forsythe, J. L. Horowitz, N. E. Savin, M. Sefton, *Games Econ. Behav.* **6**, 347 (1994).
3. S. DellaVigna, *J. Econ. Lit.* **47**, 315 (2009).
4. A. Gneezy, U. Gneezy, L. D. Nelson, A. Brown, *Science* **329**, 325 (2010).
5. D. Elfenbein, R. Fisman, B. McManus, Reputation, Altruism, and the Benefits of Seller Charity in an Online Marketplace. NBER Working Paper W15614 (2009), www.nber.org/papers/w15614.
6. S. DellaVigna, J. List, U. Malmendier, Testing for Altruism and Social Pressure in Charitable Giving, NBER Working Paper W15629 (2009), www.nber.org/papers/w15629.
7. G. W. Harrison, J. A. List, *J. Econ. Lit.* **42**, 1009 (2004).

10.1126/science.1193044

BIOGEOCHEMISTRY

The Ongoing Mystery of Sea-Floor Methane

Our understanding of a major methane sink is based on studies of quiescent sediments and dynamic seeps. But do the same processes operate in both environments?

Marc Alperin[1] and Tori Hoehler[2]

Each year, ocean sediments produce a quantity of methane equivalent to about half of the methane emitted to the atmosphere from all natural sources (*1*). Very little of the methane produced below the sea floor, however, reaches the ocean or the atmosphere; most is consumed by anaerobic microorganisms as it diffuses up through oxygen-poor (anoxic) sediments. Researchers recognized this process, known as anaerobic methane oxidation (AMO), nearly 35 years ago (*2*), but it remains poorly understood. Investigators have not been able to firmly establish the reaction mechanism, fully understand the factors that control oxidation rates, or isolate the responsible organisms. This represents a gaping hole in our understanding of one of Earth's primary sinks for methane. Recent studies of a rare but intriguing sedimentary environment–sea-floor seeps of methane-rich fluids–have provided new insights into the microorganisms that inhabit methane-rich sediments, but raised new questions regarding reaction mechanisms.

Early studies of AMO focused on quiescent anoxic sediments where molecular diffusion is the dominant process for transporting methane. Geochemical techniques have provided unequivocal evidence—shown to be internally consistent by mass balance calculations (*3*, *4*)—that net methane consumption occurs in these sediments. Such geochemical data, however, provide only indirect evidence regarding the identity of the microorganisms involved.

Recent AMO studies have focused on sediments associated with dynamic methane seeps, where rapid advection of methane-rich fluid supports dense populations of microorganisms. The complex transport physics in seeps makes it nearly impossible to definitively document net methane oxidation by the geochemical "gold standard" of mass balance. The abundant biomass, however, makes seeps ideal for applying novel methods for identifying and characterizing microorganisms.

In some of the earliest work in seep sediments, Hinrichs *et al*. (*5*) found extreme ^{13}C depletion in lipids that are specifically associated with archaea. Methane was regarded as the only possible source of carbon for these "light lipids," and their detection is now widely considered to be a proxy for the presence of anaerobic microbes that are consuming (oxidizing) methane (*6*). Recent experimental (*7*) and theoretical (*8*) studies, however, have complicated this picture, suggesting that "light" lipids can also be attributed to

[1]Marine Sciences, University of North Carolina at Chapel Hill, Chapel Hill, NC 27599, USA. [2]Exobiology Branch, NASA Ames Research Center, Moffett Field, CA 94035, USA. E-mail: alperin@email.unc.edu; tori.m.hoehler@nasa.gov

Downloaded from www.sciencemag.org on July 15, 2010

Published by AAAS

archaea that produce, not oxidize, methane.

Similar complications now surround microbial aggregations discovered in seep sediments by Boetius *et al*. (*9*). Using fluorescent-labeled ribosomal RNA probes, the researchers observed spherical aggregates composed of an inner core of archaea surrounded by sulfate-reducing bacteria. Orphan *et al*. (*10*) showed that cell carbon in the interior of these aggregates is highly ^{13}C depleted, and so concluded that the archaea must be engaged in methane oxidation. A recent study, however, showed that cell carbon in the interior of some aggregates is enriched in ^{13}C compared to methane (*11*). The authors suggest that at least some of these archaea are producing rather than oxidizing methane, using substrates produced by the fermentation of organic matter.

Are the same microbial mechanisms and processes operating in dynamic seeps and quiescent sediments? Perhaps not, since the two environments differ dramatically in terms of methane concentrations and fluxes.

AMO in diffusion-dominated sediments [such as those found in Skan Bay, Alaska (*3*)] typically occurs decimeters to meters below the surface, at the base of the sulfate reduction zone. Here, methane concentrations are moderate (~1 mM), sulfate concentrations are substantially reduced relative to seawater, and the most reactive organic matter has already decomposed (see the figure, panel A). In contrast, in seeps [such as Hydrate Ridge off Oregon (*9*)], methane processing is most active in near-surface sediments that are rich in methane (~80 mM), sulfate, and fresh organic matter derived from bacterial mats and associated chemosynthetic communities (see the figure, panel B).

Mass transport rates and the associated fluxes of energy differ even more dramatically between the two environments. In Hydrate Ridge seeps, for instance, the upward flux of dissolved methane is more than 100 times greater than at Skan Bay (*8*). Much of the upward flux reaches the sediment-water interface (*12*), where consumption by aerobic bacteria would deliver an energy yield that is 30 times higher relative to AMO. Combined, the higher methane flux and energy yield in Hydrate Ridge deliver an energy flux that is 3000-fold larger than in Skan Bay.

More than 30 years ago, Zehnder and Brock (*13*) proposed that AMO could be mediated by methane-producing archaea operating "in reverse," if the electrons produced from methane oxidation are efficiently transferred to a partner organism (e.g., a sulfate-reducing bacterium). Recently, investigators have used micrometer-scale diffusion-reaction models to estimate the upper limits on rates of such cooperative or "syntrophic" AMO for a variety of electron carriers (*14*, *15*). In diffusion-dominated systems, measured AMO rates are attainable via any of several molecules as an electron carrier (e.g., H_2, formate, or acetate). So far, however, only for H_2 are porewater concentrations consistent with thermodynamic requirements for AMO (*16*).

When applied to seep systems, the same models show that reported reaction rates are orders of magnitude too high to be accounted for by interspecies electron transport using any conceivable chemical. AMO is possible at the reported rates, however, if electrons are transferred between archaea and sulfate-reducing bacteria through electrically conductive structures ("nanowires") at rates much faster than allowed by molecular diffusion (*14*). Investigators, however, have not yet documented interspecies electron transfer through nanowires. Another explanation for the high reaction rates reported from seeps is that archaea believed to be methane oxidizers are in fact producers, using the high fluxes of H_2 and other fermentation products that are expected as the abundant organic matter in these systems decomposes (*15*). Such methane production is well documented in other high-energy-flux environments, such as fish farm sediments.

Solving the sea-floor methane mystery will involve studies that integrate microbiological and geochemical approaches across these two distinct environments. At seeps, however, it has proven challenging to establish the accuracy of interpretations of geochemical data, because of the complex transport physics in these systems. Identifying the mechanism and organism responsible for AMO will finally explain how a process with minimal energy yield can serve as an efficient biological filter for sedimentary methane. Will future studies reveal a common AMO reaction mechanism and organism or a novel pathway for interspecies electron transfer? If the past is any guide, we may be in for some surprises.

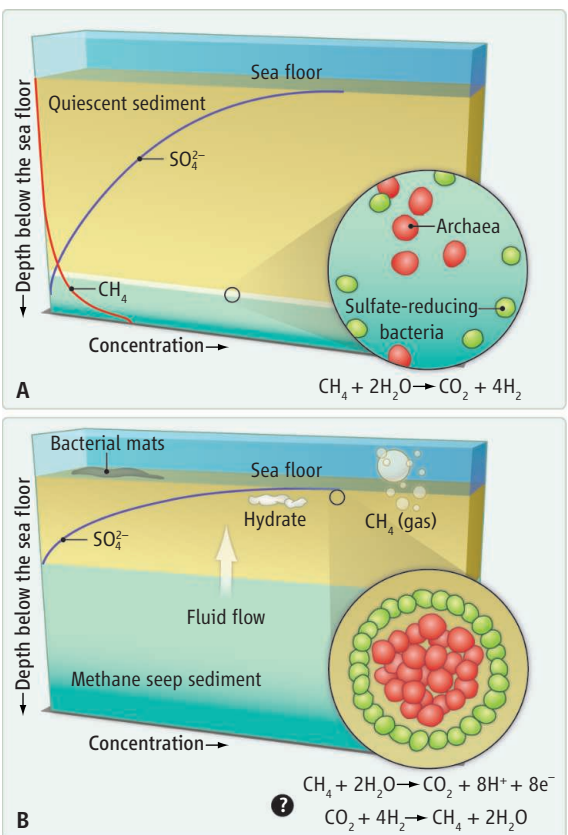

Methane pathways. Microorganisms may process methane by different mechanisms in quiescent ocean sediments (**A**) and dynamic methane seeps (**B**). In (A), methane oxidation is most active at the interface between the sulfate reduction zone (yellow) and the methane production zone (green). Here, methane oxidation is best explained by a consortium involving methanogenic archaea (red) that oxidize methane to CO_2 and H_2, and sulfate-reducing bacteria (green) that consume H_2. In contrast, at seeps (B) methane processing appears to be most active in near-surface sediments and involve aggregates of methanogen-like archaea (red) and sulfate-reducing bacteria (green). Here, archaea may be engaged in methane oxidation coupled to sulfate reduction via interspecies electron transfer facilitated by conducting filaments ("nanowires"), or in methane production fueled by organic matter fermentation.

CREDIT: P. HUEY/SCIENCE

References

1. W. S. Reeburgh, *Chem. Rev.* **107**, 486 (2007).
2. W. S. Reeburgh, *Earth Planet. Sci. Lett.* **28**, 337 (1976).
3. M. J. Alperin, W. S. Reeburgh, M. J. Whiticar, *Global Biogeochem. Cycles* **2**, 279 (1988).
4. C. S. Martens *et al*., *Am. J. Sci.* **299**, 589 (1999).
5. K.-U. Hinrichs *et al*., *Nature* **398**, 802 (1999).
6. K. Knittel, A. Boetius, *Annu. Rev. Microbiol.* **63**, 311 (2009).
7. K. L. Londry *et al*., *Org. Geochem.* **39**, 608 (2008).
8. M. J. Alperin, T. M. Hoehler, *Am. J. Sci.* **309**, 958 (2009).
9. A. Boetius *et al*., *Nature* **407**, 623 (2000).
10. V. J. Orphan *et al*., *Science* **293**, 484 (2001).
11. C. H. House *et al*., *Environ. Microbiol.* **11**, 2207 (2009).
12. S. Sommer *et al*., *Global Biogeochem. Cycles* **20**, GB2019 (2006).
13. A. J. B. Zehnder, T. D. Brock, *J. Bacteriol.* **137**, 420 (1979).
14. B. Orcutt, C. Meile, *Biogeosciences* **5**, 1587 (2008).
15. M. J. Alperin, T. M. Hoehler, *Am. J. Sci.* **309**, 869 (2009).
16. T. M. Hoehler, M. J. Alperin, D. B. Albert, C. S. Martens, *Global Biogeochem. Cycles* **8**, 451 (1994).

10.1126/science.1189966

Downloaded from www.sciencemag.org on July 15, 2010

Published by AAAS

OCEAN SCIENCE

When Still Waters Ran Deep

Near the end of the last ice age, the Pacific appears to have played a bigger role in forming deep ocean waters than it does today.

Thorsten Kiefer

"Deep water" and "bottom water"—the waters that fill the deep parts of ocean basins—form when surface waters become dense and sink. Today, this occurs in the northern North Atlantic and around Antarctica, but not in the North Pacific. There, surface waters do not become dense enough to sink more than a few hundred meters. In the past, however, it seems things were different. Recently, Okazaki *et al.* offered new insight into the ancient history of the ocean from radiocarbon data and modeling analyses (*1*). They suggest that deep water formed in the North Pacific at the beginning of the transition out of the last ice age.

In the North Atlantic, winter cooling causes salt-rich surface waters to gain density and sink. Around Antarctica, the formation of sea ice causes surface waters to become saltier and denser. Neither of these processes, however, works effectively in today's North Pacific. There, Warren concluded that surface waters, relative to the underlying layers, contain too little salt to sink, even if cooled (*2*). Generally, the Pacific is much less salty than the Atlantic. A number of processes help to maintain this salinity difference. For instance, a large quantity of atmospheric moisture (about equivalent to the discharge of the Amazon) crosses the Central American Isthmus to the Pacific. A similar quantity of fresh water may come from monsoon precipitation originating in the Indian Ocean (*3*). On a regional scale, the exceptionally low surface salinity in the subpolar North Pacific is the result of greater precipitation than evaporation due to rain associated with the Pacific storm track and prevailing cool surface temperatures. The low salinity is further maintained by a zonal circulation pattern that minimizes the transfer of warm, salty subtropical waters. Emile-Geay *et al*. further concluded that the northern moisture flux of the Asian monsoon might transport substantial amounts of fresh water into the subpolar North Pacific (*4*). Together, these processes maintain robust stratification by salinity in the North Pacific and paralyze any potential vertical overturning. Very different conditions would be required to make the Pacific a place where water can sink to substantial depths. Yet the data presented by Okazaki *et al*. convincingly suggest that the conditions existed for such deepwater formation at the beginning of the last deglaciation.

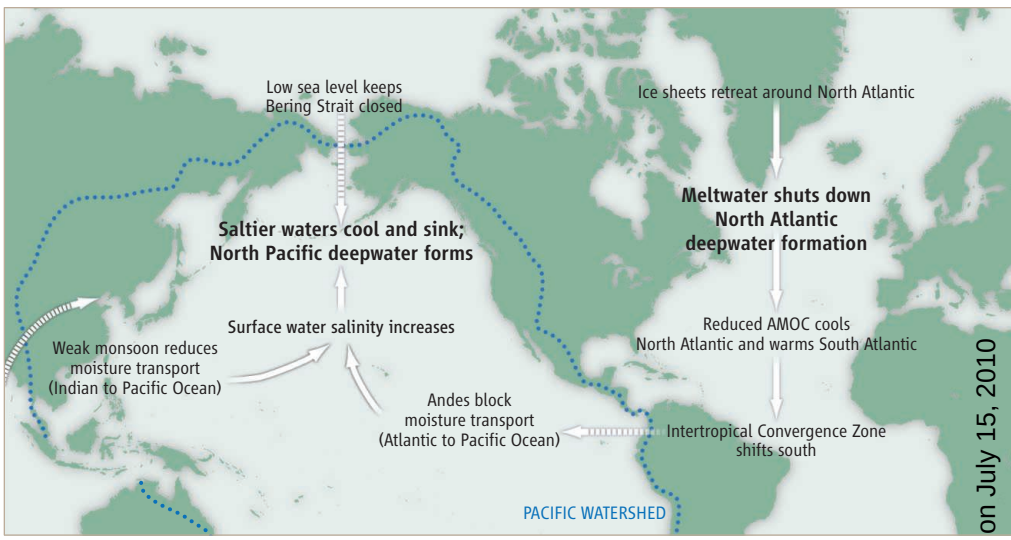

Deep history. During Heinrich event 1, a major glacial melting period terminating the last ice age, a set of atmospheric and oceanic changes appear to have enabled the formation of deep water in the North Pacific.

Recovering the history of Pacific Meridional Overturning Circulation (MOC) is a tricky task because the preservation of calcium carbonate shells—the main source of the geochemical data used to reconstruct past environments—is particularly poor in the deep Pacific. Nonetheless, over the past two decades, paleoceanographers have produced a fair number of mostly geochemical records related to the northern Pacific MOC of the last deglaciation (*5*–*7*). The uncertainties were often too large, however, to safely infer a circulation history from single data sets.

Okazaki *et al*. bypass some of these difficulties by making three pragmatic strategic choices. First, as the crown witness for overturning circulation, the authors compare the radiocarbon (^{14}C) ages of the shells of seafloor (benthic) and sea surface (planktonic) organisms found in the same samples of seafloor sediments (*8*). If the ages converge, the researchers assume the benthic organisms grew in deep water formed nearby; if the benthic shells are much older, they assume the deep water formed far from the sampling location. Relative to other geochemical proxies for MOC, this benthic-planktonic ^{14}C difference is conservative (i.e., less sensitive to local conditions and postdepositional alteration in the sediment). Second, their database is a compilation of all previously published radiocarbon records from the North Pacific, which increases the robustness of the deepwater history and reveals the spatial structure of the reconstructed ocean circulation. Third, they recalculate the radiocarbon chronologies of sediment cores, but with no attempt to obtain submillennial precision. Such chronologies of Pacific sediments are usually based on shaky ground because the old Pacific waters provide large potential for spatial and temporal variability of the water masses' radiocarbon age relative to the atmosphere (*9*). The authors account for the age uncertainty simply by reflecting it quantitatively in their data set and accepting limitations on its interpretation.

Notably, the compiled and reprocessed data show that, from approximately 17,500 to 15,000 years ago, water masses near the sea floor in the northwestern Pacific (as deep as 2800 m) were, relatively, only a little older than the surface water and the atmosphere. This suggests a rejuvenation of the water masses at depth, most plausibly by deep sinking of surface waters.

This period coincides with a period of major meltwater input into the North Atlantic known as Heinrich event 1 (H1), which was fed by the early deglacial retreat of Northern Hemisphere ice sheets. During that time, data and simulations suggest that the formation of deep water, and hence ocean overturning in the North Atlantic, was greatly reduced. So it seems the North Pacific was the more active engine for MOC in the Northern Hemisphere

PAGES International Project Office, Bern 3012, Switzerland. E-mail: kiefer@pages.unibe.ch

Downloaded from www.sciencemag.org on July 15, 2010

Published by AAAS

during several millennia at the beginning of the transition out of the last ice age.

A simulation does provide support for a scenario in which a freshwater input into the North Atlantic results in deepwater formation in the North Pacific (see the figure). The fresh water reduces the Atlantic MOC, which results in sea surface cooling in the North Atlantic. The modified temperature gradient displaces the Intertropical Convergence Zone southward, in both the Atlantic and the Pacific. This retains more moisture in the Atlantic watershed east of the South American Cordillera, rather than exporting it into the tropical Pacific. The less diluted tropical Pacific surface waters become saltier and are advected by ocean currents into the subpolar North Pacific. There, winter cooling makes them dense enough to sink to depths of up to 3 km and to spread southward in a deep western boundary current. Once the sinking of surface water is established on a large scale, it initiates a positive feedback by being replenished by more subtropical waters. The continued advection of salt further increases the density of North Pacific subpolar waters. In addition, the associated sea surface warming in the northeastern Pacific increases local evaporation, further stabilizing the Pacific MOC.

Paleoclimatic data confirm that during H1, several favorable conditions coincided to allow North Pacific deep water to form. Seawater oxygen isotope reconstructions on both sides of the Central American Isthmus support the idea that the tropical Atlantic-Pacific freshwater export was reduced (*10*). In addition, the summer monsoon in southeastern Asia was weak during H1 (*11*, *12*), which may have reduced the moisture transport from the Indian Ocean into the Pacific catchment and the atmospheric transport of fresh water into the subpolar Pacific (see the figure). Finally, sea level was still low, so that the Bering Strait was closed (*13*), allowing the gradual buildup of salinity in the subpolar North Pacific.

The data, however, are not unambiguous. In particular, the timing of changes in Pacific circulation needs to be more tightly constrained before firmly inferring synchronicity with H1 and associated changes worldwide. Other challenges include confirming the increased Pacific MOC during H1 with other proxy records, finding out whether North Pacific deep water also formed during other meltwater events, and confirming the model result with alternate modeling approaches.

Regardless of the open questions, the study is an excellent example of the knowledge that can be extracted from data compilations and data-model comparisons. A fundamental insight is that the global ocean MOC has not always been bipolar, but varied among three "poles," including the Pacific. Modelers who compare their results with paleoceanographic MOC data (*14*) should divert some of their attention from the Atlantic to check whether they can get the Pacific right as well. More generally, climate scientists need to abandon their Atlantic-centric view and adopt the Pacific Ocean as an active player.

References

1. Y. Okazaki *et al.*, *Science* **329**, 200 (2010).
2. B. A. Warren, *J. Mar. Res.* **41**, 327 (1983).
3. J. Fasullo, P. J. Webster, *J. Clim.* **15**, 3082 (2002).
4. J. Emile-Geay *et al.*, *J. Geophys. Res.* **108**, 10.1029/2001JC001058 (2003).
5. L. D. Keigwin, *Paleoceanography* **13**, 323 (1998).
6. N. Ahagon *et al.*, *Geophys. Res. Lett.* **30**, 2097 (2003).
7. E. D. Galbraith *et al.*, *Nature* **449**, 890 (2007).
8. J. F. Adkins, E. A. Boyle, *Paleoceanography* **12**, 337 (1997).
9. M. Sarnthein *et al.*, in *Ocean Circulation: Mechanisms and Impacts*, Geophysical Monograph Series 173, A. Schmittner *et al.*, Eds. (American Geophysical Union, Washington, DC, 2007), pp. 175–197.
10. G. Leduc *et al.*, *Nature* **445**, 908 (2007).
11. Y. J. Wang *et al.*, *Science* **294**, 2345 (2001).
12. H. Rashid *et al.*, *Quat. Sci. Rev.* **26**, 2586 (2007).
13. S. A. Elias, S. K. Short, C. H. Nelson, H. H. Birks, *Nature* **382**, 60 (1996).
14. Z. Liu *et al.*, *Science* **325**, 310 (2009).

10.1126/science.1192295

MEDICINE

Sickle Cell Disease at 100 Years

Effective strategies to treat sickle cell disease could involve manipulating the type of hemoglobin produced in patients.

Stuart H. Orkin[1] and Douglas R. Higgs[2]

A 100th anniversary is often a cause for celebration. However, next week's First Global Congress on Sickle Cell Disease in Accra, Ghana, marking the centenary of the description of the disease (*1*), is a sober reminder that we have far to go to meet the global challenges posed by this disorder. Just over 60 years ago, sickle cell disease (SCD) was heralded as the first "molecular" disease (*2*), resulting from a single amino acid substitution in the β-globin chain of hemoglobin (HbA). Adult hemoglobin is a tetramer of two α-globin and two β-globin polypeptides ($\alpha_2\beta_2$). Despite extensive characterization of the properties of sickle hemoglobin (HbS, $\alpha_2\beta^S_2$) and red blood cells containing HbS, and 30 years of analysis of globin genes, consistently effective therapy for individuals with SCD remains elusive. The World Health Organization estimates that many of the more than 200,000 babies with SCD born annually in Africa will die before the age of 5 years from anemia and infection (*3*, *4*). In the United States, approximately 50,000 individuals are afflicted with SCD. The global need to develop uniformly effective and inexpensive therapy is enormous, and growing.

The tendency of HbS to polymerize at low oxygen tension leads to deformation of red blood cells into the characteristic sickle shape (*5*). These inflexible cells clog small blood vessels and cause intermittent occlusion, with ensuing tissue damage, pain, and anemia. Strokes, pulmonary infarction, and cardiovascular damage cause considerable morbidity. Therapy is mainly hydration, antibiotics, and blood transfusions, but in resource-poor countries, most patients receive little or no such care. Fifteen years ago, hydroxyurea was made available for treating SCD (*6*), reducing the incidence of pain in some cases, through largely unknown mechanisms. The sole "cure" for SCD is bone marrow transplantation, but it works best with matched donors. Proof-of-principle experiments in gene therapy and gene repair with induced pluripotent stem (iPS) cells (*7*) provide rationales for ongoing research into alternative curative strategies. Although prospects for gene therapy have improved with recent trials in patients with β-thalassemia (in which β-globin is inefficiently produced) (*8*), such a resource-intensive treatment is unlikely to succeed globally. Similarly, formidable hurdles in generating and expanding blood stem cells from human iPS cells prevent consideration of this regenerative medicine approach in the near future.

Although all individuals with SCD have the same mutation in the β-globin gene, disease severity varies widely. The concentra-

[1]Children's Hospital Boston and Dana-Farber Cancer Institute, Harvard Medical School, Howard Hughes Medical Institute, Boston, MA 02115, USA. [2]Weatherall Institute of Molecular Medicine, John Radcliffe Hospital, Headington, Oxford OX3 9DS, UK. E-mail: stuart_orkin@dfci.harvard.edu

Downloaded from www.sciencemag.org on July 15, 2010

Published by AAAS

tion of fetal hemoglobin (HbF, $\alpha_2\gamma_2$) is a major genetic contributor to this variability. HbF, the predominant hemoglobin produced during fetal life, is generally present at very low concentrations (~1%) in adults, and is largely restricted to a small population of red blood cells (called F cells). The low concentration of HbF varies among individuals and is highly heritable as a quantitative trait. HbF reduces the tendency of HbS to polymerize, a salutary effect that has been appreciated for many years. Indeed, in 1948, it was hypothesized that residual HbF in infants with SCD explained the absence of sickle cells and disease symptoms (*9*).

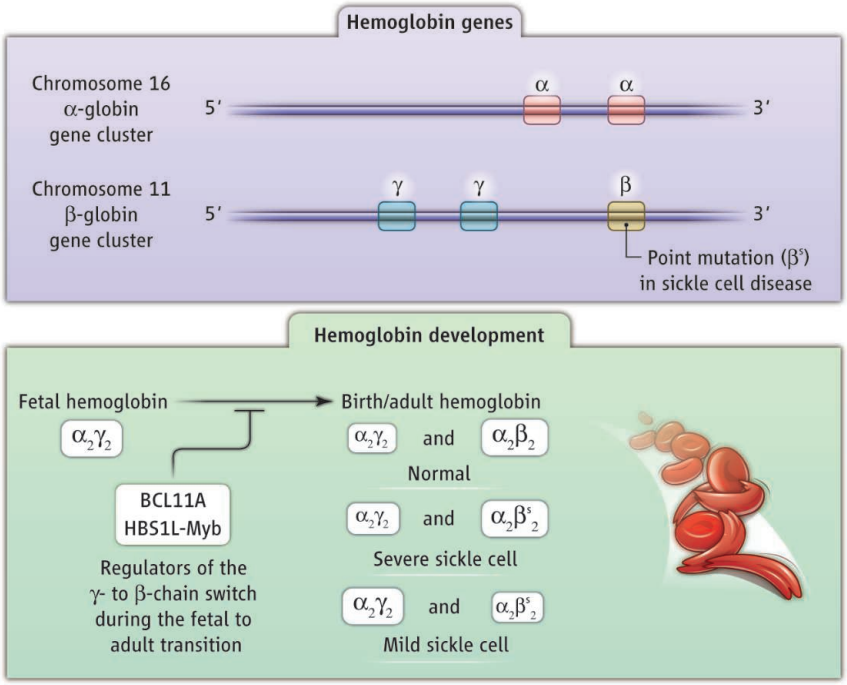

The hemoglobin switch. The fetal (γ) and adult (β) globin chains are expressed from genes on chromosome 11. SCD is caused by mutation of the β chain to the sickle (β^S) chain. Genome-wide association studies have identified loci on chromosome 2 (BCL11A) and chromosome 6 (HBS1L-Myb) that modify HbF expression. These modifiers affect the expression switch from γ to either β or β^S globin. They may affect HbF levels either directly or indirectly. Targeted therapy could reverse the fetal-to-adult switch, and hence reduce disease severity.

As the switch from γ- to β-globin gene expression occurs after birth, HbF ($\alpha_2\gamma_2$) is replaced by HbS ($\alpha_2\beta^S_2$), and symptoms of SCD ensue. Pain, the simplest measure of disease severity, is influenced by the amount of HbF present (*10*). HbF concentrations above ~15% of the total adult hemoglobin are frequently associated with relatively benign disease symptoms. Thus, reactivating HbF expression in SCD patients, even to a modest degree, could be a highly effective therapy. However, a lack of understanding how the "hemoglobin switch" is regulated has thwarted progress on this front.

The hemoglobin switch results from a transition of γ- to β-globin gene expression during human development (see the figure). The DNA sequence of the human β-globin gene cluster on chromosome 11 was determined nearly 30 years ago. Much has been learned since about regulatory elements within the cluster and the individual globin genes (*5*). Rare germline deletions within the human β-globin gene cluster, as well as specific mutations in the γ-gene promoters, are associated with substantial HbF production in adults. Yet, transacting regulators of the hemoglobin switch have remained mysterious.

New findings provide hope that a detailed understanding of the hemoglobin switch may be forthcoming and translated into mechanism-based approaches to reactivate HbF production in SCD (as well as in the β-thalassemias). Although genome-wide association studies (GWAS) have been criticized for identifying multiple loci that each contribute only minimally to the overall genetic variation of a trait or disease (*11*), independent HbF GWAS studies have revealed just a few loci with very large effects (*12*, *13*). Three genomic regions have been identified: the β-globin gene cluster itself, the gene encoding BCL11A on chromosome 2, and a region on chromosome 6 containing genes encoding HB1SL, a GTP-binding protein, and Myb, a transcription factor. Overall, these loci account for at least 40% of the genetic variation in the amount of HbF produced. The BCL11A and HBS1L-Myb regions are of particular interest because they might harbor "trans" regulators of the switch. Indirect evidence suggests that Myb, which controls hematopoiesis, rather than HBS1L, may influence HbF expression (*14*). The situation with BCL11A is clearer. It cooperates with other transcription factors and repressors to directly silence γ-globin genes in primary human erythroid cells, and controls the switch from fetal to adult β-like globin expression in mice and human red blood cells (*15*, *16*). Consistent with GWAS analyses, HbF production is controlled in a dosage-sensitive manner by BCL11A.

The identification of a genetically validated regulator of HbF production has therapeutic implications for directed reactivation of HbF in adults. Presumably, additional regulators will be discovered with ongoing research. Decreasing BCL11A expression by RNA inhibition induces the production of appreciable HbF in adult-type red blood cells (*15*), which should spur exploration of emerging in vivo RNA interference technologies (*17*). Inhibiting BCL11A function, either directly or through disruption of interactions with cooperating factors, may be an alternative strategy. Because some protein complexes containing BCL11A may include proteins with enzymatic functions, inhibiting these activities might mimic the effects of decreasing BCL11A function (*18*). Traditionally, transcription factors have been considered "undruggable" targets, but new methods for designing inhibitory small molecules based on protein chemistry and structure, and for gene expression–based screening, open the possibility for pursuing such drugs (*19*–*21*). Advances in high-throughput screening of small-molecule libraries also offer a platform for discovery and refinement of molecules that induce HbF production. Reinvigorating research for effective and hopefully low-cost therapy for SCD has never been more pressing.

References

1. J. B. Herrick, *Arch. Intern. Med.* **6**, 517 (1910).
2. L. Pauling *et al.*, *Science* **110**, 543 (1949).
3. J. Makani *et al.*, *Blood* **115**, 215 (2010).
4. D. J. Weatherall, *Blood* **115**, 4331 (2010).
5. A. N. Schechter, *Blood* **112**, 3927 (2008).
6. S. Charache *et al.*, *N. Engl. J. Med.* **332**, 1317 (1995).
7. J. Hanna *et al.*, *Science* **318**, 1920 (2007).
8. J. Kaiser, *Science* **326**, 1468 (2009).
9. J. Watson *et al.*, *Am. J. Med. Sci.* **215**, 419 (1948).
10. O. S. Platt *et al.*, *N. Engl. J. Med.* **330**, 1639 (1994).
11. D. B. Goldstein, *N. Engl. J. Med.* **360**, 1696 (2009).
12. S. Menzel *et al.*, *Nat. Genet.* **39**, 1197 (2007).
13. M. Uda *et al.*, *Proc. Natl. Acad. Sci. U.S.A.* **105**, 1620 (2008).
14. S. Menzel *et al.*, *Blood* **110**, 3624 (2007).
15. V. G. Sankaran *et al.*, *Science* **322**, 1839 (2008).
16. V. G. Sankaran *et al.*, *Nature* **460**, 1093 (2009).
17. K. Tiemann, J. J. Rossi, *EMBO Mol. Med.* **1**, 142 (2009).
18. J. E. Bradner *et al.*, *Proc. Natl. Acad. Sci. U.S.A.* (2010).
19. R. E. Moellering *et al.*, *Nature* **462**, 182 (2009).
20. J. E. Bradner *et al.*, *Nat. Protoc.* **1**, 2344 (2006).
21. K. Stegmaier *et al.*, *Nat. Genet.* **36**, 257 (2004).

10.1126/science.1194035

CREDIT: Y. GREENMAN/*SCIENCE*

Downloaded from www.sciencemag.org on July 15, 2010

Published by AAAS

Chromosome Size Differences May Affect Meiosis and Genome Size

John Wang,[1]* Pei-Jiun Chen,[2]† George J. Wang,[3] Laurent Keller[1]*

Transmission distortion has been identified by deviations from the equal representation of parental alleles in the progeny (*1*). Weak transmission bias and violations of the independent assortment of chromosomes are harder to detect, however, because large broods and a careful examination of the transmission ratios are necessary. We investigated whether weak violations of chromosome transmission or assortment exist in the nematode *Caenorhabditis elegans*, which is characterized by an XX/XO sex determination system.

We crossed males heterozygous for *mIs10* [an integrated transgene on chromosome V expressing green fluorescent protein (GFP)] to wild-type hermaphrodites and found sex-biased inheritance of *mIs10* (Fig. 1A, $P = 9.8 \times 10^{-189}$, χ^2 test). Sons were more likely to inherit the *mIs10* allele, whereas hermaphrodite daughters were more likely to receive the wild-type (*wt*) allele. This was not due to the preferential transmission of one particular chromosomal allele, because the number of total offspring inheriting *mIs10* was not different from that inheriting *wt* ($P = 0.39$, binomial test). We also ruled out mortality of males bearing the *wt* allele and of hermaphrodites bearing the *mIs10* allele, because we observed no dead larvae and only a few dead eggs. Thus, there is preferential segregation of the longer *mIs10*-bearing chromosome away from the X chromosome and of the shorter *wt* chromosome with the X. We refer to this phenomenon as skew.

To exclude the possibility that skew for *mIs10* was specific to this genetic construct or chromosome V, we investigated segregation patterns for large insertion transgenes on the other four autosomes. All four insertion transgenes also preferentially segregated away from the X chromosome (Fig. 1B) with significantly differing magnitudes of skew among the insertion lines ($P < 2.2 \times 10^{-16}$, χ^2 test) and with transmission bias ratios ranging from 1.42 (*mIs13*) to 6.55 (*mIs10*). Skew also occurred in males heterozygous for large deletions (Fig. 1C, *nDf24 I* and *tDf1 IV*).

Because these insertions and deletions (indels) are relatively large (range ~615 kb to ~7.3 Mb, table S1), we tested whether smaller indels also exhibited skew by using a small insertion (*ruIs38*, ~33 kb) and three single-gene deletions (*unc-30*, *unc-47*, and *unc-63*, range from ~1 to ~1.5 kb). In the four cases, the shorter chromosome also segregated with the X chromosome, the skew being significant for *ruIs38*, *unc-47*, and *unc-63* (fig. S1). The magnitude of bias for these four indels (1.02 to 1.21) was smaller than for the larger indels. We also observed no difference regarding the parent of origin of an indel on skew (*2*). Overall, there was a significant positive correlation between indel size and transmission bias ratio (fig. S2, $P = 0.006$, Spearman's rank correlation test).

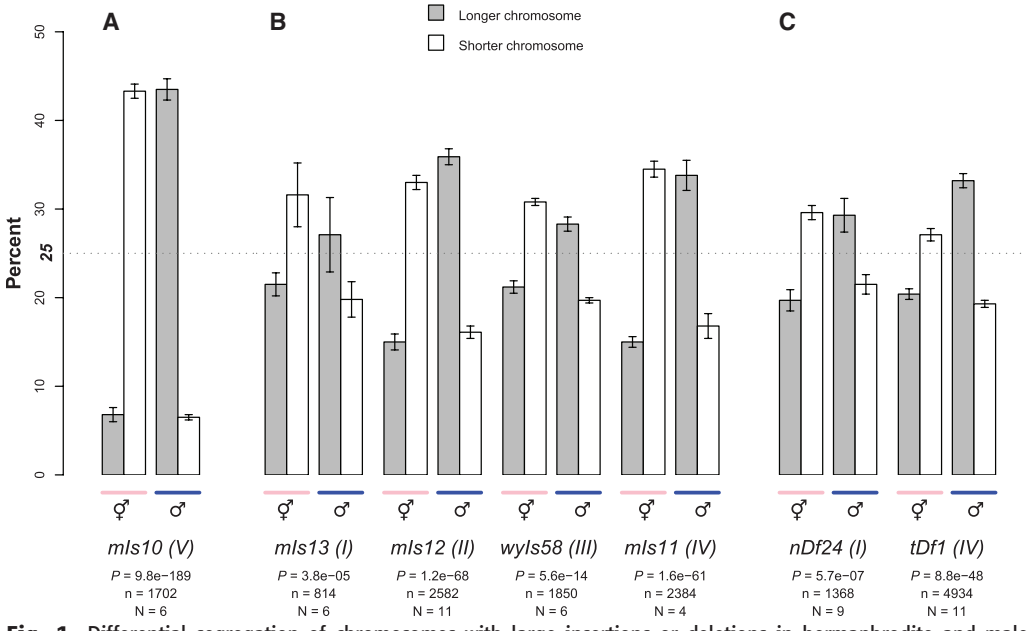

Fig. 1. Differential segregation of chromosomes with large insertions or deletions in hermaphrodite and male offspring. (**A**) *mIs10* transgene, (**B**) transgenes on chromosomes I to IV, and (**C**) deficiencies. The 25% line indicates expected values with no segregation bias. Error bars are SEM. Transgene or deficiency names and their chromosomal locations (roman numerals) are below respective bar plots. *P* values, χ^2 tests assuming random segregation of the two alternate chromosomes by sex. *N*, number of males tested; *n*, total individuals scored.

Skew may affect genome evolution and genome size. Given that hermaphrodites tend to inherit the shorter chromosome and because new populations of *C. elegans* are frequently initiated by hermaphrodites (*3*), genome size reduction may occur over evolutionary time. Simulations of hermaphroditic mating, hermaphroditic selfing-only, and gonochoristic mating systems (*2*) (fig. S3) showed that skew led to a significant reduction in genome size in the hermaphroditic mating system ($P = 2.5 \times 10^{-13}$, one-sample *t* test) but not in the gonochoristic or hermaphroditic selfing-only systems (both $P > 0.27$, one-sample *t* test).

These observations of insertion disjoining from the X, causing genome size reduction in male/hermaphrodite relative to gonochoristic mating systems, is consistent with genome sizes in the genus *Caenorhabditis*. Hermaphroditism within the genus has evolved independently at least twice (*4*). All three male/female species tested have genome sizes of >130 Mb, whereas both sequenced hermaphroditic species have genome sizes of ~100 Mb (*5*–*7*). Thus, in at least two cases, the evolution of hermaphroditism was associated with a convergent reduction in genome size relative to the ancestral male/female species.

References and Notes

1. T. W. Lyttle, *Annu. Rev. Genet.* **25**, 511 (1991).
2. Materials and methods are available as supporting material on *Science* Online.
3. A. Barrière, M. A. Félix, *Curr. Biol.* **15**, 1176 (2005).
4. K. Kiontke *et al.*, *Proc. Natl. Acad. Sci. U.S.A.* **101**, 9003 (2004).
5. E. S. Haag *et al.*, *Trends Genet.* **23**, 101 (2007).
6. L. D. Stein *et al.*, *PLoS Biol.* **1**, E45 (2003).
7. The *C. elegans* Sequencing Consortium, *Science* **282**, 2012 (1998).
8. We thank W. Herr, P. Gönczy, A. W. Murray, and A. M. Villeneuve for comments on the manuscript; S. K. Kim and R. E. Ellis for discussions; W. Herr, in whose laboratory the experiments were performed; the *Caenorhabditis* Genetics Center, funded by the NIH National Center for Research Resources, for strains; the University of Lausanne Cellular Imaging Facility; and the Vital-IT Center for high-performance computing. Supported by grants from the Swiss National Science Foundation to L.K. and W. Herr. L.K. thanks S. Leibler for hosting him during his sabbatical at Rockefeller University.

Supporting Online Material

www.sciencemag.org/cgi/content/full/329/5989/293/DC1
Materials and Methods
SOM Text
Figs. S1 to S3
Table S1
References

26 March 2010; accepted 24 May 2010
10.1126/science.1190130

[1]Department of Ecology and Evolution, University of Lausanne, CH-1015 Lausanne, Switzerland. [2]Center for Integrative Genomics, University of Lausanne, CH-1015 Lausanne, Switzerland. [3]Howard Hughes Medical Institute and Department of Biology, Stanford University, Stanford, CA 94305–5020, USA.

*To whom correspondence should be addressed. E-mail: John.Wang@unil.ch (J.W.); Laurent.Keller@unil.ch (L.K.)
†Present address: TopoGenomics Incorporated, Taipei, Taiwan.

Downloaded from www.sciencemag.org on July 15, 2010

Staphylococcus aureus Nonribosomal Peptide Secondary Metabolites Regulate Virulence

Morgan A. Wyatt,[1] Wenliang Wang,[1] Christelle M. Roux,[2] Federico C. Beasley,[3] David E. Heinrichs,[3] Paul M. Dunman,[2] Nathan A. Magarvey[1]*

Staphylococcus aureus is a major human pathogen that is resistant to numerous antibiotics in clinical use. We found two nonribosomal peptide secondary metabolites—the aureusimines, made by *S. aureus*—that are not antibiotics, but function as regulators of virulence factor expression and are necessary for productive infections. In vivo mouse models of bacteremia showed that strains of *S. aureus* unable to produce aureusimines were attenuated and/or cleared from major organs, including the spleen, liver, and heart. Targeting aureusimine synthesis may offer novel leads for anti-infective drugs.

Staphylococcus aureus is a human pathogen commonly causing hospital and community-acquired infectious diseases (*1*). It has an array of virulence factors, including surface proteins responsible for adhesion and invasion of host tissues (e.g., fibrinogen and fibronectin-binding proteins), exoproteins responsible for immune evasion (e.g., chemotaxis-inhibitory protein), and numerous hemolytic and pore-forming toxins (e.g., hemolysins, leukocidins, and enterotoxins) (*2*–*4*). For successful infection, a coordinated release of virulence factors is necessary, and redundancies exist, such that, if one factor is ablated, a productive infection can still ensue. Early research by Novick and colleagues identified an accessory gene regulator (*agr*) that controls several virulence factors (*5*). Expression of the *agr* locus is positively regulated by the *agr* pheromone, a ribosomally encoded secondary metabolite (*6*). Subsequent genomic sequencing has revealed that homologs of the *agr* pheromones exist in several Gram-positive cocci, many of which are not pathogenic (*7*–*11*). Although referred to as the "master" regulator of *S. aureus* virulence, expression of *agr* is not always detected in vivo, and *agr*-deficient clinical isolates are known, which raises the possibility that other small molecules factor prominently in the regulation of virulence factor expression (*12*).

A major class of bacterial secondary metabolites comprises the nonribosomal peptides, which are produced, in microorganisms, by multifunctional enzyme assembly lines known as nonribosomal peptide synthetases (NRPSs) (*13*). Antibiotics are the best known nonribosomal peptides produced by soil-dwelling microbes, which use them as weapons and for cell-cell communication (*14*). Penicillin, for example, is not constructed ribosomally but is dependent on an NRPS that uses valine, cysteine, and α-aminoadipic acid precursors (*15*). Although penicillin was the first nonribosomal peptide used for *S. aureus* infections, *S. aureus* itself has not previously been shown to construct nonribosomal peptides.

Cryptic nonribosomal peptide assembly in *Staphylococcus*. An NRPS uses adenylation (A) domains and adenosine triphosphate (ATP) to activate adenosine monophosphate esters of selected amino acids and delivers them to post-translationally modified (phosphopantetheine) NRPS thiolation (T) domains (*13*). Condensation reactions of the T domain–tethered amino acids produce growing peptide chains, which are released by thioesterase or reductase (Re) domains at the C terminus of the NRPS, the latter as peptide aldehydes or alcohols that frequently

[1]Department of Biochemistry and Biomedical Sciences, Department of Chemistry and Chemical Biology, M. G. DeGroote Institute for Infectious Disease Research, McMaster University, Hamilton, Ontario L8N 3Z5, Canada. [2]Department of Pathology and Microbiology, University of Nebraska Medical Center, Omaha, NE 68198, USA. [3]Department of Microbiology and Immunology, and Centre for Human Immunology, University of Western Ontario, London, Ontario N6A 5C1, Canada.

*To whom correspondence should be addressed. E-mail: magarv@mcmaster.ca

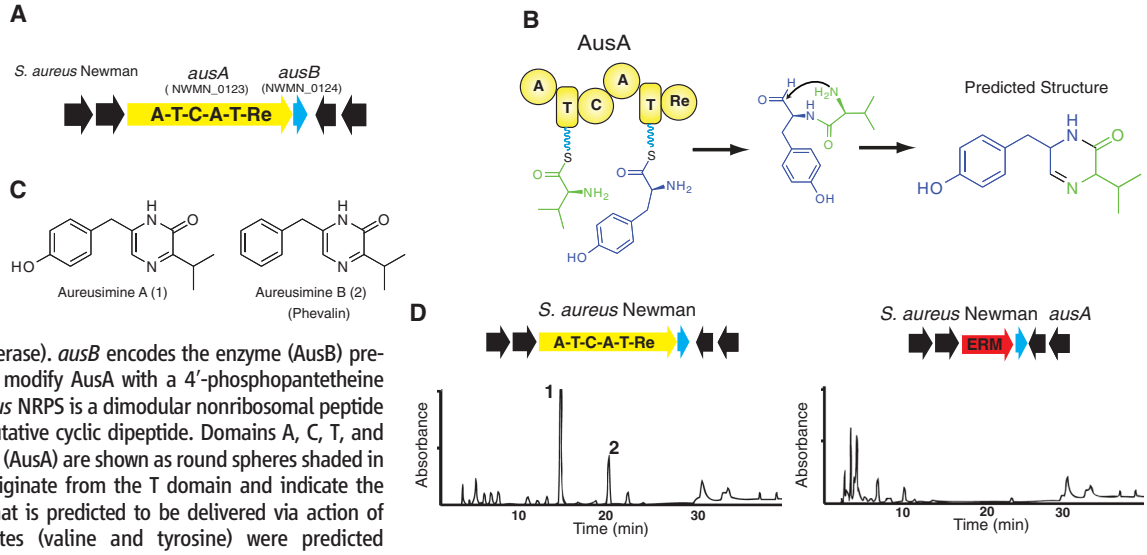

Fig. 1. Identification of a cryptic NRPS biosynthetic gene cluster within *S. aureus*. (**A**) Genetic loci of *S. aureus* Newman containing the NRPS gene. The NRPS locus is found in all sequenced *S. aureus* genomes. The NRPS cluster contains two open reading frames: *ausA* (the NRPS gene) and immediately downstream of it *ausB* (phosphopantetheinyl transferase). *ausB* encodes the enzyme (AusB) predicted to posttranslationally modify AusA with a 4′-phosphopantetheine prosthetic group. (**B**) *S. aureus* NRPS is a dimodular nonribosomal peptide assembly line encoding a putative cyclic dipeptide. Domains A, C, T, and Re within the *S. aureus* NRPS (AusA) are shown as round spheres shaded in yellow. Curved blue lines originate from the T domain and indicate the phosphopantetheinyl arm that is predicted to be delivered via action of AusB. Amino acid substrates (valine and tyrosine) were predicted according to established NRPS codes (fig. S2) (*17*, *21*). Release of a linear valine-tyrosine dipeptide aldehyde and the predicted nonribosomal peptide structure are shown. (**C**) Identification of *S. aureus* nonribosomal peptides. Structures of aureusimine A and aureusimine B (phevalin) were determined by mass spectrometry and NMR experiments (figs. S4 to S7). (**D**) Liquid chromatographic separations (HPLC chromatograms) of organic extracts of *S. aureus* Newman and *S. aureus* Newman Δ*ausA* (*19*). Aureusimine A (peak 1) and aureusimine B (phevalin) (peak 2) are present within extracts of *S. aureus* Newman but absent in extracts of *S. aureus* Newman Δ*ausA* strain. ERM, erythromycin.

Downloaded from www.sciencemag.org on July 15, 2010

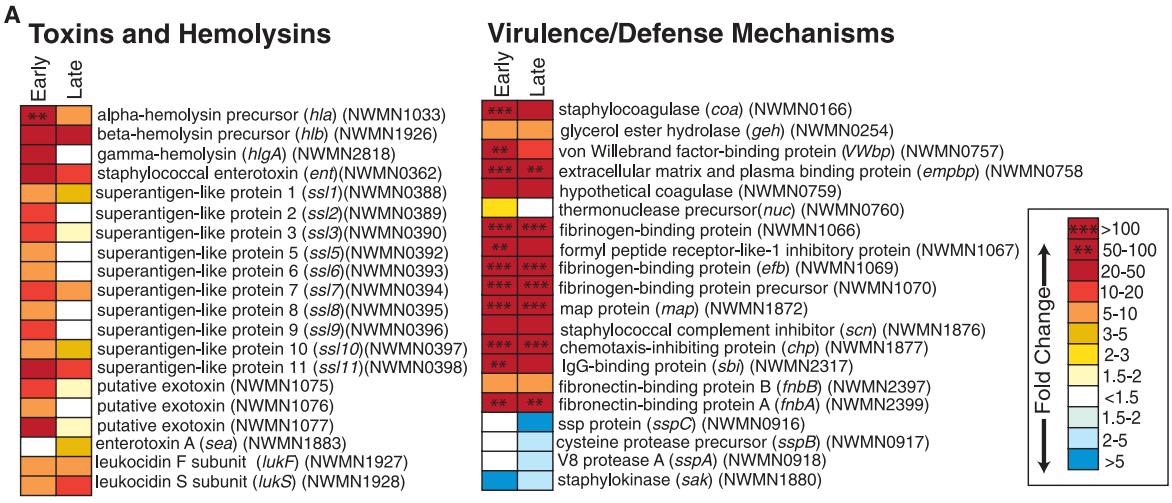

Fig. 2. Gene regulation by the aureusimines. (**A**) Differential gene expression caused by the presence of aureusimines A and B in *S. aureus* in early and late exponential phase growth. Results are presented as mean fold up-regulation (shades of red) and down-regulation (shades of blue) in three separate experiments (see scale bar). The complete microarray results of genes regulated by the aureusimines can be seen in tables S2 to S5. (**B**) Aureusimines induce hemolysis. (Left) *S. aureus* Newman wild-type and (center) *S. aureus* Newman Δ*ausA* were grown on 5% sheep blood agar; (right) *S. aureus* Newman Δ*ausA* was grown on 5% sheep blood agar supplemented with 100 μg/mL aureusimines A and B. Zones of clearance around colonies indicate hemolysis.

undergo intramolecular cyclization reactions (*13*, *16*). Details of NRPS-catalyzed reactions, structural assignments of several NRPS domains, and assembly rules for nonribosomal peptide on NRPSs are reasonably well known. Genes encoding for a given nonribosomal peptide are also clustered. Coopting these genetic and/or biochemical parameters with microbial genomic sequencing has created a link between gene and small-molecule prediction, which has assisted in the discovery of unidentified, or "cryptic," nonribosomal peptides, a process referred to as secondary metabolite genome mining (*17*, *18*).

We used a genome-mining approach to predict nonribosomal peptides that are exclusive and highly conserved within *S. aureus* (*19*). Scanning in excess of 50 *S. aureus* sequenced genomes led to the identification of a universally conserved (average of 97% identical and 97% similar), yet undescribed, NRPS gene cluster (annotated as a gramicidin synthetase or hypothetical protein) (Fig. 1A and fig. S1) (*20*, *21*). This cluster contains an NRPS gene (7.17 kb) that takes up 0.25% of the *S. aureus* genome. An ortholog is present in other staphylococci pathogenic to humans, including *Staphylococcus epidermidis* (53% identical and 71% similar), *Staphylococcus capitis* (53% identical and 70% similar), and *Staphylococcus lugdunensis* (53% identical and 70% similar), but is absent in other staphylococci or Gram-positive cocci (figs. S1 and S2) (*21*, *22*). Buoyed by the association of this NRPS with staphylococci pathogenic to humans, we predicted the structure of the encoded nonribosomal peptide.

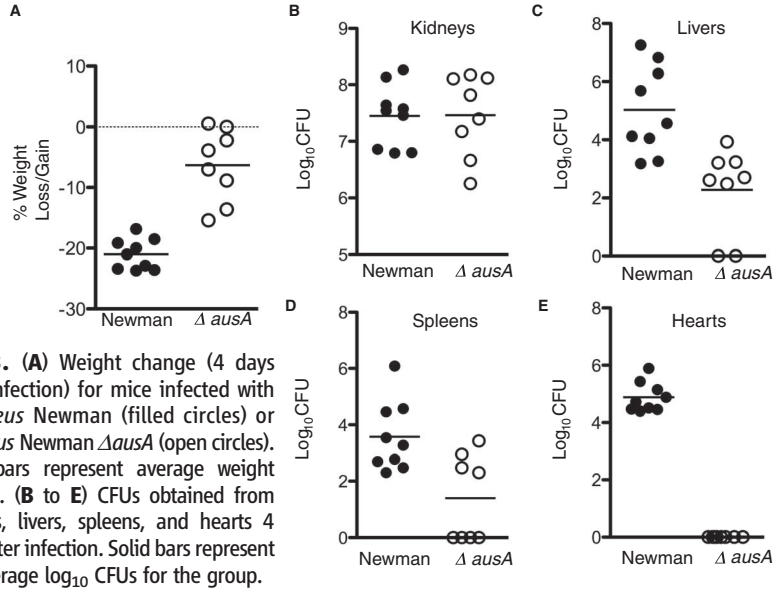

Fig. 3. (**A**) Weight change (4 days after infection) for mice infected with *S. aureus* Newman (filled circles) or *S. aureus* Newman Δ*ausA* (open circles). Solid bars represent average weight change. (**B** to **E**) CFUs obtained from kidneys, livers, spleens, and hearts 4 days after infection. Solid bars represent the average $\log_{10}$ CFUs for the group.

The *S. aureus* NRPS (2389 amino acids) is a dimodular NRPS with two adenylation (A) domains having strictly conserved NRPS codes for valine and tyrosine for all staphylococci containing the NRPS (Fig. 1B and fig. S3). A Re domain is found at the C terminus of all the *S. aureus* NRPSs and probably releases the valine-tyrosine dipeptide as an aldehyde (*23*). The proposed linear dipeptide aldehyde is likely to assume a cyclic imine conformation (predicted mass of 262.17), promoted by nucleophilic attack of the aldehyde by the α-amine of valine (Fig. 1B) (*16*, *23*).

Isolation of tyrosine-valine dipeptides. To isolate the cryptic *S. aureus* nonribosomal peptide, we collected organic solvent extracts of *S. aureus* culture broths and subjected them to high-performance liquid chromatography (HPLC) and mass spectroscopy analysis with mass-spectral filtering software to identify products within the range of the predicted dipeptide mass (*19*) (fig. S4). Two peaks were obtained, one providing a nearly exact match and the

Downloaded from www.sciencemag.org on July 15, 2010

second with a slightly later retention time and differing by 16 mass units (fig. S4). Both molecules had a common absorbance spectrum, indicating that the two were congeners (produced in a ~3:1 ratio) or sufficiently similar to suggest that they stem from a common NRPS pathway (fig. S4). One-dimensional and two-dimensional nuclear magnetic resonance (NMR) experiments (figs. S5 to S7) provided the structures of both metabolites (Fig. 1C). The most abundant matched the prediction of the cyclic valine-tyrosine dipeptide bearing a pyrazinone core (Fig. 1C), and we called it aureusimine A. The second molecule (aureusimine B) had a phenylalanine in place of the tyrosine with a structure that matched a previously identified cyclic dipeptide (phevalin) from *Streptomyces* sp. SC433 (*24*). Production of two related nonribosomal peptides from a single NRPS is commonplace and is consistent with the second A domain's incorporation of both tyrosine (aureusimine A) and phenylalanine (aureusimine B or phevalin).

To verify that the aureusimines are synthesized by the *S. aureus* NRPS (encoded by the gene we have named *ausA*), an allelic replacement was used to replace *ausA* with an erythromycin-resistance cassette (*19*). Culture broths of the resulting *ΔausA S. aureus* strain were devoid of aureusimine A and B (Fig. 1D). We next compared the growth of the *ausA* deletion strain with that of the wild type and found that the aureusimines are not necessary for growth and that the *ausA* deletion strains actually grew better than the wild type (fig. S8).

Microarray analysis of virulence expression. Our discovery of a nonribosomal peptide unique to *S. aureus* raises the possibility for its role as a regulator of *S. aureus* virulence factor expression. To evaluate the impact of aureusimine on virulence gene expression, we conducted global microarray analysis. Both *S. aureus* Newman and Newman Δ*ausA* overnight cultures were diluted 1:100 in tryptic soy broth and grown until early exponential [absorbance at 600 nm (A_{600}) = 0.3] and late exponential phase (A_{600} = 1.2). mRNA was isolated from each strain and used for microarray experiments (*19*). In three separate experiments, primary metabolic genes were largely unchanged in the Δ*ausA* strain, a result consistent with growth studies (fig. S6). However, in comparison with its isogenic parent, the *ausA* mutant displayed significant differences in expression of a large number of virulence genes, including genes encoding immunomodulatory proteins, host cell adhesins, chemotaxis-blocking proteins, and host-targeted lytic proteins and cytotoxins (Fig. 2A) (tables S2 to S5). For example, genes encoding chemotaxis-inhibiting protein and formyl peptide receptor–like 1inhibitory proteins, important for *S. aureus* immune evasion, are massively up-regulated by aureusimine production, >100 times (145.9) and >50 times (73.5), respectively (*3*, *25*). *S. aureus* adhesion molecules, such as fibrinogen-binding protein (Efb) and fibronectin-binding protein A (FnbA), are necessary for endothelial cell invasion and endocarditis and are also up-regulated 187.5- and 75.2-fold, respectively (*26*–*28*). Genes encoding for hemolysins were also significantly up-regulated in strains producing aureusimines. As an illustration showing that the transcriptional profiling corresponds to phenotypic alterations, the blood-lysing capacity of both wild-type and mutant strains was compared on blood agar plates (Fig. 2B). *S. aureus* Newman colonies lyse red blood cells, whereas little to no clearing or lysis was observed by *ΔausA* colonies. The hemolytic property of *S. aureus* could be restored to the *ΔausA* strains by the addition of aureusimines A and B (100 μg/ml) into the blood agar plates (Fig. 2B).

Role of aureusimines in vivo. To gain further insight into the role that aureusimines play in the infectivity and virulence of *S. aureus*, groups of BALB/c mice were injected intravenously with either *S. aureus* strain Newman or the isogenic *ausA* mutant (*19*). Over the course of 4 days, mice infected with wild-type *S. aureus* Newman lost, on average, 22% of their original weight, consistent with a productive *S. aureus* infection (Fig. 3A). In contrast, mice infected with the *S. aureus* Δ*ausA* deletion strain lost, on average, only 7.5% of their original weight (Fig. 3A). The weight change data for the two groups of mice are significantly different as determined by the Student's *t* test ($P < 0.001$). Organs from both groups of mice were removed and homogenized, and the resulting suspensions were surveyed for viable *S. aureus* colony-forming units (CFUs) (*19*). In the group infected with wild-type bacteria, CFUs were high in all organs examined (Fig. 3, B to E). Although CFUs in samples recovered from kidneys of mice infected with the *ausA* deletion strain were comparable to those from kidneys of mice infected with wild-type *S. aureus,* CFUs obtained from the hearts, spleens, and livers of mice infected with the *ausA* mutant were all significantly less ($P < 0.01$) than those from the respective organs of mice infected with wild-type bacteria, as determined by the Student's *t* test (Fig. 3, B to E). In fact, we could not recover detectable CFUs from the hearts of mice infected with the *ausA* mutant (Fig. 3E).

The aureusimines are previously unidentified nonribosomal peptide secondary metabolites that are integral to the ability of *S. aureus* to act as an infectious agent. Discovery of the aureusimines' control over a wide range of *S. aureus* virulence factors presents opportunities for novel anti-infective strategies. Unlike many other nonribosomal peptide secondary metabolites produced by soil microbes, such as penicillin (*29*), they do not appear to act as antibiotics. However, the original isolation of phevalin (aureusimines B) from a soil-dwelling actinomycete suggests a possible origin of the aureusimine NRPS (*24*). For *S. aureus*, acquisition of the aureusimine NRPS biosynthetic machinery was a defining moment.

References and Notes

1. F. D. Lowy, *N. Engl. J. Med.* **339**, 520 (1998).
2. R. J. Gordon, F. D. Lowy, *Clin. Infect. Dis.* **46** (suppl. 5), S350 (2008).
3. T. J. Foster, *Nat. Rev. Microbiol.* **3**, 948 (2005).
4. A. L. Cheung, A. S. Bayer, G. Zhang, H. Gresham, Y. Q. Xiong, *FEMS Immunol. Med. Microbiol.* **40**, 1 (2004).
5. P. Recsei *et al.*, *Mol. Gen. Genet.* **202**, 58 (1986).
6. R. P. Novick, E. Geisinger, *Annu. Rev. Genet.* **42**, 541 (2008).
7. N. Autret, C. Raynaud, I. Dubail, P. Berche, A. Charbit, *Infect. Immun.* **71**, 4463 (2003).
8. J. Nakayama *et al.*, *Mol. Microbiol.* **41**, 145 (2001).
9. L. E. Hancock, M. Perego, *J. Bacteriol.* **186**, 5629 (2004).
10. T. Fujii *et al.*, *J. Bacteriol.* **190**, 7655 (2008).
11. K. P. Scott, J. C. Martin, G. Campbell, C. D. Mayer, H. J. Flint, *J. Bacteriol.* **188**, 4340 (2006).
12. C. Goerke *et al.*, *Infect. Immun.* **68**, 1304 (2000).
13. M. A. Fischbach, C. T. Walsh, *Chem. Rev.* **106**, 3468 (2006).
14. G. Yim, H. H. Wang, J. Davies, *Philos. Trans. R. Soc. London Ser. B Biol. Sci.* **362**, 1195 (2007).
15. M. F. Byford, J. E. Baldwin, C. Y. Shiau, C. J. Schofield, *Chem. Rev.* **97**, 2631 (1997).
16. J. E. Becker, R. E. Moore, B. S. Moore, *Gene* **325**, 35 (2004).
17. S. Lautru, R. J. Deeth, L. M. Bailey, G. L. Challis, *Nat. Chem. Biol.* **1**, 265 (2005).
18. G. L. Challis, *J. Med. Chem.* **51**, 2618 (2008).
19. Materials and methods are available as supporting material on *Science* Online.
20. K. Liolios, N. Tavernarakis, P. Hugenholtz, N. C. Kyrpides, *Nucleic Acids Res.* **34**, D332 (2006).
21. T. Baba, T. Bae, O. Schneewind, F. Takeuchi, K. Hiramatsu, *J. Bacteriol.* **190**, 300 (2008).
22. Y. Q. Zhang *et al.*, *Mol. Microbiol.* **49**, 1577 (2003).
23. F. Kopp, C. Mahlert, J. Grünewald, M. A. Marahiel, *J. Am. Chem. Soc.* **128**, 16478 (2006).
24. M. E. Alvarez *et al.*, *J. Antibiot.* **48**, 1165 (1995).
25. C. J. C. de Haas *et al.*, *J. Exp. Med.* **199**, 687 (2004).
26. L. Piroth *et al.*, *Infect. Immun.* **76**, 3824 (2008).
27. R. Heying, J. van de Gevel, Y. A. Que, P. Moreillon, H. Beekhuizen, *Thromb. Haemost.* **97**, 617 (2007).
28. P. Moreillon *et al.*, *Infect. Immun.* **63**, 4738 (1995).
29. A. Fleming, *Br. J. Exp. Pathol.* **10**, 226 (1929).

30. This work was supported by generous gifts from McMaster University (N.A.M.), Canadian Institutes of Health Research (MOP-38002 to D.E.H.), and NIH (RA107380 to P.M.D.). For animal infections, all protocols were reviewed and approved by the University of Western Ontario's Animal Use Subcommittee, a subcommittee of the University Council on Animal Care. Gene microarray data have been deposited in National Center for Biotechnology Information, NIH (accession no. GSE21373). N.A.M. declares no competing financial interests but does declare patent applications related to this work (U.S. patent applications, no. 61/183,152 and no. 61/306,239).

Supporting Online Material

www.sciencemag.org/cgi/content/full/science.1188888/DC1
Materials and Methods
Figs. S1 to S8
Tables S1 to S5
References

1 March 2010; accepted 25 May 2010
Published online 3 June 2010;
10.1126/science.1188888
Include this information when citing this paper.

Downloaded from www.sciencemag.org on July 15, 2010

Observation of the Magnon Hall Effect

Y. Onose,[1,2]* T. Ideue,[1] H. Katsura,[3] Y. Shiomi,[1,4] N. Nagaosa,[1,4] Y. Tokura[1,2,4]

The Hall effect usually occurs in conductors when the Lorentz force acts on a charge current in the presence of a perpendicular magnetic field. Neutral quasi-particles such as phonons and spins can, however, carry heat current and potentially exhibit the thermal Hall effect without resorting to the Lorentz force. We report experimental evidence for the anomalous thermal Hall effect caused by spin excitations (magnons) in an insulating ferromagnet with a pyrochlore lattice structure. Our theoretical analysis indicates that the propagation of the spin waves is influenced by the Dzyaloshinskii-Moriya spin-orbit interaction, which plays the role of the vector potential, much as in the intrinsic anomalous Hall effect in metallic ferromagnets.

Electronics based on the spin degree of freedom (spintronics) may lead to developments beyond silicon-based technologies (*1*); spintronics avoids the dissipation from Joule heating by replacing charge currents with currents of the magnetic moment (spin currents). Phenomena such as the spin Hall effect (generation of a transverse spin current by a longitudinal electric field) in metals and semiconductors have therefore recently attracted much attention (*2*). However, some dissipation is still inevitable because the spin current in these conducting materials is carried by electronic carriers. In this sense, achieving spin transport in insulating magnets may be more promising.

In magnetic insulators, the spin moments are carried by magnons, which are quanta of magnetic excitations. A fundamental question for the magnon spin current is whether it exhibits the Hall effect, which is usually driven by the Lorentz force; therefore, charge-free particles (such as photons, phonons, and magnons) may be expected not to lead to it. However, in ferromagnets the Hall effect proportional to the magnetization—termed the anomalous Hall effect—can be driven by the relativistic spin-orbit interaction and does not require the Lorentz force (*3*). Moreover, the Hall effect of photons (*4*–*6*) and that of phonons (*7*–*9*) have been already predicted and experimentally observed. However, the Hall effect of magnons, which is relevant to spin-current electronics, has presented an experimental challenge.

We report the magnetic and thermal-transport properties of an insulating collinear ferromagnet $Lu_2V_2O_7$ with a pyrochlore structure. Figure 1A shows the vanadium sublattice in $Lu_2V_2O_7$, which is composed of corner-sharing tetrahedra. This structure can be viewed as a stacking of alternating Kagomé and triangular lattices along the [111] direction. Spin-polarized neutron diffraction suggests that the orbitals of the *d* electron are ordered so that they all point to the center of mass of the *V* tetrahedron (*10*); calculations have shown that a virtual hopping process to the high-energy state stabilizes the ferromagnetic order of the *V* spin in this orbital-ordered state (*10*). In the pyrochlore structure, because the midpoint between any two apices of a tetrahedron is not an inversion symmetry center, there is a nonzero Dzyaloshinskii-Moriya (DM) interaction

$$H_{\mathrm{DM}} = \sum_{\langle ij \rangle} \vec{D}_{ij} \cdot (\vec{S}_i \times \vec{S}_j)$$

where $\vec{D}_{ij}$ and $\vec{S}_i$ are, respectively, the DM vector between the *i* and *j* sites and the *V* spin moment at site *i*. As shown in Fig. 1B, the DM vector $\vec{D}_{ij}$ is perpendicular to the vanadium bond and parallel to the surface of the cube indicated by gray lines, according to the crystal symmetry. Even starting from the perfectly collinear ferromagnetic ground-state spin configuration, the DM interaction affects the spin wave and gives rise to the thermal Hall effect as discussed below.

The magnetic, electric, and thermal properties of $Lu_2V_2O_7$ are illustrated in Fig. 2. The spontaneous magnetization *M* emerges below Curie temperature $T_C = 70$ K (Fig. 2A). Figure 2B shows the magnetization curves along various magnetic field directions at 5 K. The magnetization saturates at relatively low field (less than 1 T), and the saturated magnetization is isotropic and almost coincides with 1 bohr magneton (μ_B), indicating the collinear ferromagnetic state with spin $S = {}^1/_2$ above the saturation field. The resistivity increases rapidly with decreasing temperature *T* (Fig. 2C). The longitudinal thermal conductivity (*11*) monotonically falls with decreasing temperature (Fig. 2D). The magnitude is small as compared with usual insulators but comparable with similar orbital-ordered materials (*12*). According to the Wiedemann-Franz law, the electric contribution of thermal conductivity is less than 10^{-5} W/K m below 100 K. Therefore, the heat current is carried only by phonons and magnons in this temperature region. From the analysis of the magnetic field variation of the thermal conductivity (*13*), we estimate the mean free paths of phonons and magnons (l_{ph} and l_{mag}, respectively) at 20 K as $l_{ph} = 3.5$ nm and $l_{mag} = 3.6$ nm. Because the obtained l_{ph} and l_{mag} are much larger than the *V*-*V* distance (0.35 nm), the Bloch waves of phonons and magnons are well defined at least at 20 K.

The thermal Hall effect (the Righi-Leduc effect) is usually induced by the deflection of elec-

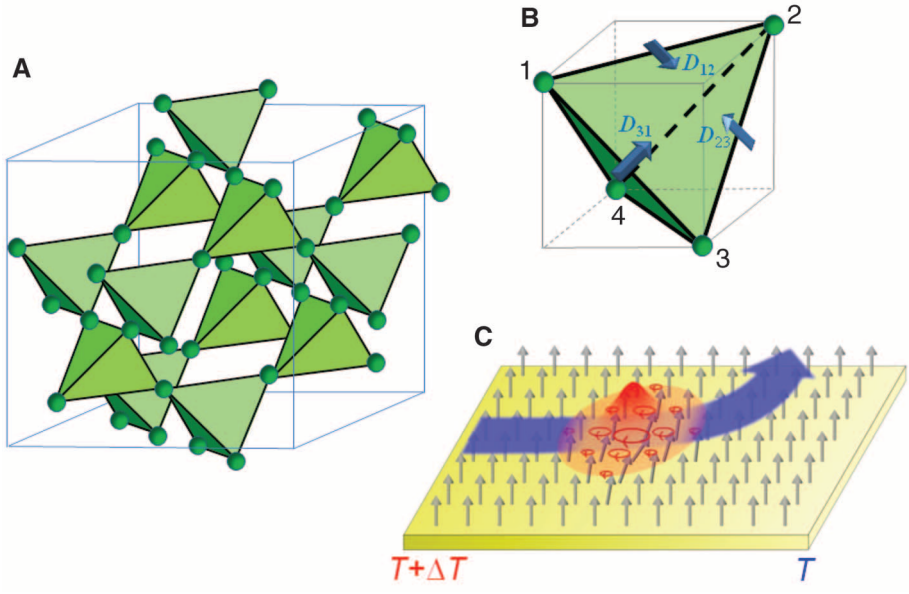

Fig. 1. The crystal structure of $Lu_2V_2O_7$ and the magnon Hall effect. (**A**) The *V* sublattice of $Lu_2V_2O_7$, which is composed of corner-sharing tetrahedra. (**B**) The direction of the Dzyaloshinskii-Moriya vector $\vec{D}_{ij}$ on each bond of the tetrahedron. The Dzyaloshinskii-Moriya interaction $\vec{D}_{ij} \cdot (\vec{S}_i \times \vec{S}_j)$ acts between the *i* and *j* sites. (**C**) The magnon Hall effect. A wave packet of magnon (a quantum of spin precession) moving from the hot to the cold side is deflected by the Dzyaloshinskii-Moriya interaction playing the role of a vector potential.

[1]Department of Applied Physics, University of Tokyo, Tokyo 113-8656, Japan. [2]Multiferroics Project, Exploratory Research for Advanced Technology, Japan Science and Technology Agency, care of Department of Applied Physics, University of Tokyo, Tokyo 113-8656, Japan. [3]Kavli Institute for Theoretical Physics, University of California, Santa Barbara, CA 93106, USA. [4]Cross-Correlated Materials Research Group and Correlated Electron Research Group, Advanced Science Institute, RIKEN, Wako 351-0198, Japan.

*To whom correspondence should be addressed. E-mail: onose@ap.t.u-tokyo.ac.jp

Downloaded from www.sciencemag.org on July 15, 2010

tronic heat current by the magnetic field in metallic materials. Because the heat current in the present material is carried only by phonons and magnons and not by charge-carriers, any observed thermal Hall conductivity would provide evidence for the Hall effect of phonons and/or magnons. Our measurements of the thermal Hall conductivity are presented in Fig. 3. Below $T_C = 70$ K, the signal is well resolved, whereas it is quite small above 80 K. The magnitude of the thermal Hall conductivity has a maximum at around 50 K. Similar to the magnetization, the thermal Hall conductivity steeply increases and saturates in the low–magnetic field region. Thus, what is presently observed in the heat transport is not the normal Hall effect proportional to the magnetic field strength but the anomalous (spontaneous) Hall effect affected by the spontaneous magnetization. However, the thermal Hall conductivity gradually decreases with magnetic field after saturation in the low-temperature region; this can be explained by the magnon gap induced by the magnetic field as discussed below. Figure 4A shows the temperature dependence of the spontaneous thermal Hall conductivity (the thermal Hall conductivity just above the saturation field) for magnetic field ∥ [100], [110], and [111]; it is independent of the field direction within the error bars.

The thermal Hall effect caused by phonons has been reported in $Tb_3Ga_5O_{12}$ (*7*) and explained by the spin-phonon interaction (*8*, *9*). The intrinsic mechanism in (*8*) does not depend on the magnon population. The mean free path of phonons is expected to increase with magnetic field as a consequence of reduced scattering by magnetic fluctuations. Therefore, our observation of the decrease of the thermal Hall conductivity in the high-field region cannot be explained in terms of the phonon mechanism. On the other hand, the reduction of the magnon population, as reflected by the behavior of the specific heat under the magnetic field (*13*), will diminish the magnon contribution of the thermal Hall conductivity. In the mechanism based on the scattering of phonons by spins (*9*), the thermal Hall angle κ_{xy}/κ_{xx} is anticipated to be proportional to the magnetization, such as in the case of $Tb_3Ga_5O_{12}$ (*7*). For $Lu_2V_2O_7$, κ_{xy} steeply decreases with increasing temperature around T_C, faster than the magnetization decreases (Fig. 4B), which contradicts the scenario of the phonon Hall effect. On the other hand, magnons propagate in terms of the exchange interaction (Eq. 3), and therefore the magnon picture cannot be valid in the magnetic field–induced spin-polarized state above T_C. Hence, the temperature dependence can be explained in terms of the magnon Hall effect.

We next turn to the quantitative calculation of the thermal Hall effect in $Lu_2V_2O_7$. This material

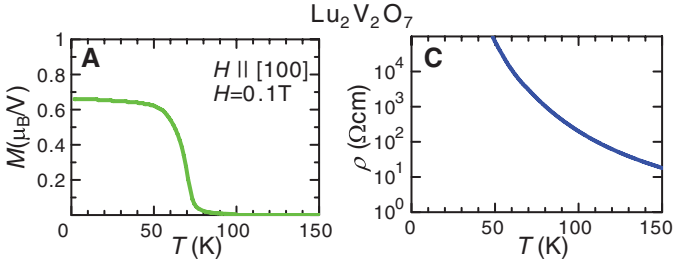

Fig. 2. Magnetic, electric, and thermal properties of $Lu_2V_2O_7$. (**A**) Temperature dependence of magnetization at the magnetic field $H = 0.1$T along the [100] direction. (**B**) Magnetization curves at $T = 5$ K for H ∥ [100], H ∥ [110], and H ∥ [111]. (**C**) Temperature variation of resistivity ρ. (**D**) Temperature variation of longitudinal thermal conductivity κ_{xx}.

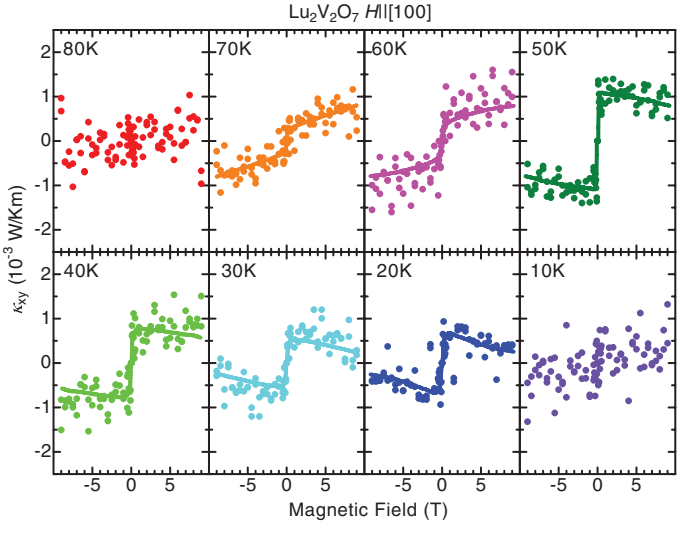

Fig. 3. Magnetic field variation of the thermal Hall conductivity of $Lu_2V_2O_7$ at various temperatures. The magnetic field is applied along the [100] direction. The solid lines are guides to the eye.

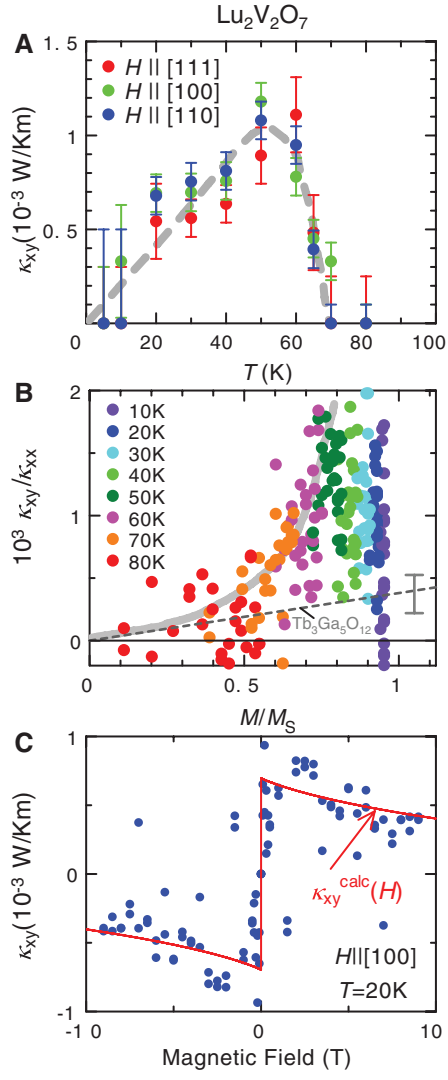

Fig. 4. (**A**) Temperature dependence of the spontaneous thermal Hall conductivity (the thermal Hall conductivity just above the saturation field) for H ∥ [100], H ∥ [110], and H ∥ [111]. The thick dashed line is a guide to the eye. (**B**) The thermal Hall angle κ_{xy}/κ_{xx} plotted against the magnetization (M). For $Tb_3Ga_5O_{12}$ (dashed line), the value of κ_{xy}/κ_{xx} divided by the magnetic field H is taken from (*7*), and the magnetic susceptibility (M/H) is estimated from the magnetization curves in (*18*). The thick solid line is a guide to the eye. (**C**) Magnetic field variation of the thermal Hall conductivity at 20 K for H ∥ [100]. The red solid line indicates the magnetic field dependence given by the theory (Eq. 4) that is based on the Dzyaloshinskii-Moriya interaction.

Downloaded from www.sciencemag.org on July 15, 2010

is a ferromagnetic Mott-insulator, and the spin-1/2 V^{4+} ions form a pyrochlore lattice (Fig. 1A). The effective spin Hamiltonian describing this system is given by

$$H_{\mathrm{eff}} = \sum_{\langle ij \rangle} \left[-J\vec{S}_i \cdot \vec{S}_j + \vec{D}_{ij} \cdot (\vec{S}_i \times \vec{S}_j) \right] - g\mu_B \vec{H} \cdot \sum_i \vec{S}_i \quad (1)$$

where $-J$ is the nearest-neighbor ferromagnetic exchange, and the last term is the Zeeman coupling with an external field $\vec{H}$. The DM interaction does not disturb the perfect ferromagnetic alignment of the spins along the direction of a weak external magnetic field $\vec{H}$ because the sum of the DM vectors on the bonds sharing the same site is zero. Because we are interested in the low-temperature regime $T << T_C$, the interactions between magnons are neglected. Therefore, we consider the Bloch state of a single magnon

$$|\vec{k}\rangle = \frac{1}{\sqrt{N}} \sum_i e^{i\vec{k} \cdot \vec{R}_i} |i\rangle \quad (2)$$

where in state $|i\rangle$ the spin at site i is pointing opposite the $\vec{H}$ direction with all the other spins aligned with the $\vec{H}$ direction. The matrix element corresponding to the transfer of magnons reads as

$$\langle i| -J\vec{S}_i \cdot \vec{S}_j + \vec{D}_{ij} \cdot (\vec{S}_i \times \vec{S}_j) |j\rangle = \langle i| -\frac{J}{2}(S_i^+ S_j^- + S_i^- S_j^+) + \frac{iD_{ij}}{2}(S_i^+ S_j^- - S_i^- S_j^+) |j\rangle = -\frac{\tilde{J}}{2} e^{i\phi_{ij}} \quad (3)$$

where $S^{\pm}$ is the operator that increases or decreases the spin component along the direction $\vec{n} = (n_x, n_y, n_z) = \vec{H}/|\vec{H}|$, $D_{ij} = \vec{D}_{ij} \cdot \vec{n}$, and $\tilde{J}e^{i\phi_{ij}} = J + iD_{ij}$. Thus, the DM interaction acts as a vector potential ϕ_{ij} and serves as the "orbital magnetic field" for the propagation of magnons. The spin-wave Hamiltonian becomes just a tight-binding Hamiltonian on a pyrochlore lattice with phase factors. Thanks to the different types of loops in the unit cell of the pyrochlore lattice, the orbital magnetic field avoids the cancellation and gives rise to the Hall effect (*14*).

The formula for the thermal Hall conductivity $\kappa_{\alpha\beta}$ of the magnon system was derived in (*14*). In the low-temperature region, the dominant contribution to $\kappa_{\alpha\beta}$ comes from the lowest magnon band and small k because of the Bose distribution function. Retaining only the first-order terms in the DM interaction, the analytic expression for the anomalous thermal Hall conductivity due to magnons is obtained as (*13*)

$$\kappa_{\alpha\beta}(H,T) = \Phi_{\alpha\beta} \frac{k_B^2 T}{\pi^{3/2}\hbar a} \left(2 + \frac{g\mu_B H}{2JS}\right)^2 \times \sqrt{\frac{k_B T}{2JS}} \mathrm{Li}_{5/2}\left[\exp\left(-\frac{g\mu_B H}{k_B T}\right)\right] \quad (4)$$

with the polylogarithm $\mathrm{Li}_n(z)$ given by $\mathrm{Li}_n(z) = \sum_{k=1}^{\infty} \frac{z^k}{k^n}$. Here, a is the lattice constant, and $\Phi_{\alpha\beta} = -\varepsilon_{\alpha\beta\gamma} n_\gamma D/(8\sqrt{2}J)$ with the totally antisymmetric tensor $\varepsilon_{\alpha\beta\gamma}$, and $D = |\vec{D}_{ij}|$. In Fig. 4C, we show the fitting of the data at $T = 20$ K to this expression with $JS = 8D_s/a^2$, where D_s is the spin stiffness constant obtained from the analysis of specific heat shown in (*13*). Therefore, the only parameter is the ratio of DM interaction strength D to the exchange coupling J. The agreement between experiment and theory is obtained for $D/J = 0.32$; this is a reasonable value for transition-metal oxides. In the spinel-type antiferromagnet $CdCr_2O_4$, for example, D/J has been estimated as 0.19 from the measured pitch of the spiral spin structure and ab initio calculations (*15*); this is of the same order of magnitude as our result.

We have observed the magnon Hall effect in the ferromagnetic insulator $Lu_2V_2O_7$. Other than the spontaneous spin current relevant to electronic polarization (*16*), the magnon spin current in insulating materials has rarely been discussed (*17*). The observation of the Hall effect of the magnon spin current may lead to applications of spin transport in magnetic insulators.

References and Notes

1. S. Maekawa, *Concepts in Spin Electronics* (Oxford Science Publication, Oxford, 2006), and references therein.
2. Y. K. Kato, R. C. Myers, A. C. Gossard, D. D. Awschalom, *Science* **306**, 1910 (2004).
3. N. Nagaosa, J. Sinova, S. Onoda, A. H. MacDonald, N. P. Ong, *Rev. Mod. Phys.* **82**, 1539 (2010).
4. G. L. J. A. Rikken, B. A. van Tiggelen, *Nature* **381**, 54 (1996).
5. M. Onoda, S. Murakami, N. Nagaosa, *Phys. Rev. Lett.* **93**, 083901 (2004).
6. O. Hosten, P. Kwiat, *Science* **319**, 787 (2008).
7. C. Strohm, G. L. J. A. Rikken, P. Wyder, *Phys. Rev. Lett.* **95**, 155901 (2005).
8. L. Sheng, D. N. Sheng, C. S. Ting, *Phys. Rev. Lett.* **96**, 155901 (2006).
9. Y. Kagan, L. A. Maksimov, *Phys. Rev. Lett.* **100**, 145902 (2008).
10. H. Ichikawa *et al.*, *J. Phys. Soc. Jpn.* **74**, 1020 (2005).
11. H. D. Zhou *et al.*, *Phys. Rev. B* **77**, 020411(R) (2008).
12. J.-G. Cheng, Y. Sui, J.-S. Zhou, J. B. Goodenough, W. H. Su, *Phys. Rev. Lett.* **101**, 087205 (2008).
13. Materials and methods are available as supporting material on *Science* Online.
14. H. Katsura, N. Nagaosa, P. A. Lee, *Phys. Rev. Lett.* **104**, 066403 (2010).
15. G.-W. Chern, C. J. Fennie, O. Tchernyshyov, *Phys. Rev. B* **74**, 060405(R) (2006).
16. H. Katsura, N. Nagaosa, A. V. Balatsky, *Phys. Rev. Lett.* **95**, 057205 (2005).
17. S. Fujimoto, *Phys. Rev. Lett.* **103**, 047203 (2009).
18. M. Guillot, A. Marchand, V. Nekvasil, F. Tcheou, *J. Phys. C Solid State Phys.* **18**, 3547 (1985).

19. The authors thank C. Terakura for the design of Fig. 1C and P. A. Lee, S. Fujimoto, and T. Arima for fruitful discussion. This work is supported by a Grant-in-Aid for Scientific Research (nos. 17071007, 17071005, 19048008, 19048015, 19684011, 20046004, 20340086, 21244053, and 22014003) from the Ministry of Education, Culture, Sports, Science and Technology of Japan and by the Funding Program for World-Leading Innovative R&D on Science and Technology (FIRST), Japan.

Supporting Online Material

www.sciencemag.org/cgi/content/full/329/5989/297/DC1
Materials and Methods
Figs. S1 to S3
References

12 February 2010; accepted 21 May 2010
10.1126/science.1188260

Single-Crystal X-ray Structure of 1,3-Dimethylcyclobutadiene by Confinement in a Crystalline Matrix

Yves-Marie Legrand, Arie van der Lee, Mihail Barboiu*

Cyclobutadiene (CBD), the smallest cyclic hydrocarbon bearing conjugated double bonds, has long intrigued chemists on account of its strained geometry and electronic instability, but the parent compound and its unperturbed derivatives have thus far eluded crystallographic characterization. In this work, we immobilize a precursor, 4,6-dimethyl-α-pyrone, in a guanidinium-sulfonate-calixarene (G_4C) crystalline network that confines the guest through a combination of CH-π and hydrogen-bond interactions. Ultraviolet irradiation of the crystals transforms the entrapped 4,6-dimethyl-α-pyrone into a 4,6-dimethyl-β-lactone Dewar intermediate that is sufficiently stable under the confined conditions at 175 kelvin to allow a conventional structure determination by x-ray diffraction. Further irradiation pushes the reaction to completion, enabling the structure determination of 1,3-dimethylcyclobutadiene Me_2CBD. Our data support experimental observation of square-planar (Me_2CBD^S) and rectangular-bent (Me_2CBD^R) geometries in the G_4C host matrix. The hydrogen-bonded, dissociated carbon dioxide coproduct interacts more strongly with Me_2CBD^S than with Me_2CBD^R.

Cyclobutadiene (CBD)—an unsaturated molecular ring of four carbon atoms, each capped by a single hydrogen atom—has intrigued chemists for the better part of a century (*1*–*8*). There is tremendous geometric strain associated with squeezing olefinic carbons down

Downloaded from www.sciencemag.org on July 15, 2010

from their traditional 120° bonding angle to the 90° motif dictated by a closed square ring. In addition, the molecule is also the paradigm of Hückel anti-aromaticity (*9*), the electronic destabilization associated with networks of π electrons delocalized over an even number of alternating cyclic double bonds. The question of whether the molecule could be prepared at all has previously been answered, when it was observed spectroscopically in an Ar matrix at 8 K upon photolysis of α-pyrone (**1**) (*4*, *5*). The sequence of transient intermediates leading to its formation was assigned, as outlined in Fig. 1. Attempts to isolate macroscopic quantities of the compound have generally furnished its dimer (*6*, *7*), which, on heating, produces cyclooctatetraene (*8*). Derivatives of CBD have also been stabilized by appending electron-donating substituents (*10*) or by coordination of metal ions and metal complexes [for example, $Ru(CO)_3$] (*11*) to the carbocycle. However, the molecule has eluded full structural characterization, which is a goal of particular interest for the clarification of the bonding impact of the compound's anti-aromaticity.

Attempts to isolate CBD in a confined, protective crystalline matrix could not furnish its crystal structure. In a seminal experiment, Cram *et al*. succeeded in isolating CBD by sequestering it in a hemicarcerand cage in solution, thereby inhibiting its dimerization (*1*). The solid-state hemicarcerand structure (Fig. 2A) (*12*–*14*), with an estimated free internal volume of ~135 $Å^3$, was most likely too large to immobilize the CBD molecule (volume V = 85 $Å^3$) sufficiently for crystallographic analysis (*15*). Our initial experiments supported this assumption: Irradiation of β-cyclodextrin ⊂ α-pyrone (βCD ⊂ **1**) inclusion crystals (with a free internal volume V = 253 $Å^3$) led to crystal structures in which the disorder in the βCD cavity was quite complex (*15*).

Stabilization of reactive species (*16*–*18*) or dynamic supramolecular self-assemblies (*19*–*21*) by encapsulation within porous crystalline networks has previously enabled characterization of the solid-state structure of such species. Likewise, the chances for success in obtaining the CBD crystal structure rely on the appropriate design of a crystalline host matrix that optimally sequesters/immobilizes the precursor, intermediate, and product molecules; free motion of guest molecules within the confined space, which leads to complex disorder in the diffraction data set, would thereby be diminished or avoided. In this context, the crystalline host matrix might encompass: (i) an optimally designed confined volume in the host, dimensionally adapted to the sequestered guest molecules, (ii) specific anchoring groups to fix the guest molecules within the

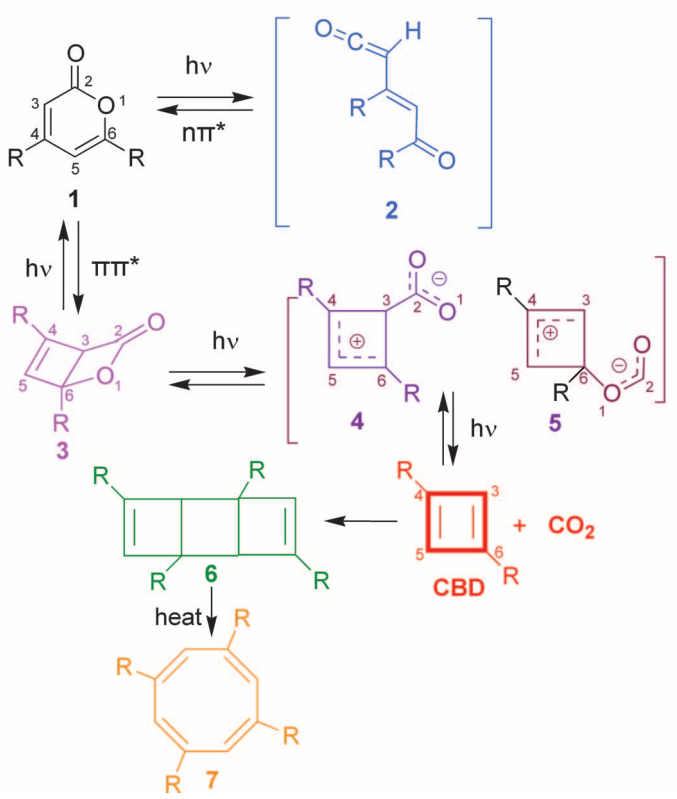

Fig. 1. Reaction sequence of α-pyrone photolysis: electrocyclic opening of α-pyrone (**1**) leads to extremely unstable aldehydeketene (**2**) or Dewar β-lactone (**3**) transient precursors. Stepwise photofragmentation of **3** occurs via cyclobutenecarboxylate zwitterions (**4**, **5**) that, by eliminating CO_2, yield CBD. The unstable CBD dimerizes to form the transient tricyclic species (**6**) that rearranges to cyclooctatetraene (**7**). R = H (*5*–*8*) or CH_3 (this paper). h, Planck's constant; ν, frequency.

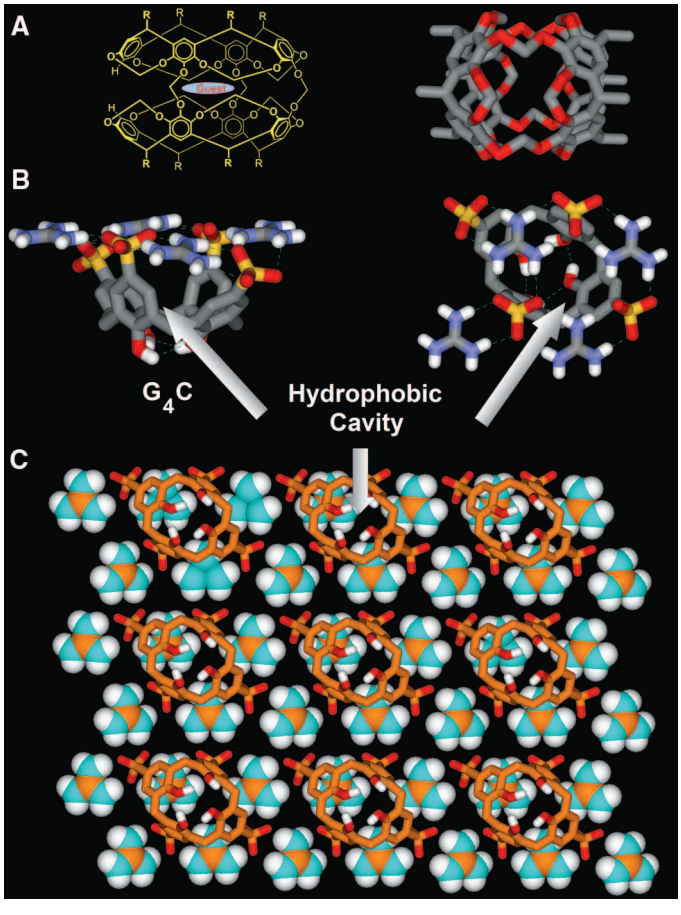

Fig. 2. (**A**) Chemical and crystal structure in stick representation (*12*–*14*) of Cram *et al*.'s hemicarcerand and of the G_4C host matrix crystallized from an aqueous solution of tetra-*p*-sulfocalix[4]arene (C) and guanidinium chloride (G) at room temperature. Gray, carbon; red, oxygen. (**B**) Side (left) and top (right) views in stick representation of the G_4C complex. Orange, carbon; purple, oxygen; white, hydrogen. (**C**) Crystal packing of the hexagonal H-bonded guanidinium-sulfonate sheets, stabilizing the C molecules in a cone conformation that affords a free hydrophobic calixarene internal cavity. Some hydrogen atoms have been omitted for clarity. Blue, nitrogen.

Adaptive Supramolecular Nanosystems Group, Institut Européen des Membranes, Ecole Nationale Supérieure de Chimie de Montpellier–Université Montpellier II-UMR-CNRS 5635, Place Eugène Bataillon CC047, 34095 Montpellier Cedex 5, France.

*To whom correspondence should be addressed. E-mail: mihai.barboiu@iemm.univ-montp2.fr

Downloaded from www.sciencemag.org on July 15, 2010

confined space, and finally (iii) a propensity for high-quality diffraction data. These considerations inspired us to design a distinctly appropriate crystalline framework to use as a porous host matrix for CBD synthesis.

In contrast with Cram *et al.*'s hemicarcerand cage (Fig. 2A), we employed slow crystallization from aqueous solution (*15*) to prepare a guanidinium-sulfonate-calixarene (G_4C) host-matrix (Fig. 2, B and C) of restricted internal free volume ($V = 45$ Å^3) (*15*, *22*) optimally available to immobilize the 4,6-dimethyl-α-pyrone $Me_2$1 molecule during assembly of the crystal lattice. The cone conformation of tetra-*p*-sulfocalix[4]arene (C) (*22*) is stabilized by the guanidinium cations (G) that form hydrogen bonds with the sulfonate moieties of C (Fig. 2 and fig. S4) (*23*). The inclusion of $Me_2$1 within the matrix was achieved by using a fresh aqueous solution of G, C, and $Me_2$1 to form included single crystals of $G_4C\{Me_2\mathbf{1}\}$ with completely filled host pockets (*15*). The use of the 4,6-dimethyl-α-pyrone, $Me_2$1, was not arbitrary: Attempts to irradiate $G_4C \subset$ α-pyrone ($G_4C \subset$ **1**) inclusion crystals led once again to crystal structures in which the disorder was very complex. In contrast, the 4-methyl group of $Me_2$1 is tightly confined in a fixed position within the G_4C host matrix through three CH-π interactions with neighboring aromatic units of the calixarene pocket (*15*). The encapsulation of $Me_2$1 also induces an unexpectedly drastic change in the orientation of the guanidinium cations (G). Here, the structural behavior of G extends beyond its role in the free porous host of stabilizing the cone conformation of C via hydrogen bonding; in the inclusion crystals, the planar compound $Me_2$1 (dimensionally fitting within the overall superstructure of the G_4C host) is supplementally sandwiched between two G groups (stacking distance: $d_{stacking} = 3.5$ Å), whereas the carbonyl oxygen points outward, forming anchoring H bonds ($d_{N-O} = 2.89$ Å) with a third quasi-coplanar G cation (Fig. 3A). All combined host-guest interactions are vital for the encapsulation and insulation, as well as for the low mobility of the guest molecules in the G_4C host cavity. As a result, the $Me_2$1 molecule is well defined in the diffraction data set, with sharp electron-density sites. The x-ray structure of $Me_2$1 is structurally similar to previously reported fully localized canonical structures of α-pyrone **1** (*24*).

Upon irradiation of $G_4C\{Me_2\mathbf{1}\}$ at wavelength λ = 320 to 500 nm, we observed separate density maxima in the electronic-density map on both sides of the $Me_2$1 ring, but one was substantially more intense than the other. In the resulting $G_4C\{Me_2\mathbf{1}'\}$ structure (Fig. 3B), the C(3) site starts to depopulate; this disorder can be modeled with 50% density on the C(3) site and 50% density on the major off-cycle site, an apparent result of the equilibrium between the initial $Me_2$1 structure and an initial irradiation product $Me_2$1′.

Further irradiation induced conversion of $G_4C\{Me_2\mathbf{1}'\}$ into $G_4C\{Me_2$3 and $Me_2CBD^R\}$ (here, Me_2CBD^R indicates the rectangular-bent conformation) (Fig. 3C). An increase in the off-plane maximum density site supported conversion of $Me_2$1 into its Dewar-β-lactone valence isomer, 1,5-dimethyl-2-oxa-3-oxobicyclo[2,2,0]hex-5-ene, $Me_2$3 (77.3%), previously predicted by theory (*25*) and experimentally observed (*4*, *5*). Supplementary separate density maxima on the electronic-density map were detected on both sides of $Me_2$3, corresponding to 22.7% conversion of $Me_2$3 to

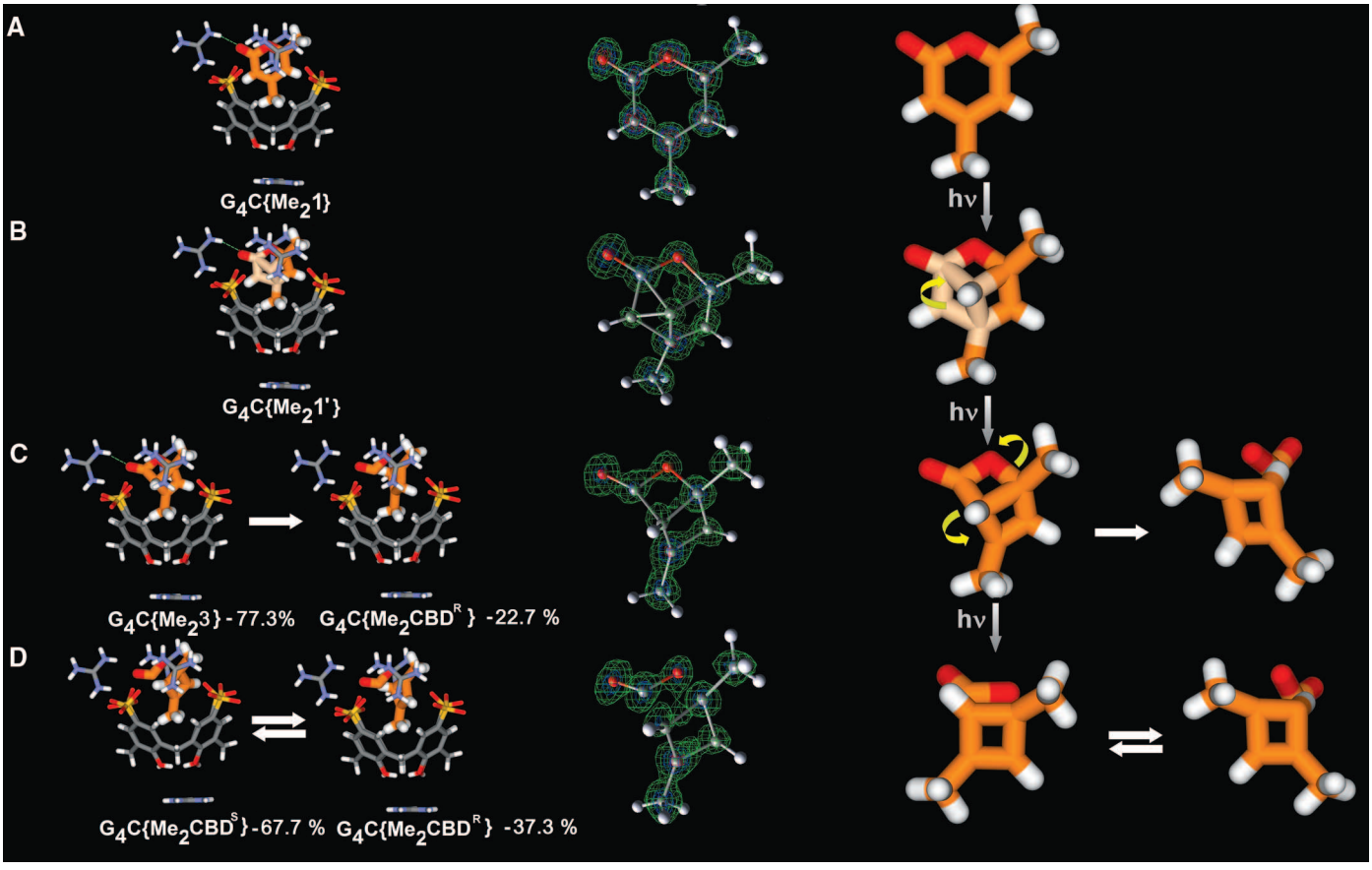

Fig. 3. X-ray crystallographic observation of the Me_2CBD formation pathway from photolysis of 4,6-dimethyl-α-pyrone ($Me_2$1) within the pores of a G_4C crystalline matrix, crystallized from an aqueous solution at room temperature. Single-crystals mounted on the diffractometer were coated with protective silicone oil and held at a temperature of 175 K. Structures in stick representation and electron-density maps are shown for (**A**) $Me_2$1; (**B**) a transient intermediate $Me_2$1′ obtained after irradiation for 25 min; (**C**) the Dewar valence isomer $Me_2$3 (77.3%), in equilibrium with rectangular-bent Me_2CBD^R (22.7%) in close proximity to a noninteracting orthogonal CO_2 molecule, obtained after irradiation for 25 additional minutes; and (**D**) square-planar 1,3-dimethylcyclobutadiene Me_2CBD^S (62.7%) in van der Waals contact with the CO_2 molecule, and the rectangular-bent Me_2CBD^R (37.3%), orthogonally oriented with respect to the plane of Me_2CBD^S, after irradiation for 60 additional minutes.

Downloaded from www.sciencemag.org on July 15, 2010

Me_2CBD^R and CO_2. The butterfly type geometry of $Me_2$3, kinetically stabilized at 175 K, exhibits bond lengths similar to those predicted by theory, with the exception of the bridging bond ($d_{C3\text{-}C6}$ = 1.70 versus 1.55 Å in theory) and its direct neighbors ($d_{C2\text{-}C3}$ = $d_{C3\text{-}C4}$ = 1.37 versus 1.53 Å in theory), inducing a ±10% variation of the angle values (*25*). The –C=O·····HN– hydrogen bond ($d_{N\ldots O}$ = 2.89 Å) anchoring the confined $Me_2$3 to the crystal matrix and the position of the methyl group interacting inside the calixarene pocket remain constant. The free motion of $Me_2$3 within these confined conditions is highly restricted; thus, we were able to determine its crystallographic structure unequivocally by x-ray analysis. The present results suggest that under confinement in the calixarene cavity, the mechanistic pathway for the transformation of $Me_2$1 into $Me_2$3 favors the ππ* photochemical channel over the nπ* channel (*26*), producing the Dewar valence isomer $Me_2$3 rather than ketene **2**; no α-bond cleavage intermediate was observed at any stage of the irradiation (Fig. 1). The Me_2CBD^R molecule presents a rectangular-bent geometry oriented at 90° relative to the $C_3C_4C_5C_6$ ring of $Me_2$3 in the G_4C host matrix. The CO_2 is orthogonally oriented with respect to the Me_2CBD^R ring (Fig. 4B). The C6–O1 (1.58 Å) and C2–C3 (1.57 Å) bonds point more to a non-interactive contact than to covalent bonding, as is possible in zwitterionic structure **5** (Fig. 1).

Further irradiation led to the quantitative transformation of $Me_2$3 into 1,3-dimethylcyclobutadiene (Me_2CBD) and CO_2. Based on the diffraction data, we assigned two different geometries—square-planar (Me_2CBD^S, 62.7%) and rectangular-bent (Me_2CBD^R, 37.3%)—in the crystalline structure of G_4C{Me_2CBD^S and Me_2CBD^R} under confined conditions (Fig. 3D and fig. S7). They are disposed in an orthogonal relative orientation along the axes lining the opposite alternative sulfonate moieties of C (fig. S2). The bridging bond in $Me_2$3 ($d_{C3\text{-}C6}$ = 1.70 Å) is substantially longer than the edge bond C3–C6 (1.48 Å) observed in Me_2CBD^S, though the C6–O1 (1.48 Å) and C2–C3 (1.35 Å) bonds expand by ~0.15 to 1.61 and 1.50 Å, respectively, between Me_2CBD^S and CO_2. These data are more indicative of a strong van der Waals contact than of covalent bonding between the confined CO_2 and Me_2CBD^S molecules in the calixarene cavity.

The presence of CO_2, sequestered via hydrogen bonding within the G_4C host matrix, is clearly an important influence on the observed structures; its interaction is stronger with Me_2CBD^S than with the Me_2CBD^R isomer in the G_4C host matrix environment. Through this interaction, the CO_2 may stabilize Me_2CBD^S in the G_4C host matrix (Fig. 4B), helping to account for its abundance that is a factor of 2 greater than that of the rectangular isomer Me_2CBD^R. The hydrogen-bonded CO_2 molecule generates an asymmetry in the G_4C host matrix cavity: Whereas the Me_2CBD^S molecule, interacting with the CO_2, presents a square-planar geometry, the Me_2CBD^R ring shows a relaxed rectangular-bent geometry that is asymmetrically distorted, its plane slightly flipped with the methyl groups lying out of the plane (Fig. 4B and fig. S2).

The automerization reaction of CBD (Fig. 4A), previously predicted by modeling (*27*), is experimentally supported by the crystal structure of G_4C{Me_2CBD^S and Me_2CBD^R} determined here. We observed both distinct geometries: (i) the thermodynamic square planar Me_2CBD^S/CO_2 complex and (ii) the kinetic rectangular-bent Me_2CBD^R molecule, stabilized under confinement by the G_4C host matrix in different orientations.

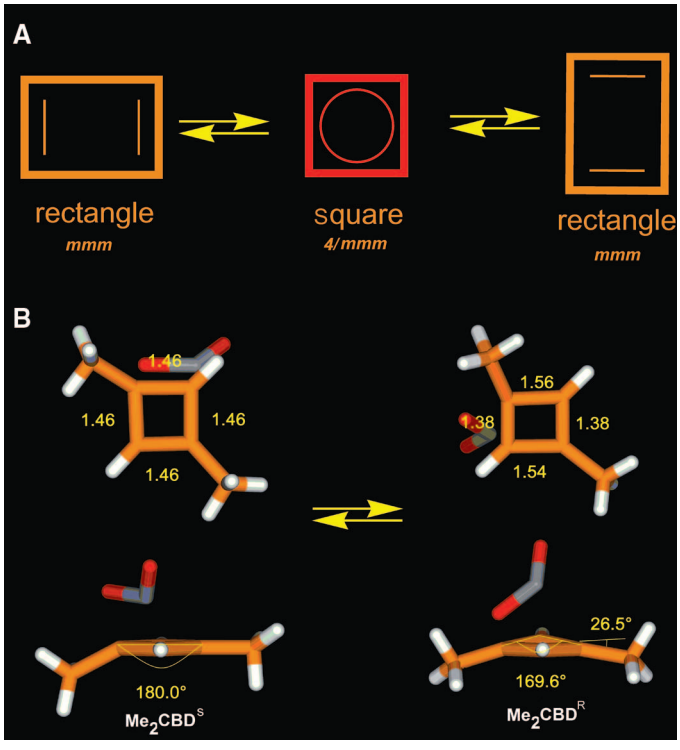

Fig. 4. Mechanistic considerations. (**A**) Automerization reaction of CBD including an equilibrium between two rectangular *mmm* ground states, proceeding through the square-shaped triplet state *4/mmm*. (**B**) Side- (top) and top-view (bottom) stick representation of the confined square-planar Me_2CBD^S molecule (62.7%) in equilibrium with distorted rectangular Me_2CBD^R (37.3%).

References and Notes

1. D. J. Cram, M. E. Tanner, R. Thomas, *Angew. Chem. Int. Ed. Engl.* **30**, 1024 (1991).
2. D. J. Cram, *Angew. Chem. Int. Ed. Engl.* **27**, 1009 (1988).
3. R. Warmuth, *J. Incl. Phenom. Macrocycl. Chem.* **37**, 1 (2000).
4. G. Maier, *Angew. Chem. Int. Ed. Engl.* **13**, 425 (1974).
5. O. L. Chapman, C. L. McIntosh, J. Pacansky, *J. Am. Chem. Soc.* **95**, 244 (1973).
6. M. Avram, G. Mateescu, I. G. Dinulescu, E. Marica, C. D. Nenitzescu, *Tetrahedron Lett.* **2**, 21 (1961).
7. I. G. Dinulescu, *Rev. Chim.* **43**, 502 (1992).
8. J. Limanto, M. L. Snapper, *J. Am. Chem. Soc.* **122**, 8071 (2000).
9. E. Hückel, in *Grundzüge der Theorie Ungesättiger und Aromatischer Verbindungen* (Verlag Chemie, Berlin, 1938), pp. 77–85.
10. L. T. J. Delbaere, M. N. G. James, N. Nakamura, S. Masamune, *J. Am. Chem. Soc.* **97**, 1973 (1975).
11. M. Avram *et al.*, *Tetrahedron* **19**, 187 (1963).
12. D. J. Cram, M. E. Tanner, C. B. Knobler, *J. Am. Chem. Soc.* **113**, 7717 (1991).
13. M. E. Tanner, C. B. Knobler, D. J. Cram, *J. Am. Chem. Soc.* **112**, 1659 (1990).
14. R. C. Helgeson, C. B. Knobler, D. J. Cram, *Chem. Commun.* **3**, 307 (1995).
15. Materials and methods are available as supporting material on *Science* Online.
16. T. Kawamichi, T. Haneda, M. Kawano, M. Fujita, *Nature* **461**, 633 (2009).
17. T. Kawamichi, T. Kodama, M. Kawano, M. Fujita, *Angew. Chem. Int. Ed.* **47**, 8030 (2008).
18. S. L. Zheng *et al.*, *Chemistry* **14**, 706 (2008).
19. T. Mitra *et al.*, *Chemistry* **15**, 1844 (2009).
20. F. Dumitru, Y. M. Legrand, A. Van der Lee, M. Barboiu, *Chem. Commun. (Camb.)* **2009**, 2667 (2009).
21. A. Cazacu *et al.*, *Proc. Natl. Acad. Sci. U.S.A.* **106**, 8117 (2009).
22. J. L. Atwood, L. J. Barbour, M. J. Hardie, C. L. Raston, *Coord. Chem. Rev.* **222**, 3 (2001).
23. K. T. Holman, A. M. Pivovar, M. D. Ward, *Science* **294**, 1907 (2001).
24. A. J. Blake, R. O. Gould, S. G. Harris, H. McNab, S. Parsons, *Acta Crystallogr. C* **50**, 1938 (1994).
25. F. Neumann, K. Jug, *J. Org. Chem.* **59**, 6437 (1994).
26. S. Breda, L. Lapinski, I. Reva, R. Fausto, *J. Photochem. Photobiol. A* **162**, 139 (2004).
27. M. Eckert-Maksić, M. Vazdar, M. Barbatti, H. Lischka, Z. B. Maksić, *J. Chem. Phys.* **125**, 064310 (2006).

28. This work—conducted as part of the award "Dynamic adaptive materials for separation and sensing Microsystems" (M.B.) made under the European Heads of Research Councils and European Science Foundation European Young Investigator (EURYI) Awards scheme in 2004—was supported by funds from the Participating Organizations of EURYI and the European Comission Sixth Framework Program (see www.esf.org/euryi). The x-ray crystallographic coordinates for structures reported in this paper have been deposited at the Cambridge Crystallographic Data Centre (CCDC) under deposition numbers CCDC 764864 to 764868. These data can be obtained free of charge from the CCDC (www.ccdc.cam.ac.uk/data_request/cif).

Supporting Online Material

www.sciencemag.org/cgi/content/full/329/5989/299/DC1
Materials and Methods
Scheme S1
Figs. S1 to S7
Table S1
References

5 February 2010; accepted 19 May 2010
10.1126/science.1188002

Downloaded from www.sciencemag.org on July 15, 2010

Disordering of an Organic Overlayer on a Metal Surface Upon Cooling

A. Schöll,[1]* L. Kilian,[1] Y. Zou,[1] J. Ziroff,[1] S. Hame,[1] F. Reinert,[1,2] E. Umbach,[1]† R. H. Fink[1]‡

Inverse melting or disordering, in which the disordered phase forms upon cooling, is known for a few cases in bulk systems under high pressure. We show that inverse disordering also occurs in two dimensions: For a monolayer of 1,4,5,8-naphthalene-tetracarboxylic dianhydride on Ag(111), a completely reversible order-disorder transition appears upon cooling. The transition is driven by strongly anisotropic interactions within the layer versus with the metal substrate. Spectroscopic data reveal changes in the electronic structure of the system corresponding to a strengthening of the interface bonding at low temperatures. We demonstrate that the delicate, temperature-dependent balance between the vertical and lateral forces is the key to understanding this unconventional phase transition.

In almost all materials, less ordered phases form at temperatures above those of the more ordered phase. For example, a conventional first-order melting process at constant pressure requires the addition of heat to the system, and the entropy of the liquid phase exceeds that of the crystal. The opposite process, a first-order transition from the crystalline into a liquid or disordered phase upon cooling, is rare but does occur (*1*, *2*). Such inverse melting occurs for ^{3}He below about 0.3 kelvin and at pressures of about 30 bar (*3*). A few more examples are known for order-disorder transitions upon cooling. In some bimetallic alloys, inverse melting is described in terms of an undercooled melt, in which the chemical order energetically stabilizes the melt as compared to the mixed crystalline phases (*4*, *5*).

The reported examples of inverse melting or disordering occur at extreme pressure conditions for bulk phases. We now report the experimental observation of an inverse disordering transition in two dimensions without an application of external pressure. For a two-dimensional adsorbate system, competing interactions can be strongly anisotropic. That is, the lateral interaction between the adsorbate molecules and those between the substrate and the adsorbate can occur on different energy scales and have different dependence on temperature. These observations require an extension of the established description of inverse melting; therefore, the present findings may trigger further experimental and theoretical studies (*6*).

The high-resolution low-energy electron diffraction (LEED) pattern recorded for a 1,4,5,8-naphthalene-tetracarboxylic dianhydride (NTCDA) monolayer film on a Ag(111) surface at room temperature (the RT phase) is shown in Fig. 1A (see the supporting online material for experimental details). The coverage corresponds to about 70% of a saturated monolayer and was previously termed a relaxed monolayer (*7*). It refers to a commensurate superstructure described by the superstructure matrix $\mathbf{M} = \begin{pmatrix} 4 & 0 \\ 3 & 6 \end{pmatrix}$. The sharp diffraction spots indicate a high degree of lateral order with large domains. The real-space structure and unit cell of one of the six symmetry-equivalent rotation and mirror domains of the RT phase are displayed in Fig. 1B (*8*). The simulated diffraction spots agree very well with the experimental LEED pattern in Fig. 1A.

Upon cooling to temperature (T) = 155 K, the previous diffraction spots completely disappear (Fig. 1C). The long-range order gets lost, and a disordered low-temperature monolayer phase (the LT phase) is formed. Upon subsequent heating, the LEED spots reappear, and at a substrate temperature of $T \sim 190$ K, the RT LEED pattern is completely restored. This cycle is reversible and can be repeated numerous times.

The question arises whether the loss of lateral order is based on a loss of orientational order (tilting) with respect to the (111) plane. The molecules in the RT phase (measurements between 200 and 300 K) lie flat on the substrate surface, as deduced from near-edge x-ray absorption fine structure (NEXAFS) dichroism (*9*) and x-ray standing wave studies (*10*). The comparison of the NEXAFS spectra with p- and s-polarization of the incident light in Fig. 2A shows identical dichroic behavior (*11*) for the RT phase (upper spectra) and the LT phase (lower spectra): no π^* resonances are observed for s-polarization for both temperatures. We conclude that the molecular planes are coplanar with the substrate in both phases.

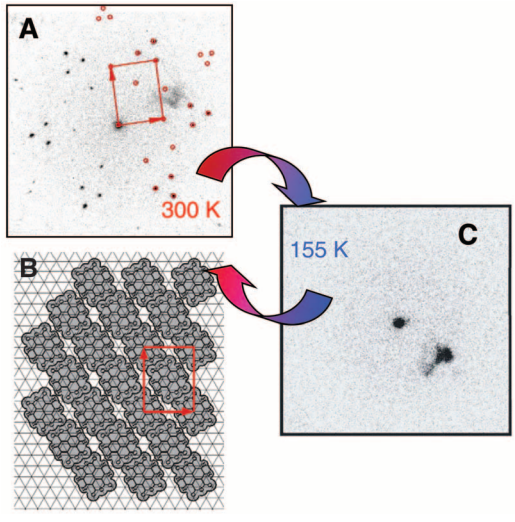

Fig. 1. SPA-LEED pictures of the relaxed NTCDA monolayer on Ag(111) at 300 K (**A**) and at 155 K (**C**). The reversibility of the phase transition is indicated by arrows. (**B**) Real space structure of the RT phase with the commensurate unit cell.

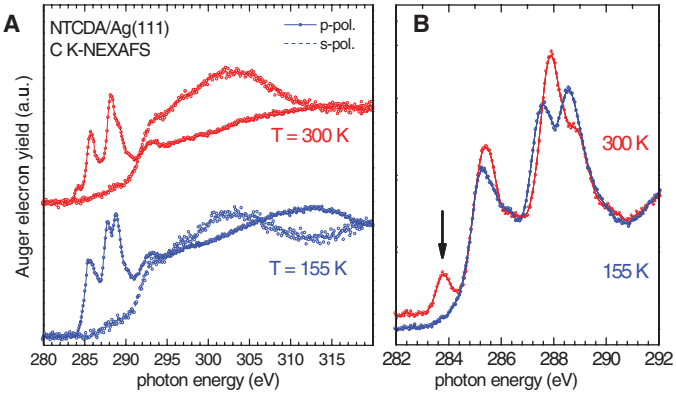

Fig. 2. (**A**) Carbon K-edge NEXAFS spectra of the RT phase (top) and LT phase (bottom) recorded with p- (continuous lines/points) and s-polarization (dashed lines/open symbols). (**B**) π^* regimes (p-polarization) compared on expanded scales.

[1]Universität Würzburg, Experimentelle Physik VII, D-97074 Würzburg, Germany. [2]Gemeinschaftslabor für Nanoanalytik, Karlsruhe Institute of Technology, 76021 Karlsruhe, Germany.

*To whom correspondence should be addressed. E-mail: achim.schoell@physik.uni-wuerzburg.de

†Present address: Karlsruhe Institute of Technology, 76021 Karlsruhe, Germany.

‡Present address: Physikalische Chemie II and Interdisciplinary Center for Molecular Materials/Interdisciplinary Center for Interface-Controlled Processes, Universität Erlangen, Egerlandstrasse 3, D-91058 Erlangen, Germany.

Downloaded from www.sciencemag.org on July 15, 2010

A closer inspection of the NEXAFS data recorded with p-polarization reveals details on the interaction of the molecules with the substrate. We compare the respective RT and LT spectra in Fig. 2B. From previous NEXAFS investigations and theoretical calculations, we could assign the various resonances for multilayer samples, which are due to transitions from the four symmetry-inequivalent C1s sites into the unoccupied π* orbitals LUMO (lowest unoccupied molecular orbital) to LUMO+4 (*12*). The RT spectrum generally resembles the multilayer data, but the LT spectrum shows a strongly altered signature indicative of stronger substrate bonding. Although various resonances are affected, the most striking difference occurs for the peak at 283.8 eV, which can be assigned to transitions from C1s sites located at the naphthalene core into the LUMO. This peak is less intense for the RT sample than for the multilayer (*12*) sample, and it completely vanishes for the LT phase. Evidently, the (former) LUMO becomes completely occupied in the disordered phase.

This finding is corroborated by the photoelectron spectroscopy (PES) data of the valence levels recorded along the phase transition (Fig. 3). All spectra show a new occupied state near the Fermi level (E_F) that can be attributed to the interaction-induced charge transfer from the substrate into the former molecular LUMO level (*13*, *14*). For the RT phase, this former LUMO state is centered at 0.22 eV and cut by E_F, resulting in a metal-like, partially occupied state. The transition into the LT phase, however, leads to a complete occupation of the LUMO and a further downshift of the respective signal to a binding energy of 0.48 eV. The sharp peak occurring directly at E_F in the case of the RT spectra can be attributed to a Fermi resonance.

The present spectroscopic results can be consistently explained in agreement with earlier core-level PES data (*15*) and high-resolution electron energy-loss spectroscopy experiments by a covalent interaction of the NTCDA molecules with the Ag(111) substrate that becomes stronger in the disordered LT phase. The latter finding may reflect decreased substrate bonding lengths, as previously reported for the similar molecule 3,4,9,10-perylene-TCDA (*16*).

Moreover, the characteristic signatures in the NEXAFS spectra of Fig. 2 allow distinguishing of the RT and LT fractions quantitatively during the transition. Figure 4 shows a series of NEXAFS scans recorded while the temperature was decreased for a RT sample until the LT phase was reached (Fig. 4A), and increased again until the RT phase was recovered (Fig. 4B). The cooling and heating rates were ±0.1 K/s, respectively. The change of the spectroscopic signature from RT to LT was gradual, but the strongest changes occurred between 170 and 160 K. Upon heating, the strongest changes could be observed between 180 and 187.5 K (Fig. 4C). We obtained these data points by deconvoluting the temperature-dependent spectra using the RT and LT spectra [that is, spectrum(T) = c × RT spectrum + (1 – c) × LT spectrum] as references for the respective phases. The parameter c corresponds to the fraction of NTCDA molecules in the ordered RT phase and is plotted against sample temperature in Fig. 4C. As indicated by the arrows, the plot shows a steep decrease in the fraction of molecules in the ordered phase around 165 K upon cooling, whereas upon heating, the ordered phase is recovered around 180 K. The clear hysteresis indicates a first-order phase transition, as generally expected for inverse melting (*1*). Moreover, from time-dependent spot profile analysis (SPA)–LEED measurements at temperatures between 140 and 160 K (fig. S2) an activation energy of E_A = 60 meV is deduced for the transition into the disordered phase.

Generally, the driving force for phase transitions at constant pressure is the gain in Gibbs free energy $\Delta G = \Delta H - T \times \Delta S$ (where H is enthalpy and S is entropy). Our spectroscopic data indicate a stronger molecule-substrate bonding in the disordered LT phase. The latter is on the order of electron volts (*17*, *18*) and largely exceeds the intermolecular interaction, and can be understood as a more negative enthalpic contribution ΔH. As a consequence, the heat absorbed while transferring the system into the ordered RT state can be considered as the energy required to reduce the bonding to the substrate.

What about the entropic term? The phase at higher temperature must have a higher degree of disorder or entropy S, because $\Delta S \sim \Delta Q$. Another degree of freedom must adjust the entropy balance, because the long-range order increases ($\Delta S < 0$) (*2*, *19*). Apparently, the structurally long-range ordered phase has to be more disordered in total than the amorphous phase, which seems

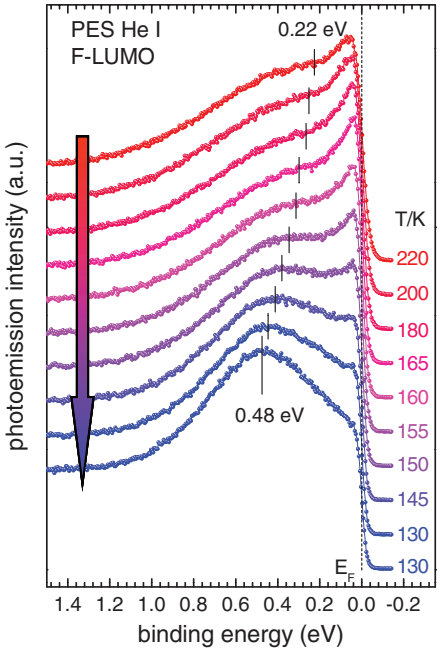

Fig. 3. PES data recorded at the Fermi edge for temperatures in the transition regime during cooling. F-LUMO, former-LUMO.

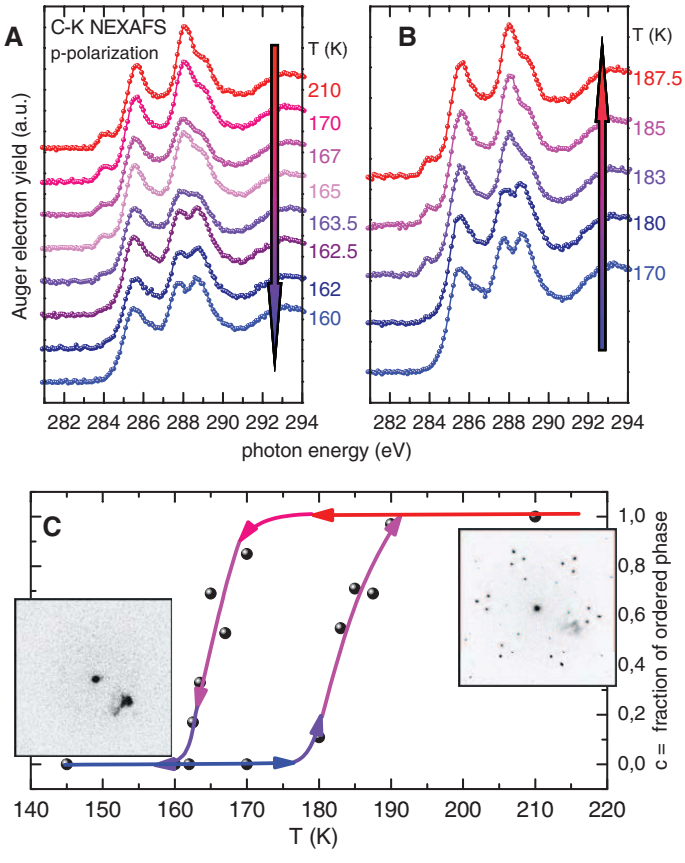

Fig. 4. Rapid NEXAFS scans (p-polarization) of the π* regimes recorded during cooling (**A**) and heating (**B**). (**C**) Hysteresis curve of the inverse melting phase transition derived from the data in (A) and (B).

Downloaded from www.sciencemag.org on July 15, 2010

counterintuitive. Based on the finding of a much stronger molecule-substrate interaction in the LT phase, we believe that the local atomic order at the interface, although different from molecule to molecule (no long-range order), is considerably higher in the LT (compared to the RT) phase, connected with a shorter distance between substrate and adsorbate atoms. Thus, heating leads to a reduction of the short-range order ($\Delta S > 0$), which is not completely compensated for by the appearance of long-range order ($\Delta S < 0$).

The reduction of the bonding strength is most probably accompanied by an increase of the vertical bond lengths, perhaps induced by the excitation of vertical molecular vibrations (*20*). Consequently, the lateral interaction between the molecules gains more weight and induces the lateral ordering (*16*).

At low temperature, the structural reorganization may be explained by different, energetically favorable adsorption sites of the NTCDA molecules if they are near the substrate, perhaps involving a distortion of the adsorbed molecule. If the molecules thereby differ slightly, such as in their rotational and/or translational alignment (the local bonding geometry), a statistic population of the respective sites would result in the observed loss of long-range order. The occurrence of both translational and rotational disorder upon cooling may occur, according to the existing data, and the order-disorder transition can thus indeed be a real melting process or a transition into a glassy state.

This scenario may bear some analogy to the description of inverse melting in metallic alloys (*4*). There, the phenomenon is possible because the (low-temperature) amorphous phase gains energy against the crystal because of increased chemical short-range order (*4*). The very pronounced anisotropy of the forces involved in the present strongly anisotropic (quasi-two-dimensional) case, where the ratio of the respective energy scales is extremely crucial, requires a different theoretical description.

References and Notes

1. N. Schupper, N. M. Shnerb, *Phys. Rev. E Stat. Nonlin. Soft Matter Phys.* **72**, 046107 (2005).
2. A. L. Greer, *Nature* **404**, 134 (2000).
3. P. M. Tedrow, D. M. Lee, *Phys. Rev.* **181**, 399 (1969).
4. W. Sinkler, C. Michaelsen, R. Bormann, D. Spilsbury, N. Cowlam, *Phys. Rev. B* **55**, 2874 (1997).
5. H. Y. Bai, C. Michaelsen, R. Bormann, *Phys. Rev. B* **56**, R11361 (1997).
6. M. R. Feeney, P. G. Debenedetti, F. H. Stillinger, *J. Chem. Phys.* **119**, 4582 (2003).
7. U. Stahl, D. Gador, A. Soukopp, R. Fink, E. Umbach, *Surf. Sci.* **414**, 423 (1998).
8. L. Kilian, thesis, Universität Würzburg, Würzburg, Germany (2002).
9. D. Gador *et al.*, *J. Electron Spectrosc. Relat. Phenom.* **101–103**, 523 (1999).
10. C. Stadler, S. Hansen, A. Schöll, C. Kumpf, E. Umbach, *N. J. Phys.* **9**, 50 (2007).
11. J. Stöhr, *NEXAFS Spectroscopy*, R. Gomer, Ed. (Spinger Series in Surface Science, Springer, Berlin, 1992), vol. 25.
12. A. Schöll *et al.*, *Phys. Rev. Lett.* **93**, 146406 (2004).
13. Y. Zou *et al.*, *Surf. Sci.* **600**, 1240 (2006).
14. A. Bendounan *et al.*, *Surf. Sci.* **601**, 4013 (2007).
15. A. Schöll, Y. Zou, T. Schmidt, R. Fink, E. Umbach, *J. Phys. Chem. B* **108**, 14741 (2004).
16. L. Kilian *et al.*, *Phys. Rev. Lett.* **100**, 136103 (2008).
17. F. S. Tautz, *Prog. Surf. Sci.* **82**, 479 (2007).
18. J. Ziroff, P. Gold, A. Bendounan, F. Forster, F. Reinert, *Surf. Sci.* **603**, 354 (2009).
19. N. Schupper, N. M. Shnerb, *Phys. Rev. Lett.* **93**, 037202 (2004).
20. O. Skibbe *et al.*, *J. Chem. Phys.* **131**, 024701 (2009).

21. Fruitful discussions with M. Sokolowski and Th. Schmidt are gratefully acknowledged. This work was funded by the German Bundesministerium für Bildung und Forschung (contracts 05 KS1WWA-5 and 05 KS7WE1) and by the Deutsche Forschungsgemeinschaft (contract DFG Re 1469/3-2). Experimental support by the BESSY (Berlin Electron Storage Ring Society for Synchrotron Radiation) staff during beam time is gratefully acknowledged.

Supporting Online Material

www.sciencemag.org/cgi/content/full/329/5989/303/DC1
Methods
SOM Text
Figs. S1 and S2
References

4 March 2010; accepted 8 June 2010
10.1126/science.1189106

Downloaded from www.sciencemag.org on July 15, 2010

Biocatalytic Asymmetric Synthesis of Chiral Amines from Ketones Applied to Sitagliptin Manufacture

Christopher K. Savile,[1]* Jacob M. Janey,[2]* Emily C. Mundorff,[1] Jeffrey C. Moore,[2] Sarena Tam,[1] William R. Jarvis,[1] Jeffrey C. Colbeck,[1] Anke Krebber,[1] Fred J. Fleitz,[2] Jos Brands,[2] Paul N. Devine,[2] Gjalt W. Huisman,[1] Gregory J. Hughes[2]

Pharmaceutical synthesis can benefit greatly from the selectivity gains associated with enzymatic catalysis. Here, we report an efficient biocatalytic process to replace a recently implemented rhodium-catalyzed asymmetric enamine hydrogenation for the large-scale manufacture of the antidiabetic compound sitagliptin. Starting from an enzyme that had the catalytic machinery to perform the desired chemistry but lacked any activity toward the prositagliptin ketone, we applied a substrate walking, modeling, and mutation approach to create a transaminase with marginal activity for the synthesis of the chiral amine; this variant was then further engineered via directed evolution for practical application in a manufacturing setting. The resultant biocatalysts showed broad applicability toward the synthesis of chiral amines that previously were accessible only via resolution. This work underscores the maturation of biocatalysis to enable efficient, economical, and environmentally benign processes for the manufacture of pharmaceuticals.

Asymmetric hydrogenation technologies are being increasingly used for commercial-scale manufacture of fine chemicals and pharmaceuticals (*1*). Solutions that address remaining shortcomings of such technologies, including the need for high-pressure hydrogen, the use and subsequent removal of precious and toxic transition metals, the oftentimes lengthy process of ligand screening and synthesis, and the generally insufficient stereoselectivity (requiring further upgrading of the product), are still being sought. Even though biocatalysis is rarely constrained by these shortcomings, enzymes may suffer from other limitations, such as low turnover numbers, instability toward the demanding conditions of chemical processes, and postreaction processing issues.

The current synthesis of sitagliptin (*2*, *3*) involves asymmetric hydrogenation of an enamine at high pressure [250 pounds per square inch (psi)] using a rhodium-based chiral catalyst (Fig. 1A) (*4*). Within the manufacturing scheme, the chemistry suffers from inadequate stereoselectivity and a product stream contaminated with rhodium, necessitating additional purification steps at the expense of yield to upgrade both enantiomeric excess (e.e.) and chemical purity. By using a transaminase (*5*–*8*) scaffold and various protein engineering technologies, we have developed a catalyst and process that substantially improve the efficiency of sitagliptin manufacturing (Fig. 1B).

Transaminases have a limited substrate range, most accepting only substrates with a substituent no larger than a methyl group at the position adjacent to the ketone (Fig. 2A) (*9*–*14*). Not surprisingly, screening a variety of commercially available transaminases provided no enzyme with detectable activity for amination of the prositagliptin ketone (Fig. 2B). We therefore applied a combination of in silico design and directed evolution in an effort to confer such activity.

An (*R*)-selective transaminase [ATA-117 (*15*), a homolog of an enzyme from *Arthrobacter sp.*] (*16*) was previously used for *R*-specific transamination of methyl ketones and small cyclic ketones

[1]Codexis, Incorporated, 200 Penobscot Drive, Redwood City, CA 94063, USA. [2]Department of Process Research, Merck Research Laboratories, Merck and Company, Incorporated, Rahway, NJ 07065, USA.

*To whom correspondence should be addressed. E-mail: christopher.savile@codexis.com (C.K.S.); jacob_janey@merck.com (J.M.J.)

(*11*, *12*). To assess the feasibility of developing an enzyme for sitagliptin synthesis, we generated a structural homology model of ATA-117 (*17*) to develop hypotheses for initial library designs. Docking studies using this model suggested that the enzyme would be unable to bind prositagliptin ketone (Fig. 2B) because of steric interference in the small binding pocket and potentially undesired interactions in the large binding pocket (Fig. 2C). By using a substrate walking approach (*18*) with a truncated substrate (Fig. 2D), we first engineered the large binding pocket of the enzyme and then evolved that enzyme for activity toward prositagliptin ketone.

Consistent with the model, ATA-117 was poorly active on the truncated methyl ketone analog (Fig. 2D), giving 4% conversion at 2 g/l substrate loading (table S2). Site saturation libraries of residues lining the large pocket of the active site provided new variants with increased activity toward the methyl ketone analog. The best variant contained a $S^{223} \rightarrow P^{223}$ [S223P (*19*)] mutation and showed an 11-fold activity improvement (Fig. 3 and table S1). On the basis of this improved variant (ATA-117: S223P), we generated a small library of enzyme variants for potential activity on prositagliptin ketone. Analysis of the enzyme model suggested four residues that could potentially interact with the trifluorophenyl group [V69, F122, T283, and A284 (*19*)]. Each of these positions was individually subjected to saturation mutagenesis and also included in a combinatorial library that evaluated several residues at each position on the basis of structural considerations [$V^{69} \rightarrow G^{69}$ and $V^{69} \rightarrow A^{69}$ (V69GA), F122AVLIG, T283GAS, and A284GF; library size of 216 variants]. A variant containing four mutations, three in the small binding pocket and one in the large pocket, provided the first detectable transaminase activity on prositagliptin ketone (Fig. 3 and table S3). No detectable activity was identified in any of the variants from the single amino acid site saturation libraries. Initial activity was accomplished via an F122I, V, or L mutation in combination with V69G or A284G. Docking studies indicated that these mutations may relieve the steric interference in the small binding pocket (Fig. 2E). Enzyme loading of 10 g/l provided 0.7% conversion of 2 g/l of ketone over 24 hours, corresponding to an estimated turnover of 0.1 per day. Screening the same combinatorial library in the ATA-117 context without the S223P large binding pocket mutation did not provide any variant with detectible activity toward prositagliptin ketone. Having attained activity through computer-aided catalyst design, we started evolving an enzyme variant for a practical, large-scale process.

The variant with the highest activity toward prositagliptin ketone from round 1b was chosen as the parent for the second round of evolution, and all the beneficial mutations from both the small-pocket combinatorial library and the large-pocket saturation mutagenesis libraries were combined into a new library. Screening of this library resulted in a variant with 75-fold increased

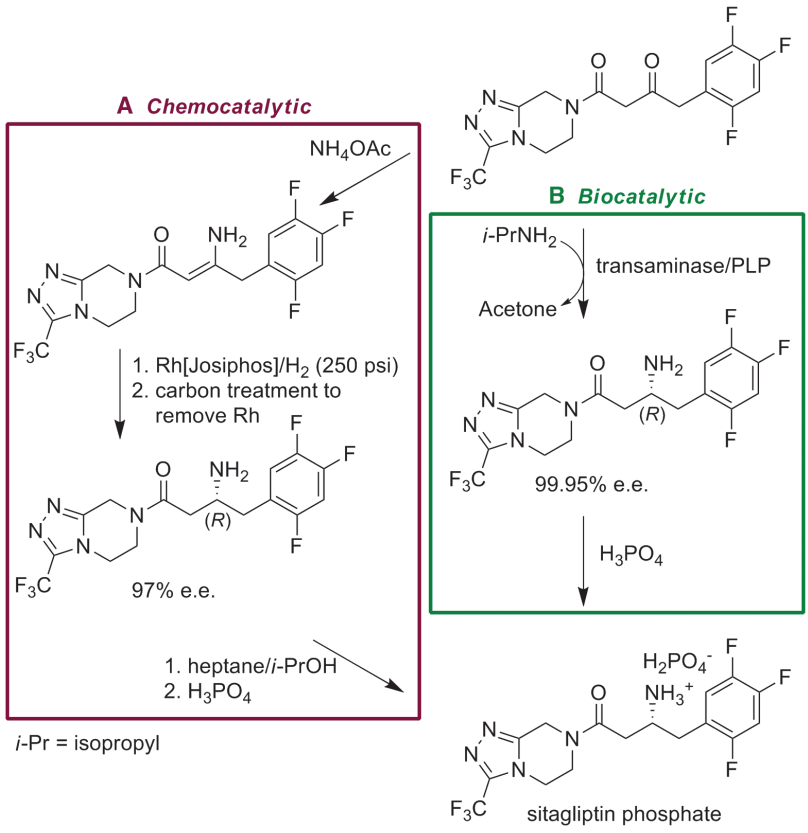

Fig. 1. (**A**) The current synthesis of sitagliptin involves enamine formation followed by asymmetric hydrogenation at high pressure (250 psi) using a rhodium-based chiral catalyst, providing sitagliptin in 97% e.e., with trace amounts of rhodium. Recrystallization to upgrade e.e. followed by phosphate salt formation provides sitagliptin phosphate. (**B**) Our biocatalytic route features direct amination of prositagliptin ketone to provide enantiopure sitagliptin, followed by phosphate salt formation to provide sitagliptin phosphate.

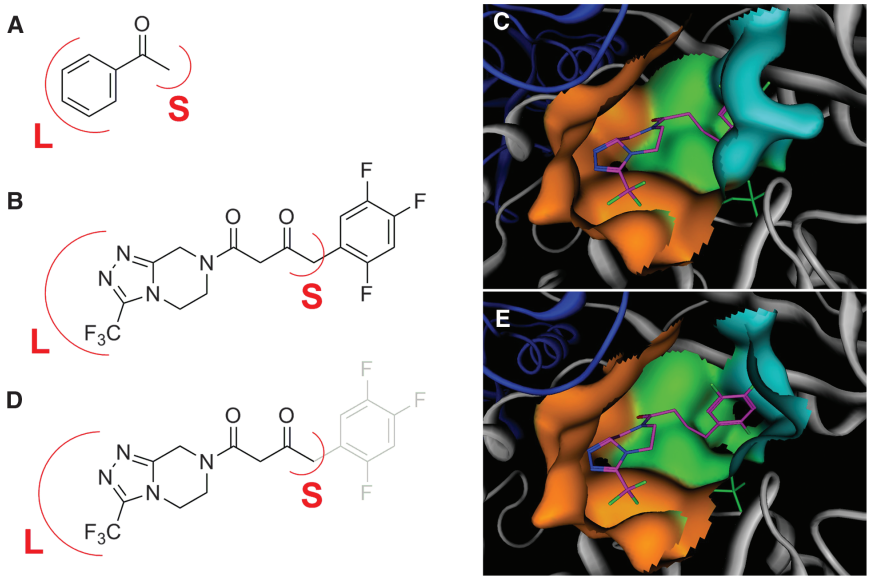

Fig. 2. Previous substrate range studies suggested that the active site of transaminase consists of large (L) and small (S, typically limited to substituents about the size of a methyl group) binding pockets as mapped on the structure of acetophenone (**A**). Accordingly, the structure of prositagliptin ketone (**B**) can be mapped on these binding pockets and docked into the active site of the homology model (**C**). A prositagliptin ketone analog (**D**) was designed to fit the large pocket for initial optimization of this part of the active site. After initial engineering of the large pocket, an enzyme variant was generated with activity on the desired substrate (**E**) by excavating the small pocket (gray/blue, transaminase homology model; orange, large binding pocket; turquoise, small binding pocket; green, PLP and catalytic residues).

Downloaded from www.sciencemag.org on July 15, 2010

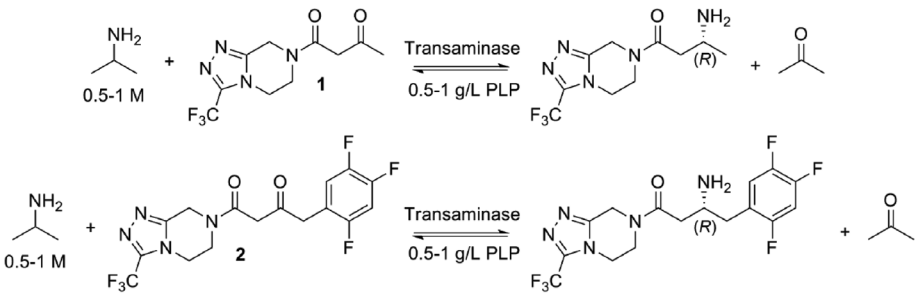

Substrate	Added Mutations*	[Substrate] in g/l	Assay changes	Round identified	Improvement over parent†
1	ATA-117	2		–	N/A
1	G136Y	2		1a	6
1	S223P	2		1a	11
2	S223P	2		1a	Not active
2	Y26H;‡ V65A;‡ V69G; F122I; A284G	2		1b	first active
2	H62T; G136Y; E137I; V199I; A209L; T282S	2		2	75
2	S8P; H26Y; G69C; M94I; I137T; G215C	5	5% DMSO to 5% MeOH; RT to 30°C	3	9
2	L61Y; C69T; Y136F; T137E	10	0.5 to 1 M $iPrNH_2$; pH 7.5 to pH 8.5	4	4
2	D81G; I94L; I96L; T178S; L269P; P297S; S321P	40	5 to 10% MeOH; 30 to 45°C	5	1.4
2	Y60F; L94I; A169L; S178T; G217N; L273Y	100	10 to 20% MeOH	6	1.6
2	S124H	100	20% MeOH to 25% DMSO	7	1.1
2	I122M; H124N	100		8	1.1
2	Q329H	100		9	1.9
2	N124T; Y150S; V152C; H329Q	50	25 to 50% DMSO; 0.5% acetone	10	2
2	S126T	50		11	1.4

Fig. 3. Performance of evolvants in HTP screening over the course of evolution. *Mutations accumulated in each round of evolution; reference amino acid refers to parent from previous round of evolution. †Fold improvement over parent refers to the parent for that round of evolution. ‡Mutagenesis experiments showed that these mutations were not critical for activity toward prositagliptin ketone. The top variant from round 1b contained three mutations in the small pocket; however, two are sufficient for achieving detectable activity. Dash entry indicates starting enzyme; RT, room temperature.

activity compared with that of the second-round parent. This variant contained 12 mutations, 10 of which map to the binding pocket model (Fig. 3 and table S5).

Despite this substantial activity enhancement, this catalyst was not yet of practical utility. Reaction conditions in a chemical plant are much different from the conditions that an enzyme encounters in nature, making the development of practical biocatalytic processes a multidimensional challenge (*20*, *21*). The solubility of the prositagliptin ketone in water is low (<1 g/l), necessitating a substantial amount of organic cosolvent to prevent precipitation during reaction. After an evaluation of various cosolvents, methanol and dimethylsulfoxide (DMSO) were identified as optimal with regard to both enzyme performance and ketone solubility (table S7). Solubility can also be enhanced by operating at higher temperatures, prompting our selection of higher boiling DMSO as the preferred solvent. Because transaminase-catalyzed reactions are equilibrium controlled, product accumulation is favored by a large excess of the amine donor isopropylamine (*i*-$PrNH_2$) and/or removal of acetone coproduct. Thus, in order to meet the required performance for practical application, the biochemical characteristics of the transaminase needed to be improved to withstand the harsh conditions of at least 100 g/l (250 mM) prositagliptin ketone, 1 M *i*-$PrNH_2$, >25% DMSO, and a temperature of >40°C for a period of 24 hours, and to give product with >99.9% e.e.

Biocatalyst libraries were generated by using a variety of methods in subsequent iterative rounds of directed evolution (*22*–*25*). Screening of these libraries under processlike conditions provided variants that were increasingly tolerant to the desired process conditions. Specific reaction conditions could not be devised at project inception because no catalyst was available for evaluation of such conditions. Consequently, chemical process development and enzyme optimization were performed in parallel, with process conditions iteratively optimized as improved enzymes became available. Over the course of 11 rounds of evolution, high throughput (HTP) screening conditions were rendered more stringent with the rising activity and tolerance of the biocatalyst. Specifically, we increased the substrate concentration from 2 to 100 g/l, the *i*-$PrNH_2$ concentration from 0.5 to 1 M, the cosolvent from 5 to 50% DMSO, the pH from 7.5 to 8.5, and the temperature from 22° to 45°C, ultimately leading to a catalyst that met the required process targets (table S8). All active transaminase variants tested met the >99.9% e.e. target. Variants generated via this approach were simultaneously optimized for several performance criteria: activity; tolerance to DMSO, acetone, and *i*-$PrNH_2$; stability to the elevated temperature of the reaction medium; and expression in an *Escherichia coli* manufacturing host.

The sequence changes accumulated through this process gave rise to a compounded improvement of four orders of magnitude in activity from the initial prositagliptin transaminase (*26*). The final catalyst contained 27 mutations; of the 17 noncatalytically essential amino acid residues predicted to be interacting with the substrate, 10 were mutated in the final variant. The 27 mutations were obtained by screening various libraries that included diversity identified via structure-aided design of the small binding pocket (4 mutations), site saturation mutagenesis of the large binding pocket (5 mutations), site saturation mutagenesis of the small binding pocket (1 mutation), site saturation mutagenesis of positions outside the binding pockets (2 mutations), homology libraries (10 mutations), and random mutagenesis (5 mutations). The progression of mutagenesis is depicted on the homology model (Fig. 4). After the active site was engineered to accommodate the substrate in the initial rounds, further improvements to generate a productive catalyst came from substantial modification in the dimer interfacial region. The enzyme is presumably active only as a dimer (*27*); we can speculate that these mutations serve to strengthen dimer interactions in the face of increasingly destabilizing reaction conditions (*28*).

Under optimal conditions (*17*), the best variant converted 200 g/l prositagliptin ketone to sitagliptin of >99.95% e.e. (the undesired enantiomer was never detected) by using 6 g/l enzyme in 50% DMSO with a 92% assay yield at the end of reaction (table S11). In comparison with the rhodium-catalyzed process (Fig. 1A), the biocatalytic process provides sitagliptin with a 10 to 13% increase in overall yield, a 53% increase in

Downloaded from www.sciencemag.org on July 15, 2010

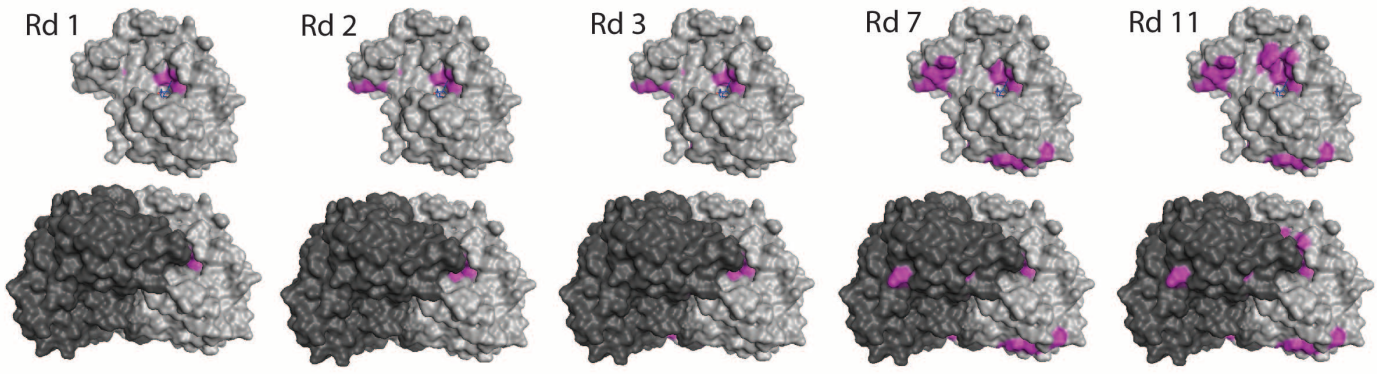

Fig. 4. Structural models of variants from sequential stages of the evolution program. Accumulated mutations are highlighted in purple on the homology model of the transaminase used in this study (size exclusion chromatography data show that the enzyme forms a dimer). The top row shows the mutations mapped on the monomer with the active site of the enzyme exposed and substrate bound. The bottom row shows the mutations mapped on the dimer. The active site, the subunit interface, and a few exposed surface areas can be identified as structural hot spots for mutations.

Fig. 5. Transaminase (TA)–catalyzed amination reactions that were heretofore not feasible either enzymatically or chemically but now proceed with the enzymes described in this work.

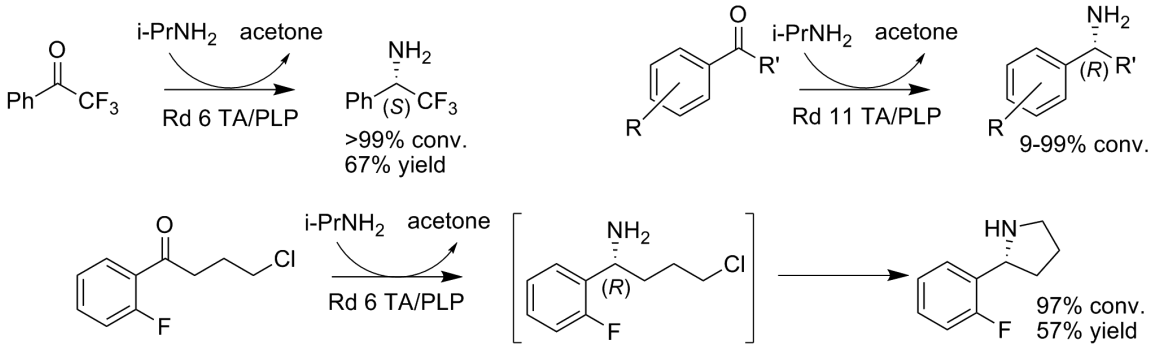

productivity (kg/l per day), a 19% reduction in total waste, the elimination of all heavy metals, and a reduction in total manufacturing cost; the enzymatic reaction is run in multipurpose vessels, avoiding the need for specialized high-pressure hydrogenation equipment.

The enzymes developed for sitagliptin synthesis have a broad substrate range and increased tolerance to high concentrations of *i*-PrNH$_2$ and organic solvent that enhances their practical utility. For instance, various trifluoromethyl-substituted amines as well as phenylethylamines with electron-rich substituents (Fig. 5 and fig. S6), which cannot be generated via traditional reductive amination, were prepared with near-perfect stereopurity. The engineered transaminases also enabled efficient access to chiral pyrrolidines. As such, these enzymes provide a general approach for the practical synthesis of chiral amines from prochiral ketones, which is of general interest in pharmaceutical manufacturing (*29*).

Although naturally occurring enzymes rarely offer ideal manufacturing catalysts, directed evolution provides an effective means to overcome this limitation. We have demonstrated that combining modeling with directed evolution offers a rapid means of creating an active enzyme that can operate under the demanding conditions required for the manufacture of pharmaceuticals. In addition, we have removed the intrinsic limitation that transaminases accept only a methyl substituent adjacent to the carbonyl functionality, thereby making substantial progress toward a general approach for the safe, efficient, environmentally friendly production of chiral primary amines. The manufacture of chiral alcohols is already often accomplished with biocatalysts (*30*–*32*); chiral amine synthesis via the enzymatic platform described here is expected to reach a similar level of broad utility and robustness. This development will serve as a model for the implementation of other biocatalytic manufacturing processes in which enzymes can be evolved to meet desired chiral process targets.

References and Notes

1. N. B. Johnson, I. C. Lennon, P. H. Moran, J. A. Ramsden, *Acc. Chem. Res.* **40**, 1291 (2007).
2. D. M. Kendall, R. M. Cuddihy, R. M. Bergenstal, *Eur. J. Intern. Med.* **20** (suppl.), S329 (2009).
3. D. Williams-Herman *et al.*, *BMC Endocr. Disord.* **8**, 14 (2008).
4. K. B. Hansen *et al.*, *J. Am. Chem. Soc.* **131**, 8798 (2009).
5. α-Transaminases are pyridoxal 5′-phosphate (PLP)-dependent enzymes widespread in nature for the synthesis of α-amino acids from the corresponding α-keto acids; comparatively few ω-transaminases, for the synthesis of chiral amines that are not adjacent to carboxylic acid functionalities, are known.
6. S. P. Crump, J. D. Rozzell, in *Biocatalytic Production of Amino Acids and Derivatives*, J. D. Rozzell, F. Wagner, Eds. (Wiley, New York, 1992), pp. 43–58.
7. J.-S. Shin, B.-G. Kim, *J. Org. Chem.* **67**, 2848 (2002).
8. B.-K. Cho *et al.*, *Biotechnol. Bioeng.* **99**, 275 (2008).
9. M. Höhne, S. Kühl, K. Robins, U. T. Bornscheuer, *ChemBioChem* **9**, 363 (2008).
10. M. D. Truppo, J. D. Rozzell, J. C. Moore, N. J. Turner, *Org. Biomol. Chem.* **7**, 395 (2009).
11. M. D. Truppo, N. J. Turner, J. D. Rozzell, *Chem. Commun.* **2009**, 2127 (2009).
12. D. Koszelewski, D. Clay, D. Rozzell, W. Kroutil, *Eur. J. Org. Chem.* **2009**, 2289 (2009).
13. D. Koszelewski *et al.*, *Angew. Chem. Int. Ed.* **47**, 9337 (2008).
14. D. Koszelewski, I. Lavandera, D. Clay, D. Rozzell, W. Kroutil, *Adv. Synth. Catal.* **350**, 2761 (2008).
15. The complete amino acid sequence of ATA-117 is as follows: MAFSADTSEIVYTHDTGLDYITYSDYELDPANPLAGGAA-WIEGAFVPPSEARISIFDQGYLHSDVTYTVFHVWNGNAFRLD-DHIERLFSNAESMRIIPPLTQDEVKEIALELVAKTELREAFVSVSITR-GYSSTPGERDITKHRPQVYMYAVPYQWIVPFDRIRDGVHAM-VAQSVRRTPRSSIDPQVKNFQWGDLIRAVQETHDRG-FEAPLLLDGDGLLAEGSGFNVVVIKDGVVRSPGRAALPGITRKTV-LEIAESLGHEAILADITLAELLDADEVLGCTTAGGVWPFVSVDGN-PISDGVPGPVTQSIIRRYWELNVESSSLLTPVQY.
16. A. Iwasaki, Y. Yamada, N. Kizaki, Y. Ikenaka, J. Hasegawa, *Appl. Microbiol. Biotechnol.* **69**, 499 (2006).
17. Materials and methods are detailed in supporting online material on *Science* Online.
18. Z. Chen, H. Zhao, *J. Mol. Biol.* **348**, 1273 (2005).
19. Single-letter abbreviations for the amino acid residues are as follows: A, Ala; C, Cys; D, Asp; E, Glu; F, Phe; G, Gly; H, His; I, Ile; K, Lys; L, Leu; M, Met; N, Asn; P, Pro; Q, Gln; R, Arg; S, Ser; T, Thr; V, Val; W, Trp; and Y, Tyr.
20. G. W. Huisman, J. J. Lalonde, in *Biocatalysis in the Pharmaceutical and Biotechnology Industries*, R. N. Patel, Ed. (CRC, Boca Raton, FL, 2006), pp. 717–742.
21. I. W. Davies, C. J. Welch, *Science* **325**, 701 (2009).
22. R. J. Fox *et al.*, *Nat. Biotechnol.* **25**, 338 (2007).
23. J. H. Zhang, G. Dawes, W. P. Stemmer, *Proc. Natl. Acad. Sci. U.S.A.* **94**, 4504 (1997).
24. K. Stutzman-Engwall *et al.*, *Metab. Eng.* **7**, 27 (2005).
25. J. Liao *et al.*, *BMC Biotechnol.* **7**, 16 (2007).
26. See "quantitation of catalyst improvement," figs. S1 and S2, and tables S10 and S11 in supporting online material (SOM) on *Science* Online.

Downloaded from www.sciencemag.org on July 15, 2010

27. Size exclusion chromatography data show the enzyme forms a dimer (fig. S4).
28. V. G. H. Eijsink *et al.*, *J. Biotechnol.* **113**, 105 (2004).
29. D. J. C. Constable *et al.*, *Green Chem.* **9**, 411 (2007).
30. S. M. A. De Wildeman, T. Sonke, H. E. Schoemaker, O. May, *Acc. Chem. Res.* **40**, 1260 (2007).
31. J. C. Moore, D. J. Pollard, B. Kosjek, P. N. Devine, *Acc. Chem. Res.* **40**, 1412 (2007).
32. G. W. Huisman, J. Liang, A. Krebber, *Curr. Opin. Chem. Biol.* **14**, 122 (2010).
33. We thank C. Ng, D. Standish, M. Mayhew, D. Gray, C. Fletcher, F. Mazzini, P. Lattik, T. Brandon, and J. Postlethwaite for developing the transaminase production system; R. Fox for bioinformatics support; M. Jefferson, R. Trinidad, and M. Whitehorn for assay support; V. Mitchell for molecular biology support; J. Munger and O. Gooding for process development support; P. Fernandez, S. Grosser, and M. Mohan for pilot scale development; K. Morley and B. Grau for additional synthesis support; M. Foster and N. Wu for analytical support; and L. Moore, S. Lato, P. Seufer-Wasserthal, J. Grate, J. Liang, and J. Lalonde for helpful suggestions. Merck and Codexis have filed patent applications on the transaminases, the genes encoding them as well as their use. Materials can be provided under a materials transfer agreement; requests for enzymes should be directed to C.K.S. (christopher.savile@codexis.com), whereas requests for substrates, products, and process information should be directed to J.M.J. (jacob_janey@merck.com).

Supporting Online Material

www.sciencemag.org/cgi/content/full/science.1188934/DC1
Materials and Methods
Figs. S1 to S6
Tables S1 to S12
References

1 March 2010; accepted 19 May 2010
Published online 17 June 2010;
10.1126/science.1188934
Include this information when citing this paper.

Computational Design of an Enzyme Catalyst for a Stereoselective Bimolecular Diels-Alder Reaction

Justin B. Siegel,[1,2]* Alexandre Zanghellini,[1,2]*† Helena M. Lovick,[3] Gert Kiss,[4] Abigail R. Lambert,[5] Jennifer L. St.Clair,[1] Jasmine L. Gallaher,[1] Donald Hilvert,[6] Michael H. Gelb,[3] Barry L. Stoddard,[5] Kendall N. Houk,[4] Forrest E. Michael,[3] David Baker[1,2,7]‡

The Diels-Alder reaction is a cornerstone in organic synthesis, forming two carbon-carbon bonds and up to four new stereogenic centers in one step. No naturally occurring enzymes have been shown to catalyze bimolecular Diels-Alder reactions. We describe the de novo computational design and experimental characterization of enzymes catalyzing a bimolecular Diels-Alder reaction with high stereoselectivity and substrate specificity. X-ray crystallography confirms that the structure matches the design for the most active of the enzymes, and binding site substitutions reprogram the substrate specificity. Designed stereoselective catalysts for carbon-carbon bond-forming reactions should be broadly useful in synthetic chemistry.

Intermolecular Diels-Alder reactions are important in organic synthesis (*1*–*3*), and enzyme Diels-Alder catalysts could be invaluable in increasing rates and stereoselectivity. No naturally occurring enzyme has been demonstrated (*4*) to catalyze an intermolecular Diels-Alder reaction (*1*, *2*), although catalytic antibodies have been generated for several Diels-Alder reactions (*3*, *4*). We have previously used the Rosetta computational design methodology to design novel enzymes (*5*, *6*) that catalyze bond-breaking reactions. However, bimolecular bond-forming reactions present a greater challenge, because both substrates must be bound in the proper relative orientation in order to accelerate the reaction and impart stereoselectivity. Also, previous successes with computational enzyme design have involved general acid-base catalysis and covalent catalysis, but the Diels-Alder reaction provides the opportunity to alter the reaction rate by modulation of molecular orbital energies (*7*). To investigate the feasibility of designing intermolecular Diels-Alder enzyme catalysts, we chose to focus on the well-studied model Diels-Alder reaction between 4-carboxybenzyl *trans*-1,3-butadiene-1-carbamate and *N,N*-dimethylacrylamide (Fig. 1, substrates 1 and 2, respectively) (*8*).

The first step in de novo enzyme design is to decide on a catalytic mechanism and an associated ideal active site. For normal-electron-demand Diels-Alder reactions, frontier molecular orbital theory dictates that the interaction of the highest occupied molecular orbital (HOMO) of the diene with the lowest unoccupied molecular orbital (LUMO) of the dienophile is the dominant interaction in the transition state (*7*). Narrowing the energy gap between the HOMO and LUMO will increase the rate of the Diels-Alder reaction. This can be accomplished by positioning a hydrogen bond acceptor to interact with the carbamate NH of the diene (thus raising the energy of the HOMO energy and stabilizing the positive charge accumulating in the transition state), and a hydrogen bond donor to interact with the carbonyl of the dienophile (lowering the LUMO energy and stabilizing the negative charge accumulating in the transition state) (*9*). Quantum mechanical (QM) calculations predict that these hydrogen bonds can stabilize the transition state by up to 4.7 kcal mol^{-1}. (fig. S1). In addition to electronic stabilization, binding of the two substrates in a relative orientation optimal for the reaction is expected to produce a large increase in rate through entropy reduction (*10*). Thus, a protein with a binding pocket (Fig. 1) that positions the two substrates in the proper relative orientation and has appropriately placed hydrogen bond donors and acceptors is expected to be an effective Diels-Alder catalyst.

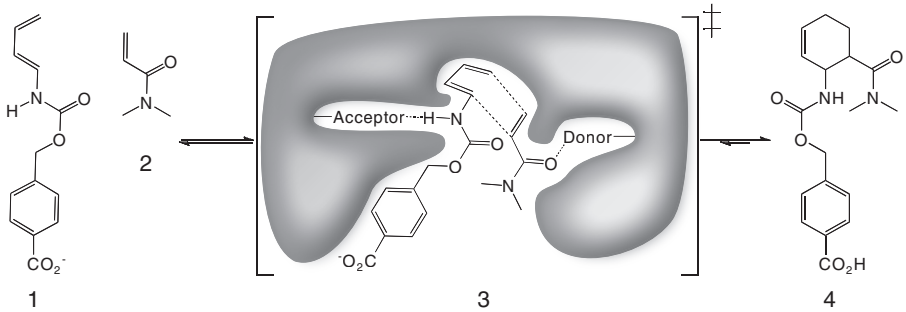

Fig. 1. The Diels-Alder reaction. Diene (1) and dienophile (2) undergo a pericyclic [4 + 2] cycloaddition (3) to form a chiral cyclohexene ring (4). Also shown in (3) is a schematic of the design target active site, with hydrogen bond acceptor and donor groups activating the diene and dienophile and a complementary binding pocket holding the two substrates in an orientation optimal for catalysis.

[1]Department of Biochemistry, University of Washington, Seattle, WA 98195, USA. [2]Biomolecular Structure and Design Program, University of Washington, Seattle, WA 98195, USA. [3]Department of Chemistry, University of Washington, Seattle, WA 98195, USA. [4]Department of Chemistry and Biochemistry, University of California, Los Angeles, CA 90095, USA. [5]Division of Basic Sciences, Fred Hutchinson Cancer Research Center, Seattle, WA 98109, USA. [6]Laboratory of Organic Chemistry, Eidgenössische Technische Hochschule (ETH) Zürich, 8093 Zürich, Switzerland. [7]Howard Hughes Medical Institute (HHMI), University of Washington, Seattle, WA 98195, USA.

*These authors contributed equally to this work.
†Present address: Arzeda Corporation, 2722 Eastlake Avenue East, Suite 150, Seattle, WA 98102, USA.
‡To whom correspondence should be addressed. E-mail: dabaker@u.washington.edu

Downloaded from www.sciencemag.org on July 15, 2010

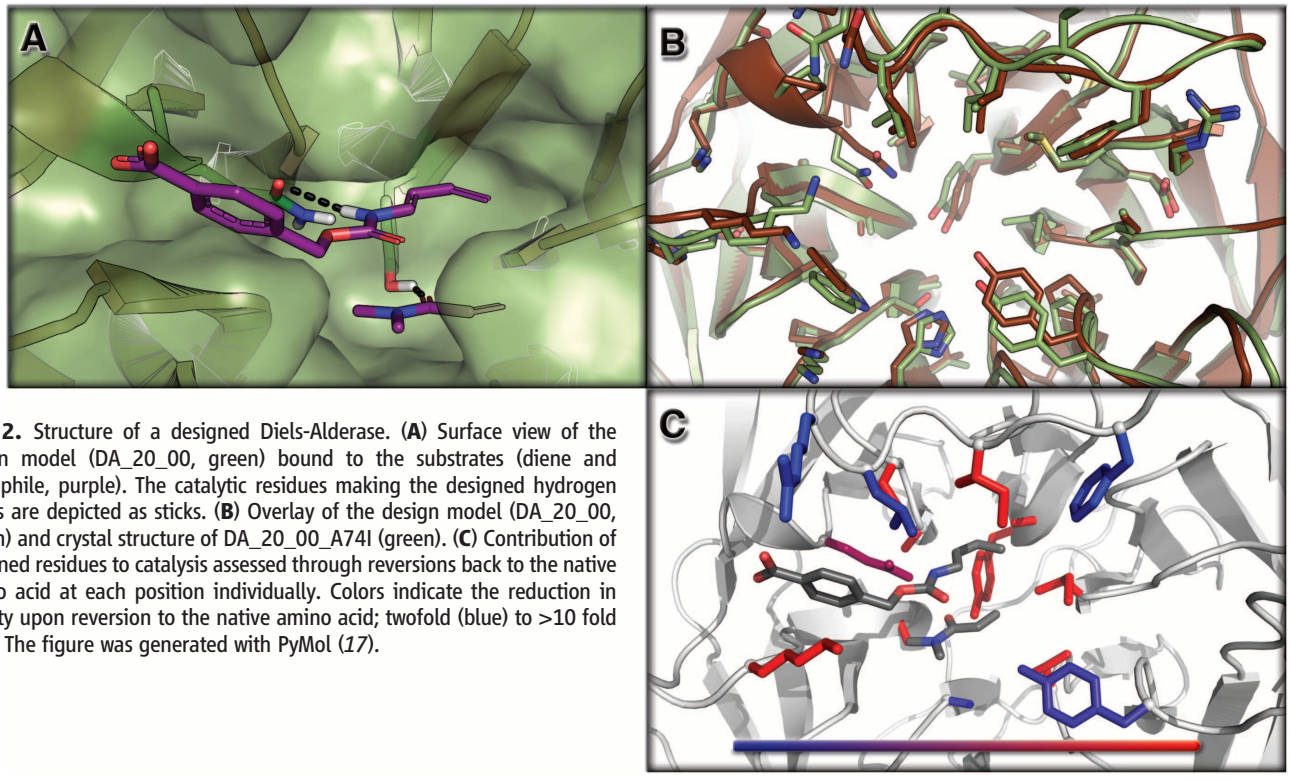

Fig. 2. Structure of a designed Diels-Alderase. (**A**) Surface view of the design model (DA_20_00, green) bound to the substrates (diene and dienophile, purple). The catalytic residues making the designed hydrogen bonds are depicted as sticks. (**B**) Overlay of the design model (DA_20_00, brown) and crystal structure of DA_20_00_A74I (green). (**C**) Contribution of designed residues to catalysis assessed through reversions back to the native amino acid at each position individually. Colors indicate the reduction in activity upon reversion to the native amino acid; twofold (blue) to >10 fold (red). The figure was generated with PyMol (*17*).

We used the Rosetta methodology to design in silico enzyme models containing active sites with the desired properties (Fig. 1). The design methodology starts from three-dimensional atomic models of minimal active sites (theozymes) consisting of the reaction transition state and protein functional groups involved in binding and catalysis. We chose the carbonyl oxygen from a glutamine or asparagine to hydrogen bond with the N-H of the diene carbamate and the hydroxyl from a serine, threonine, or tyrosine to hydrogen bond with the carbonyl oxygen of the dienophile amide moiety (Fig. 1). QM calculations were carried out to determine the geometry of the lowest free energy barrier transition state between substrates and product in the presence of these hydrogen bonding groups. Starting from these coordinates, a large and diverse ensemble of distinct minimal active sites was then generated by systematically varying the identity and rotameric state of the catalytic side chains, the hydrogen bonding geometry between these residues and the transition state, and the internal degrees of freedom of the transition state (figs. S4 and S5).

By using RosettaMatch (*11*), we searched a set of 207 stable protein scaffolds for backbone geometries that allow the two catalytic residues and the two substrates, oriented as in one of the minimal active sites, to be placed without making substantial steric clashes with the protein backbone. A hashing technique allows efficient searching through the very large number of distinct sites (*4*). From the set of 10^{19} possible active site configurations, about 10^{6} could be matched in a stable protein scaffold. Each match was then optimized by using RosettaDesign (*12*) to maximize transition state binding while not clashing with bound substrates or product (*4*). These designs were filtered on the basis of satisfaction of catalytic geometry, transition state binding energy, and shape complementarity between designed pocket and the transition state (*4*). A total of 84 designs were selected for experimental validation.

Genes encoding these 84 designs were synthesized with a C-terminal six-histidine affinity tag and expressed in *Escherichia coli*. Fifty of the designed proteins were soluble; these were purified by using affinity chromatography, and Diels-Alder activity was monitored by using a liquid chromatography–tandem mass spectrometry assay in a phosphate-buffered saline (PBS) solution at pH = 7.4 and 298 K (*4*). Two designs (DA_20_00 and DA_42_00) were found to have Diels-Alderase activity. The active design DA_20_00 was created from a six-bladed β-propeller scaffold [Protein Data Bank identification code (PDB ID) 1E1A; a diisopropylfluorophosphatase from *Loligo vulgaris*, 13 mutations, fig. S6A]. As observed for many native β-propeller enzymes, the functional groups that play key roles in catalysis—a glutamine carbonyl group and a tyrosine hydroxyl group that provide the activating hydrogen bonds—are located in the middle of one side of the propeller. The rest of the pocket is lined with hydrophobic residues that form a tight shape-complementary surface (Fig. 2A). The active design DA_42_00 was created from the ketosteroid isomerase scaffold (PDB-ID 1OHO, 14 mutations, fig. S4B). The active site is quite different than that of DA_20_00 in that only the carbon-carbon bond-forming portion of the diene and dienophile is actually buried within the protein.

Table 1. Kinetic parameters for DA_20_00, DA_20_10, and DA_42_04. Reactions for DA_20_00, DA_20_10, and DA_42_04 were carried out at 298 K (*4*). The errors represent the calculated 95% confidence interval. Kinetic parameters for catalytic monoclonal antibodies (mAb) 7D4 and 4D5 at 310 K were taken from (*9*, *14*). The k_{uncat} for the Diels-Alder reaction at 298 K was found to be 2.44×10^{-2} M^{-1} $hour^{-1}$, in good agreement with the previously reported value at 310 K of 4.29×10^{-2} M^{-1} $hour^{-1}$.

Catalyst	k_{cat} ($hour^{-1}$)	$K_{M\text{-diene}}$ (mM)	$K_{M\text{-dienophile}}$ (mM)	$k_{cat}/K_{M\text{-diene}}$ (s^{-1} M^{-1})	$k_{cat}/K_{M\text{-dienophile}}$ (s^{-1} M^{-1})	$k_{cat}/(K_{M\text{-diene}} \times K_{M\text{-dienophile}})$ (s^{-1} M^{-1} M^{-1})
DA_20_00	0.10 ± 0.02	3.5 ± 1.5	146.0 ± 2.5	0.008	0.0002	0.06
DA_20_10	2.13 ± 0.24	1.3 ± 0.1	72.8 ± 5.1	0.455	0.0081	6.23
DA_42_04	0.03 ± 0.01	0.5 ± 0.1	16.2 ± 3.2	0.017	0.0005	1.03
mAb 7D4	0.21	1.0	1.7	0.058	0.0343	20.18
mAb 4D5	0.21	1.6	5.9	0.036	0.0099	6.19

Downloaded from www.sciencemag.org on July 15, 2010

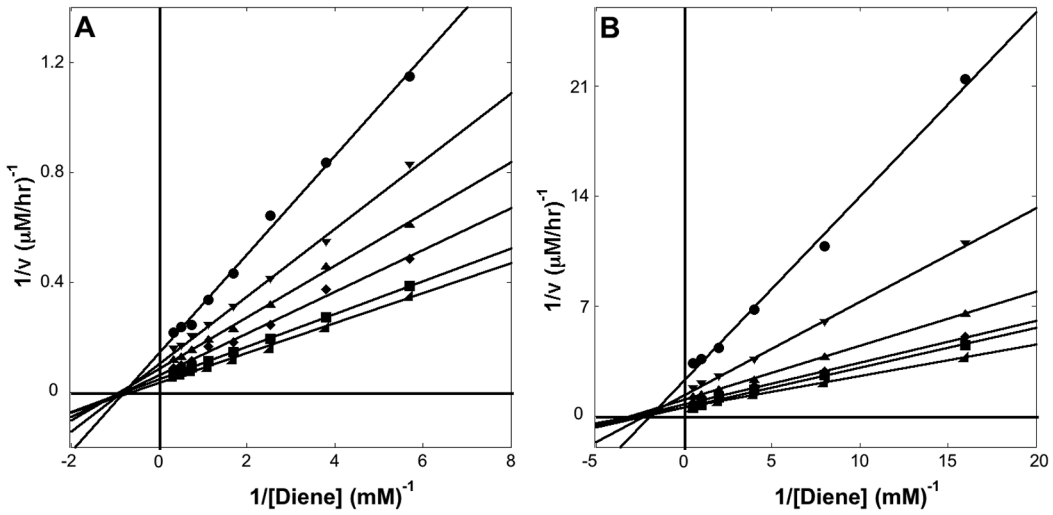

Fig. 3. Kinetic characterization. (**A**) Dependence of reaction velocity for DA_20_10 on diene concentration for different fixed dienophile concentrations. The diene concentration was varied from 3.0 to 0.18 mM with fixed concentrations of 100 mM (◢), 66 mM (■), 44 mM (◆), 30 mM(▲), 20 mM(▼), and 13 mM (●) dienophile. (**B**) Dependence of reaction velocity for DA_42_04 at varying diene concentrations for different fixed dienophile concentrations. The diene concentration was varied from 2.0 to 0.06 mM with fixed concentrations of 100 mM (◢), 50 mM (■), 25 mM (◆), 13 mM(▲), 7 mM(▼), and 3 mM (●) dienophile. Reaction conditions are described in (*4*).

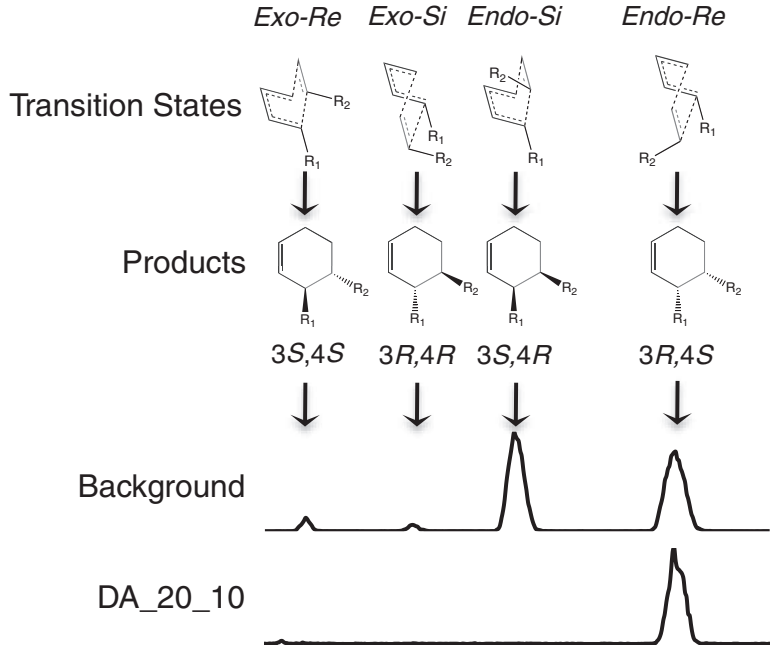

Fig. 4. Absolute stereoselectivity of DA_20_10. The transition states that lead to the four possible ortho-stereoisomers are shown above the reaction chromatograms. Background reaction: 2 mM diene and 70 mM dienophile in a PBS solution for 24 hours at 298 K. DA_20_10 reaction: 50 μM protein, 0.5 mM diene, and 10 mM dienophile in a PBS solution for 48 hours at 298 K (*4*).

To further improve the catalytic activity of DA_20_00 and DA_42_00, we mutated residues that were in direct contact with the transition state in each designed enzyme individually to sets of residues that were predicted to retain or improve transition state binding and bolster the two catalytic residues. A set of six mutations [$A^{21} \rightarrow T^{21}$ (A21T) (*13*), A74I, Q149R, A173C, S271A, and A272N] was found to increase the overall catalytic efficiency of DA_20_00 by over 100-fold relative to the original design model (Table 1; we refer to the DA_20_00 protein with these six additional mutations as DA_20_10, fig. S6C). Three of the mutations improve the packing around the transition state (A74I and A21T) and the catalytic glutamine (A173C). Two of the mutations likely improve the overall electrostatic complementarity with the bound substrates: Q149R hydrogen bonds to the carboxylate on the diene, and S271A makes the dienophile environment more nonpolar. The last mutation (A272N) reverts a designed alanine residue back to the native asparagine: Molecular dynamics simulations (*4*) suggested that the catalytic tyrosine can flip into an alternative conformation not positioned to activate the dienophile, and a larger residue at 272, such as the native asparagine, was predicted to hold the tyrosine in the conformation required for catalysis.

For DA_42_00, a set of four mutations (Q58R, L61M, A99N, and V101I) (*13*) was found to increase the observed catalytic activity roughly 20-fold over the original design (Table 1; we refer to the DA_42_00 protein with four additional mutations as DA_42_04, fig. S6D). As in the case of DA_20_00, all of these mutations increase the size of the amino acid and either improve packing or electrostatic interactions with the ligand.

To investigate the contributions of the two catalytic residues in DA_20_10 to catalysis, we mutated glutamine 195 into a glutamate (Q195E) and tyrosine 121 into a phenylalanine (Y121F) (*13*). We had originally incorporated a glutamine rather than a glutamate at position 195, despite the fact that the carboxylate is more effective than the amide at increasing the energy of the diene HOMO, because we were concerned about the unfavorable contribution of carboxylate desolvation to substrate binding. Furthermore, QM calculations predict that the amide group of glutamine can simultaneously interact with the diene and dienophile, resulting in a 2 kcal mol^{-1} lower activation barrier than if glutamate was used as a catalytic residue (fig. S1C). Indeed, the Q195E mutation showed almost complete loss of activity (450-fold less activity), illustrating the sensitivity of the enzyme to the details of the designed active site. The Y121F mutation decreases catalytic activity 27-fold, consistent with the removal of a hydrogen bond that contributes to dienophile binding and a lowering of its LUMO.

The kinetic parameters of the DA_20_00, DA_20_10, and DA_42_04 catalyzed reactions were determined by measuring the dependence of the reaction velocity on the concentration of both diene and dienophile (*4*). The kinetic parameters are summarized in Table 1, and double reciprocal plots for DA_20_10 and DA_42_04 are shown in Fig. 3, A and B. DA_20_10 has an effective molarity [catalytic rate constant/uncatalyzed rate constant (k_{cat}/k_{uncat}) = 89 M] 20 times greater than those of the catalytic antibodies 7D4 (*9*) and 4D5 (*14*) previously elicited for the same reaction. DA_42_04 binds both the diene and the dieno-

Downloaded from www.sciencemag.org on July 15, 2010

phile more tightly [significantly lower Michaelis constant (K_M)] than DA_20_10, but the k_{cat} is 100-fold lower, suggesting that the orientation of the two substrates relative to each other and/or to the catalytic groups is not optimal.

At high substrate concentrations, DA_20_10 proceeds for more than 30 turnovers with some loss of activity over time due to aggregation (*4*). At high enzyme concentrations, more than 80% of the diene substrate is converted to product (fig. S7). These properties suggest that de novo designed enzymes could be useful as catalysts in production-level chemical syntheses.

Some Diels-Alder reactions can be accelerated by binding within a nonspecific hydrophobic pocket (*15*). This, however, does not appear to be the case for the reaction studied here: *E. coli* cell lysate, cyclodextrins, and bovine serum albumin have either no effect or actually inhibit the reaction (table S2). The importance of the active site binding geometry is highlighted by a comparison of DA_42_04 and DA_20_10: DA_42_04 binds the substrates much more tightly but has a much lower k_{cat}. To further probe the sensitivity of DA_20_10 catalysis to the details of the active site geometry, we reverted each of the 15 residues constituting the active site one at a time to its identity in the original scaffold. Remarkably, nine of the reversions completely abolished activity; the other six mutations decreased activity by 1.5-fold to 10-fold (Fig. 2C and table S5). The reversions that significantly reduced the catalytic activity of DA_20_10 are primarily in the core of the binding site, whereas mutations that had less of an effect on activity are closer to the active site rim. Similar sensitivities were observed for mutations that disrupt binding in DA_42_04 (*4*). Thus, although the catalytic efficiencies of the computationally designed Diels-Alderases are small in comparison with those of native enzymes, they exhibit similar sensitivity to the details of the active site and provide much more than a general hydrophobic environment.

To determine how well the structure of DA_20_00 matched the design model, we solved the crystal structure of one of the active variants of DA_20_00 (harboring the A74I mutation; Fig. 2B). The crystal structure solved to 1.5 Å resolution (table S4 and Fig. 2B) shows atomic-level agreement with the design model, with an all-atom root mean square deviation (RMSD) of 0.5 Å. The major deviation between the crystal structure and the design model is in a surface loop, which appears to be pulled back from the predicted active site (RMSD on residues 32 to 46, 0.93 Å). The conformations of the side chains at the active site in the crystal structure are close to those in the design model; taken together with the reversion data described above and the complete lack of activity observed for the starting scaffold (fig. S8), these results strongly suggest that the experimentally observed activity is generated by the designed active site.

The Diels-Alder reaction studied here can, in principle, produce eight different isomeric products, four of which are experimentally observed in the reaction in solution (*9*). The computational design was directed at the transition state that yields the 3*R*,4*S* endo product, which only comprises 47% of the total product mixture formed in the uncatalyzed reaction. To determine the stereoselectivity of DA_20_10 (Fig. 4), we used a previously described liquid chromatography–tandem mass spectrometry assay with a chiral column (*16*). Consistent with the design, DA_20_10 only catalyzes the formation of the expected 3*R*,4*S* product (>97%, fig. S9).

Besides stereoselectivity, the level of control over a chemical reaction by a designed enzyme is reflected by its substrate specificity. To investigate the substrate specificity of DA_20_10, we characterized product formation with six different dienophiles that share the same acrylamide core but have different nitrogen substituents (Fig. 5). The catalytic activity against each of the substrates was measured by using a liquid chromatography mass spectrometry assay (*4*). DA_20_10 was observed to strongly favor the substrate for which it was designed. Even slight changes, such as adding a methyl group to the *N,N*-dimethylacrylamide (Fig. 5, 2A versus 2B), significantly decreased the activity of DA_20_10, consistent with the tight packing of the active site around the two substrates.

In addition to the ability to catalyze new reactions with high substrate specificity and stereoselectivity, one of the promises of de novo enzyme design is that once an initial active enzyme is engineered it can be easily modified to catalyze similar reactions with alternate substrates. To explore this possibility, we mutated histidine 287 on one side of the dienophile binding pocket in DA_20_10 to asparagine and several other residues. The H287N mutation has a substrate specificity profile different from DA_20_10; in particular there is a 13-fold switch in specificity for dienophile 2E relative to 2A, while the selectivity against 2F is maintained (Fig. 5). The specificity switch may have two origins: The histidine in the crystal structure clashes with the larger substrates, and the amino group on the asparagine can hydrogen bond with the hydroxyl in 2E.

Although we have succeeded in computationally designing an enzyme that catalyzes an enantio- and diastereoselective intermolecular reaction, there is much room for improvement in our computational design methods. Only 2 of the 50 designed enzymes tested had measurable activity, and a much higher success rate and higher overall activities are desirable. The differences in k_{cat} of the two designed enzymes suggest that more precise control over the orientation of the two substrates relative to one another and to the catalytic residues could result

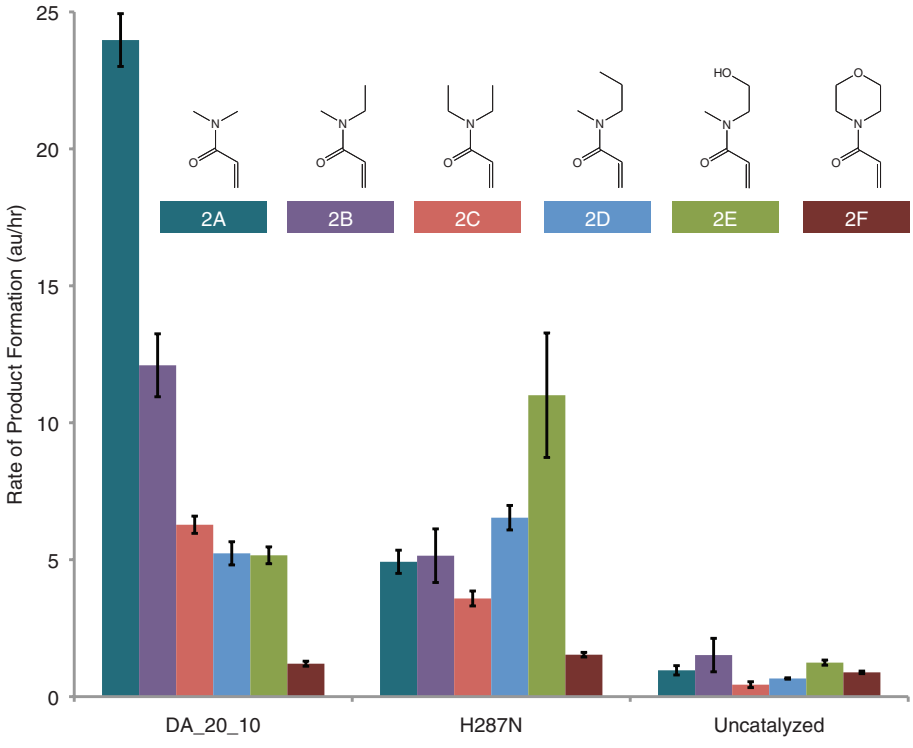

Fig. 5. Control of substrate specificity. Reactions were carried out with 0.2 mM diene 1 (Fig. 1), and 10 mM of one of the six dienophiles depicted above in PBS at 298 K in the absence or presence of 60 μM DA_20_10 or DA_20_10_H287N. The values in the figure are the mean (colored bars) and standard deviation (error bars) of four independent measurements of the product peak area (arbitrary units) formed per hour (*4*).

Downloaded from www.sciencemag.org on July 15, 2010

in considerably more active designs. On the experimental side, by analogy with our previous results with computationally designed Kemp eliminases (*5*), it should be possible to increase the activity of these enzymes by directed evolution.

The agreement between the designed and the experimentally observed substrate specificity and stereoselectivity of DA_20_10 is notable given the importance of selectivity in organic chemistry reactions. The capability to rationally control both substrate specificity and stereoselectivity via designed enzymes opens up new avenues of research in both basic and applied chemistry.

References and Notes

1. T. Ose *et al.*, *Nature* **422**, 185 (2003).
2. J. M. Serafimov, D. Gillingham, S. Kuster, D. Hilvert, *J. Am. Chem. Soc.* **130**, 7798 (2008).
3. S. P. Kim, A. G. Leach, K. N. Houk, *J. Org. Chem.* **67**, 4250 (2002).
4. Materials and methods are available as supporting material on *Science* Online.
5. D. Röthlisberger *et al.*, *Nature* **453**, 190 (2008).
6. L. Jiang *et al.*, *Science* **319**, 1387 (2008).
7. D. L. Boger, in *Modern Organic Synthesis: Lecture Notes* (The Scripps Research Institute Press, San Diego, CA, 1999), pp. 213–272.
8. V. E. Gouverneur *et al.*, *Science* **262**, 204 (1993).
9. J. F. Blake, D. Lim, W. L. Jorgensen, *J. Org. Chem.* **59**, 803 (1994).
10. M. I. Page, W. P. Jencks, *Proc. Natl. Acad. Sci. U.S.A.* **68**, 1678 (1971).
11. A. Zanghellini *et al.*, *Protein Sci.* **15**, 2785 (2006).
12. B. Kuhlman, D. Baker, *Proc. Natl. Acad. Sci. U.S.A.* **97**, 10383 (2000).
13. Single-letter abbreviations for the amino acid residues are as follows: A, Ala; C, Cys; D, Asp; E, Glu; F, Phe; G, Gly; H, His; I, Ile; K, Lys; L, Leu; M, Met; N, Asn; P, Pro; Q, Gln; R, Arg; S, Ser; T, Thr; V, Val; W, Trp; and Y, Tyr.
14. J. T. Yli-Kauhaluoma *et al.*, *J. Am. Chem. Soc.* **117**, 7041 (1995).
15. R. Breslow, S. D. Dong, *Chem. Rev.* **98**, 1997 (1998).
16. C. E. Cannizzaro, J. A. Ashley, K. D. Janda, K. N. Houk, *J. Am. Chem. Soc.* **125**, 2489 (2003).
17. The PyMOL Molecular Graphics System, Schrödinger, LLC, Version 1.2r3pre.

18. This work was supported by the Defense Advanced Research Projects Agency (DARPA), the Howard Hughes Medical Institute (HHMI), a Molecular Biophysics traineeship from the NIH for J.B.S., and the Lawrence Livermore National Laboratory Lawrence Scholars program for G.K. We thank M. Toscano (ETH) and C. Rosewall (University of Washington) for chemical synthesis and B. Siegel and Y.-h. Lam for helpful comments on the manuscript. The x-ray crystallographic coordinates have been deposited in the Protein Data Bank with accession ID 3I1C. The University of Washington has submitted a patent application on the protein sequence coding for the engineered enzymes reported here as well as some of the design methodology.

Supporting Online Material

www.sciencemag.org/cgi/content/full/329/5989/309/DC1
Materials and Methods
SOM Text
Figs. S1 to S13
Tables S1 to S5
References

30 March 2010; accepted 1 June 2010
10.1126/science.1190239

Meniscus-Confined Three-Dimensional Electrodeposition for Direct Writing of Wire Bonds

Jie Hu and Min-Feng Yu*

Continued progress in the electronics industry depends on downsizing, to a few micrometers, the wire bonds required for wiring integrated chips into circuit boards. We developed an electrodeposition method that exploits the thermodynamic stability of a microscale or nanoscale liquid meniscus to "write" pure copper and platinum three-dimensional structures of designed shapes and sizes in an ambient air environment. We demonstrated an automated wire-bonding process that enabled wire diameters of less than 1 micrometer and bond sizes of less than 3 micrometers, with a breakdown current density of more than 10^{11} amperes per square meter for the wire bonds. The technology was used to fabricate high-density and high-quality interconnects, as well as complex three-dimensional microscale and even nanoscale metallic structures.

As an essential part of any integrated chip, interconnects provide the electrical paths needed in a circuit to pass signals and data among electrical devices or device units. The increasing device density in electronic chips has led to exponential growth in the density of interconnects and the complexity of their design. With the introduction of three-dimensional (3D) chip architecture, interchip vias (*1*) constitute one method to integrate devices in 3D stacks, but alternative interconnect technologies that can provide flexible means to electrically wire microscale device components in three dimensions are still required.

Traditional wire-bonding technology has served the electronics industry for many decades, satisfying the interconnection needs for device packaging (*2*). Recently, flip-chip interconnect technology was introduced as a means of increasing the interconnect density and improving device performance for high-frequency operation (*3*). However, downscaling this technology to interconnect pad pitches on the order of a few micrometers has proven to be difficult. Thermosonic gold wire bonding has a limiting pitch of ~40 μm, whereas flip-chip technology can achieve a pitch of ~100 μm in industrial practices. This increases the on-chip space needed for the interconnect pads, reduces the number of chips that can be produced per wafer, and consequently increases the cost per chip. It is expected that downscaling the traditional solder-based interconnect cannot meet either the thermomechanical reliability requirement or the current density requirement at very fine pitches (*4*).

Among the 3D microfabrication technologies that are compatible with electronic devices, e-beam– or focused ion beam–based deposition (*5*) and direct writing with metal colloidal ink (*6*) have been explored as methods for fabricating 3D interconnects with nanoscale or microscale dimensions. E-beam– or focused ion beam–based

Department of Mechanical Science and Engineering, University of Illinois, 1206 West Green Street, Urbana, IL 61801, USA.

*To whom correspondence should be addressed. E-mail: mfyu@illinois.edu

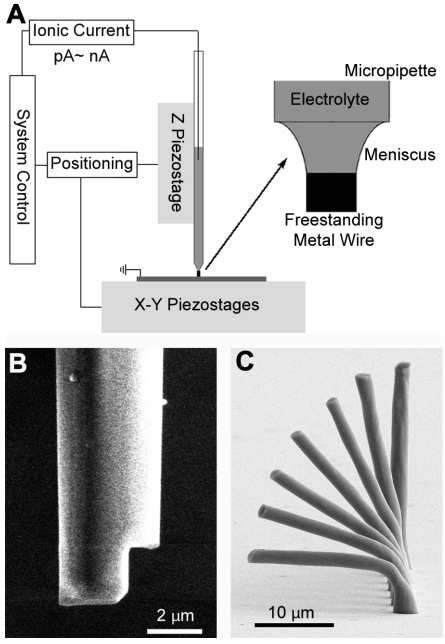

Fig. 1. (**A**) Schematic showing the general setup for meniscus-confined 3D electrodeposition. The long-travel piezostages (nominal resolution <10 nm) provide the fine positioning needed to control the travel path of the micropipette in the 3D space. The high-sensitivity electrometer circuit (resolution <1 pA) monitors and controls the ionic current. A magnified view at the nozzle–metal wire interface shows the formation of a meniscus (liquid bridge) serving as the stable confinement needed for the continuous electrodeposition of a uniform-diameter microscale or nanoscale metal wire as the micropipette is continuously withdrawn from the substrate surface. (**B**) SEM image showing the nozzle at the end of a glass micropipette with a side cut made by focused ion beam machining. (**C**) Electrodeposited Cu wires with different inclination angles fabricated with the use of a side-cut micropipette.

Downloaded from www.sciencemag.org on July 15, 2010

Overall, reducing the wire diameter and increasing the lateral length of the wire can also effectively benefit the lowering of such stresses.

The growth rate of an electrodeposited wire is intrinsically limited by the rate of electroreduction, or more specifically by the diffusion-limited ionic current (*22*) described by a recessed microelectrode (the growth front of the deposited metal wire) in a truncated cone (the tapered dispensing end of the micropipette). Nonetheless, the growth rate might be increased through an increase in electrolyte concentration and/or the use of a short tapered micropipette. Alternatively, an array of micropipettes can be deployed to increase the wire-bonding throughput.

With the proper mechanical design and system control, this meniscus-confined 3D electrodeposition method can be used to fabricate more intricate microscale and nanoscale structures than those described here. Such structures could include designed structural and device functionalities integrating a variety of metallic materials, such as magnetic and noble metals and even metal alloys. Moreover, because it is intrinsically a low-cost direct-writing technology, this technique can be used to fabricate such micro- or nanostructures on existing micro- or nanostructures when such fabrication becomes difficult or expensive with the traditional lithography process (fig. S3).

References and Notes

1. P. Ramm, J. M. Wolf, B. Wunderle, in *3-D IC Integration: Technology and Applications*, P. E. Garrou, P. Ramm, C. A. Bower, Eds. (Wiley-VCH, New York, 2008), pp. 289–318.
2. G. Harman, *Wire Bonding in Microelectronics* (McGraw-Hill, New York, 2009).
3. C. Harper, *Electronic Packaging and Interconnection Handbook* (McGraw-Hill, New York, 2005).
4. International Technology Roadmap for Semiconductors (ITRS-2007) (www.itrs.net/Links/2007ITRS/Home2007.htm).
5. T. Morita *et al.*, *J. Vac. Sci. Technol. B* **21**, 2737 (2003).
6. B. Y. Ahn *et al.*, *Science* **323**, 1590 (2009); published online 12 February 2009 (10.1126/science.1168375).
7. Y. Li, B. W. Maynor, J. Liu, *J. Am. Chem. Soc.* **123**, 2105 (2001).
8. J. D. Madden, I. W. Hunter, *J. Microelectromech. Syst.* **5**, 24 (1996).
9. J. Jang, G. C. Schatz, M. A. Ratner, *Phys. Rev. Lett.* **92**, 085504 (2004).
10. J. Jang, G. C. Schatz, M. A. Ratner, *Phys. Rev. Lett.* **90**, 156104 (2003).
11. R. C. Major, J. E. Houston, M. J. McGrath, J. I. Siepmann, X.-Y. Zhu, *Phys. Rev. Lett.* **96**, 177803 (2006).
12. A. P. Suryavanshi, M.-F. Yu, *Appl. Phys. Lett.* **88**, 083103 (2006).
13. A. P. Suryavanshi, M.-F. Yu, *Nanotechnology* **18**, 105305 (2007).
14. See supporting material on *Science* Online.
15. M. E. Toimil Molares *et al.*, *Appl. Phys. Lett.* **82**, 2139 (2003).
16. Q. Huang, C. M. Lilley, M. Bode, R. Divan, *J. Appl. Phys.* **104**, 023709 (2008).
17. Q. Huang, C. M. Lilley, R. Divan, *Nanotechnology* **20**, 075706 (2009).
18. S. Karim, K. Maaz, G. Ali, W. Ensinger, *J. Phys. D* **42**, 185403 (2009).
19. R. Defay, I. Prigogine, *Surface Tension and Adsorption* (Longman, London, 1966).
20. H. Ghasemi, C. A. Ward, *J. Phys. Chem. C* **114**, 5088 (2010).
21. Y. A. Tatarchenko, *Shaped Crystal Growth* (Kluwer Academic, New York, 1993).
22. Y. H. Lanyon *et al.*, *Anal. Chem.* **79**, 3048 (2007).

23. Supported by the Grainger Foundation. We acknowledge the use of microscopy facilities in the Center for Microanalysis of Materials at the University of Illinois at Urbana-Champaign. A U.S. patent application based on this work was filed by the University of Illinois on 7 June 2010.

Supporting Online Material

www.sciencemag.org/cgi/content/full/329/5989/313/DC1
Materials and Methods
Figs. S1 to S3

5 April 2010; accepted 10 June 2010
10.1126/science.1190496

Cenozoic Tectonics of Western North America Controlled by Evolving Width of Farallon Slab

W. P. Schellart,[1]* D. R. Stegman,[2,3] R. J. Farrington,[4] J. Freeman,[4,5] L. Moresi[1,4]

Subduction of oceanic lithosphere occurs through two modes: subducting plate motion and trench migration. Using a global subduction zone data set and three-dimensional numerical subduction models, we show that slab width (*W*) controls these modes and the partitioning of subduction between them. Subducting plate velocity scales with $W^{2/3}$, whereas trench velocity scales with 1/*W*. These findings explain the Cenozoic slowdown of the Farallon plate and the decrease in subduction partitioning by its decreasing slab width. The change from Sevier-Laramide orogenesis to Basin and Range extension in North America is also explained by slab width; shortening occurred during wide-slab subduction and overriding-plate–driven trench retreat, whereas extension occurred during intermediate to narrow-slab subduction and slab-driven trench retreat.

Understanding the partitioning of plate consumption at subduction zones is vital for constraining its effect on mantle anisotropy, dynamic topography, and overriding plate deformation at subduction zones (*1*–*3*). Subduction partitioning also exerts an important control on slab geometry (*4*, *5*) and the style of mantle stirring [i.e., poloidal versus toroidal flow (*5*–*8*)], providing constraints on the geochemical heterogeneity of the mantle. It remains unclear, however, how the rate of plate consumption at oceanic trenches [the subduction velocity ($v_{S\perp}$)] is partitioned into its two primary components, the trench-normal subducting plate velocity ($v_{SP\perp}$) and trench velocity ($v_{T\perp}$), and what controls such partitioning. At present, variation in subduction partitioning ($v_{SP\perp}/v_{S\perp}$) ranges from subducting-plate-motion–controlled ($v_{SP\perp}/v_{S\perp} > 0.5$, such as for Sunda and Mexico–Central America) to trench-motion–controlled ($v_{SP\perp}/v_{S\perp} < 0.5$, such as for Scotia and Cascadia).

Previous research suggests that plate age correlates with subducting plate velocity (*9*, *10*) and trench velocity (*11*), but early work on global trench velocities contradicts the latter correlation (*12*). Other research suggests that plate velocity is controlled by plate boundary fraction that is a subduction margin (*13*), but this provides no explanation for the global variation in trench velocity.

We present results from a global compilation of present-day subduction zone kinematics for 17 subduction zones and three-dimensional numerical models of buoyancy-driven progressive free subduction of a dense four-layer plate into a stratified linear-viscous mantle (*14*). In the models, the plate has a strong viscous core 300 times more viscous than the upper mantle; however, because it is only 25 km thick, the lithosphere is still weak with respect to bending (*15*–*17*), in accordance with slab geometries, slab pull forces, and geoid signatures at subduction zones (*5*, *15*, *17*, *18*). The subducting plate is laterally homogeneous, and slab width (*W*)—the trench-parallel extent of a subducted slab that is limited by its lateral slab edges—varies between 300 and 7000 km. The causes for lateral slab edge formation are manifold, including slab tearing, slab window (gap) formation, subduction termination, and slab detachment.

The global data set of current subduction kinematics indicates negligible to moderate correlations between plate boundary fraction that is a subduction margin and $v_{SP\perp}$ (Fig. 1A) and between plate age and $v_{SP\perp}$ or $v_{T\perp}$ (Fig. 1, B and C). In contrast, both the global data set and the dynamic models show that average $v_{SP\perp}$, $v_{T\perp}$, and $v_{SP\perp}/v_{S\perp}$ vary nonlinearly with *W* along with strong correlations (Fig. 2). In nature and models, $v_{SP\perp}/v_{S\perp}$ and $v_{SP\perp}$ show a nonlinear increase with increasing *W*, whereas $v_{T\perp}$ shows a nonlinear decrease.

The nonlinear increase of $v_{SP\perp}$ with *W* (Fig. 2, A and D) can be explained with Stokes-like sinking of an oblate ellipsoid (analog for slab) parallel

[1]School of Geosciences, Monash University, Melbourne, Victoria 3800, Australia. [2]Scripps Institution of Oceanography, University of California, San Diego, La Jolla, CA 92093, USA. [3]School of Earth Sciences, University of Melbourne, Melbourne, Victoria 3010, Australia. [4]School of Mathematical Sciences, Monash University, Melbourne, Victoria 3800, Australia. [5]Bureau of Meteorology, Melbourne, Victoria 3001, Australia.

*To whom correspondence should be addressed. E-mail: wouter.schellart@monash.edu

Downloaded from www.sciencemag.org on July 15, 2010

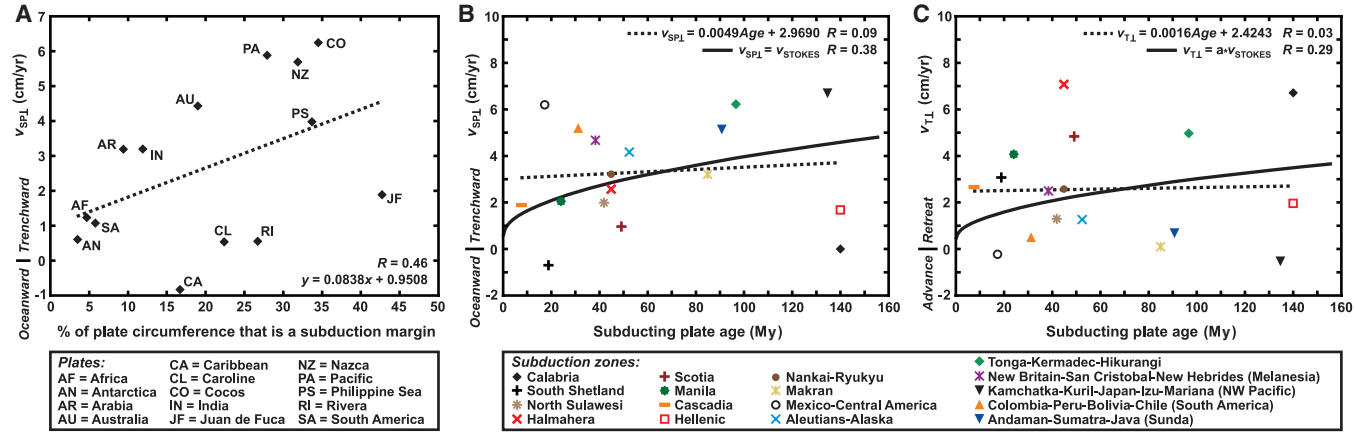

Fig. 1. Low to moderate correlations of subduction kinematics as a function of two subduction zone parameters (*14*). (**A**) Average trench-normal subducting plate velocity ($v_{SP\perp}$) for 14 plates as a function of percentage of plate circumference connected to a slab. (**B**) Average $v_{SP\perp}$ as a function of average subducting plate age at the trench for 17 subduction zones. (**C**) Average trench-normal trench migration velocity ($v_{T\perp}$) as a function of average subducting plate age at the trench for 17 subduction zones. Uncertainty in average age is ±20% for Makran, ±30% for Calabria and Hellenic, and not more than ±10% for others (*14*). Dotted lines indicate linear best-fit lines. Continuous lines in (B) and (C) indicate best-fit nonlinear curves for $v_{SP\perp}$ and $v_{T\perp}$ assuming slab-age–dependent Stokes sinking for upper mantle slabs (*10*, *14*). Correlation in (A) is statistically not significant at 95% confidence level, and correlations for the nonlinear curves in (B) and (C) are statistically not significant at 90% confidence level using Fisher's *z*.

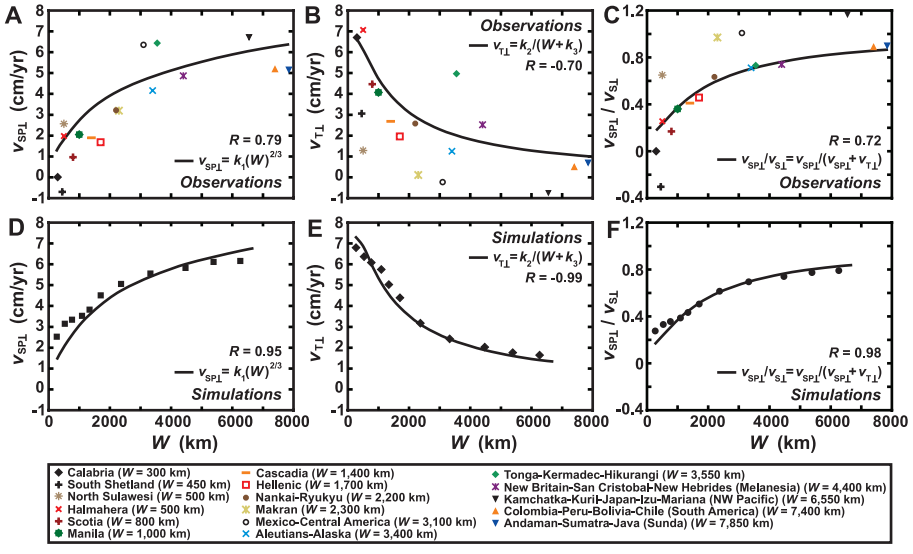

Fig. 2. Diagrams showing the influence of slab width (*W*) on (**A** and **D**) the trench-normal subducting plate velocity ($v_{SP\perp}$), (**B** and **E**) the trench-normal trench migration velocity ($v_{T\perp}$), and (**C** and **F**) the subduction partitioning ratio ($v_{SP\perp}/v_{S\perp}$). Data in (A) to (C) are from observations of 17 subduction zones on Earth, and data in (D) to (F) are from 11 numerical models of progressive subduction (*14*). Plots of the numerical models include time-weighted mean $v_{SP\perp}$, $v_{T\perp}$, $v_{SP\perp}/v_{S\perp}$, and *W*. We excluded subduction zones for which the average $v_{S\perp} \leq 1.5$ cm/year. Correlations in (A) to (C) are statistically significant at 99% confidence level, and correlations in (D) to (F) are statistically significant at 99.9% confidence level using Fisher's *z*.

to its flat side by using an analytical formulation: $v_{SP\perp} = k_1(W)^{2/3}$, with $k_1 = S\Delta\rho g(LT)^{2/3}/18c_1\eta_{UM}$ (*14*). Here, *S* is the shape factor (*19*); $\Delta\rho$ is the density contrast between ellipsoid and fluid; *g* is the gravitational acceleration; *L* and *T* are the ellipsoid length and thickness, respectively; c_1 is a constant; and η_{UM} is the upper mantle viscosity. The nonlinear decrease of $v_{T\perp}$ with *W* (Fig. 2, B and E) is explicable in terms of mantle return flow required for lateral slab migration, which is quasi-toroidal and occurs exclusively around the lateral slab edges (*5*, *7*, *8*, *20*). The viscous resistance to such flow originates from viscous drag at the slab-mantle interface, scaling with the slab surface area (and thus with *W*), and from viscous drag at the upper-lower mantle boundary, scaling with W^2 (*14*). Therefore, the velocity is approximately inversely dependent on *W*: $v_{T\perp} \approx k_2/(W + k_3)$, where $k_2 = 2c_2\Delta\rho g L T z_{UM}/\pi\eta_{UM}$, $k_3 = (4L/\pi)(1 + T/W)$, c_2 is a constant, and z_{UM} is the upper mantle thickness (*14*). Because $v_{SP\perp}/v_{S\perp} = v_{SP\perp}/(v_{SP\perp} + v_{T\perp})$, the nonlinear increase of $v_{SP\perp}/v_{S\perp}$ with *W* (Fig. 2, C and F) is also explained.

The control of *W* on $v_{SP\perp}/v_{S\perp}$ (Fig. 2) affects many aspects of Earth dynamics, including upper plate deformation, slab geometry, potential slab ponding at the transition zone, style of mantle flow, mantle anisotropy, and chemical heterogeneity in the mantle. This relation explains the rapid motion and high partitioning of the Pacific, Nazca, Australian, and Cocos plates ($v_{SP\perp} \geq 4$ cm/year and $v_{SP\perp}/v_{S\perp} > 0.70$) (Fig. 2, A and C) by the wide slabs attached to these plates (3100 to 7850 km). Slab age cannot explain such fast motion because average subducting plate velocities for Nazca and Pacific are similar (5.7 and 5.9 cm/year, respectively), whereas average ages at the trench are appreciably different [33 and 105 million years (My), respectively] (Fig. 1).

The Juan de Fuca plate has the largest percentage of subduction zone plate boundary of all plates (43%), yet it is one of the slowest subducting plates (average $v_{SP\perp} = 1.9$ cm/year) (Fig. 1A). We suggest that slow motion and low partitioning of the Juan de Fuca plate (mean $v_{SP\perp}/v_{S\perp} = 0.41$) result predominantly from its narrow slab (~1400 km), enhancing slab rollback driven by its own negative buoyancy. Such rollback is consistent with the complex upper mantle anisotropy observed beneath the western United States (*3*) and active Basin and Range extension directed toward the Cascadia subduction zone (*21*).

The Juan de Fuca plate is currently one of the smallest plates on Earth, but in the geological past (referred to as Farallon plate) it was much larger. Indeed, the Farallon plate and slab decreased dramatically in trench-parallel extent by an order of magnitude during Cenozoic eastward subduction below the west coast of the Americas (Fig. 3A), resulting in a decrease in $v_{SP\perp}/v_{S\perp}$ and $v_{SP\perp}$ (Fig. 3B). Applying the best-fit curves for $v_{SP\perp}/v_{S\perp}$ and $v_{SP\perp}$ from the numerical models (Fig. 2, D and F) to the Farallon plate, we can explain the decrease in $v_{SP\perp}/v_{S\perp}$ from 0.8 to 0.4 and most (~70%, or ~5 cm/year) of the decrease in $v_{SP\perp}$ from ~9 to ~2 cm/year (Fig. 3B). The moderate decrease in slab age from ~35 to ~10 My during the Cenozoic

Downloaded from www.sciencemag.org on July 15, 2010

(Fig. 3C) might account for another ~1 cm/year (~15%) of decrease in $v_{SP\perp}$, as suggested by the best-fit nonlinear curve for slab age and $v_{SP\perp}$ (Fig. 1B). Furthermore, the fraction of Farallon plate boundary that existed as a subduction zone cannot explain any decrease in $v_{SP\perp}$ because it increased slightly during the Cenozoic (Fig. 3C).

The progressive decrease in Farallon slab width can also explain the temporal and spatial change in overriding plate deformation in North America [shortening during the Sevier-Laramide orogeny in the Cretaceous to Early Eocene (*22*), followed by widespread extension from the Eocene to present in the Basin and Range province (*23*)]. These episodes of contrasting deformation took place during continued trench retreat and west-to-southwestward motion of the North American plate (*24*) (Fig. 3, B and D to H). During the Late Cretaceous and Early Cenozoic, the subducting Farallon slab was very wide (>10,000 km), resisting slab retreat, but was pushed back by the overriding North American plate (Fig. 3D), which was rapidly driven westward because of fast poloidal corner flow and strong basal tractions resulting from rapid Farallon plate motion. This caused major overriding plate shortening in North America, in places exceeding 300 km (*22*), and would have enhanced flat slab subduction of the Farallon plate. As the slab segmented and slab windows started to form, slab width decreased and quasi-toroidal return flow around the lateral slab edges increased, which initiated slab-buoyancy–driven trench retreat, caused upper-plate extension (Fig. 3, E to H), and facilitated slab steepening. Furthermore, slower Farallon plate velocities reduced poloidal corner flow rates and basal tractions below North America. This might explain the Cenozoic slowing of the North American plate (Fig. 3, B and D to H) and the general decrease in spreading velocities in the northern Atlantic Ocean (*25*).

The gravitational potential energy stored in the thickened orogenic crust facilitated Basin and Range extension (*26*) and migration of the subduction hinge. Furthermore, in conjunction with the weakened (hot) lithosphere due to the overriding plate setting and the protracted period of orogenesis [~100 My (*22*)], this energy storage promoted the distributed style of deformation in the Basin and Range, as predicted by geodynamic models of lithospheric extension (*27*). Because extension occurred over a vast area (Fig. 3, F to H), we argue that it is not a consequence of asthenosphere upwelling above the Californian slab window as previously proposed (*28*); the horizontally projected extent of the window was at least an order of magnitude smaller than the extent of Basin and Range extension at 30 to 20 million years ago (Ma).

Buoyancy-driven slab retreat and incipient extension started in the Eocene at the northern edge of the Farallon slab (~45 Ma) when a slab window formed at the Pacific-Farallon–North American triple junction because of different subduction velocities on either side of the junction (Fig. 3E). This window grew dramatically when subduction stopped north of the triple junction and a northern slab edge formed, further enhancing rollback and causing widespread extension in the northern Basin and Range (Fig. 3F). Another slab window formed in the Baja California region at ~30 Ma (*29*) with slab edges on each side, allowing efficient mantle return flow and slab rollback that subsequently lead to widespread extension in the southern Basin and Range (Fig. 3F). The proposed slab behavior is in accordance with the model results, which show that wide slabs (~4000 to 7000 km) retreat near their lateral edges because of efficient toroidal-type mantle return flow (fig. S3C) (*20*). At ~15 Ma, slab width reduced to only ~2300 km (Fig. 3A), allowing buoyancy-driven rollback for the whole slab, as observed in

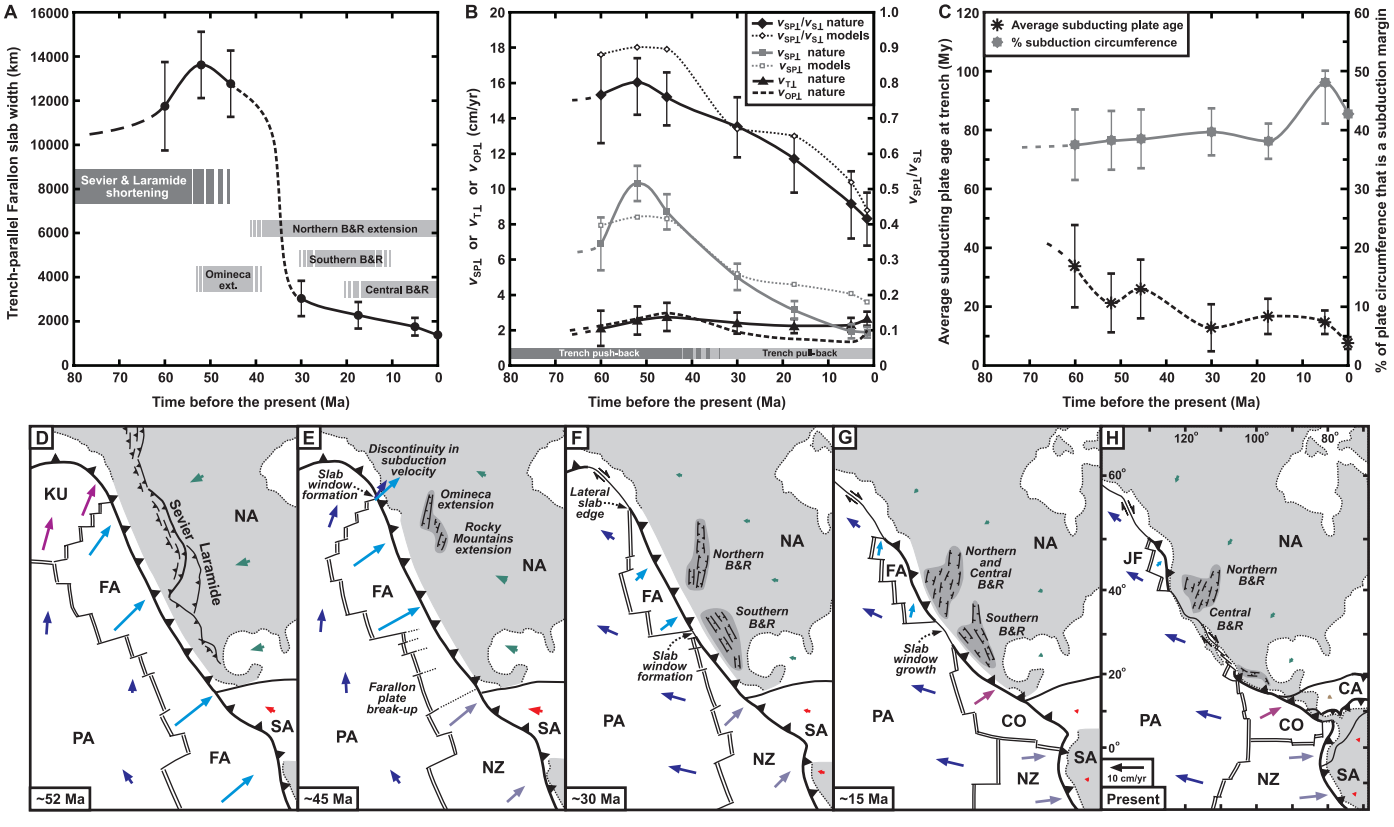

Fig. 3. The kinematics and several physical characteristics of the Farallon plate during the Cenozoic (*14*). (**A**) Evolution of trench-parallel Farallon slab width (*W*) [compiled from (*24*, *29*)]. (**B**) Evolution of average subduction partitioning ($v_{SP\perp}/v_{S\perp}$), trench-normal subducting plate velocity ($v_{SP\perp}$), trench-normal trench velocity ($v_{T\perp}$), and trench-normal overriding plate velocity ($v_{OP\perp}$) with data compiled from (*22*–*24*). Also shown is timing of trench push-back ($v_{T\perp} < v_{OP\perp}$) and trench pull-back ($v_{T\perp} > v_{OP\perp}$). (**C**) Evolution of percentage of Farallon plate circumference that is connected to a slab and evolution of average Farallon slab age at the trench (*14*). (**D** to **H**) Reconstructions of the Farallon-western North American subduction margin at (D) ~52 Ma (Early Eocene), (E) ~45 Ma (Middle Eocene), (F) ~30 Ma (Oligocene), (G) ~15 Ma (Middle Miocene), and (H) 0 Ma (present). Reconstructions were compiled from (*22*–*24*, *29*), and plate motions are from (*24*). Plate abbreviations are CA, Caribbean; CO, Cocos; FA, Farallon; JF, Juan de Fuca; KU, Kula; NA, North America; NZ, Nazca; PA, Pacific; SA, South America.

Downloaded from www.sciencemag.org on July 15, 2010

models with narrow and intermediate-width slabs (fig. S3, A and B). Such rollback drove the main phase of Basin and Range extension (Fig. 3, G and H).

References and Notes

1. R. M. Russo, P. G. Silver, *Science* **263**, 1105 (1994).
2. M. D. Long, P. G. Silver, *Science* **319**, 315 (2008).
3. G. Zandt, E. Humphreys, *Geology* **36**, 295 (2008).
4. E. Di Giuseppe, J. van Hunen, F. Funiciello, C. Faccenna, D. Giardini, *Geochem. Geophys. Geosyst.* **9**, Q02014 (2008).
5. W. P. Schellart, *Geochem. Geophys. Geosyst.* **9**, Q03014 (2008).
6. C. Kincaid, R. W. Griffiths, *Nature* **425**, 58 (2003).
7. W. P. Schellart, *J. Geophys. Res.* **109** (B7), B07401 (2004).
8. D. R. Stegman, J. Freeman, W. P. Schellart, L. Moresi, D. May, *Geochem. Geophys. Geosyst.* **7**, Q03012 (2006).
9. R. L. Carlson, T. W. C. Hilde, S. Uyeda, *Geophys. Res. Lett.* **10**, 297 (1983).
10. S. Goes, F. A. Capitanio, G. Morra, *Nature* **451**, 981 (2008).
11. P. Molnar, T. Atwater, *Earth Planet. Sci. Lett.* **41**, 330 (1978).
12. R. D. Jarrard, *Rev. Geophys.* **24**, 217 (1986).
13. D. W. Forsyth, S. Uyeda, *Geophys. J. R. Astron. Soc.* **43**, 163 (1975).
14. Materials and methods are available as supporting material on *Science* Online.
15. F. A. Capitanio, G. Morra, S. Goes, *Geochem. Geophys. Geosyst.* **10**, Q04002 (2009).
16. G. Morra, K. Regenauer-Lieb, D. Giardini, *Geology* **34**, 877 (2006).
17. D. R. Stegman, R. Farrington, F. A. Capitanio, W. P. Schellart, *Tectonophysics* **483**, 29 (2010).
18. L. Moresi, M. Gurnis, *Earth Planet. Sci. Lett.* **138**, 15 (1996).
19. R. C. Kerr, J. R. Lister, *J. Geol.* **99**, 457 (1991).
20. W. P. Schellart, J. Freeman, D. R. Stegman, L. Moresi, D. May, *Nature* **446**, 308 (2007).
21. C. Kreemer, W. C. Hammond, *Geology* **35**, 943 (2007).
22. P. G. DeCelles, *Am. J. Sci.* **304**, 105 (2004).
23. L. J. Sonder, C. H. Jones, *Annu. Rev. Earth Planet. Sci.* **27**, 417 (1999).
24. R. G. Gordon, D. M. Jurdy, *J. Geophys. Res.* **91** (B12), 12389 (1986).
25. R. D. Müller, M. Sdrolias, C. Gaina, W. R. Roest, *Geochem. Geophys. Geosyst.* **9**, Q04006 (2008).
26. L. M. Flesch, W. E. Holt, A. J. Haines, B. Shen-Tu, *Science* **287**, 834 (2000).
27. W. R. Buck, *J. Geophys. Res.* **96** (B12), 20161 (1991).
28. W. R. Dickinson, W. S. Snyder, *J. Geol.* **87**, 609 (1979).
29. T. Atwater, *Geol. Soc. Am. Bull.* **81**, 3513 (1970).

30. We appreciate discussions and interactions with R. Kerr, R. Govers, F. Capitanio, S. Zlotnik, M. Sandiford, R. Griffiths, and R. Weinberg. We thank the Victorian Partnership for Advanced Computing, the National Computational Infrastructure, and AuScope for computational resources and technical support. This work was supported by an award under the Merit Allocation Scheme on the National Computational Infrastructure National Facility at the Australian National University. W.P.S. was supported by a QE II Fellowship and Discovery grant DP0771823 from the Australian Research Council, a Monash Fellowship from Monash University, and a J. G. Russell Award from the Australian Academy of Science. D.R.S. was supported in part by a Centenary Research Fellowship from the University of Melbourne and in part by the G. Unger Vetlesen Foundation. L.M. and R.J.F. were supported by Discovery grant DP0878501.

Supporting Online Material

www.sciencemag.org/cgi/content/full/329/5989/316/DC1
Materials and Methods
Figs. S1 to S3
Table S1
References

1 April 2010; accepted 11 June 2010
10.1126/science.1190366

Simulated Rapid Warming of Abyssal North Pacific Waters

Shuhei Masuda,[1]* Toshiyuki Awaji,[2,3] Nozomi Sugiura,[2] John Philip Matthews,[3,4] Takahiro Toyoda,[1] Yoshimi Kawai,[1] Toshimasa Doi,[1] Shinya Kouketsu,[1] Hiromichi Igarashi,[2] Katsuro Katsumata,[1] Hiroshi Uchida,[1] Takeshi Kawano,[1] Masao Fukasawa[1]

Recent observational surveys have shown significant oceanic bottom-water warming. However, the mechanisms causing such warming remain poorly understood, and their time scales are uncertain. Here, we report computer simulations that reveal a fast teleconnection between changes in the surface air-sea heat flux off the Adélie Coast of Antarctica and the bottom-water warming in the North Pacific. In contrast to conventional estimates of a multicentennial time scale, this link is established over only four decades through the action of internal waves. Changes in the heat content of the deep ocean are thus far more sensitive to the air-sea thermal interchanges than previously considered. Our findings require a reassessment of the role of the Southern Ocean in determining the impact of atmospheric warming on deep oceanic waters.

The densest waters of the world's oceans are formed around Antarctica where heat exchange with the atmosphere and subsequent ice formation create uniquely dense water masses that sink rapidly and move northward. This Antarctic Bottom Water (AABW) (*1*, *2*) remains largely isolated from further heat exchange as it spreads over much of the world's ocean floor. By replenishing the supply of AABW, highly productive source regions such as the Weddell and Ross seas (Fig. 1) play an important role in the maintenance of the global thermohaline circulation system.

Recent observational surveys conducted during the World Ocean Circulation Experiment (WOCE) and the WOCE revisit (WOCE_rev) have revealed that the deepest waters of the major oceans have warmed during recent decades (*3*–*5*). This bottom-water warming ranges in magnitude from 0.003° to 0.01°C in the Pacific Ocean over the period 1985 to 1999 (*3*, *6*). Such temporal changes are of particular interest as they can constrain estimates of the variability of abyssal circulation. The latter have implications for large-scale thermohaline transport and thus for the global three-dimensional heat budget that is presently of vital concern (*7*).

Despite its crucial importance, the physical mechanisms governing bottom-water warming are poorly understood because in situ observations are spatially and temporally sporadic. Recently, a highly accurate ocean data assimila-

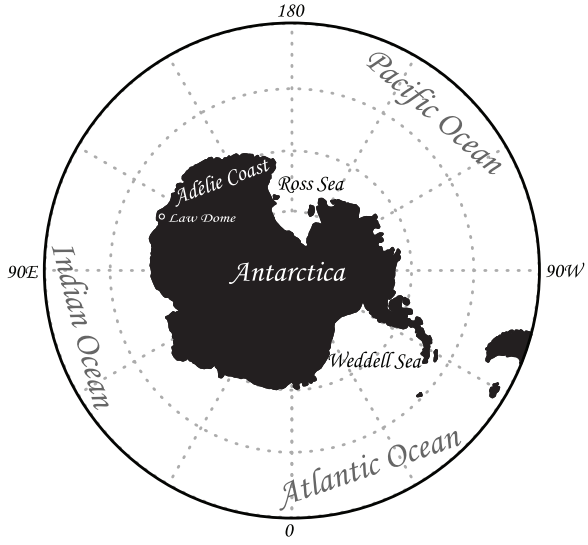

Fig. 1. Antarctic region. The Weddell and Ross seas are major source regions for Antarctic Bottom Water because here the dense, cold, and relatively saline shelf waters formed through air-sea heat exchange sink down the continental slope into the deep Southern Ocean.

[1]Research Institute for Global Change, Japan Agency for Marine-Earth Science and Technology (JAMSTEC), Yokohama 236-0001, Japan. [2]Data Management and Engineering Department, Data Research Center for Marine-Earth Sciences, JAMSTEC, Yokohama 236-0001, Japan. [3]Department of Geophysics, Kyoto University, Kyoto 606-8502, Japan. [4]Environmental Satellite Applications, Llys Awel, Mount Street, Menai Bridge LL595BW, UK.

*To whom correspondence should be addressed. E-mail: smasuda@jamstec.go.jp

Downloaded from www.sciencemag.org on July 15, 2010

tion system has been constructed (*8*), based on a four-dimensional variational (4D-VAR) adjoint approach (*9*, *10*) [supporting online material (SOM)], which can define the mechanism causing an oceanic climate fluctuation by an adjoint sensitivity analysis method that moves the ocean representation backward in time (*11*, *12*) (SOM). We used the "Earth Simulator" supercomputer to perform the major numerical simulations required for this analysis (SOM).

The adjoint sensitivity analysis gives the temporal rate of change of a physical variable in a fixed time and space when model variables (e.g., water temperature, velocity, or surface air-sea fluxes) are arbitrarily changed in the 4D continuum of one temporal and three spatial coordinates. This is equivalent to specifying the "sensitivity" of a variable to small perturbations in the parameters governing the oceanic state (*8*, *13*–*15*). It has been applied to identify the possible causal dynamics, time scales, and pathways involved in the bottom-water warming.

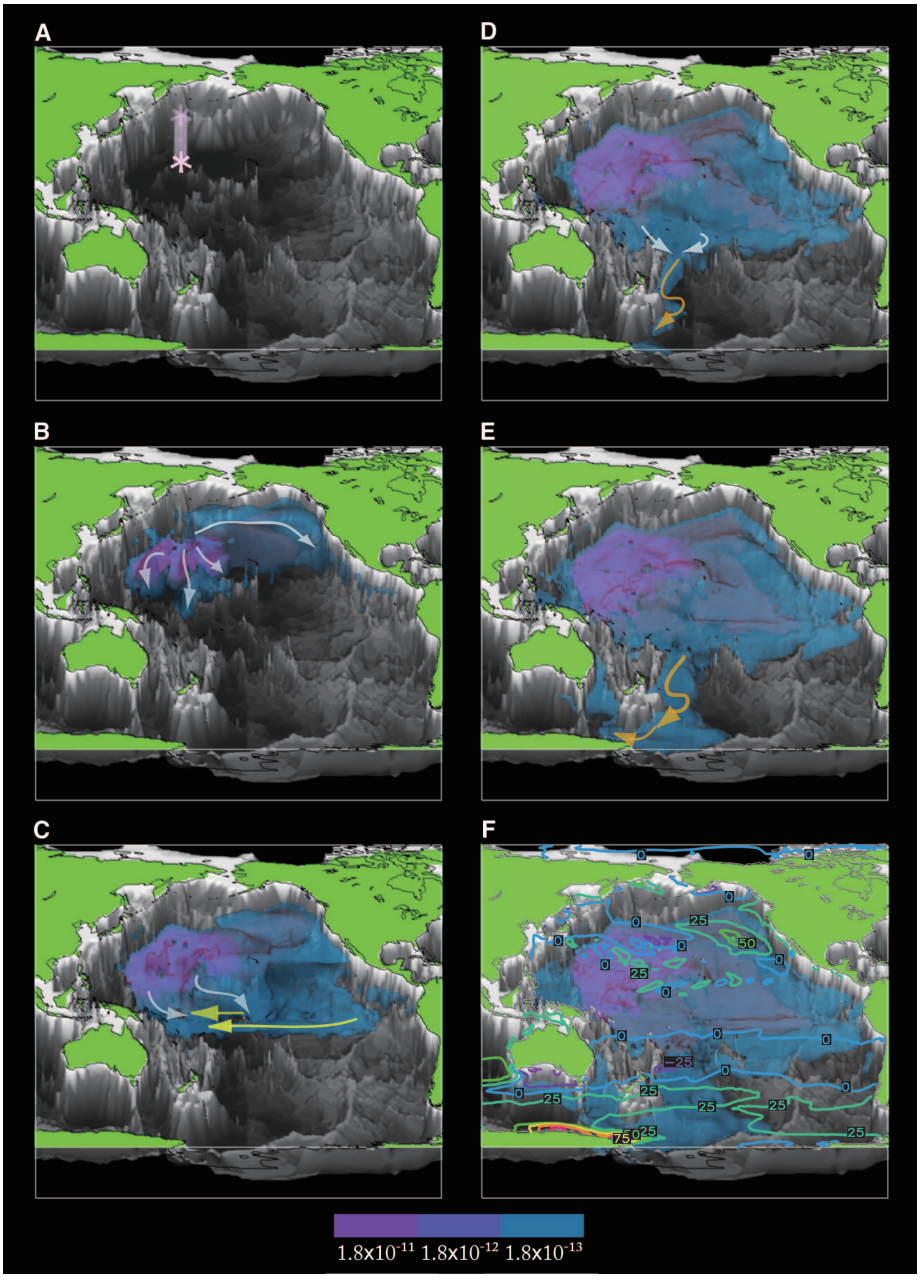

Fig. 2. Bottom-water warming signal identified by an adjoint sensitivity analysis. Temporal rate of change of bottom-water temperature taking place at 47°N-170°E [5200-m depth marked by an asterisk (*) in (A)] in an allocated model time (defined as year zero) when water temperature changes by 1 K in an arbitrary grid point, and showing the pathway of the change in deep-water temperature that will cause the bottom-water warming after (**A**) 0, (**B**) 5, (**C**) 15, (**D**) 25, (**E**) 35, and (**F**) 45 years. The units are dimensionless. Orange and yellow arrows denote the Kelvin and equatorial Rossby wave propagations, respectively. Contours of the temporal rate of change of bottom-water temperature developing at the same location when the net surface air-sea heat flux is steadily changed are traced onto (F). These show the modeled impact of the change in surface air-sea heat flux required to cause the bottom-water warming after 40 years. The units are 1.0×10^{-4} K W^{-1} m^2.

Figure 2 shows the values of the temporal rate of change of bottom-water temperature taking place at 47°N-170°E (5200-m depth) in an allocated model time (defined as year zero) when water temperature changes by 1 K in an arbitrary grid point over a specific time period (in this case, from 0 to −45 years in reverse chronological order). Positive values (indicative of warming in the lowest layer) gradually fill the North Pacific Ocean floor over a 15-year period (Fig. 2, B and C) and then penetrate into the South Pacific through the narrow passage located to the northwest of New Zealand (Fig. 2D). This warming trend can be traced back to the deep Southern Ocean across the Antarctic Circumpolar Circulation region (Fig. 2E) where it then ascends the continental shelf slope around Antarctica. At the end of a 40-year period, the warm signature finally appears at the sea surface in a confined source region that lies off the Adélie Coast (Fig. 2F). The values of the temporal rate of the change, when the net surface air-sea heat flux is changed by 1 W m^{-2} in an arbitrary surface grid point (rather than through a change in water temperature), consistently suggest that the cause of the bottom-water warming in the North Pacific is the increase in the net surface air-sea heat flux into this localized source region (Fig. 2F). (The integrated effect in this region covers 73% of that over the whole Pacific basin, when the values of the temporal rate of the change are effectively assessed with the variance of the heat flux at each surface grid point.) This result implies that a reduction in the volume of AABW due to an increase in the net surface air-sea heat flux in this Southern Ocean region initiates the North Pacific abyssal warming.

Our simulation result reveals a subtle and prompt influence of the Southern Ocean source region on changes in deep-ocean temperature and thus ocean heat budgets. However, the 40-year time scale necessary for these thermal changes to manifest is much shorter than that required by the conventional mechanism, which relies on mass movement (*16*). In the case of an abyssal current flowing northward at a speed of 10^{-3} m s^{-1} (*17*), it would require more than 350 years to cover a distance of 12,000 km.

A more rapid teleconnection between the Southern Ocean surface heating and bottom-water warming in the North Pacific can nevertheless be effected through oceanic internal waves. A thinning of abyssal layers caused by a reduction in AABW formation in a Southern Ocean source region leads to a depression of isopycnal surfaces in the deep ocean (*18*). These isopycnal changes are transmitted as internal oceanic waves, which alter the pressure force

Downloaded from www.sciencemag.org on July 15, 2010

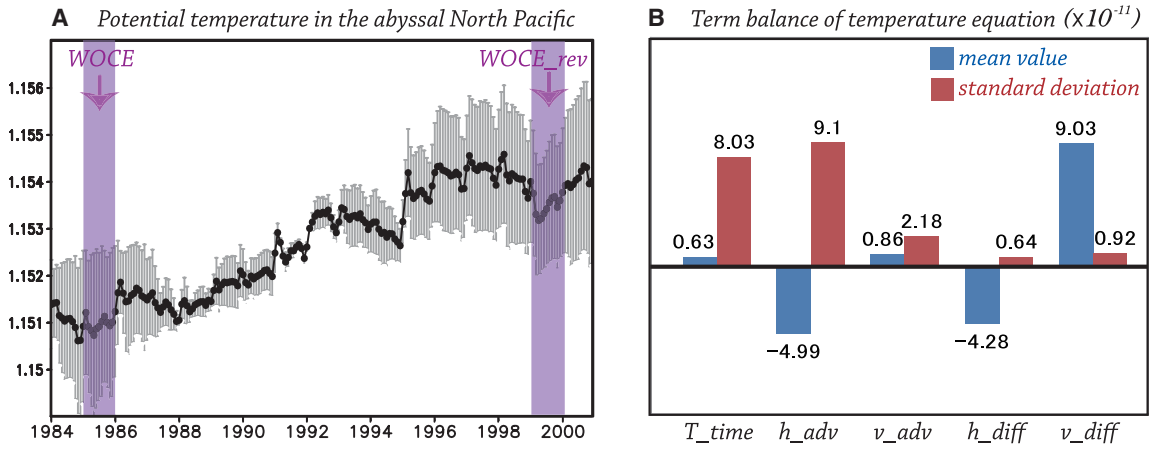

Fig. 3. Bottom-water warming in the synthesized data set. (**A**) Temporal evolution of water temperature from 1984 to 2000 averaged within the North Pacific abyssal basin (155°-170°E, 40°-50°N, 4500- to 5200-m depth). The error bars show the accuracy afforded by the synthesized data set. The units are in kelvin. (**B**) Mean value (blue bar) and standard deviation (red) of each term of the temperature equation averaged over the same abyssal region for the period 1984 to 2000. T_time, local time change; h_adv, horizontal advection; v_adv, vertical advection; h_diff, horizontal diffusion; and v_diff, vertical diffusion. The units are in kelvin per second.

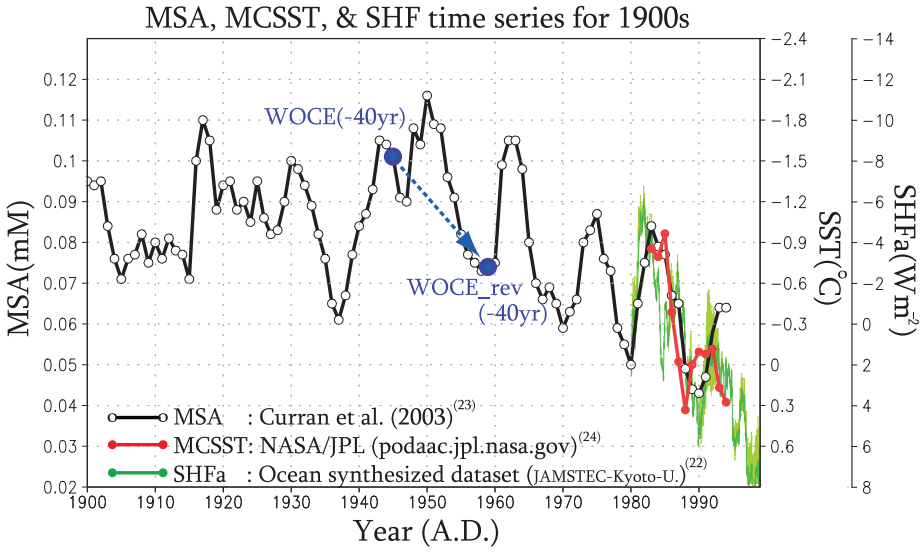

Fig. 4. Evidence of climate change around Antarctica. Law Dome methanesulphonic acid (MSA) record (1900 to 1995; black curve) (*23*), sea surface temperature values (MCSST; for November months during 1982 to 1995; red) (*24*), and estimated downward net surface heat flux anomaly values (SHFa; 1980 to 2000; green) (*22*). The MCSST and SHFa values are averaged over a region off the Adélie Coast (120°E-170°E, 65°S-60°S). The MCSST and SHFa values are plotted with reversed vertical axis. A 3-year running mean has been applied to all the variables. The error bars for the SHFa show the accuracy afforded by the data set. The correlation coefficient value between the MSA and MCSST is 0.73 ($P < 0.01$, $n = 10$), and that between the MSA and SHFa is 0.67 ($P < 0.01$, $n = 13$).

locally and weaken the deep-water current through geostrophic adjustment (*19*, *20*). Bottom-water warming could be then achieved by a reduction in the deep-water current that transports the cool waters of the AABW (*3*).

Internal topographic Kelvin waves are mainly responsible for the rapid transmission of the changes in the Southern Ocean to the equator (orange arrows in Fig. 2, D and E). The Kelvin waves travel along the deep-ocean trench east of New Zealand in a direction for which the lateral boundary is always on the left (in the Southern Hemisphere; SOM). They propagate along the density interfaces of the deep ocean at internal-wave speeds (*21*) of ~7.0×10^{-2} m s^{-1}, corresponding to 2208 km per year (SOM). The signal travels in the opposite direction (with the lateral boundary on the right) in this sensitivity analysis because the calculation moves the ocean representation backward in time.

Internal and topographic Rossby waves are also responsible for the transmission over the undulating bottom topography in the west-central region of the Northern Hemisphere (Fig. 2B). Internal equatorial Kelvin waves, whose (reversed) propagation is identified by the westward equatorially trapped wave track in the deep layers (yellow arrows in Fig. 2C), drive the link between northern and southern hemispheres.

We have examined the proposed mechanism by using a new synthesized ocean data set from 4D-VAR data assimilation (*22*) (SOM). In this synthesized data set, the bottom-water warming is successfully reproduced as a positive temperature trend of ~0.003 K from 1985 to 1999 (between the WOCE and WOCE_rev observational periods) in the North Pacific (Fig. 3A). The term balance of the temperature equation in this abyssal region from the synthesized field (SOM) shows that an overall balance between the horizontal advective and diffusive cooling, and the vertical diffusive heating, is present throughout the period (blue bars in Fig. 3B). The geothermal heating effect is implicitly incorporated in the vertical diffusive heating. Local time change is a subtle positive value, representing the bottom-water warming, as a residual of these major terms. The standard deviation of each term shows that the temporal change in the horizontal advection mainly causes the variations of the local time change (red bars), implying that the changes in the abyssal circulation due to the wave propagations (SOM) constrain the bottom-water warming.

In addition, our results are also consistent with fragmental direct evidence reported in previous observational work. Figure 4A shows the time series of change in methanesulphonic acid (MSA) concentrations within a Law Dome ice core (*23*) obtained from a location near the Adélie Coast (Fig. 1). This MSA record is highly correlated with local sea ice extent and hence should be closely connected with the net surface air-sea heat flux in this region. Indeed, the highly significant correlation between the MSA record and sea surface temperature derived from satellite missions (1981 to 2001) (*24*) underlines this close relation (red curve). Actually, the time change in the net surface air-sea heat flux estimation from the synthesized data set (*22*) is well correlated with that in the MSA record in this region (green curve). Also, the correlative time change in the sea-level anomaly derived from high-precision multisatellite altimetry products possibly further supports the proposed link between the changes in the surface conditions and the supply of AABW (SOM). Again, this is

Downloaded from www.sciencemag.org on July 15, 2010

consistent with a recent reduction in bottom-water formation around Antarctica (*25*).

In this context, our derivation of a 40-year response time implies that the bottom-water warming from 1985 to 1999 in the subarctic North Pacific is linked to the decrease in the MSA value from 1945 to 1959, which corresponds to an increase in the net surface air-sea heat flux off the Adélie Coast. Quantitative diagnosis, based on values of the temporal rate of change of bottom-water temperature when net surface air-sea heat flux is steadily changed (Fig. 2F), shows that an observed bottom-water warming from 0.003 to 0.01 K is equivalent to an increase in the net heat flux from 1.0×10^{-1} to 3.2×10^{-1} W m^{-2} per year into the Southern Ocean off the Adélie Coast (SOM). This net heat flux enhancement is broadly consistent with the relevant decadal increase (3.8×10^{-1} W m^{-2} year^{-1}) from 1945 to 1959, as estimated from the ratio of the MSA values (black curve in Fig. 4) to the net surface heat flux (green curve).

In summary, an increase in the heat input into the Southern Ocean off the Adélie Coast leads to bottom-water warming in the North Pacific on a relatively short time scale (within four decades). A reduction in bottom-water formation off the Adélie Coast due to enhanced heat input leads to a change in the configuration of the isopycnal surfaces through the action of oceanic internal waves and thus determines the pressure forcing over the whole abyssal region of the North Pacific. The consequent reduction in abyssal cooling by the deep-ocean current enables the substantial heating by the vertical diffusion inclusive of the geothermal effect to warm the bottom waters. The propagation speed of the internal waves determines the time scale of this teleconnection. The resulting increase in the integrated heat content can reach 1.2×10^{20} J year^{-1} below 4000-m depth in the Pacific basin.

These results suggest that the present global-change paradigm involving a warming surface regime over an abyssal ocean which, through its very slow response time, can be assumed to be a relatively stable regulator of Earth's climate, must be revisited. Our finding of an invasive and rapid teleconnection between polar surface air-sea heat flux change and distant bottom-water warming indicates that the multicentennial-to-millennial developmental time scales currently envisaged in the predicted oceanic response to climate warming are probably too long.

References and Notes

1. A. W. Mantyla, J. L. Reid, *Deep Sea Res. A* **30**, 805 (1983).
2. A. H. Orsi *et al.*, *Prog. Oceanogr.* **43**, 55 (1999).
3. M. Fukasawa *et al.*, *Nature* **427**, 825 (2004).
4. G. C. Johnson, S. C. Doney, *Geophys. Res. Lett.* **33**, L14614 (2006).
5. M. P. Meredith, A. C. N. Garabato, A. L. Gordon, G. C. Johnson, *J. Clim.* **21**, 3327 (2008).
6. T. Kawano *et al.*, *Geophys. Res. Lett.* **33**, L23613 (2006).
7. S. Levitus *et al.*, *Geophys. Res. Lett.* **32**, L02604 (2005).
8. S. Masuda *et al.*, *Geophys. Res. Lett.* **30**, 1868 (2003).
9. Y. Sasaki, *Mon. Weather Rev.* **98**, 875 (1970).
10. C. Wunsch, *The Ocean Circulation Inverse Problem* (Cambridge Univ. Press, New York, 1996).
11. J. Marotzke *et al.*, *J. Geophys. Res.* **104** (c12), 29529 (1999).
12. A. Köhl, *J. Phys. Oceanogr.* **35**, 1455 (2005).
13. J. Schröter, C. Wunsch, *J. Phys. Oceanogr.* **16**, 1855 (1986).
14. I. Fukumori, T. Lee, B. Cheng, D. Menemenlis, *J. Phys. Oceanogr.* **34**, 582 (2004).
15. A. M. Moore, H. G. Arango, E. Di Lorenzo, A. J. Miller, B. D. Cornuelle, *J. Phys. Oceanogr.* **39**, 702 (2009).
16. W. J. Schmitz Jr., *Rev. Geophys.* **33**, 151 (1995).
17. H. M. van Aken, *The Oceanic Thermohaline Circulation* (Springer, New York, 2006).
18. H. Nakano, N. Suginohara, *J. Geophys. Res.* **107**, 3219 (2002).
19. M. Kawase, *J. Phys. Oceanogr.* **17**, 2294 (1987).
20. N. Suginohara, M. Fukasawa, *J. Oceanogr. Soc. Japan* **44**, 315 (1988).
21. J. Pedlosky, *Ocean Circulation Theory* (Springer, New York, 1996).
22. The details of these data are provided on the DIAS Earth Observation Data Sets Web site (www.jamstec.go.jp/e/medid/dias/kadai/clm/clm_or.html).
23. M. A. J. Curran, T. D. van Ommen, V. I. Morgan, K. L. Phillips, A. S. Palmer, *Science* **302**, 1203 (2003).
24. Multi-channel sea surface temperature data (http://podaac.jpl.nasa.gov/PRODUCTS/p016.html), maintained by NASA Jet Propulsion Laboratory Physical Oceanography Distributed Active Archive Center, Pasadena, CA (2003).
25. S. T. Gille, *Science* **295**, 1275 (2002).

26. We thank Y. Ishikawa and the late I. Kaneko for helpful discussions and Y. Sasaki and Y. Hiyoshi for technical support. This work was supported in part by the Data Integration and Analysis System of the Ministry of Education, Culture, Sports, Science and Technology, Japan (MEXT).

Supporting Online Material

www.sciencemag.org/cgi/content/full/science.1188703/DC1
Materials and Methods
Figs. S1 to S3
References

23 February 2010; accepted 8 June 2010
Published online 24 June 2010;
10.1126/science.1188703
Include this information when citing this paper.

Ocean Warming Slows Coral Growth in the Central Red Sea

Neal E. Cantin,* Anne L. Cohen,* Kristopher B. Karnauskas, Ann M. Tarrant, Daniel C. McCorkle

Sea surface temperature (SST) across much of the tropics has increased by 0.4° to 1°C since the mid-1970s. A parallel increase in the frequency and extent of coral bleaching and mortality has fueled concern that climate change poses a major threat to the survival of coral reef ecosystems worldwide. Here we show that steadily rising SSTs, not ocean acidification, are already driving dramatic changes in the growth of an important reef-building coral in the central Red Sea. Three-dimensional computed tomography analyses of the massive coral *Diploastrea heliopora* reveal that skeletal growth of apparently healthy colonies has declined by 30% since 1998. The same corals responded to a short-lived warm event in 1941/1942, but recovered within 3 years as the ocean cooled. Combining our data with climate model simulations by the Intergovernmental Panel on Climate Change, we predict that should the current warming trend continue, this coral could cease growing altogether by 2070.

Hermatypic corals contribute up to 75% of the calcium carbonate ($CaCO_3$) budget of modern reefs through the process of skeleton building (*1*). Today, rates of $CaCO_3$ production by reef corals, thought to be enhanced by the photosynthetic activities of symbiotic algae (zooxanthellae) (*2*, *3*), far exceed carbonate production rates in the absence of biological activity and ensure that rates of reef accretion exceed natural rates of bioerosion, dissolution, and offshore transport (*4*). For individual corals, rapid rates of skeletal growth are essential for successful recruitment, in order to reach a size refuge from mortality (*5*) and to maximize colony surface area for photosynthesis (*6*).

Predictions based on experimental and field observations indicate that the combined effects of rising temperatures and ocean acidification could increase the frequency of bleaching events and reduce coral calcification by 80% of modern values when atmospheric CO_2 concentrations reach 560 parts per million around 2055 (*7*, *8*, *9*). At this point, if rates of $CaCO_3$ production by corals and other reef calcifiers cannot keep up with rates of erosion, the majority of coral reefs could switch from net accreting to net eroding structures. Elevated temperatures suppress the calcification rates of reef-building corals (*10*) by affecting the relationship between the coral host and its algal symbionts (zooxanthellae). As temperatures rise above threshold summertime values, the photosynthetic capacity of the symbiotic zooxanthellae declines (*11*), reducing the availability of algal-derived photosynthate that fuels light-enhanced calcification (*12*). A prolonged increase of ~1°C or more above historical maximum sea surface temperatures (SSTs)

Woods Hole Oceanographic Institution, Woods Hole, MA 02543, USA.
*These authors contributed equally to this work.

Downloaded from www.sciencemag.org on July 15, 2010

(*13*) can result in substantial loss of zooxanthellae or "bleaching," cessation of calcification, and in some cases coral mortality. The model predictions in (*8*, *9*) consider the temperature at which bleaching occurs as the "threshold" temperature at which coral calcification begins to decline. However, elevated temperatures can negatively affect calcification long before bleaching is evident. Indeed, laboratory-based culture studies and field observations have shown the optimum temperature for calcification by several tropical coral species to be several degrees below their ambient summertime SSTs (*14*–*16*).

Mean annual SSTs across much of the global tropics and subtropics have increased between 0.4° and 1°C in the past four decades (*17*). However, in the central Red Sea, home to extensive reef growth and a high diversity of scleractinian corals, the extent of warming exceeds the observed mean tropical warming. For the past decade, summertime SSTs [July, August, and September (JAS)] in this region have remained on average 1.46°C above the historical mean [relative to 1950–1997 National Oceanic and Atmospheric Administration (NOAA) Extended Reconstructed Sea Surface Temperature (ERSST) v3b climatology]. Nevertheless, although localized bleaching to depths of 20 m was reported in 1998 (*18*), large-scale bleaching and the mortality typically associated with persistent warm SST anomalies have not been observed, suggesting that Red Sea corals may be naturally adapted to extremes of temperature and salinity. The lack of empirical data documenting the effects of thermal stress on coral growth in this region limits our ability to predict how future increases in SST will shape the coral reef landscape of the central Red Sea over the next century.

We used historical temperature records to quantify the temperature dependence of skeletal growth and calcification rates of the massive reef-building coral *Diploastrea heliopora* in the central Red Sea and to investigate the potential for subliminal (nonvisible) effects of recently rising SSTs. The coral colonies showed no outward signs of thermal stress, bleaching, or disease at the time of sampling. Skeletal cores were removed from six colonies with a submersible hydraulic drill, and the holes were filled with premade cement plugs. In the lab, the intact cores were scanned with a Siemens Volume Zoom Spiral Computerized Tomography (CT) Scanner to reveal the annual growth bands (*19*). In *D. heliopora*, as with other architecturally complex coral skeletons, annual growth bands can be difficult to visualize and quantify with conventional two-dimensional (2D) x-ray techniques. The 3D imaging capabilities of the CT scanner allow us to digitally rotate the reconstructed core images to accurately identify the maximum vertical growth axis of the coral and to then slice the 3D image electronically to an optimal thickness, thus revealing the high- and low-density couplets that constitute each annual growth band.

By sampling colonies at different times of the year (*20*), we deduced that *D. heliopora* at this Red Sea site forms a narrow high-density skeletal band in the spring and that ~75% of skeletal extension occurs over the remainder of the year, as a wide low-density band (Fig. 1). We established the age of each coral by counting the number of high-density bands visible in the CT images and obtained a precise measure of their annual linear extension (upward growth) rates (SE ± 0.5 mm) by measuring the distance between successive high-density bands [see the supporting online material (SOM)]. Using the NOAA ERSST v3b (*21*), we quantified the relationship between coral growth and SST over the collective time period represented by the cores [1930 to 2008; see (*20*) for the age of each individual core]. Coral growth and summertime (JAS) SSTs are significantly coherent (95%) at periods longer than 10 years (fig. S1). A second-order Butterworth low-pass filter with a cutoff frequency of 10 years was applied to the coral and SST data sets to remove high-frequency variability and reveal the temperature-dependent signal. Average JAS SSTs account for 68% of the variance in *D. heliopora* skeletal growth on decadal time scales (R^2 = 0.676, P < 0.001, effective number of samples = 7; Fig. 2B). Skeletal growth correlates inversely with temperature, and growth rates are highest when JAS SSTs remain below 30.25°C. When the average JAS SST exceeds 30.5°C, *D. heliopora* growth declines rapidly, by 0.12 mm (5%) for every 0.2°C increase in summer SST (Fig. 2C).

Average summertime SSTs have exceeded 30.5°C at our study site twice in the past 85

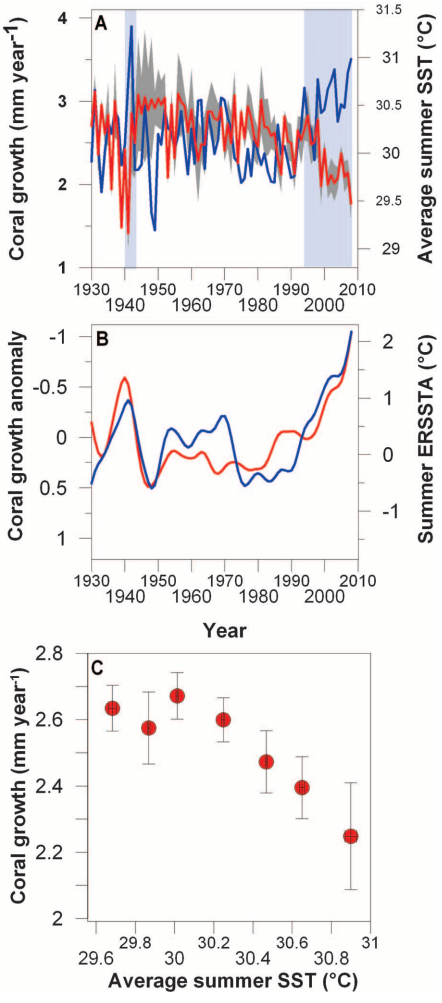

Fig. 2. Calibration of the coral growth dependence on SST. (**A**) Averaged annual growth of six corals ± 1 SE (red line ± gray shading) measured from CT scans compared with average annual summer SSTs (JAS, ERSST v3b, blue line), 1925–2008. SSTs exceeded 30.5°C twice in the past 83 years (vertical blue shading). (**B**) 10-year filtered coral growth anomaly (red line) and ERSST anomaly (ERSSTA, blue line) (coral growth and ERSST anomalies relative to the 1950–1997 mean for each time series) data show inverse correlation on multi-year time scales (r^2 = 0.68). (**C**) Model I regression of mean annual coral growth ± 1 SE against average summer SST (±1 SE for each SST bin) from six *D. heliopora* colonies (n = 318 total observations of unfiltered data). The red circles indicate the regression of average coral extension rate within each SST range indicated by the SE bars. The optimum temperature for *D. heliopora* skeletal growth, <30.5°C, was determined as the point at which average annual skeletal growth deviates from the mean annual baseline extension rate [2.69 mm year^{-1}, model I regression, $F_{5,300}$ = 2.73 P < 0.05].

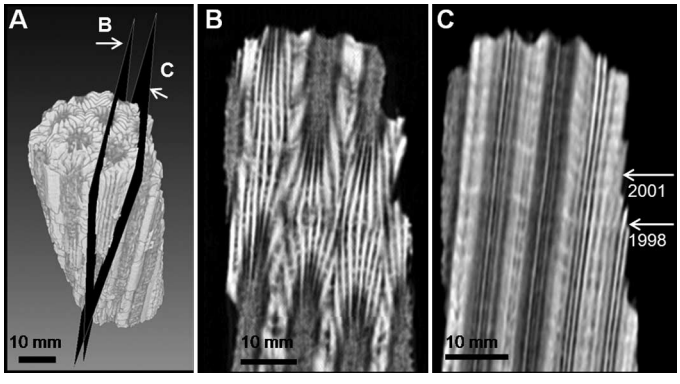

Fig. 1. Quantification of annual coral growth by 3D CT scanning. (**A**) 3D CT scan reconstruction of the skeleton of *D. heliopora* from a small core. Virtual 2D slices (B and C), 2.5 mm thick, are cut digitally along two planes. (**B**) Slice B is subparallel to the upward growth axis, and the annual growth bands are not visible. (**C**) Slice C, cut parallel to the upward growth axis, reveals annual growth bands, including two anomalously high-density bands coincident with the 1998 and 2001 high-temperature events.

Downloaded from www.sciencemag.org on July 15, 2010

years (Fig. 2A). In the early 1940s, SSTs remained +3°C above the historical mean for two successive summers (1941 and 1942). In both coral cores that span this time, average annual growth rates decreased by 44% over the corresponding period (Fig. 2A). In this case, however, the anomaly was short-lived; summer SSTs dropped below the historical average JAS SST in the following year, and coral growth rates quickly recovered. Conversely, the most recent warm SST anomaly is persistent. Since 1998, JAS SSTs at our study site have remained at 0.9° to 2.2°C above historical mean values. A 30% decline in mean linear extension [$F_{1,27}$ = 32.04, $P < 0.001$, $n = 6$ coral colonies] relative to pre-1997 extension rates is recorded over this time period. Using the CT scan images, we also calculated the change in average annual calcification rate—that is, $CaCO_3$ production—by each coral associated with the drop in skeletal extension. Skeletal densities (in grams per cubic millimeter) were quantified from the CT images of each core by converting grayscale values to apparent absolute density using hydroxyapatite standards of known density [see the CT scanning methods (*20*)]. Average annual calcification by *D. heliopora*, defined as the product of annual linear extension and annual density (*14*), declined by 0.05 g mm^{-2} $year^{-1}$ [$F_{1,29}$ = 8.04, P = 0.008) or 18% from 1998 to 2008 relative to the 1976–1997 mean.

This decline in coral growth rates is probably a consequence of the impact of thermal stress on the coral host–symbiont relationship. The NOAA degree heating weeks (DHWs, see SOM) product provides a measure of the likelihood that thermal stress will induce coral bleaching [loss of symbiotic zooxanthellae (*22*)]. Over a 12-week period, DHWs ≥4°C weeks indicate that some coral bleaching is likely, and as DHWs reach ≥8°C weeks, widespread and severe bleaching and some coral mortality can be expected (*23*). Weekly SST data are available at our study site from 1982 through 2008 [from the Integrated Global Ocean Services System (IGOSS) nmc Reyn_SmithOIv2 data set (*24*)], allowing us to calculate the DHW index for this time period (Fig. 3). A significant increase in the duration as well as the intensity of heat stress over the past decade corresponds directly with the decline in skeletal growth and calcification measured in our coral cores (Fig. 3). Thus, although the coral colonies sampled for this study exhibited no obvious signs of thermal stress, such as bleaching or disease, the skeletal growth histories provide evidence for prolonged thermal stress that has inhibited the recovery of *D. heliopora* skeletal growth since 1998. Indeed, rates of skeletal growth and calcium carbonate production are lower now than they have been since at least 1940.

The aragonite saturation state values [$\Omega_{(arag)}$] of seawater at the coral sampling sites are relatively high in both summer (4.08) and winter (3.94) (SOM). Calculations using the few available historical data suggest that $\Omega_{(arag)}$ values in the Red Sea have risen over the past 30 years; apparently, the effect of rising SST [which tends to increase $\Omega_{(arag)}$] has more than offset the effect of rising atmospheric CO_2 [which tends to lower $\Omega_{(arag)}$]. We therefore think it is unlikely that ocean acidification has caused or contributed to the observed drop in Red Sea *D. heliopora* calcification over the past decade. Instead, the timing and intensity of the decline in skeletal growth are most consistent with the impact of thermal stress on physiological processes involved in calcification.

The skeletal growth response to historical SST variability shows that these corals can recover from major warming anomalies if the episodes are short-lived. What, then, is the likelihood that summer temperatures in the Red Sea will return to pre-1998 values fostering coral recovery? Using the output from a suite of 17 global, fully coupled climate model simulations from the Fourth Assessment Report of the Intergovernmental Panel on Climate Change (IPCC AR4), we examined projections of future trends in summer SSTs in the Saudi Red Sea (20° to 24°N) under the IPCC AR4 A1B and A2 CO_2 emissions scenarios. The multimodel mean results (Fig. 4) indicate that summer SSTs in the central Red Sea will continue to rise as atmospheric CO_2 concentration rises through the 21st century, reaching a high of 2.5° to 3°C relative to the 2000–2008 mean by 2099. Extrapolating our empirically derived coral growth–SST relationship, we expect that *D. heliopora* will cease calcifying altogether by 2070, when summer SSTs will exceed current summer values by 1.85°C (Fig. 4B). This is probably a conservative estimate, given that the corals studied were not visibly bleached at the time of sampling. As temperatures continue to rise, events that cause significant loss of zooxanthellae and depletion of energetic reserves will become more frequent, and coral mortality from the effects of bleaching may occur long before calcification rates approach zero.

Recent work suggests that photoprotective mechanisms of both the coral host and symbionts (*25*), as well as shuffling of the dominant

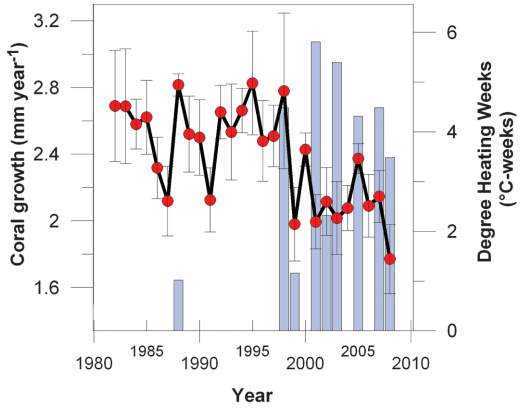

Fig. 3. Impact of accumulated thermal stress on coral growth. Annual growth rates of *D. heliopora* (red circles, mean ± 1 SE) versus the annual DHWs product (blue bars) for this site. In general, moderate coral bleaching is expected above 4 DHWs and severe bleaching and mortality above 8 DHWs. The corals in this study were not visibly bleached at the time of sampling. However, their skeletal growth record reveals the significant impact of chronic thermal stress over the past decade.

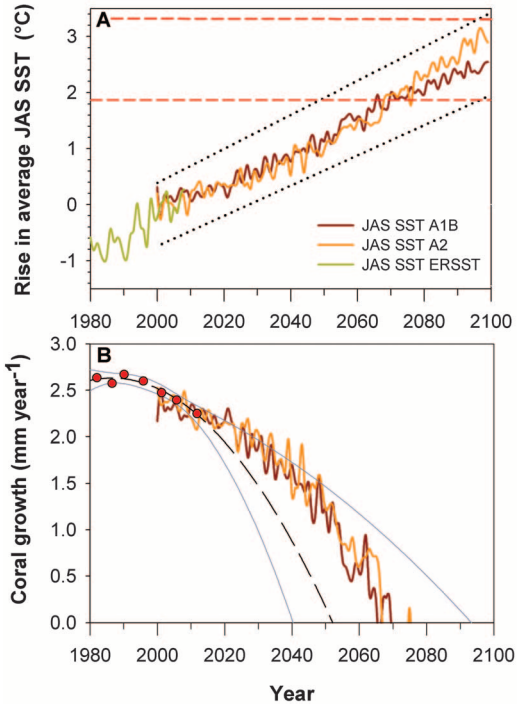

Fig. 4. Predicted rise in summertime SST in the central Red Sea: 1980–2100. (**A**) JAS SST trajectory (0°C is the average 2000–2008 JAS SST) averaged over 17 IPCC AR4 climate models for two midrange emissions scenarios (A1B and A2, ± 1 SE, dotted black lines). Dashed red lines depict the SST threshold for zero coral growth for *D. heliopora* [1.85°C above average 2000–2008 JAS SST, upper 95% confidence limit], using the SST–coral growth relationship derived in Fig. 2C. (**B**) Statistical inverse model to predict future coral growth rates based on the current rate of SST rise (1980–2008, black dashed line) and the projected coral growth rates based on IPCC model A1B and A2 SSTs (2000–2100). Gray lines are the 95% confidence interval surrounding the inverse model coral growth projection. Red circles indicate coral growth (in millimeters per year).

Downloaded from www.sciencemag.org on July 15, 2010

symbiont assemblage to more thermally tolerant zooxanthellae genotypes (*26*–*28*), could increase the tolerance of reef-building corals to future ocean warming. However, existing data suggest that symbiont shuffling to thermally tolerant genotypes would increase thermal tolerance by 1° to 1.5°C, which is insufficient to cope with the magnitude of SST change predicted for the Red Sea and much of the tropical oceans over this century (*29*). Indeed, our data do not suggest that *D. heliopora* has acquired enhanced resistance, despite a decade of exposure to persistent thermal stress. Continued efforts to quantify the thermal tolerances of other coral species and important reef calcifiers will improve our predictions of how climate change will affect coral reefs of the central Red Sea. However, the data in hand suggest that without immediate, aggressive global intervention to reduce carbon emissions below IPCC A1B and A2 scenarios, the pressures of predicted annual heat stress will most certainly result in further deterioration of coral health in the central Red Sea over this century.

References and Notes

1. D. E. Hart, P. S. Kench, *Coral Reefs* **26**, 53 (2007).
2. P. Furla, I. Galgani, I. Durand, D. Allemand, *J. Exp. Biol.* **203**, 3445 (2000).
3. A. L. Cohen, T. A. McConnaughey, *Rev. Mineral. Geochem.* **54**, 151 (2003).
4. E. A. Burton, L. M. Walter, *Geology* **15**, 111 (1987).
5. T. P. Hughes, J. B. C. Jackson, *Ecol. Monogr.* **55**, 141 (1985).
6. J. A. Kleypas, C. Langdon, *Coast. Estuar. Stud.* **61**, 73 (2006).
7. O. Hoegh-Guldberg *et al.*, *Science* **318**, 1737 (2007).
8. S. D. Donner, W. Skirving, C. M. Little, M. Oppenheimer, O. Hoegh-Guldberg, *Glob. Change Biol.* **11**, 2251 (2005).
9. J. Silverman, B. Lazar, L. Cao, K. Caldeira, J. Erez, *Geophys. Res. Lett.* **36**, L05606 (2009).
10. G. De'ath, J. M. Lough, K. E. Fabricius, *Science* **323**, 116 (2009).
11. R. J. Jones, O. Hoegh-Guldberg, A. W. D. Larkum, U. Schreiber, *Plant Cell Environ.* **21**, 1219 (1998).
12. F. A. Al-Horani, S. M. Al-Moghrabi, D. de Beer, *Mar. Biol.* **142**, 419 (2003).
13. P. L. Jokiel, S. L. Coles, *Coral Reefs* **8**, 155 (1990).
14. J. M. Lough, D. J. Barnes, *J. Exp. Mar. Biol. Ecol.* **245**, 225 (2000).
15. T. F. Cooper, G. De'ath, K. E. Fabricius, J. M. Lough, *Glob. Change Biol.* **14**, 529 (2008).
16. A. T. Marshall, P. Clode, *Coral Reefs* **23**, 218 (2004).
17. J. A. Kleypas, G. Danabasoglu, J. M. Lough, *Geophys. Res. Lett.* **35**, L03613 (2008).
18. L. DeVantier, N. Pilcher, *The Status of Coral Reefs in Saudi Arabia–2000* (National Commission for Wildlife Conservation and Development, Jeddah, Saudi Arabia, 2000).
19. C. Saenger, A. L. Cohen, D. W. Oppo, R. B. Halley, J. E. Carilli, *Nat. Geosci.* **2**, 492 (2009).
20. Materials and methods are available as SOM on *Science* Online.
21. T. M. Smith, R. W. Reynolds, T. C. Peterson, J. Lawrimore, *J. Clim.* **21**, 2283 (2008).
22. M. W. Gleeson, A. E. Strong, *Adv. Space Res.* **16**, 151 (1995).
23. G. Liu, A. E. Strong, W. Skirving, *Eos* **84**, 137 (2003).
24. R. W. Reynolds, N. A. Rayner, T. M. Smith, D. C. Stokes, W. Wang, *J. Clim.* **15**, 1609 (2002).
25. W. K. Fitt *et al.*, *J. Exp. Mar. Biol. Ecol.* **373**, 102 (2009).
26. R. W. Buddemeier, D. G. Fautin, *Bioscience* **43**, 320 (1993).
27. A. M. Jones, R. Berkelmans, M. J. H. van Oppen, J. C. Mieog, W. Sinclair, *Proc. Biol. Sci.* **275**, 1359 (2008).
28. A. C. Baker, C. J. Starger, T. R. McClanahan, P. W. Glynn, *Nature* **430**, 741 (2004).
29. A. C. Clement, A. C. Baker, J. Leloup, *Nat. Geosci.* **3**, 8 (2010).

30. The authors thank G. P. Lohmann, C. Saenger, M. X. Weber, and A. Venti for their assistance with fieldwork. A. Al Suwailem; Y. Kattan; H. Al Jahdali; W. Moazen; Nageeb from King Abdullah University of Science and Technology (KAUST); and E. Mason, R. Maravilla, and the staff at Dream Divers provided logistical support in Saudi Arabia. D. Ketten and J. Arruda provided invaluable technical support and advice for the CAT scanning of our coral cores. Comments from D. Oppo and two anonymous reviewers helped to improve the original manuscript. This research was funded by award no. USA 00002/KSA 00011 from KAUST to A.L.C. and D.C.M.

Supporting Online Material

www.sciencemag.org/cgi/content/full/329/5989/322/DC1
Materials and Methods
SOM Text
Fig. S1
References

10.1126/science.1190182

Shared Social Responsibility: A Field Experiment in Pay-What-You-Want Pricing and Charitable Giving

Ayelet Gneezy,[1]* Uri Gneezy,[1] Leif D. Nelson,[2] Amber Brown[1,3]

A field experiment (N = 113,047 participants) manipulated two factors in the sale of souvenir photos. First, some customers saw a traditional fixed price, whereas others could pay what they wanted (including $0). Second, approximately half of the customers saw a variation in which half of the revenue went to charity. At a standard fixed price, the charitable component only slightly increased demand, as similar studies have also found. However, when participants could pay what they wanted, the same charitable component created a treatment that was substantially more profitable. Switching from corporate social responsibility to what we term shared social responsibility works in part because customized contributions allow customers to directly express social welfare concerns through the purchasing of material goods.

In a provocative article some 40 years ago, Milton Friedman stated that "the social responsibility of business is to increase its profits" (*1*). According to this view, private companies should focus on the provision of profits for shareholders, leaving the provision of public goods to others. The boldness of the prescription provoked a countermovement in favor of broad social consciousness from private companies to prioritize corporate social responsibility (CSR).

Today CSR is practiced by many firms worldwide, yet often CSR-related costs are higher than their commercial benefits (*2*). Two major factors may contribute to this limited success. First, customers might assume that CSR practitioners have ulterior motives (*3*). Consider a company choosing between high- and low-cost manufacturing options (e.g., using recycled or natural resource–intensive materials). The "good," CSR-consistent, option is profitable only if it generates enough customer interest to offset increased costs. However, if consumers are suspicious of the firm's intentions, the goodwill behind CSR may appear to be just another consumer manipulation (*4*).

Second, CSR purchases send a weak signal to oneself and to others regarding the buyer's "social intentions." People identify with the social causes they support, but purchasing from a CSR-oriented company leaves that cause too remote from their core identity. Buying a pair of shoes from an ecologically friendly company sends a signal (to self and to others) that the customer cares about the environment, but it also sends a signal that the customer simply likes the shoes. What part of the purchase reflects style consciousness, and what part reflects social consciousness?

We propose a new CSR strategy, which we term shared social responsibility (SSR). To improve programs based on social preferences, companies need to specifically engage the social preferences of their consumers. If social responsibility is to provide any benefit to a company, its customers, and the community, it should go beyond the priorities of the firm and instead express the priorities that the firm shares with its customers.

For our investigation we used a recently emerged pricing strategy hinging on the social preferences of customers, referred to as "pay what you want" (PWYW). In this strategy, in

[1]Rady School of Management, University of California, San Diego, 9500 Gilman Drive, La Jolla, CA 92093, USA. [2]Haas School of Business, University of California, Berkeley, 545 Student Services #1900, Berkeley, CA 94720, USA. [3]Disney Research, 1401 Flower Street, Glendale, CA 91201, USA.

*To whom correspondence should be addressed. E-mail: agneezy@ucsd.edu

Downloaded from www.sciencemag.org on July 15, 2010

lieu of a fixed price, a firm offers a good or service for whatever price customers want to pay (typically including $0). If people only cared about money, they would pay the lowest price possible, yet in practice people frequently pay more (*5*–*7*).

We created a SSR situation through the combination of PWYW pricing and CSR. When paired with corporate giving, PWYW may help the firm mitigate the aforementioned problems; because the firm explicitly exposes itself to financial risk, a customer is unlikely to infer sinister ulterior motives. Thus, we used a pricing strategy that reduces customers' concerns about ulterior motives while also enhancing their identification with the cause, as every dollar spent directly reflects this self-identification. The design does not test the individual contributions of these two possible shortcomings of CSR, but by reducing both, SSR offers a plausible alternative to traditional CSR efforts.

Taken from a different perspective, SSR should also benefit the effectiveness of PWYW. It is theorized that the effectiveness of PWYW hinges on how much a consumer wants the good or service, as well as on how much he or she wants to help the company. Under the proposed SSR method, each purchase directly represents the customer's desire to support both the company and the charitable partner.

We conducted a field study at a large amusement park (*8*). Participants (N = 113,047) rode a roller coaster–like attraction, were photographed during the ride, and later chose whether to purchase a print of the photo.

We used a 2 × 2 between-participants design. The first dimension was the price of the picture (either a regular $12.95 price or PWYW). The second dimension was Charity (either no charitable contribution or half of the revenue going to charity). The charitable partner was a nationally recognized patient-support foundation. Each of the four treatments was conducted over two full days.

The results of the two fixed $12.95 price conditions reveal low and similar purchase rates (0.50% without charity, 0.59% with). PWYW substantially increased purchase rates to 4.49% in the PWYW + Charity treatment and to 8.39% in the simple PWYW treatment. In the PWYW treatments, buyers paid significantly more per photo when half of the revenues went to charity (M = $5.33 per photo) than with no charity [M = $0.92; $t(3535) = 43.24$, $P < 0.001$ (*9*)]. Figure 1 presents the resulting profits.

Despite the observation in the literature that CSR is not profitable, many companies (including the one in question) contribute substantially to charity independent of specific product promotions. Accordingly, we identify all post-cost revenue as profit. By this account, both Charity treatments are the most profitable, and a t test confirms that SSR is substantially more profitable than traditional CSR ($M_{\$12.95+Charity}$ = $0.071 per rider versus $M_{PWYW+Charity}$ = $0.198 per rider; $P < 0.001$) (*9*).

With more than 5 million riders per year, there is a potential annual increase of more than $600,000 in profits. Does increased photo purchasing crowd out spending elsewhere in the amusement park (e.g., for popcorn or gifts)? Clearly, if SSR merely cannibalizes another element of the business, we should be more circumspect in our inferences. Although we cannot speak to every possible case of crowding out, our data suggest that this is not the case. Immediately after leaving the photo area, customers passed through a merchandise area (containing T-shirts, keychains, etc.). Total sales data from those days (Table 1) suggest that increased photo revenue does not lead to decreased merchandise revenue in the immediate store, but future research is needed to thoroughly investigate the incidence of product cannibalization.

SSR increased profit, perhaps because it minimized suspicion of the firm's intentions and maximized the identity expressiveness in the purchase. This contention is further supported by an intriguing piece of evidence in the purchase rates of PWYW and PWYW + Charity customers: The addition of the charitable promotion actually suppressed purchasing [$\chi^2 = 336.17$, P = 0.001 (*9*)]. This is consistent with our explanation that with fixed prices, customers buy only when the benefits outweigh the costs. In the PWYW + Charity condition, the cost of sending a bad signal looms large, so customers with a low value for the picture will prefer not to buy it over buying it either for a low price (bad signal) or for a high price (not worth it).

Historically, company ethics are seen as competing with company economics (*10*–*14*), but our study suggests a method in which the pursuit of social good does not undermine the pursuit of profit. Under SSR, the consumer chooses a price, thereby actively determining his or her contribution to the cause. Apparently, a company can best serve its community and its shareholders by sharing its social responsibility with its customers.

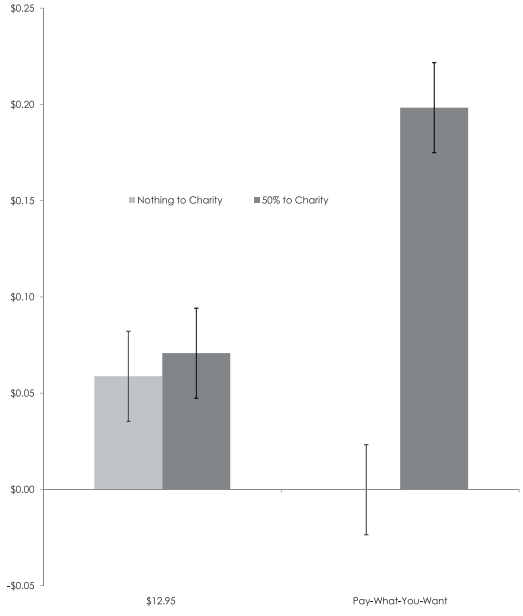

Fig. 1. Profit per rider (amount paid minus production costs). Photo sales were most profitable for the firm and made the largest contribution to charity when participants could pay what they wanted and half of their payment went to charity—the shared social responsibility treatment.

Table 1. Treatment effects on photo revenue and merchandise revenue. Merchandise refers to items such as souvenir keychains whose prices were not directly manipulated in the experiment. There were essentially no differences in merchandise sales over the same days. If anything, people spent slightly more on merchandise in the PWYW + Charity condition. We can likely rule out concerns that increased photo revenue was cannibalizing from other sources.

Treatment	Photo revenue	Merchandise revenue	Riders	Merchandise revenue per rider
$12.95	$1823	$11,280.98	28,224	$0.40
$12.95 + Charity	$2331	$12,322.72	30,592	$0.40
PWYW	$2175.80	$11,833.90	28,263	$0.42
PWYW + Charity	$6224.22	$11,694.03	25,968	$0.45

References and Notes

1. M. Friedman, *N.Y. Times Mag.* **32**, 22 (1970).
2. S. Sen, C. B. Bhattacharya, *J. Mark. Res.* **38**, 225 (2001).
3. P. David, S. Kline, Y. Dai, *J. Public Relat. Res.* **17**, 291 (2005).
4. M. Friestad, P. Wright, *J. Consum. Res.* **21**, 1 (1994).
5. A. Gneezy, U. Gneezy, L. D. Nelson, "Pay what you want: On fairness in markets," working paper (2010).

Downloaded from www.sciencemag.org on July 15, 2010

6. P. A. Gautier, B. van der Klaauw, *J. Appl. Econometrics* 10.1002/jae.1184 (2010).
7. T. Regner, J. A. Barria, *J. Econ. Behav. Organ.* **71**, 395 (2009).
8. J. A. List, *Science* **321**, 207 (2008).
9. Neither of these tests controls for day-to-day variation, as we did not have PWYW data outside of the experimental treatments. Nonetheless, their respective *P* values (10^{-300} and 10^{-75}) indicate that the effect would likely still be reliable even after adjusting the error term in the analysis. See supporting material on *Science* Online.
10. T. Besley, M. Ghatak, *J. Publ. Econ.* **91**, 1641 (2007).
11. J. A. List, D. Lucking-Reiley, *J. Polit. Econ.* **110**, 215 (2002).
12. S. Meier, *J. Eur. Econ. Assoc.* **5**, 1203 (2007).
13. J. Andreoni, B. T. Harbaugh, L. Vesterlund, in *The New Palgrave Dictionary of Economics, Vol. 1*, S. Durlauf, L. Blume, Eds. (Palgrave Macmillan, Houndmills, UK, ed. 2, 2007), pp. 34–138.
14. R. J. M. Benabou, J. Tirole, *Economica* **77**, 1 (2010).
15. We thank K. Baca and K. Poor for their contributions in planning and conducting the experiment, and Z. Ben David and K. T. Hansen for assisting in the statistical analysis.

Supporting Online Material
www.sciencemag.org/cgi/content/full/329/5989/325/DC1
Materials and Methods
Figs. S1 and S2

6 January 2010; accepted 18 May 2010
10.1126/science.1186744

The Structure of *cbb*$_3$ Cytochrome Oxidase Provides Insights into Proton Pumping

Sabine Buschmann, Eberhard Warkentin, Hao Xie, Julian D. Langer, Ulrich Ermler, Hartmut Michel*

The heme-copper oxidases (HCOs) accomplish the key event of aerobic respiration; they couple O_2 reduction and transmembrane proton pumping. To gain new insights into the still enigmatic process, we structurally characterized a C-family HCO—essential for the pathogenicity of many bacteria—that differs from the two other HCO families, A and B, that have been structurally analyzed. The x-ray structure of the C-family *cbb*$_3$ oxidase from *Pseudomonas stutzeri* at 3.2 angstrom resolution shows an electron supply system different from families A and B. Like family-B HCOs, C HCOs have only one pathway, which conducts protons via an alternative tyrosine-histidine cross-link. Structural differences around hemes *b* and b_3 suggest a different redox-driven proton-pumping mechanism and provide clues to explain the higher activity of family-C HCOs at low oxygen concentrations.

In all organisms, energy is stored in electrochemical ion gradients across biological membranes and used for solute transport and for synthetic processes like adenosine triphosphate (ATP) synthesis. Electrochemical gradients are mainly generated by vectorial membrane reactions—for example, electron transfer from one side of the membrane and proton uptake from the opposite side—and/or by pumping ions, normally protons, across the membrane using the energy of light or of chemical processes such as ATP hydrolysis or redox reactions. How proton pumps function on an atomic scale has been a central theme of bioenergetics for three decades.

Heme- and copper-containing terminal oxidases (HCOs) function as cytochrome *c* oxidases or as quinol oxidases in aerobic respiration but also play a role in oxygen scavenging and in maintaining redox homeostasis by coupling the exothermic four-electron reduction of O_2 to H_2O with proton pumping (*1*, *2*). Experiments on these integral membrane protein complexes are, however, severely hampered by a complex reaction cycle involving eight protons (four pumped plus four consumed), four electrons, and O_2, and the fact that both pumped and consumed protons contribute to the formation of the electrochemical gradient. Therefore, processes such as the coordination of electron transfer and proton pumping without wasting energy, the kinetic barriers that ensure unidirectional productive proton transfer, and the nature of the gates that separate protons that are consumed in water formation from those that are pumped are far from understood (*1*, *3*).

HCOs are diverse in terms of subunit composition, electron donor, and heme type, resulting in different electron and proton transfer characteristics. However, they share a central subunit built up of 12 membrane-spanning helices (α1 to α12) that contains a low-spin heme (*a* or *b*) and a high-spin heme (a_3, o_3, or b_3)–copper (Cu_B) binuclear center to which O_2 is bound and reduced during the catalytic cycle. Based on overall amino acid similarities of the central subunit and specific differences of the proton channels, the HCO superfamily is subdivided into three major families: A, B, and C (*4*). The A HCOs, which comprise the mitochondrial and many bacterial cytochrome *c* oxidases, and the B HCOs require, in addition to the central subunit, at least one other subunit (II), which usually contains a binuclear Cu_A center to channel electrons toward the buried O_2 binding site. Whereas family-A HCOs use at least two proton pathways (*5*), B HCOs appear to use only one (*6*). The prototypes of family C, comprising ~20% of HCOs (*7*), are the *cbb*$_3$ oxidases. These are characterized by reduced proton pumping (*8*) and by a higher catalytic activity at low oxygen concentrations [the Michaelis constant (K_M) for O_2 of ~7 nM is lower by a factor of 6 to 8 than that determined for family-A HCOs (*9*)]. This property is exploited in nature (*10*) by many pathogenic proteobacteria that colonize microaerobic host tissues and by agronomically important symbiotic diazotrophs that can simultaneously perform aerobic respiration and nitrogen fixation, which involves an oxygen-sensitive nitrogenase. Interestingly, *cbb*$_3$ oxidases also reduce NO to N_2O (*11*). Family-C HCOs contain the central subunit (N) and either one (O) or two (O + P) additional subunits that are completely different from family A and B subunits. Subunits O and P contain one- and two-heme C molecules, respectively, and are predicted to possess cytochrome *c* folds (*7*, *12*, *13*). Because some family-C HCOs, similar to the evolutionary closely related NO reductases, are composed of only subunits N and O, these are defined as the core complex (*14*). Family-C HCOs optionally associate a fourth subunit (Q) that is involved in stabilizing the interactions of subunit P with the core complex at least in *Rhodobacter capsulatus* (*15*).

We crystallized the *cbb*$_3$ oxidase from the bacterium *Pseudomonas stutzeri* strain ZoBell using pentaerythritol ethoxylate as precipitant and a dodecyl-α-D-maltoside/decanoylsucrose/undecyl-α-D-maltoside detergent mixture. Its structure was determined by applying the favorable anomalous properties of iron for phase determination [see supporting online material (SOM)]. We independently determined the sequences used for model building because published sequences (*12*) were not compatible with the results of our mass spectrometric analysis (see SOM and fig. S1). The reliability factors R and R_{free} of the refined structure were 18.3% and 22.4% in the resolution range 10 to 3.2 Å. *Cbb*$_3$ oxidase has a size of about 45 by 65 by 100 Å, with subunit N localized in the membrane and subunits O and P predominantly in the periplasm (Fig. 1). Despite the low sequence identity [pairwise below 20%, overall 4% (fig. S1)], subunit N has the expected architecture of the central subunit (*16*, *17*) indicated by low root mean square deviations [2.5 to 3.0 Å (fig. S1)] between subunit N and the other structurally known HCOs [A-family *Paracoccus denitrificans* (*5*, *18*, *19*), *Rhodobacter sphaeroides* (*20*, *21*), bovine heart (*22*) cytochrome oxidases, and *Escherichia coli* quinol oxidase (*23*), as well as the B-family *Thermus thermophilus* cytochrome oxidase (*24*)]. The analysis of the interactions between the protein and the high-spin heme b_3, and low-spin heme *b* in

Max-Planck-Institut für Biophysik, Max-von-Laue-Straße 3, D-60438 Frankfurt/Main, Germany.

*To whom correspondence should be addressed. E-mail: hartmut.michel@mpibp-frankfurt.mpg.de

Downloaded from www.sciencemag.org on July 15, 2010

cbb_3 oxidase revealed both common and markedly varying features between the HCO families (Fig. 2). Heme b_3 is in a more bent conformation than in other HCOs, perhaps induced by the absence of the hydroxyethylfarnesyl substituent of pyrrole B in heme *b*. The iron of heme b_3 is ligated at its distal side by a small ligand (fig. S2) unidentifiable at the current resolution and at its proximal site by the invariant His^{345}. As already inferred from mutational and EPR data (*25*) His^{345} is hydrogen-bonded to Glu^{323} (only in cbb_3 oxidases), which is further hydrogen-bonded to Trp^{341} and Trp^{400} (Fig. 2A). The noncovalent fixation of the heme b_3 propionates (Fig. 2B) is achieved by coordinating its ring D carboxylate to a Ca^{2+} ion [based on inductively coupled plasma mass spectrometric (ICP-MS) data], which is further ligated to Glu^{122}-OE2, Ser^{102}-OG of subunit O and the pyrrole D propionate of heme *b* (Fig. 2B). As in other HCOs, Cu_B is tetrahedrally ligated to three histidines and to the unknown heme b_3 iron ligand (Fig. 2A and fig. S2). The covalent linkage between His^{207}-Tyr^{251} in cbb_3 oxidase previously identified by mass-spectrometric methods (*26*, *27*) is well compatible with our structural data (Fig. 2A). In contrast to the other HCOs, however, the catalytically important tyrosine side chain protrudes from helix α7 and not from helix α8 toward the active site. Heme *b* exhibits a nearly flat macrocyclic ring structure, as in other HCOs, but is turned toward heme b_3, thereby creating van der Waals contacts between the heme *b* CMA and the heme b_3 CMD methyl groups, as well as between the two propionate ligands of the Ca^{2+} complex (Fig. 2B).

Subunit O is composed of one N-terminal transmembrane helix and a soluble cytochrome *c* domain carrying one heme C molecule. Segment 64 to 118, referred to as loop O (Fig. 2B), which connects the first two conserved α helices, binds to hemes b_3, *b*, and C and interacts with the loops α3-α4, α5-α6, α7-α8, α9-α10, and α11-α12 of subunit N, as well as with several residues of subunit P. The considerable sequence identities between the core complex of cbb_3 oxidase and the NO reductases imply that the present structure also serves as a reasonable model for this key denitrification enzyme (*28*). Subunit P consists of two N-terminal transmembrane helices, a long helical linker of nearly 40 Å, and a soluble globular unit built up by two cytochrome domains with one heme C bound to each. The two cytochrome *c* domains are not folded consecutively because their third canonical α helices are subjected to an interdomain helix swapping.

The electron supply apparatus of cbb_3 oxidases completely differs from that of the other HCOs, which presumably influences electron transfer rates and, concomitantly, catalysis and proton pumping. Based on the crystal structure, the electron transfer pathway is confidently traceable (Fig. 1B) using the known distance criteria between electron carriers (*29*). First, the external electron donor—a periplasmic cytochrome *c* in the case of cbb_3 oxidase of *P. stutzeri*—transfers an electron to the outer heme C molecule of subunit P, whose pyrroles C and D are largely solvent-exposed. Next, the electron flows from the outer to the inner heme C of subunit P and from there to the heme C of subunit O (Fig. 1B). Subsequently, the electron is shuttled from the subunit O heme C to heme *b*, the edge-to-edge distance being clearly shorter than between Cu_A and heme *a*(*b*) in A(B)-family HCOs. Electron transfer continues from heme *b* to heme b_3, which, in contrast to the other HCO families, are in van der Waals contact with each other as described above (Fig. 2A). From heme b_3, the electron can rapidly equilibrate with Cu_B. After a second electron transfer to the binuclear site, O_2 will be bound to the heme b_3 iron, reduced and cleaved by receiving electrons from the heme b_3 iron, Cu_B, and the putatively redox-active cross-linked Tyr^{251}, as in family-A HCOs (*1*). The shorter edge-to-edge distances between the subunit O heme C and heme *b* and between the hemes *b* and b_3 imply an increased electron transfer rate between them and

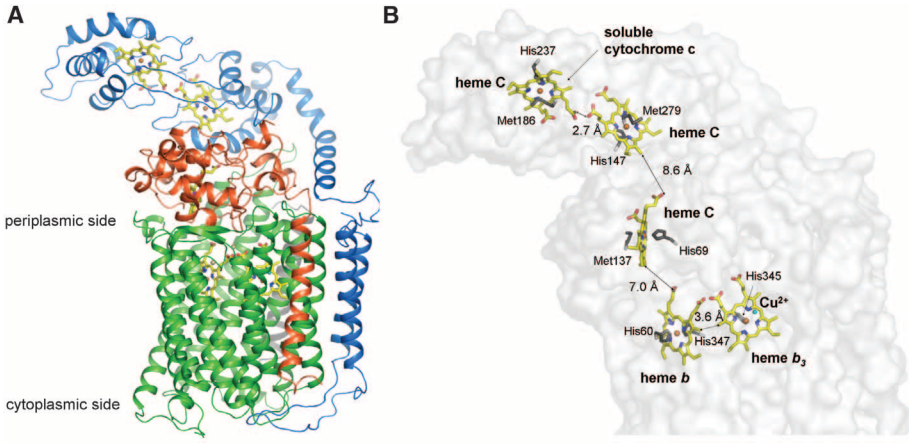

Fig. 1. Structure and heme group arrangement of the cbb_3 oxidase from *Pseudomonas stutzeri*. (**A**) Structure (ribbon model). The multisubunit complex consists of subunits N (green), O (red), and P (blue). An additional transmembrane α helix (gray) could be detected but not assigned to subunit Q, neither by side-chain recognition nor by mass spectrometric analysis of dissolved crystals. The hemes are shown as sticks; iron and copper as spheres. Only one of the cytochrome *c* domains of subunit P, referred to as inner domain, forms an interface with the core complex; the outer cytochrome *c* domain projects into the bulk solvent. (**B**) Electron transfer pathway. For a complete oxygen reduction, four electrons have to be successively shuttled along a 70 Å long electron transfer route that involves all five heme molecules according to distance criteria (*29*) and observed ultraviolet/visible spectral changes during O_2 reduction (*34*). The irons of heme b_3 and *b* are coordinated by the invariant residues His^{345}, His^{60}, and His^{347}. The heme C iron of subunit O is axially ligated to His^{69} and to Met^{137}, the heme C irons of subunit P to His^{147} and Met^{279} and to His^{237} and Met^{186}, respectively, which partly deviates from results based on spectroscopic data (*12*) due to the not-predictable helix-swapping event.

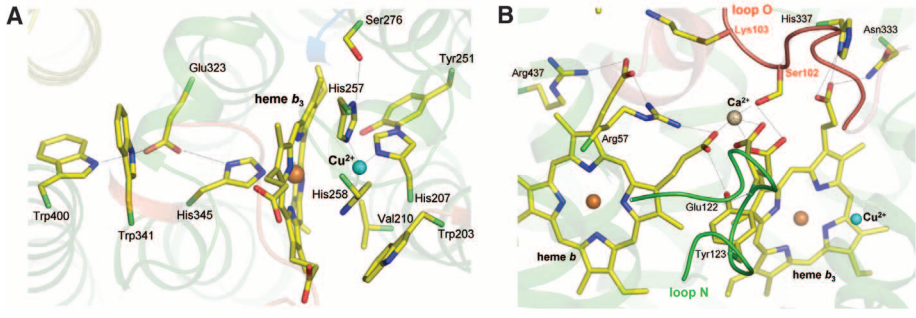

Fig. 2. Hemes b_3+*b* and O_2 binding site. (**A**) The O_2 binding site at the distal side of heme b_3 is fairly conserved in HCOs, including the hydrogen bond between His^{257} and Ser^{276} (some HCOs alternatively contain a threonine at this position), the characteristic Trp^{203} side chain (also proposed as an alternative electron donor for oxygen reduction) flanking the His^{258} imidazole ring, and the covalent bond between Tyr^{251} and His^{207}. In contrast to other HCOs, the high-spin heme b_3 in cbb_3 oxidase is activated from the proximal heme side by the His^{345}-Glu^{323}-Trp^{400} (Trp^{341}) triad. (**B**) Protein-hemes b_3 and *b* propionate interactions. The periplasmic membrane side of cbb_3 oxidase is characterized by an extended interface between subunits N and O that is not present in other HCOs. The most prominent feature is the linkage of heme b_3 and heme *b* with the contact loops N and O by a putative Ca^{2+} ion. Other notable interactions include hydrogen bonds between the pyrrole A propionate of heme b_3 and His^{337} in a bidentate manner and between the A and D propionate carboxylate groups of heme *b* and the guanidinium group of Arg^{57}.

Downloaded from www.sciencemag.org on July 15, 2010

perhaps a faster trapping and reduction of O_2 (*30*). In addition, the conformation of the heme rings and propionates, the position of the cross-linked tyrosine phenol group, and the environment of the histidine ligated to the heme b_3 iron might contribute to the lower K_M value for O_2 of cbb_3 oxidases.

Pathways are required for O_2 and protons to reach the buried catalytic site, for water release, and for proton transfer across the membrane. We find two functionally relevant and voluminous cavities (Fig. 3A). A periplasmic cavity is sandwiched between loop O and the loop connecting helices α3 and α4, called loop N. It extends more than 15 Å from the Cu_B ligand His^{258} to Thr^{118} at a postulated exit to the periplasm. This cavity is absent in the other structurally known HCOs and provides an attractive exit path for water and protons between the catalytic site and the periplasmic bulk solvent (Fig. 3A). The second void referred to as the membrane cavity is found below loop N. It is located in a position equivalent to the end of the D proton pathway in A-family HCOs (*5*). There is a similar cavity in B-family HCOs (*24*) (Fig. 3A) and in the A-family *R. sphaeroides* HCO. It is connected by narrow and rather hydrophobic channels to the membrane and the catalytic site, thus offering an access path for O_2. This cavity might additionally be linked to the periplasm (Fig. 3A) by a channel along the side chains of Glu^{131}, Glu^{181}, Ser^{189}, and Glu^{127}. An extra electron density and the geometry of main and side-chain oxygens of Ala^{124}, Leu^{162}, Asn^{179}, and Asp^{131}, however, suggests the binding of a metal ion (a second Ca^{2+} ion would agree with our ICP-MS analysis) into the channel, which could prevent solvent and proton exchange.

The cavities only provide pathways for O_2, H_2O, and protons between the active site and the periplasm and the membrane. Proton permeability routes between the cytoplasm and the active site (or the membrane cavity) are built up by protonable amino acids and water molecules. Although they cannot be definitively assessed on the basis of a static structure, the structural data support the existence of one pathway from the cytoplasm to the active site that is positioned equivalently to the K pathway in family-A HCOs (*5*) (Fig. 3B) but not of further pathways. A putative D-pathway analog connecting the cytoplasm and the membrane cavity would contain serious barriers (fig. S3). The observed K pathway extends by way of Ser^{240}-OG, Tyr^{223}-OH, His^{243}-NE2, Tyr^{317}-OH, and Thr^{215}-OG1 to the cross-linked Tyr^{251}-OH that is ~4 Å away from the O_2 binding site (Fig. 3B) and substantiates some predictions of recent modeling and mutagenesis studies on cbb_3 oxidases (*16*, *17*, *31*). The polar side chains are either directly hydrogen-bonded to each other or bridged by (modeled) water molecules that are not experimentally detectable at the current structural resolution. An uninterrupted chain of hydrogen donors/acceptors requires that the His^{243} imidazole side chain rotates in order to transfer a proton from Tyr^{223}-OH to a postulated water molecule linked to Tyr^{317}-OH (Fig. 3B). The importance of His^{243} has been experimentally shown for *Rhodobacter capsulatus* cbb_3 oxidase (*32*). However, in contrast to other residues of the chain, His^{243} is not conserved in the cbb_3 oxidases, but when absent it is replaced by smaller residues like alanine or serine that provide space for a water molecule. None of the residues lining this K pathway is present in family-A HCOs. In contrast, Tyr^{223} is conserved and Tyr^{317} has a structural equivalent in family-B HCOs.

Despite the described differences, the known HCO structures reveal a relatively conserved O_2 binding mode, suggesting a similar catalytic mechanism for O_2 reduction. In contrast, the structural basis for the electron and proton transfer processes differs substantially between family A+B and family-C HCO members. Global differences exist at the periplasmic membrane side adjacent to the interface of subunits N and O where the electron and proton routes and the O_2 reduction site coincide (Fig. 3A) and where the coupling between the redox reaction and the selective transfer of consumed and pumped protons to different proton acceptors occurs (*1*, *3*). Three structural features in the interface region most likely play a crucial role in defining the proton pumping in family-C HCOs. First, the K pathway below heme b_3 is slightly enlarged because of the different origin of the histidine-cross-linked tyrosine and the absence of the hydroxyethylfarnesyl substituent, which alters proton access to the O_2 binding site. The small void generated is lined by Thr^{215}, Tyr^{251}, Ser^{283}, Tyr^{317}, and Thr^{321} and presumably occupied by a few water molecules. Assuming only one proton pathway present in cbb_3 oxidase, conformational and/or pK_a (negative logarithm of the acid dissociation constant) shifts during catalysis might allow proton transfer toward the periplasmic side of the heme groups along the O_2 binding site or alternatively via Thr^{321}, Ser^{320}, and Glu^{323} to the periplasm (Fig. 3B). Second, a Ca^{2+} complex clamps together hemes *b* and b_3 with loops N and O. The presence of the Ca^{2+} ion makes it less likely that the heme b_3 propionate A and the heme *b* propionate D are involved in proton transfer. Third, loop N, which in families A and B is found in a conformation markedly different from family C, is strictly conserved in C-family HCOs (Fig. 3A). It protrudes from the periphery of the transmembrane region to the interior and is also involved in heme *b* binding via Tyr^{123}. The Ca^{2+} complex and loops N and O also participate in forming and separating the periplasmic and membrane cavities that are connected to the catalytic site and likely have essential functions as H_2O, proton, and O_2 pathways. In addition, the cavities might be used as proton pathways from the periplasm to the catalytic site required for NO reduction in cbb_3 oxidases, and most likely also in NO reductases (*33*), because crucial residues in this region such as Glu^{122} and Glu^{125} are conserved in both enzymes (Fig. 3A).

Despite the development of distinct structural solutions in the three HCO families to cope with complex mechanistic challenges, the underlying basic principles might be universal. Thus, cbb_3 oxidases also must install a gating event, as proton pumping found for O_2 but not for NO reduction implies that oxygen intermediates must

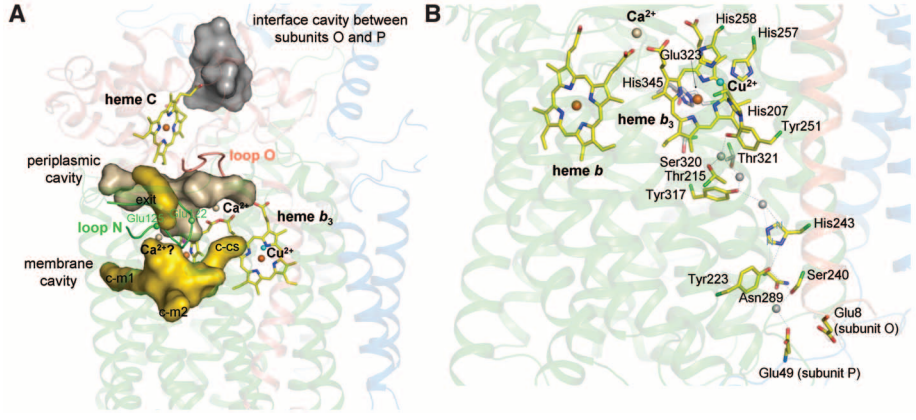

Fig. 3. Cavities and proton pathways. (**A**) Cavities. The periplasmic cavity (wheat) is lined by several residues like Glu^{122}, Tyr^{123}, Glu^{125}, Pro^{57}, and Arg^{58} conserved in C-family HCOs. The border of the water-filled cavity does not offer an attractive exit for water; however, a gap between Gly^{116} and Thr^{118} of subunit N and Ile^{61} and Arg^{62} of subunit O might be just sufficiently wide. The membrane cavity (gold) lies below loop N and is connected to the catalytic site by channel c-cs and to the membrane by channels c-m1 and c-m2. (**B**) Architecture of the K pathway. The sole clearly detectable proton pathway extends from Glu^{49} of subunit P (which is reminiscent of a glutamate from subunit II at the entrance of family-A HCOs) to Tyr^{251} over a distance of 25 Å. Water molecules were modeled if sufficient space was available and at least one polar contact to the polypeptide existed. The mutations Tyr^{223}Phe, Tyr^{317}Phe, Thr^{215}Val, Asn^{289}Asp, and His^{243}Val in *R. sphaeroides*, *R. capsulatus*, or *Vibrio cholerae* significantly reduced the catalytic activity (*16*, *31*, *32*), corroborating its participation in proton transfer. A Ser^{240}Ala mutation had no effect. Asn^{289} is hydrogen-bonded to Ser^{240} but is not considered to be a component of the K pathway. The positions of the nitrogen atoms after the postulated rotation of the His^{243} imidazole ring are marked with an N. The carbon atoms of residues Thr^{321}, Ser^{320}, Glu^{323}, and His^{345} are shown in gray.

Downloaded from www.sciencemag.org on July 15, 2010

abstract protons faster from the cytoplasmic than from the periplasmic side. The rate of proton abstraction must be reversed for NO intermediates, perhaps because a high pK_a value prohibits protonation from a donor loaded from the cytoplasm (*33*, *34*). How these intricate processes are spatially and temporally coordinated on an atomic scale remains open. The structure will, however, facilitate focused site-directed mutagenesis and functional experiments that will contribute to a better understanding of the fundamental HCO reaction and of redox-driven proton translocation processes in general.

References and Notes

1. J. P. Hosler, S. Ferguson-Miller, D. A. Mills, *Annu. Rev. Biochem.* **75**, 165 (2006).
2. O. M. Richter, B. Ludwig, *Biochim. Biophys. Acta* **1787**, 626 (2009).
3. M. Wikström, M. I. Verkhovsky, *Biochim. Biophys. Acta* **1767**, 1200 (2007).
4. M. M. Pereira, F. L. Sousa, A. F. Veríssimo, M. Teixeira, *Biochim. Biophys. Acta* **1777**, 929 (2008).
5. S. Iwata, C. Ostermeier, B. Ludwig, H. Michel, *Nature* **376**, 660 (1995).
6. H. Y. Chang, J. Hemp, Y. Chen, J. A. Fee, R. B. Gennis, *Proc. Natl. Acad. Sci. U.S.A.* **106**, 16169 (2009).
7. R. S. Pitcher, N. J. Watmough, *Biochim. Biophys. Acta* **1655**, 388 (2004).
8. E. Arslan, A. Kannt, L. Thöny-Meyer, H. Hennecke, *FEBS Lett.* **470**, 7 (2000).
9. O. Preisig, R. Zufferey, L. Thöny-Meyer, C. A. Appleby, H. Hennecke, *J. Bacteriol.* **178**, 1532 (1996).
10. R. A. Weingarten, J. L. Grimes, J. W. Olson, *Appl. Environ. Microbiol.* **74**, 1367 (2008).
11. E. Forte *et al.*, *Eur. J. Biochem.* **268**, 6486 (2001).
12. R. S. Pitcher, M. R. Cheesman, N. J. Watmough, *J. Biol. Chem.* **277**, 31474 (2002).
13. A. Urbani, S. Gemeinhardt, A. Warne, M. Saraste, *FEBS Lett.* **508**, 29 (2001).
14. A. L. Ducluzeau, S. Ouchane, W. Nitschke, *Mol. Biol. Evol.* **25**, 1158 (2008).
15. A. Peters, C. Kulajta, G. Pawlik, F. Daldal, H. G. Koch, *J. Bacteriol.* **190**, 5576 (2008).
16. V. Sharma, A. Puustinen, M. Wikström, L. Laakkonen, *Biochemistry* **45**, 5754 (2006).
17. V. Sharma, M. Wikström, L. Laakkonen, *Biochemistry* **47**, 4221 (2008).
18. C. Ostermeier, A. Harrenga, U. Ermler, H. Michel, *Proc. Natl. Acad. Sci. U.S.A.* **94**, 10547 (1997).
19. J. Koepke *et al.*, *Biochim. Biophys. Acta* **1787**, 635 (2009).
20. L. Qin, C. Hiser, A. Mulichak, R. M. Garavito, S. Ferguson-Miller, *Proc. Natl. Acad. Sci. U.S.A.* **103**, 16117 (2006).
21. M. Svensson-Ek *et al.*, *J. Mol. Biol.* **321**, 329 (2002).
22. T. Tsukihara *et al.*, *Science* **272**, 1136 (1996).
23. J. Abramson *et al.*, *Nat. Struct. Biol.* **7**, 910 (2000).
24. T. Soulimane *et al.*, *EMBO J.* **19**, 1766 (2000).
25. V. Rauhamäki, D. A. Bloch, M. I. Verkhovsky, M. Wikström, *J. Biol. Chem.* **284**, 11301 (2009).
26. V. Rauhamäki, M. Baumann, R. Soliymani, A. Puustinen, M. Wikström, *Proc. Natl. Acad. Sci. U.S.A.* **103**, 16135 (2006).
27. J. Hemp *et al.*, *Biochemistry* **45**, 15405 (2006).
28. W. G. Zumft, *J. Inorg. Biochem.* **99**, 194 (2005).
29. C. C. Moser, C. C. Page, P. L. Dutton, *Philos. Trans. R. Soc. London B Biol. Sci.* **361**, 1295 (2006).
30. M. I. Verkhovsky, J. E. Morgan, A. Puustinen, M. Wikström, *Nature* **380**, 268 (1996).
31. J. Hemp *et al.*, *Biochemistry* **46**, 9963 (2007).
32. M. Oztürk, S. Mandaci, *Mol. Biol. Rep.* **34**, 165 (2007).
33. J. Reimann, U. Flock, H. Lepp, A. Honigmann, P. Adelroth, *Biochim. Biophys. Acta* **1767**, 362 (2007).
34. Y. Huang, J. Reimann, H. Lepp, N. Drici, P. Adelroth, *Proc. Natl. Acad. Sci. U.S.A.* **105**, 20257 (2008).

35. This work was supported by the Max Planck Society, the Deutsche Forschungsgemeinschaft (SFB 472), and the Cluster of Excellence Macromolecular Complexes Frankfurt. We thank the staffs of the Swiss Light Source and the European Synchrotron Radiation Facility for assistance. Coordinates and structure factors of cbb_3 oxidase of *P. stutzeri* have been deposited under the pdb accession code 3MK7, the nucleotide sequences under gene bank accession number HM130676.

Supporting Online Material

www.sciencemag.org/cgi/content/full/science.1187303/DC1
Materials and Methods
SOM Text
Figs. S1 to S3
Table S1
References

20 January 2010; accepted 4 June 2010
Published online 24 June 2010;
10.1126/science.1187303
Include this information when citing this paper.

Asymmetric Density Dependence Shapes Species Abundances in a Tropical Tree Community

Liza S. Comita,[1,2]* Helene C. Muller-Landau,[2,3] Salomón Aguilar,[3] Stephen P. Hubbell[3,4]

The factors determining species commonness and rarity are poorly understood, particularly in highly diverse communities. Theory predicts that interactions with neighbors of the same (conspecific) and other (heterospecific) species can influence a species' relative abundance, but empirical tests are lacking. By using a hierarchical model of survival for more than 30,000 seedlings of 180 tropical tree species on Barro Colorado Island, Panama, we tested whether species' sensitivity to neighboring individuals relates to their relative abundance in the community. We found wide variation among species in the effect of conspecific, but not heterospecific, neighbors on survival, and we found a significant relationship between the strength of conspecific neighbor effects and species abundance. Specifically, rare species suffered more from the presence of conspecific neighbors than common species did, suggesting that conspecific density dependence shapes species abundances in diverse communities.

An understanding of the causes of commonness and rarity in ecological communities is essential for determining how communities are structured and for designing effective strategies for biodiversity conservation (*1*–*3*). However, such understanding has eluded scientists (*3*–*5*), particularly in highly diverse communities such as tropical forests (*6*), where hundreds of species coexist with abundances that vary by several orders of magnitude. In these communities, individuals that are surrounded by neighbors of the same species (that is, conspecifics) often exhibit lower growth and survival (*7*–*11*). This phenomenon is attributed to shared natural enemies or strong intraspecific competition for resources (*12*, *13*). Many studies have emphasized the importance of such negative density dependence (NDD) for species coexistence (*14*–*17*), yet little attention has been paid to variation among species in the strength of NDD experienced and the possible consequences of that variation for determining species abundances (*11*).

The strength of NDD that is experienced by a species, defined here as the degree to which an individual's probability of survival is reduced by the addition of a conspecific neighbor, could, in theory, be positively or negatively related, or unrelated, to species abundance in natural communities. First, rare species may be rare because they suffer more when local densities are high (*11*), resulting in a positive relationship between the effect of conspecific neighbors and species abundance in the community (that is, more-common species are less negatively affected by conspecifics). Alternatively, rare species may occur at densities that are too low to sustain viable populations of specialist enemies (*18*) and thus may be less affected by density dependence than more-common species are (*19*). Another possibility is that the strength of NDD varies among species but shows no relationship to species abundance in the community. Species abundance is influenced by a number of factors, including habitat affinity (*2*), regeneration requirements (*20*), and resource use (*21*), which could override the effect of NDD on abundance. Landscape-scale processes, such as predator satiation and long-distance seed dispersal (*22*, *23*), may further decouple the relationship between species abundance and NDD, which typically acts over smaller spatial scales [<30 m (*11*)].

To evaluate these competing hypotheses, we used a hierarchical Bayesian approach (*24*)

[1]National Center for Ecological Analysis and Synthesis, 735 State Street, Suite 300, Santa Barbara, CA 93101, USA. [2]Department of Ecology, Evolution, and Behavior, University of Minnesota, Saint Paul, MN 55108, USA. [3]Smithsonian Tropical Research Institute, Post Office Box 0843-03092, Balboa Ancón, Republic of Panamá. [4]Department of Ecology and Evolutionary Biology, University of California, Los Angeles, CA 90024, USA.

*To whom correspondence should be addressed. E-mail: comita@nceas.ucsb.edu

Downloaded from www.sciencemag.org on July 15, 2010

to analyze recently collected data from 20,000 1-m^2 seedling plots in the lowland tropical forest of Barro Colorado Island (BCI), Panama. We specifically evaluated how survival was influenced by the density and identity of neighboring seedlings and trees. A key challenge in quantifying interspecific variation within diverse plant communities is that many species occur at extremely low densities, making it infeasible to collect sufficient data for meaningful statistical analyses at the species level for most species (*25*). Previous studies of density dependence have dealt with this by limiting analyses to the most abundant species in the community [for example (*15*, *16*)] or lumping species into broad functional groups [for example, (*8*)] or abundance classes [for example, (*11*)]. In contrast, our hierarchical (that is, mixed model) approach allows us to quantify the distribution of density-dependent effects and their relationship to abundance across the entire community, including rarer species, while properly accounting for differences in sample size, and thus confidence (*25*), among the 180 tree species encountered. We used a two-level hierarchical model in which individual survival is a species-specific function of the density of conspecific and heterospecific neighbors, and species-level parameters are functions of species abundance in the community (*26*). We also included shade tolerance as a species-level covariate in the model, because shade tolerance may influence both species abundance and the strength of NDD in tropical tree communities (*27*, *28*). In this way, we not only quantified the strength and variation of NDD for the community but also tested whether variation in the effect of neighbors among species is related to differences in relative abundance or life-history strategy (specifically, shade tolerance).

We found significant variation in the strength of NDD among tree species in the BCI forest (Fig. 1). At the community level, both conspecific seedling and conspecific adult neighbors had a significant negative effect on the probability of seedling survival (Table 1). The strength of conspecific neighbor effects varied widely among species but was overwhelmingly negative (Fig. 1, A and B, and table S2). In contrast, effects of heterospecific seedling and adult neighbors were close to zero, with community-level means weakly positive (Fig. 1, C and D, and table S2). Compared with the variation in conspecific neighbor effects, heterospecific neighbor effects varied little among species (Fig. 1). Thus, our results suggest a limited role for heterospecific density in driving patterns of seedling survival, although heterospecific neighbors may have stronger effects at later life stages.

A significant portion of the variation among species in conspecific neighbor effects was explained by species abundance in the community. The effect of conspecific neighbors on survival was significantly and positively related to species abundance, with less-common species experiencing stronger NDD (Table 1 and Fig. 2). This relationship was found for both seedling and adult neighbors, with stronger statistical support at the seedling stage (Table 1). In principle, these relationships might be driven by shade tolerance, because light-demanding species are expected to be both rarer and more vulnerable to natural enemy attack than shade-tolerant species are (*29*). However, we found that species shade tolerance explained little of the variation in the strength of conspecific neighbor effects (Table 1). Conversely, effects of heterospecific neighbors were not related to species abundance in the community but were related to shade tolerance (Table 1), which is consistent with the fact that light-demanding species are more sensitive to shading by neighbors. Thus, our results indicate that species interactions with conspecific, but not heterospecific, neighbors influence species relative abundance, and this relationship is not explained by variation in species shade tolerance.

In the BCI tree community, species abundances range over more than four orders of magnitude (table S1). Our results indicate that this variation can be explained, in part, by variation in the strength of NDD experienced by species. These results suggest that local-scale density dependence constrains a species' abundance in a community and that these constraints vary among species. In our system, the most common species are those whose seedling survival is minimally affected by the local density of conspecific neighbors. In contrast, species having a strong impact on themselves typically occur at lower abundances.

Negative conspecific effects have been linked to abundance in a previous study of native and invasive species in a temperate old field (a post-agriculture successional community) (*30*), in which abundance was negatively related to the rate and degree to which species accumulated host-specific pathogens in the soil. Our results indicate that the extent to which species inhibit their own regeneration shapes species abundances not only during succession and invasion, but also in intact systems. In addition, given that previous studies of NDD have typically focused on the most common

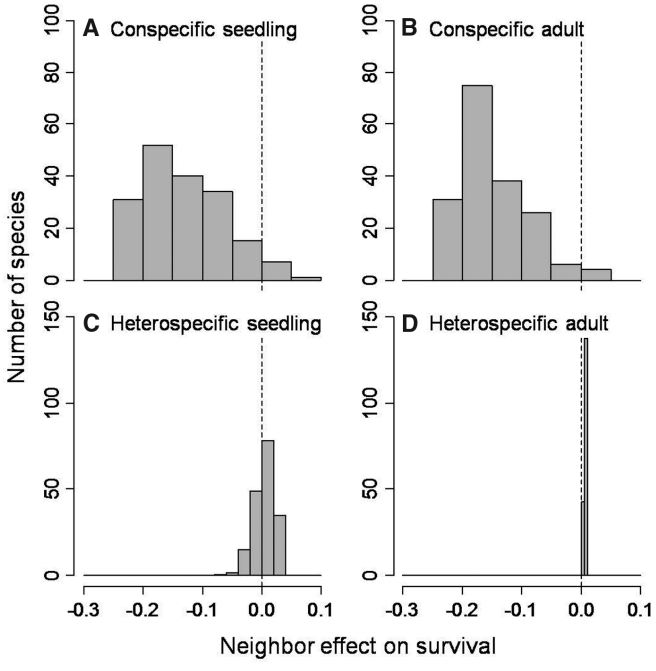

Fig. 1. (**A** to **D**) Distribution of effects of conspecific and heterospecific neighbors on seedling survival. Histogram bars are based on posterior means of coefficients for 180 tree species in central Panama. Bars to the left of the dashed zero line indicate species whose survival is reduced by increasing density of neighbors. The same scale is used for the *x* axis in all panels to facilitate comparisons.

Table 1. Coefficient means (±1 SD) from the hierarchical Bayesian model of seedling survival. Survival was modeled as a function of the density of neighboring conspecific (CON) and heterospecific (HET) seedlings (S) and adult tree basal area (BA). The probability of survival (p) for a seedling of species j in plot k was modeled as $\text{logit}(p_{jk}) = \beta_{0j} + \beta_{1j} \times \text{CONS}_{jk} + \beta_{2j} \times \text{HETS}_{jk} + \beta_{3j} \times \text{CONBA}_{jk} + \beta_{4j} \times \text{HETBA}_{jk} + \phi_k$, where ϕ_k is a random effect for seedling plot. Values for each parameter (β_m) varied among species, and were modeled as functions of size-weighted species abundance (ABUND) and shade tolerance (SHADE), where $\beta_{mj} = \gamma_{m0} + \gamma_{m1} \times \text{ABUND}_j + \gamma_{m2} \times \text{SHADE}_j$. Means were calculated from posterior distributions. Bold values are significantly different from zero (based on 95% credible intervals). Species information and species-specific estimates are presented in tables S1 and S2.

Survival model parameters	Intercept (γ_0)	Species-level predictors	
		Abundance (γ_1)	Shade tolerance (γ_2)
Intercept (β_0)	**–1.464 (0.285)**	0.120 (0.146)	**0.598 (0.141)**
Conspecific seedling effect (β_1)	**–0.133 (0.036)**	**0.045 (0.019)**	–0.029 (0.016)
Heterospecific seedling effect (β_2)	0.005 (0.006)	–0.004 (0.003)	**0.013 (0.005)**
Conspecific adult effect (β_3)	**–0.150 (0.037)**	0.032 (0.019)	0.008 (0.023)
Heterospecific adult effect (β_4)	**0.006 (0.001)**	–0.001 (0.001)	0.001 (0.001)

Downloaded from www.sciencemag.org on July 15, 2010

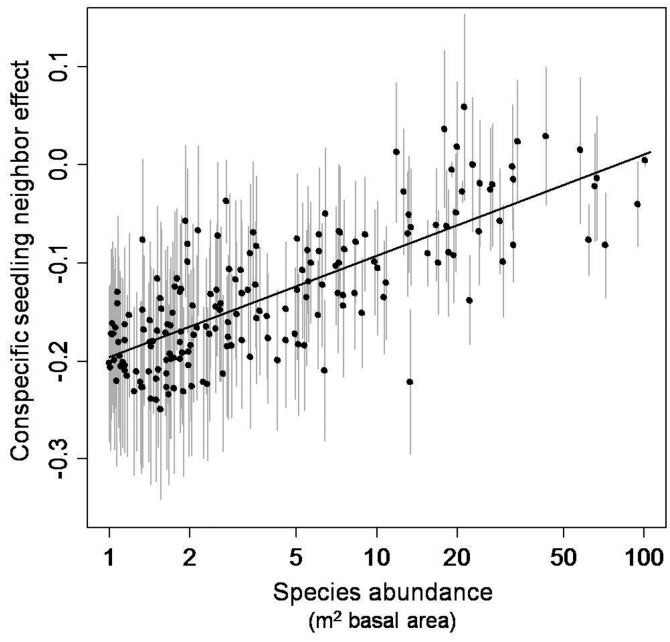

Fig. 2. The mean strength of conspecific NDD exhibited by individual tree species on BCI (points; vertical gray lines show ±1 SD) is significantly related to size-weighted species abundances in the 50-ha Forest Dynamics Plot. The overall relationship fitted by the hierarchical Bayesian model is strongly positive (black line), indicating that rare species experience stronger density dependence than common species do.

species in the community, which we show exhibit the least NDD, our results indicate that past studies probably underestimated both the variation and the mean strength of density dependence in plant communities.

The mechanisms underlying the observed NDD are an important area for future investigation. In tropical forests, negative effects of conspecific neighbors are commonly thought to result primarily from density-dependent, host-specific natural enemies (*12*, *13*), with several studies suggesting that soil pathogens play a key role at the seedling stage (*23*). Recent field and growing-house experiments on a subset of the species analyzed here found that soil pathogens were key drivers of density dependence, with a significant relationship between species sensitivity to negative plant-soil feedbacks and species abundance in the forest (*31*), which is consistent with the results presented here. Strong intraspecific competition for shared resources could, in theory, also contribute to density dependence, but probably plays a small role in explaining the patterns we found, because competition between seedlings has been shown to be weak or nonexistent in tropical forests (*32*). Within communities, differences among species in vulnerability to natural enemies could relate in part to the degree to which species are well adapted to the local environment; that is, species at the edge of their habitat tolerances may be more vulnerable to or less able to recover from attack. Regardless of the specific mechanisms operating, the clear negative effect of conspecific neighbor densities across the community emphasizes the importance of local-scale interactions in driving spatial patterns of survival and shaping species abundances in tropical forests.

The significant variation in NDD among species reported here and its relationship to abundance suggest that theoretical models of plant communities should incorporate this asymmetry. Current models that include NDD almost invariably assume that it is identical in strength across all species (*33*). One such model, the symmetric density-dependent neutral model (*34*), nonetheless succeeds in providing a good fit to the species-abundance curve for the BCI tree community and other tropical forests, but recent studies show that fits to species abundance distributions are not strong tests of theoretical models, because models with different underlying mechanisms can provide equally good fits (*21*, *35*). That we found the strength of NDD to be related to species abundance confirms that the variation in NDD is not only statistically significant but also biologically meaningful. This underscores the need to incorporate species asymmetry into future theoretical efforts (*33*). Understanding of the processes structuring diverse communities may be better advanced by shifting focus away from the shape of the species-abundance curve to assessing what determines the position of species on the curve (*35*).

Our results also have important implications for biodiversity conservation. Understanding the drivers of species abundance is critical for identifying and protecting rare species that have an inherently higher risk of extinction (*2*). Previous efforts to identify key traits that correlate with species rarity have had limited success (*3*, *5*). The results here suggest that such studies should look beyond morphological and physiological traits to include species sensitivity to biotic interactions, namely, the degree to which species inhibit their own regeneration.

References and Notes

1. K. J. Gaston, *Rarity* (Chapman & Hall, London, 1994).
2. S. P. Hubbell, R. B. Foster, in *Conservation Biology: The Science of Scarcity and Diversity*, M. Soule, Ed. (Sinauer, Sunderland, MA, 1986), pp. 205–231.
3. B. J. McGill, *Science* **314**, 770 (2006).
4. R. May, A. Frs, *Philos. Trans. R. Soc. London Ser. B* **354**, 1951 (1999).
5. W. E. Kunin, K. J. Gaston, Eds., *The Biology of Rarity: Causes and Consequences of Rare-Common Differences* (Chapman & Hall, London, 1997).
6. N. C. A. Pitman *et al.*, *Ecology* **82**, 2101 (2001).
7. C. Wills, R. Condit, R. B. Foster, S. P. Hubbell, *Proc. Natl. Acad. Sci. U.S.A.* **94**, 1252 (1997).
8. L. S. Comita, S. P. Hubbell, *Ecology* **90**, 328 (2009).
9. S. A. Queenborough, D. F. R. P. Burslem, N. C. Garwood, R. Valencia, *Ecology* **88**, 2248 (2007).
10. M. Uriarte, C. D. Canham, J. Thompson, J. K. Zimmerman, *Ecol. Monogr.* **74**, 591 (2004).
11. S. P. Hubbell, J. A. Ahumada, R. Condit, R. B. Foster, *Ecol. Res.* **16**, 859 (2001).
12. D. H. Janzen, *Am. Nat.* **104**, 501 (1970).
13. J. H. Connell, in *Dynamics of Populations*, P. J. den Boer, G. R. Gradwell, Eds. (Centre for Agricultural Publishing and Documentation, Wageningen, Netherlands, 1971), pp. 298–312.
14. J. H. Connell, J. G. Tracey, L. J. Webb, *Ecol. Monogr.* **54**, 141 (1984).
15. C. O. Webb, D. R. Peart, *Ecology* **80**, 2006 (1999).
16. K. E. Harms, S. J. Wright, O. Calderón, A. Hernández, E. A. Herre, *Nature* **404**, 493 (2000).
17. C. Wills *et al.*, *Science* **311**, 527 (2006).
18. V. Novotny *et al.*, *Science* **315**, 1666c (2007).
19. This differs from the pattern of common species having lower survival rates on average simply because individuals are more likely to be surrounded by conspecifics [that is, a community-level compensatory trend (*14*)], not because they suffer stronger density dependence.
20. P. J. Grubb, *Biol. Rev. Camb. Philos. Soc.* **52**, 107 (1977).
21. W. Stanley Harpole, D. Tilman, *Ecol. Lett.* **9**, 15 (2006).
22. E. W. Schupp, *Am. Nat.* **140**, 526 (1992).
23. R. P. Freckleton, O. T. Lewis, *Proc. R. Soc. London Ser. B* **273**, 2909 (2006).
24. A. Gelman, J. Hill, *Data Analysis Using Regression and Multilevel/Hierarchical Models* (Cambridge Univ. Press, Cambridge, 2006).
25. R. Condit *et al.*, *Science* **313**, 98 (2006).
26. Materials and methods are available as supporting material on *Science* Online.
27. S. McCarthy-Neumann, R. K. Kobe, *Ecology* **89**, 1883 (2008).
28. P. D. Coley, J. A. Barone, *Annu. Rev. Ecol. Syst.* **27**, 305 (1996).
29. In tropical forests, light-demanding species, which require large canopy gaps for recruitment, may be less common than shade-tolerant species are because of their reliance on these rare and ephemeral high-resource environments (*1*). Light-demanding species also typically allocate more resources to growth than to defense (*28*), and as a result may suffer more from density-dependent natural enemy attack (*27*).
30. J. N. Klironomos, *Nature* **417**, 67 (2002).
31. S. A. Mangan *et al.*, *Nature* (2010).
32. C. E. T. Paine, K. E. Harms, S. A. Schnitzer, W. P. Carson, *Biotropica* **40**, 432 (2008).
33. D. Alonso, A. Ostling, R. S. Etienne, *Ecol. Lett.* **11**, 93 (2008).
34. I. Volkov, J. R. Banavar, F. L. He, S. P. Hubbell, A. Maritan, *Nature* **438**, 658 (2005).
35. B. J. McGill *et al.*, *Ecol. Lett.* **10**, 995 (2007).

36. We thank the dozens of field assistants who conducted the seedling and tree censuses; R. Perez for assistance with species identifications; S. Lao for help with data management; and S. Banerjee, S. M. Lee, M. Schofield, and A. Gelman for statistical advice. The study was financially supported by a Packard Fellowship for Science and Engineering (to H.C.M.), NSF (grants DEB-0075102, 0425651, 0710211, and 0823728 to S.P.H.), the Andrew W. Mellon Foundation, and the HSBC Climate Partnership, with logistical support from the Center of Tropical Forest Science, Smithsonian Tropical Research Institute, and University of Georgia.

Supporting Online Material

www.sciencemag.org/cgi/content/full/science.1190772/DC1
Materials and Methods
Fig. S1
Tables S1 to S3
References

12 April 2010; accepted 10 June 2010
Published online 24 June 2010;
10.1126/science.1190772
Include this information when citing this paper.

Downloaded from www.sciencemag.org on July 15, 2010

Trophic Structure and Community Stability in an Overfished Ecosystem

Anne C. Utne-Palm,[1]* Anne G. V. Salvanes,[1] Bronwen Currie,[2] Stein Kaartvedt,[3,10] Göran E. Nilsson,[4] Victoria A. Braithwaite,[5,1] Jonathan A. W. Stecyk,[4] Matthias Hundt,[1] Megan van der Bank,[7] Bradley Flynn,[7] Guro K. Sandvik,[4] Thor A. Klevjer,[3] Andrew K. Sweetman,[8] Volker Brüchert,[9] Karin Pittman,[1] Kathleen R. Peard,[6] Ida G. Lunde,[4] Rønnaug A. U. Strandabø,[4] Mark J. Gibbons[7]

Since the collapse of the pelagic fisheries off southwest Africa in the late 1960s, jellyfish biomass has increased and the structure of the Benguelan fish community has shifted, making the bearded goby (*Sufflogobius bibarbatus*) the new predominant prey species. Despite increased predation pressure and a harsh environment, the gobies are thriving. Here we show that physiological adaptations and antipredator and foraging behaviors underpin the success of these fish. In particular, body-tissue isotope signatures reveal that gobies consume jellyfish and sulphidic diatomaceous mud, transferring "dead-end" resources back into the food chain.

The northern Benguela upwelling system on the southwest coast of Africa has historically been one of the world's most productive ocean areas, supporting industrial-scale fisheries (*1*, *2*). However, overexploitation coupled with unfavorable environmental conditions drove the collapse of the sardine fishery in the late 1960s (*3*, *4*). Loss of the filter-feeding sardine (*Sardinops sagax*) changed the structure and function of the ecosystem, and it became dominated by jellyfish, bearded goby *(Sufflogobius bibarbatus)*, horse mackerel (*Trachurus trachurus capensis*), and hake (*Merluccius capensis*) (*5*). The massive increase in jellyfish biomass after the collapse (*2*, *6*) has been regarded as a trophic dead end (*7*). The loss of the sardine has forced many higher trophic animals, including predatory seabirds, mammals, and fish, to switch to feeding almost exclusively on the bearded goby (*3*, *8*, *9*). Thus, the bearded goby has come to play a key role in the food web of northern Benguela [(*8*, *5*) and see also figures 8 and 9 of (*5*)]. Paradoxically, despite increased predation pressure, the goby population thrives, but the reasons for this have remained obscure.

The gobies live in a hypoxic environment. As in other nutrient-rich upwelling areas, high productivity along the inner shelf area has created extensive diatomaceous mud belts, where intense decay processes create hypoxic conditions, with high concentrations of hydrogen sulphide (H_2S) and methane in the sediment surface layers (*10*). Sediments in these hypoxic conditions (<1 μM dissolved oxygen, which corresponds to <0.4% oxygen saturation at 12C°) cover over 8944 km^2 and represent 50% of the shelf area (*11*). 7000 km^2 are sulphidic (*12*) and can be dominated by white mats of large sulphide-oxidizing bacteria (*13*) and chemolithotrophic bacteria (*12*). Diffusion and methane-driven ebullition of H_2S gas from the sediment have been involved in massive killing events of fish and invertebrates (*10*, *14*, *15*). For the Benguela upwelling system, sulphidic water column conditions can be dated back to the early 1900s (*15*, *16*), but their frequency seems to have increased in the past three decades (*17*). One of the unresolved questions is how the inhospitable benthic conditions, ranging from hypoxic to anoxic, link with and affect the pelagic ecosystem, and what role hypoxic-tolerant fish play in the transfer of energy from the biogeochemical cycle in the bottom sediments to the pelagic food web [(*18*), p. 12].

We conducted a cross-shelf survey off Namibia in April 2008 (23°20′S, 14°12′E to 23°40′S, 13°15′E). We combined direct ecosystem observations made with acoustic methods, trawl sampling, and environmental data from the water column and sediments with onboard controlled experiments on the behavior and physiology of *S. bibarbatus* (*19*). We further analyzed diurnal and depth variations in the stomach contents of bearded gobies and used stable isotope analysis on goby muscle and its potential prey species (*19*). This multidisciplinary approach allowed us to determine diel movement and feeding patterns for the bearded goby and its trophic links with other organisms, and to obtain evidence for its behavioral and physiological adaptations.

An acoustic transect across the shelf revealed a layer apparently void of life, extending from the bottom up to 20 to 60 m above the bottom (fig. S1). This empty pocket corresponds with water masses having oxygen levels below 10%. Environmental data showed a gradually decreasing temperature and oxygen level from the surface to the bottom (fig. S2; O_2 is also indicated in Fig. 1,

[1]Department of Biology, University of Bergen, Bergen, Norway. [2]National Marine Information and Research Centre, Swakopmund, Namibia. [3]Department of Biology, University of Oslo, Oslo, Norway. [4]Department of Molecular Biosciences, University of Oslo, Oslo, Norway. [5]School of Forest Resources and Department of Biology, Pennsylvania State University, State College, PA, USA. [6]Ministry of Fisheries and Marine Resources, Lüderitz, Namibia. [7]Department of Biodiversity and Conservation Biology, University of the Western Cape, Bellville, South Africa. [8]Norwegian Institute for Water Research (NIVA), Regional Office Bergen, Bergen, Norway. [9]Department of Sciences, Stockholm University, Stockholm, Sweden. [10]King Abdullah University of Science and Technology, Thuwai, Saudi Arabia.

*To whom correspondence should be addressed. E-mail: anne.palm@bio.uib.no

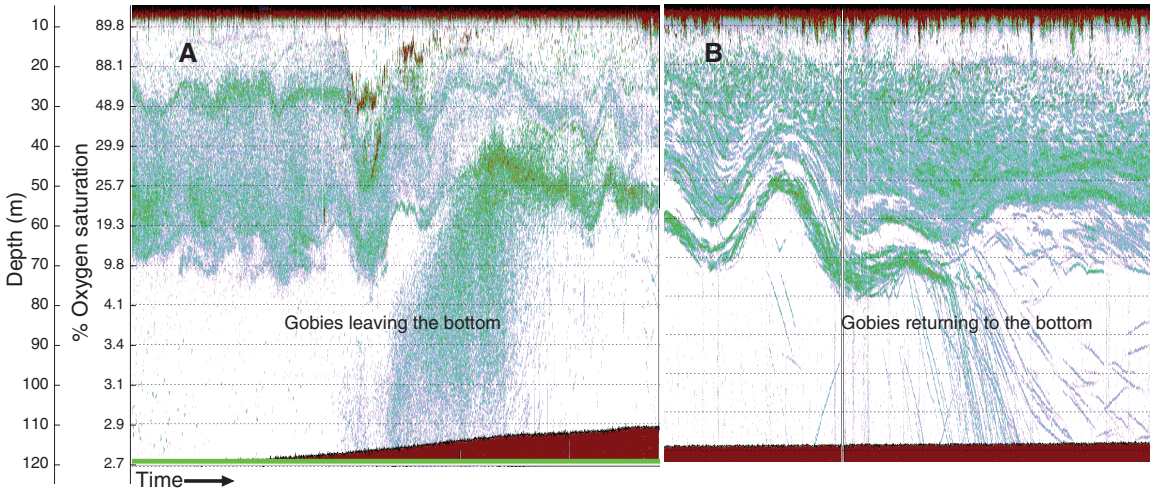

Fig. 1. Acoustic record (at 38 kHz) (**A**) showing gobies ascending from the sediment in the afternoon (time interval on the *x* axis is UTC 16:30 to 18:00 time), joining an acoustic SL of jellyfish, and (**B**) returning to the sediment in the morning (time interval on the *x* axis is UTC 03:50 to 05:20). Sequential near-bottom pelagic trawling produced no catches before the ascent and a monospecific catch of gobies during the ascent. The vessel was stationary during the acoustic observations; therefore, many echoes were returned from each fish, depicted by lines. The average oxygen level is given at 10-m depth intervals. Temperature decreased gradually from 18°C at the surface to 13°C above the bottom.

Downloaded from www.sciencemag.org on July 15, 2010

A and B). The highest densities (average catch, 40 kg/hour) of *S. bibarbatus* occurred over the inner shelf, where the seabed is a thick layer of diatomaceous mud characterized by millimolar concentrations of total sulphide (1 to 2 mmol) in the topmost 3 cm [(*11*) and fig. S3]. Here, oxygen levels were very low (4.7% oxygen saturation), and no other vertebrates were present. Acoustic measurements (Fig. 1, A and B) and trawls, however, confirmed that *S. bibarbatus* were on the seabed during daylight hours, as has previously been shown by video photography [(*20*) and fig. S4].

Acoustic and trawl data showed that gobies ascend from the bottom in the evening to join an existing acoustic scattering layer (SL) in the water column (Fig. 1A) and then return to the bottom in the early morning (Fig. 1B) (*19*). The pelagic SLs were dominated by two species of large jellyfish [*Aequorea forskalea* and *Chrysaora fulgida* (= *hysoscella*)] whose biomass is currently estimated to exceed that of finfish off Namibia (*2*). *S. bibarbatus* are found significantly more often with jellyfish than other fish species are [data from >11,000 samples of pelagic fish landings at Walvis Bay, 1991–2006 (Kruskal-Wallis test, $H = 18.18$, $P = 0.001$, $n = 40$ observations)], and they are six times more often associated with jellyfish in commercial catches than is their predator, the horse mackerel (*T. trachurus capensis*) (Table 1), suggesting that *S. bibarbatus* may choose to associate with jellyfish when in the water column.

Goby and horse mackerel (a goby predator) aversion to jellyfish (*C. fulgida*) was examined by allowing individual fish to swim between two chambers, one with and one without jellyfish during 300-s trials (*19*). Horse mackerel strongly avoided jellyfish and either fled the jellyfish chamber within 18 ± 11 s (mean ± SEM) or never moved across the mesh divider to associate with jellyfish. In contrast, gobies took significantly (two-sided *t* test, $n = 14$ horse mackerel and $n = 13$ gobies, $P < 0.001$; df = 25) longer (210 ± 37 s, mean ± SEM) to leave the jellyfish chamber and frequently moved between the two chambers.

Habitat choice experiments showed that gobies preferred to stay on diatomaceous mud as compared to a sand alternative (*t* test on normalized arc-sine–transformed data: $t = 3.29$; $P = 0.0017$, $n = 30$ individuals) (*19*). We also observed fish burrowing into the hypoxic diatomaceous mud, especially if threatened or disturbed. These observations support the acoustic and trawl data showing that gobies associate with jellyfish but their predators do not, and also that gobies choose to rest on, and hide within, mud during the day.

S. bibarbatus was found to have an extremely low critical oxygen level {$[O_2]_{crit} = 5.3 \pm 0.3\%$ (mean ± SD) of air saturation, which is the lowest $[O_2]$ at which resting oxygen uptake can be maintained, marked with a dotted line in Fig. 2A}, allowing it to sustain aerobic metabolism even in deeper waters below the main SL where oxygen saturation is ~10% (Fig. 1, A and B). Although *S. bibarbatus* built up an oxygen debt during anoxia (Fig. 2C), probably related to lactate oxidation, the rate of lactate accumulation in the blood declined markedly after 1 hour (Fig. 2D), suggesting metabolic depression. Metabolic depression is also indicated by a suppressed ventilation rate at $[O_2]$ below $[O_2]_{crit}$ (Fig. 2B) (*19*).

H_2S is a respiratory poison that blocks cytochrome c (*21*). The rate of oxygen consumption by *S. bibarbatus* was virtually unaffected by 100 to 200 μM total sulphide [corresponding to 6 to 12 μM H_2S (*21*, *22*)], although it became 98% suppressed at a total sulphide level of 500 μM (= 30 μM H_2S) (Fig. 2E). These physiological data for *S. bibarbatus* correspond with known effects on isolated mitochondria (from relatively sulphide-tolerant fish and mammals), in which [H_2S] below 6 μM are found to stimulate oxygen consumption (probably because mitochondria use oxygen to detoxify H_2S to thiosulphate), whereas H_2S levels above 11 to 14 μM inhibit mitochondrial respiration (*21*, *23*). Thus, *S. bibarbatus* possesses a H_2S-sensitive cytochrome c, and its H_2S tolerance probably relies on anoxia tolerance, allowing fish to be temporarily independent of mitochondrial respiration through a sufficiently high capacity for anaerobic (glycolytic) adenosine triphosphate production, combined with metabolic depression. Thus. the anoxia tolerance of the bearded goby is extreme, surpassing that of other marine teleosts surveyed in a recent meta study (*24*), and allows *S. bibarbatus* to survive the very high [H_2S] in the mud where these fish forage and hide (fig. S3).

Hypoxia may impair escape responses, making gobies more vulnerable to predators (*25*). This was not the case. Touching them with a lever mounted through the lid of the sealed aquaria caused an escape response even after 7 to 9 hours of exposure to oxygen levels below their $[O_2]_{crit}$ and a subsequent 4 to 5 hours in complete anoxia ($n = 7$ individuals) (*19*). Thus, anoxic gobies remain alert.

Anoxia tolerance in *S. bibarbatus* and one of its predators, the hake *M. capensis*, was compared by measuring the performance of excised hearts (*19*). These experiments showed that the pumping capacity [heart rate times contraction force (*26*)] of both species' hearts was reduced by ~80% after 20 min of anoxia. After 40 min of subsequent reoxygenation, only goby hearts recovered to pre-anoxic values, suggesting that the hake hearts had sustained permanent damage (Fig. 2F). Thus, hake are unable to tolerate the hypoxic seafloor, thereby providing the gobies with a refuge from these predators.

Comparative analyses of the stable isotope composition of carbon and nitrogen of *S. bibarbatus* muscle, *A. forskalea*, *C. fulgida*, euphausiids (krill), and sediment show that jellyfish contributed a minimum of 17 to 37% and a maximum of 40 to 60% to the diet of *S. bibarbatus* (Fig. 3 and fig. S6), significantly more than did euphausiids and sediment (Kruskal-Wallis test, $H = 65.34$, $P < 0.001$) (*19*). Whether gobies scavenge on moribund jellyfish on the sea floor or feed on them while swimming in the SL at night is uncertain. However, in support of a benthic feeding hypothesis, the low stable sulfur isotope values of gobies as compared to those of zooplankton and jellyfish indicated that the gobies derive part of their diet from the sulphidic benthos (fig. S5 and table S1) (*19*). The isotope results indicated that the gobies may derive 34.2 ± 6.7% ($n = 7$ individuals) of their diet from the sulphidic benthos (fig. S7) and the associated sulfur-containing bacterial mats of *Thiomargarita namibiensis* and *Beggiatoa* spp. present on the benthos (*10*). The benthophagy interpretation is supported by stomach contents analysis showing that gobies feed on benthic polychaetes (fig. S8) (*19*).

At night, *S. bibarbatus* enter pelagic waters. This may be to reoxygenate, as recently shown for sprat (*Sprattus sprattus*) in hypoxic Norwegian fjords (*27*), but it may also be for digestion.

Table 1. Temporal changes in the frequency at which the dominant species of pelagic fish were caught with jellyfish, expressed as monthly variation in total number of catches of each fish species together with jellyfish, divided by the total number of catches of the same species when jellyfish were not present. Data were collected from randomly selected samples of the landings of the pelagic fleet in Walvis Bay, Namibia, for the period 1990–2007. Only months where the total number of samples (*N*) was greater than 100 are shown. Information for juvenile hake (*M. capensis*) was not available, as this species is not a routine part of the pelagic fishery.

Month	Total *N*	*Sardinops sagax*	*Engraulis encrasicolus*	*Trachurus trachurus capensis*	*Etrumeus whitheadi*	*Sufflogobius bibarbatus*
January	1066	18	23	13	22	75
February	1757	17	26	10	19	151
March	1982	19	28	14	20	508
April	1749	18	18	10	14	130
May	2088	38	27	13	35	80
June	1113	49	124	48	103	182
July	1038	73	131	95	147	175
August	318	48	40	44	70	233
Average		35	52	31	54	192

Downloaded from www.sciencemag.org on July 15, 2010

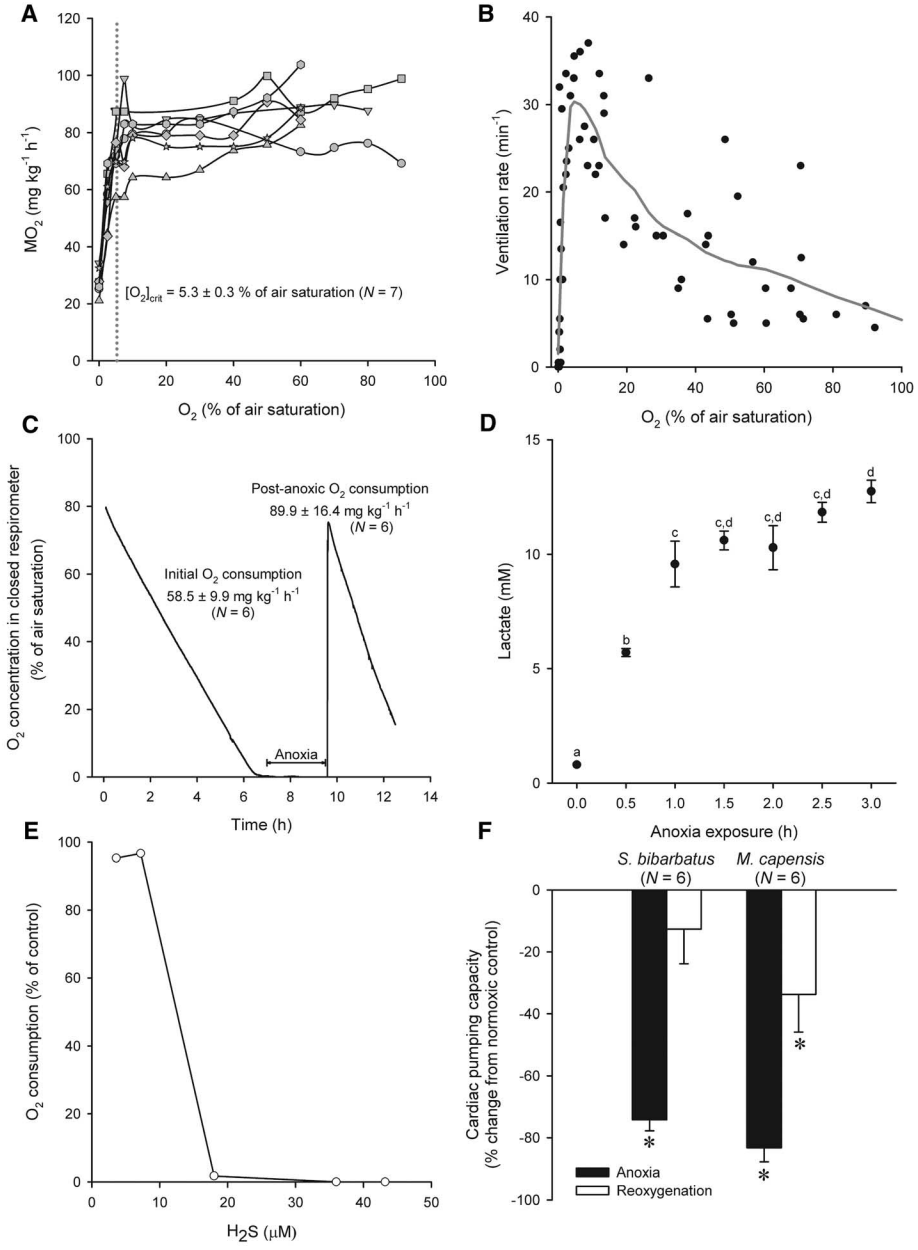

Fig. 2. Physiological studies on *S. bibarbatus* [(A) to (D) and (F)] and *M. capensis* (E) (*19*). (**A**) Gobies maintained a constant oxygen consumption rate until $[O_2]_{crit}$ of 5.3 ± 0.3% (mean ± SD) of air saturation (~0.3 ml of O_2 liter^{-1}) was reached. $[O_2]_{crit}$ is the lowest $[O_2]$ in which the animal is able to maintain its resting rate of O_2 consumption (*35*) (n = 7 individuals). Different symbols represent individual fish. (**B**) Ventilation rate increased in response to falling water $[O_2]$ until $[O_2]_{crit}$, then ceased (the regression line was obtained by locally weighted scatterplot smoothing) (n = 7 individuals). (**C**) Representative trace showing that 3 hours of exposure to anoxia caused an oxygen debt, because post-anoxia oxygen consumption was increased by ~35% (n = 6 individuals). (**D**) Accumulation of blood lactate during 3 hours of anoxia (O_2 < 0.5% air saturation). The rate of increase slowed after 1 hour, indicating metabolic depression. Significant differences (P < 0.05; one-way analysis of variance; Student-Newman-Keuls post-test) between time points are indicated by dissimilar letters. n = 33 fish in total and 3 to 6 fish at each time point. Values are means ± SEM. (**E**) Oxygen consumption of gobies exposed to different sulphide concentrations at a normoxic oxygen level (>50% of air saturation) (n = 5 individuals). (**F**) Isolated, spontaneously contracting heart preparations of *S. bibarbatus* (n = 6 hearts) successfully recovered from 20 min of anoxia, whereas hearts of its predator *M. capensis* (n = 6 hearts) were irreversibly damaged. Asterisks indicate a statistically significant difference (P < 0.05; one-way repeated measures analysis of variance performed on non-normalized data; Student-Newman-Keuls post-tests) from the control normoxic level (0%). Values are means ± SEM.

Gut fullness was significantly higher and stomach contents were less digested in fish ascending from, than in those returning to, the sea floor (fig. S9 and table S2, proportion odds logistic regression, P < 0.001, n = 75 individuals). Delayed digestion due to lack of oxygen is, to our knowledge, a previously unknown phenomenon.

Besides polychaetes, diatoms were the most common item in *S. bibarbatus* stomachs (fig. S8). Because *S. bibarbatus* is not a filter feeder [their branchiospines are merely stumps and too far apart to filter diatoms (fig. S10)], our data suggest that they feed partly on the benthos taken directly from the sulphide-rich diatomaceous mud (figs. S7 and S8), similar to *Gobionellus sagittula* in the Pacific (*28*). Collectively, our results indicate that, owing to digestion suppression in hypoxic situations (*29*), gobies feed on the benthos within hypoxic water during the day, and then move to oxygen-richer pelagic waters at night, when predation pressure is lower, to digest, and possibly feed on live jellies.

The marine ecosystem off Namibia has witnessed a number of profound ecological and environmental changes since the collapse of the commercial pelagic fisheries at the end of the 1960s, including a proliferation of jellyfish (*2*), a change in the fish community structure (*9*), a possible increase in hypoxia and toxic gas eruptions (*17*), and consequently a change in the food web dynamics (*3*). The fact that gobies feed on jellyfish means that the commercially harvested fish species off Namibia are now feeding from a higher trophic level than they were earlier and that here, at least, there is evidence of fishing up the food chain (*30*). We would expect such a shift in trophic relations to result in lower production and harvests at higher trophic levels, as has indeed been witnessed in the northern Benguela system after the late 1960s (*31*).

Climate change will probably increase the inflow of hypoxic waters from the tropics and increase coastal upwelling (*4*), which in an area such as the Benguela could lead to an increase in the frequency of sulphide eruptions and anoxic water masses (*17*), events that are expected to put harvested species and thus local fisheries under severe stress (*32*). Such events will relax the predation pressure on the bearded goby population. Owing to the goby's tolerance of low oxygen and high H_2S levels, and their antipredator and feeding strategies, these fish have the possibility of increasing their biomass. The population may act as a stabilizing production unit of the Benguela and between their predator populations and the ecosystem. An increase in goby biomass produced during severely hypoxic years will probably be a mechanism whereby food can be stored within the system for harvested fish populations that return in years with favorable environmental conditions (*33*).

Organisms able to tolerate such extreme conditions may be successful in many rapidly changed environments (*34*). The bearded goby, with its remarkable suite of behavioral, physiological,

Downloaded from www.sciencemag.org on July 15, 2010

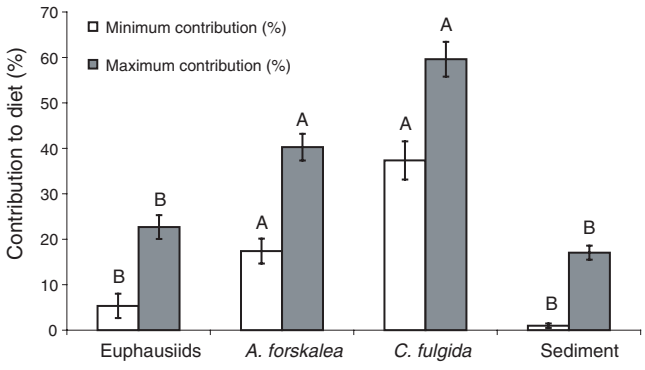

Fig. 3. Isotope analyses showing maximum and minimum contribution of euphausiids, jellyfish, and sediment to the diet of *S. bibarbatus*, as determined by a four-endpoint Isosource model (based on carbon and nitrogen) (*19*). Bars denote mean ± SEM. Bars with identical letters were not significantly different from each other at an α level of 5% (Tukey test, $P < 0.05$; *A. forskalea*, $n = 11$; euphausiids, $n = 6$; *C. fulgida* $n = 25$; mud, $n = 5$ samples; *S. bibarbatus*, $n = 41$).

and ecological adaptations, is already playing a critical role in the ecosystem off Namibia, and it is likely to continue to do so into the future.

References and Notes

1. M. E. Carr, *Deep Sea Res. Part II Top. Stud. Oceanogr.* **49**, 59 (2001).
2. C. P. Lynam *et al.*, *Curr. Biol.* **16**, 1976 (2006).
3. P. Cury, L. Shannon, *Prog. Oceanogr.* **60**, 223 (2004).
4. A. Bakun, *Science* **247**, 198 (1990).
5. C. D. van der Lingen *et al.*, in *Benguela: Predicting a Large Marine Ecosystem. Large Marine Ecosystems 14*, L. V. Shannon, G. Hempel, P. Malanotte-Rizzoli, C. L. Moloney, J. Woods, Eds. (Elsevier, Amsterdam, 2006), pp. 147–184.
6. A. J. Richardson, A. Bakun, G. C. Hays, M. J. Gibbons, *Trends Ecol. Evol.* **24**, 312 (2009).
7. J. Yamamoto *et al.*, *Mar. Biol.* **153**, 311 (2008).
8. R. J. M. Crawford, L. V. Shannon, D. E. Pollock, *Oceanogr. Mar. Biol. Ann. Rev.* **25**, 353 (1987).
9. D. J. Boyer, I. Hampton, *S. Afr. J. Mar. Sci.* **23**, 5 (2001).
10. V. Brüchert, B. Currie, K. R. Peard, *Prog. Oceanogr.* **83**, 169 (2009).
11. V. Brüchert *et al.*, in *Past and Present Water Column Anoxia*, L. N. Neretin, Ed. (Springer, Netherlands, 2006), pp. 161–194.
12. G. Lavik *et al.*, *Nature* **457**, 581 (2009).
13. H. N. Schulz *et al.*, *Science* **284**, 493 (1999).
14. S. J. Weeks, B. Currie, A. Bakun, *Nature* **415**, 493 (2002).
15. S. J. Weeks, B. Currie, A. Bakun, K. R. Peard, *Deep Sea Res. Part I Oceanogr. Res. Pap.* **51**, 153 (2004).
16. J. Rogers, J. M. Bremner, *Oceanogr. Mar. Biol.* **29**, 1 (1991).
17. A. Bakun, S. J. Weeks, *Ecol. Lett.* **7**, 1015 (2004).
18. P. Fréon, M. Barange, J. Arístegui, *Prog. Oceanogr.* **83**, 1 (2009).
19. Materials and methods are available as supporting material on *Science* Online.
20. M. J. Gibbons *et al.*, *S. Afr. J. Mar. Sci.* **22**, 1 (2000).
21. T. Bagarinao, *Aquat. Toxicol.* **24**, 21 (1992).
22. F. J. Millero, T. Plese, M. Fernandez, *Limnol. Oceanogr.* **33**, 269 (1988).
23. T. Bagarinao, R. D. Vetter, *J. Comp. Physiol. B* **160**, 519 (1990).
24. R. Vaquer-Sunyer, C. M. Duarte, *Proc. Natl. Acad. Sci. U.S.A.* **105**, 15452 (2008).
25. P. Domenici, C. Lefrançois, A. Shingles, *Philos. Trans. R. Soc. London Ser. B* **362**, 2105 (2007).
26. N. Matikainen, M. Vornanen, *J. Exp. Biol.* **167**, 203 (1992).
27. S. Kaartvedt, A. Røstad, T. A. Klevjer, *Mar. Ecol. Prog. Ser.* **390**, 237 (2009).
28. E. S. Todd, *Copeia* **2**, 374 (1976).
29. H. Pang, K. N. Bitar, *Am. J. Physiol. Cell Physiol.* **289**, C982 (2005).
30. D. Pauly, V. Christensen, V. J. Dalsgaard, R. Froese, F. Torres Jr., *Science* **279**, 860 (1998).
31. J. J. Heymans, L. J. Shannon, A. Jarre, *Ecol. Model.* **172**, 175 (2004).
32. P. M. S. Monteiro, A. K. van der Plas, J.-L. Melice, P. Florenchie, *Deep Sea Res. Part I Oceanogr. Res. Pap.* **55**, 435 (2008).
33. H. Hamukuaya, M. J. O'Toole, P. M. J. Woodhead, *S. Afr. J. Mar. Sci.* **19**, 57 (1998).
34. R. J. Diaz, R. Rosenberg, *Science* **321**, 926 (2008).
35. C. L. Prosser, F. A. Brown, *Comparative Animal Physiology* (Saunders, Philadelphia, 1961).

36. We thank the crew of the *G. O. Sars*; F. Midtøy for assistance; and P. Ellitson, M. Hordnes, R. Jones, R. Amundsen and the rest of the scientific crew. We thank the National Research Foundation of South Africa, the Research Council of Norway, and our home institutions for funding and support. We thank BENEFIT (Benguela Environment Fisheries Interaction and Training), S. Sundby, D. C. Boyer, J. Otto Krakstad, and the crew of the research vessel *Dr. Fridtjof Nansen* for support with earlier goby cruises, laying the basis for the present study. We thank K. Helge Jensen for statistical support. We appreciate the comments on this manuscript by J. Giske, C. Jørgensen, M. P. Heino, and the anonymous reviewers. Care and handling of experimental animals were performed in accordance with institutional guidelines. J.A.W.S. was a postdoctoral researcher funded by the Natural Sciences and Engineering Reserach Council of Canada at the time when the research was conducted.

Supporting Online Material

www.sciencemag.org/cgi/content/full/329/5989/333/DC1
Materials and Methods
Figs. S1 to S10
Tables S1 and S2
References

9 April 2010; accepted 4 June 2010
10.1126/science.1190708

Small Peptides Switch the Transcriptional Activity of Shavenbaby During *Drosophila* Embryogenesis

T. Kondo,[1,2]*† S. Plaza,[3,4]* J. Zanet,[3,4] E. Benrabah,[3,4] P. Valenti,[3,4] Y. Hashimoto,[1,6]† S. Kobayashi,[1,5] F. Payre,[3,4]‡ Y. Kageyama[1,6]‡

A substantial proportion of eukaryotic transcripts are considered to be noncoding RNAs because they contain only short open reading frames (sORFs). Recent findings suggest, however, that some sORFs encode small bioactive peptides. Here, we show that peptides of 11 to 32 amino acids encoded by the *polished rice* (*pri*) sORF gene control epidermal differentiation in *Drosophila* by modifying the transcription factor Shavenbaby (Svb). Pri peptides trigger the amino-terminal truncation of the Svb protein, which converts Svb from a repressor to an activator. Our results demonstrate that during *Drosophila* embryogenesis, Pri sORF peptides provide a strict temporal control to the transcriptional program of epidermal morphogenesis.

Studies of eukaryotic genomes have revealed that a large proportion of genomic DNA produces atypical long transcripts, the functions of which are controversial (*1*–*4*). These transcripts contain only short open reading frames (sORFs, <100 codons) and thus are generally considered to be non-protein-coding RNAs (ncRNAs). However, there is growing evidence that the sORFs present in some ncRNAs are actually translated into small peptides, the abundance of which is probably greatly underestimated (*5*–*7*). Whereas sORF-encoded peptides may represent an overlooked repertoire of bioactive molecules (*8*), their functions and the mechanisms by which they operate are largely unknown.

We and others recently identified an evolutionarily conserved sORF gene, referred to as *polished rice* (*pri*) or *tarsal-less* (*tal*) in *Drosophila,* and *mille-pattes* (*mlpt*) in *Tribolium* (*9*–*11*). *pri* mRNA is a polycistronic transcript that encodes four similar peptides, 11 to 32 amino acids in length, that play a redundant role in *Drosophila* embryogenesis (*9*, *10*). Embryos that lack *pri* display prominent defects, including the absence of trichomes and aberrant tracheal architecture (*9*, *10*). Reduced *pri* activity in imaginal development results in abnormal leg morphogenesis (*10*, *12*). Similarly, *mlpt* knockdown in *Tribolium* leads to appendage defects and the transformation of segmental identity (*11*).

To gain insight into the molecular function of Pri peptides, we focused on their role in trichome formation during *Drosophila* embryogenesis.

Downloaded from www.sciencemag.org on July 15, 2010

Epidermis differentiation results in a pattern of smooth cells and cells that form apical extensions, called trichomes (ventral denticles and dorsal hairs) (Fig. 1A) (*13*). Modifications of the trichome pattern that have been examined in insects (resulting from laboratory-induced mutations or evolutionary diversification) are so far all attributable to changes in expression of *shavenbaby* (*svb*) (*14*–*16*). Indeed, *svb* encodes a transcription factor that directly regulates the expression of target effectors, which are collectively responsible for trichome formation (*17*, *18*). Although the absence of *pri* results in trichome loss, the expression of *svb* is not altered in *pri* mutants (*9*). Reciprocally, *pri* is expressed normally in *svb* mutants (*9*), showing that *svb* and *pri* act in parallel in trichome formation (fig. S1). Expression of Svb target genes, such as *miniature* and *shavenoid* (*17*), is lost in *pri* mutants, whereas the expression of other epidermal genes is unaffected (Fig. 1B and S2). The activity of isolated Svb-responsive enhancers was also strongly reduced in *pri* mutants (fig. S3). Therefore, *pri* is specifically required for the transcription of Svb downstream targets in trichome cells.

How can Pri peptides regulate the expression of Svb target genes without affecting *svb* expression? The *svb* locus encodes three overlapping protein isoforms: Svb and the germline-specific proteins OvoA and OvoB (Fig. 2A) (*19*, *20*). Ovo/Svb proteins all share the same DNA-recognition and transcriptional-activation domains but differ in their N-termini (Fig. 2A). The shortest isoform, OvoB, is a transcriptional activator and induces trichomes when artificially expressed in the epidermis (Fig. 2F) (*19*). OvoA contains an extended N-terminal region, which switches its function toward active transcriptional repression and thus dominantly inhibits trichome formation (Fig. 2C) (*19*). Svb contains a further N-terminal extension, compared to OvoA, and promotes the formation of ectopic trichomes like OvoB (Fig. 2D) (*20*). To evaluate the specificity of Pri/Svb interaction, we examined the influence of *pri* on the different Ovo/Svb isoforms with respect to trichome formation. In wild-type embryos, seven rows of ventral cells per segment express *svb* and form trichomes (Fig. 2B) (*13*, *15*). Upon its ectopic expression in smooth cells, Svb [or Svb:green fluorescent protein (GFP)] induced supernumerary trichomes in control embryos (Fig. 2D) but not in *pri* mutants (Fig. 2E). In contrast, OvoB (or OvoB:GFP) was insensitive to *pri*, with ectopic trichomes forming in both control and *pri* mutant embryos (Fig. 2, F

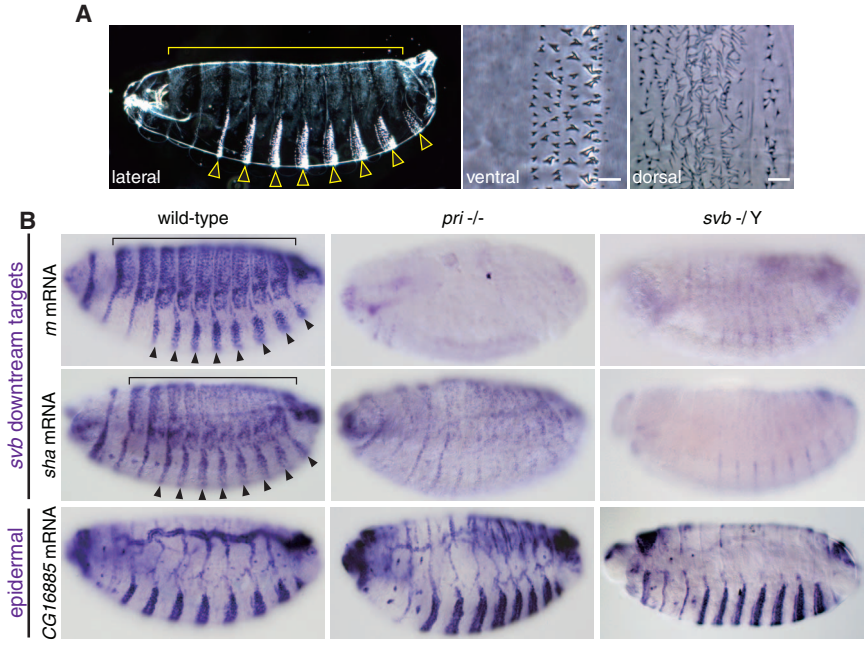

Fig. 1. *pri* is required for the expression of Svb target genes. (**A**) Embryonic cuticle specimens, showing the two types of trichomes, ventral denticles (arrowheads and middle close-up) and dorsal hairs (bracket and right close-up). (**B**) Two Svb downstream targets, *miniature* (*m*) and *shavenoid* (*sha*) are expressed in trichome cells at stages 15 and 16 in wild type, but not in *pri* and *svb* mutants. As a control of *pri* specificity for Svb function, the epidermal expression of *CG16885* (independent of *svb*) was not affected in *pri* mutants. Anterior is to the left and dorsal is to the top, except for the close-ups in (A). Scale bar, 10 μm.

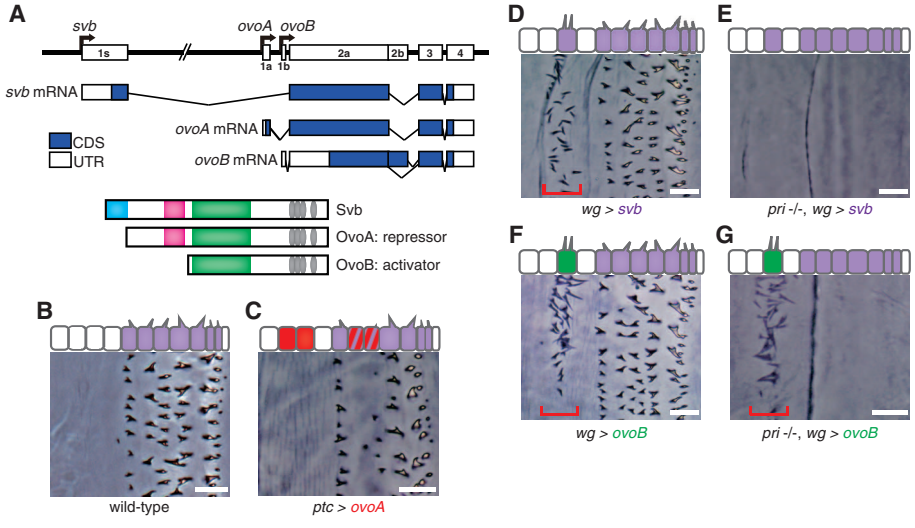

Fig. 2. The ability of Svb to induce trichomes depends on *pri*. (**A**) Scheme of the *ovo/svb* locus and protein isoforms. Coding (CDS) and untranslated regions (UTR) of mRNAs are represented by blue and white boxes, respectively. The Svb-specific protein region is in turquoise; the repression, activation, and DNA-binding domains are in red, green, and gray, respectively. (**B** to **G**) Micrographs of ventral trichomes (A4 segment) and illustrations of epidermal cells expressing *svb* (purple), *ovoA* (red), and *ovoB* (green) in embryos of different backgrounds. *pri* mRNA is widely expressed in epidermis and reinforced in trichome cells (fig. S1F). (B) Wild-type embryo. (C) Embryo expressing *UAS-ovoA:GFP* under the control of *ptc-GAL4*. (D) and (E) Embryos expressing *UAS-svb:GFP* under the control of *wg-Gal4* in the presence (D) or absence (E) of *pri*. (F) and (G) Embryos expressing *UAS-ovoB:GFP* under the control of *wg-Gal4* in the presence (F) or absence (G) of *pri*. Red brackets indicate ectopic trichomes. Scale bar, 10 μm.

[1]Okazaki Institute for Integrative Bioscience, National Institute for Basic Biology (NIBB), National Institutes of Natural Sciences, 5-1 Myodaiji-Higashiyama, Okazaki 444-8787, Japan. [2]Graduate School of Biological Sciences, Nara Institute of Science and Technology, 8916-5 Takayama, Ikoma, Nara 630-0192, Japan. [3]Université de Toulouse, Université Paul Sabatier, Centre de Biologie du Développement, Bâtiment 4R3, 118 route de Narbonne, F-31062 Toulouse, France. [4]CNRS, UMR 5547, Centre de Biologie du Développement (CBD), F-31062 Toulouse, France. [5]Department of Basic Biology, School of Life Science, Graduate University for Advanced Studies (SOKENDAI), 38 Myodaiji-Nishigonaka, Okazaki 444-8585, Japan. [6]Precursory Research for Embryonic Science and Technology (PRESTO), Japan Science and Technology Agency (JST), 4-1-8 Honcho, Kawaguchi, Saitama 332-0012, Japan.

*These authors contributed equally to this work.
†Present address: RIKEN Center for Developmental Biology, 2-2-3 Minatojima-Minamimachi, Chuo-ku, Kobe 650-0047, Japan.
‡To whom correspondence should be addressed. E-mail: payre@cict.fr (F.P.); kageyama@nibb.ac.jp (Y.K.)

Downloaded from www.sciencemag.org on July 15, 2010

and G). In the latter case, we observed only OvoB-induced ectopic trichomes and no Svb-dependent endogenous trichomes (Fig. 2G). These results show that whereas *pri* has no effect on the shorter OvoB isoform, *pri* peptides specifically control the ability of Svb to induce trichomes.

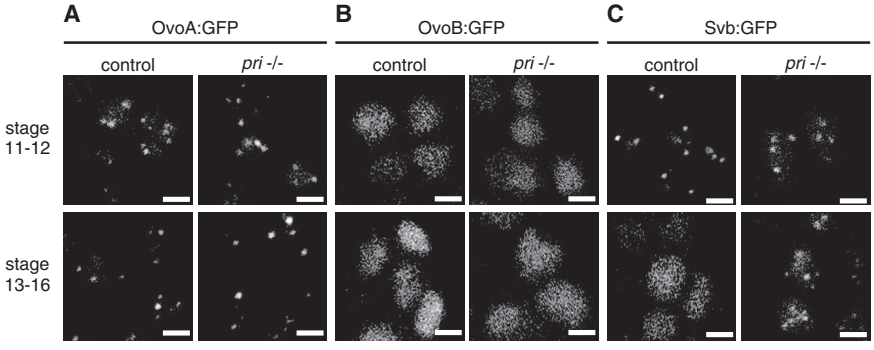

Fig. 3. *pri* regulates the subnuclear localization of Svb in living embryos. Distribution of (**A**) OvoA:GFP, (**B**) OvoB:GFP, and (**C**) Svb:GFP driven by *wg-GAL4* in control (*pri* +/–) or *pri* mutant embryos at stages 11 and 12 and stages 13 to 16. In all cases, the GFP signal was restricted to nuclei (fig. S4). Although the distribution of OvoA (focal) and OvoB (diffuse) was insensitive to *pri*, Svb switched from foci to diffuse in a *pri*-dependent manner. Scale bar, 10 μm.

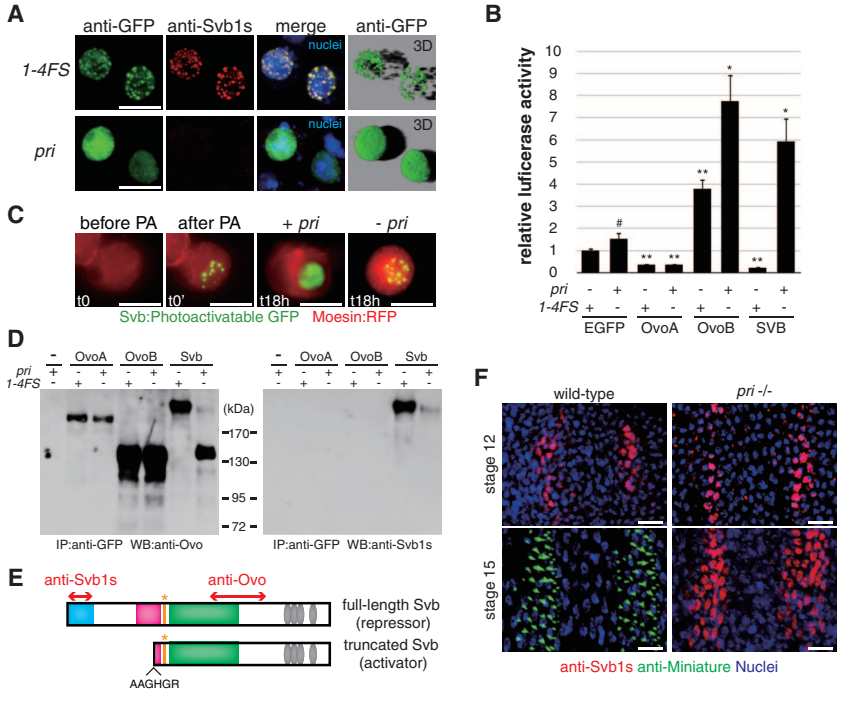

Fig. 4. Pri converts the Svb protein from a transcriptional repressor to an activator by N-terminal truncation. (**A**) Subnuclear localization of Svb:GFP in S2 cells when *pri* is co-expressed. *1-4FS*, a full-length *pri* mRNA with frame-shift mutations in ORF1-4 (*9*), was used as control. Cells were stained with antibody to GFP (green) and anti-Svb1s (red). Nuclei are in blue. The rightmost panel is a three-dimensional representation of Svb nuclear distribution. (**B**) Transcriptional activity of OvoA, OvoB, and Svb in S2 cells. Luciferase activity was used as a reporter for the transcriptional activity of the Enh-*m* enhancer. Error bars represent SE, and significance against GFP/*1-4FS*–transfected cells was evaluated with *t* tests (*$P < 0.05$, **$P < 0.01$, #$P > 0.05$). (**C**) Distribution of Svb:PA-GFP (green) in S2 cells, before photoactivation (t0), after photoactivation (t0′), and after the induction of *pri* expression (t18h). Without *pri* induction, Svb:PA-GFP was retained in foci (–*pri,* t18h). Red is Moesin:red fluorescent protein (RFP) used as a transfection control. (**D**) Western blots analysis of S2 cells expressing OvoA:GFP, OvoB:GFP, and Svb:GFP. Protein extracts were immunoprecipitated with antibody to GFP and probed with antibody to Ovo or anti-Svb1s. (**E**) Schematic representation of predicted form of truncated Svb. The N terminus of truncated Svb matches the sequence AAGHGR, which is located 56 amino acids upstream of the OvoB-initiating methionine (asterisk). Red arrows indicate the regions used to generate antibodies. (**F**) Ventral views of wild-type and *pri* mutant embryos stained with anti-Svb1s (red), and antibody to Miniature (green) that underlies nascent trichomes. Nuclei are in blue. Scale bar, 10 μm.

We next examined whether Pri peptides affect the synthesis or trafficking of Ovo/Svb proteins. Using transgenic C-terminal GFP-fusions (proven functional as described above), we observed that *pri* does not influence the production of Ovo/Svb proteins or their import to the nucleus (Fig. 3 and fig. S4). However, we noticed different patterns of their intranuclear distribution. Regardless of *pri* activity, throughout embryogenesis OvoA accumulated in discrete foci (Fig. 3A), and OvoB was distributed diffusely in the nucleoplasm (Fig. 3B). During stages 11 and 12, before *pri* is expressed in the epidermis (fig. S1), Svb formed intranuclear foci, like OvoA (Fig. 3C). At the onset of *pri* epidermal expression (stage 13 onwards) (fig. S1), the nuclear distribution of Svb became diffuse (Fig. 3C). Therefore, Svb distribution changes from a pattern similar to the OvoA repressor to that of the OvoB activator, and the timing of this conversion correlates with the expression of *pri*. This redistribution of Svb was abolished in *pri* mutants, in which Svb remained in nuclear foci throughout embryogenesis (Fig. 3C). Thus, *pri* participates in the conversion of nuclear distribution of Svb from punctate to diffuse.

The nonpunctuated, diffuse nuclear distribution of Svb in epidermal cells correlates with its ability to induce trichomes, suggesting that Svb redistribution coincides with active transcription of its targets. We explored this hypothesis using assays in *Drosophila* Schneider cells (S2 cells), which are of embryonic origin. Similarly to observations in embryos, the nuclear pattern of Svb was converted from punctate to diffuse in a *pri*-dependent manner in S2 cells (Fig. 4A). We quantified the transcriptional activity of Svb/Ovo using the Enh-*m* enhancer, which is directly activated by Svb in vivo (*17*) (fig. S3). OvoB strongly stimulated the transcription driven by Enh-*m,* and OvoA repressed transcription, both with or without *pri* (Fig. 4B). In contrast, Svb behaved like OvoA in the absence of *pri*, but similar to OvoB, activated Enh-*m* in the presence of Pri peptides (Fig. 4B). Inactivation of the Svb-binding site of Enh-*m* (*17*) suppressed this activation (fig. S5), indicating that *pri* is required for the direct activation of Enh-*m* by Svb. These results demonstrate that Pri peptides switch the transcriptional activity of Svb from that of a repressor accumulated in nuclear foci to a nucleoplasmic activator.

To explore the mechanisms by which Pri peptides trigger this switch in Svb intranuclear distribution, we examined whether Pri requires de novo synthesis of the Svb protein. Using a photoactivatable-GFP (PA-GFP), we observed that photoactivated Svb:PA-GFP switched from foci to diffuse distribution after the induction of *pri* expression (Fig. 4C). Therefore, the same Svb molecules are relocated within the nucleus, suggesting that the action of Pri peptides relies on posttranslational modifications of Svb. Accordingly, Western blot analysis showed that whereas the size of OvoA and OvoB proteins (including that of their minor species) were not affected by *pri*, Svb exhibited a differential electrophoretic mobility in a *pri*-dependent manner (Fig.

Downloaded from www.sciencemag.org on July 15, 2010

4D). In the absence of *pri*, Svb appeared slightly larger than OvoA, as deduced from the cDNA sequences (Fig. 2A). Upon *pri* expression, the Svb protein displayed a faster mobility, corresponding to a truncation of approximately 50 kD, without apparent modification in the size of *svb* mRNA (fig. S6). An antibody raised against the N-terminal Svb-specific region (anti-Svb1s) recognized only the larger Svb protein but not the truncated product formed upon *pri* expression. This truncated Svb protein was detected by antibodies to Ovo and GFP (Fig. 4, A and D, and fig. S7A), showing that it lacks the N-terminal region but retains an intact C terminus. To further characterize Svb truncation, we purified the truncated Svb protein and microsequenced its N-terminal end (fig. S8A). The N terminus of truncated Svb matches the sequence AAGHGR, which is located 56 amino acids upstream of the OvoB-initiating methionine and within a protein region that shows strong evolutionary conservation in insects (Fig. 4E and fig. S8B). The corresponding DNA sequence displays synonymous nucleotide substitutions across species and lacks canonical or alternative initiation codons (fig. S8B), further supporting the view that Svb truncation results from a posttranslational cleavage. Hence, the *pri*-induced truncated form of Svb contains the DNA-binding and activation domains but not the repression domain, explaining why it acts as a transcriptional activator.

Consistent with this idea, we observed a *pri*-dependent truncation of the endogenous Svb protein during embryogenesis. In wild-type embryos, anti-Svb1s detected a transient nuclear signal in trichome cells, at stages 11 and 12, that disappeared at later stages (Fig. 4F and fig. S7B). The loss of the Svb N-terminal region coincided with the onset of *pri* expression in the epidermis (fig. S1). Indeed, *pri* is required for Svb truncation in vivo—as revealed by the persistence of anti-Svb1s signal in *pri* mutants—throughout embryogenesis (Fig. 4F). We conclude that Pri peptides convert Svb from a transcriptional repressor to an activator via the truncation of its N-terminal region.

This study demonstrates that 11– to 32–amino acid peptides encoded by sORFs orchestrate epidermal differentiation through the control of Svb transcriptional activity. At stages 11 and 12, *svb* is already expressed and restricted to presumptive trichome cells, in which the full-length Svb repressor probably prevents the premature expression of cellular effectors. At stages 13 and 14, the expression of *pri* in epidermal cells then triggers N-terminal truncation of the Svb protein, probably through a proteolytic release of the repressor domain, causing a rapid conversion of Svb function toward activation. Thus, although *svb* expression defines the spatial pattern of trichomes, the action of Pri peptides defines the temporality of trichome formation.

Besides the mechanisms of epidermal differentiation, our studies suggest broader functions for Pri peptides. Although *pri* is also required for tracheal morphogenesis (*9*), we observed normal trachea in *svb* mutant embryos (fig. S9), indicating that Pri peptides probably regulate additional developmental factors. Recent large-scale analyses indicate that thousands of unexplored transcripts are also probably encoding polypeptides of less than 100 amino acids in mice and humans (*1*, *21*, *7*). Future functional analyses should elucidate how small peptides encoded by transcripts improperly termed ncRNAs contribute to various biological processes including development and differentiation.

References and Notes

1. P. Carninci *et al.*, RIKEN Genome Exploration Research Group and Genome Science Group (Genome Network Project Core Group), *Science* **309**, 1559 (2005).
2. S. Inagaki *et al.*, *Genes Cells* **10**, 1163 (2005).
3. T. Ota *et al.*, *Nat. Genet.* **36**, 40 (2004).
4. J. L. Tupy *et al.*, *Proc. Natl. Acad. Sci. U.S.A.* **102**, 5495 (2005).
5. K. Hanada, X. Zhang, J. O. Borevitz, W. H. Li, S. H. Shiu, *Genome Res.* **17**, 632 (2007).
6. J. P. Kastenmayer *et al.*, *Genome Res.* **16**, 365 (2006).
7. M. C. Frith *et al.*, *PLoS Genet.* **2**, e52 (2006).
8. Y. Hashimoto, T. Kondo, Y. Kageyama, *Dev. Growth Differ.* **50** (suppl. 1), S269 (2008).
9. T. Kondo *et al.*, *Nat. Cell Biol.* **9**, 660 (2007).
10. M. I. Galindo, J. I. Pueyo, S. Fouix, S. A. Bishop, J. P. Couso, *PLoS Biol.* **5**, e106 (2007).
11. J. Savard, H. Marques-Souza, M. Aranda, D. Tautz, *Cell* **126**, 559 (2006).
12. J. I. Pueyo, J. P. Couso, *Dev. Biol.* **324**, 192 (2008).
13. F. Payre, *Int. J. Dev. Biol.* **48**, 207 (2004).
14. A. P. McGregor *et al.*, *Nature* **448**, 587 (2007).
15. F. Payre, A. Vincent, S. Carreno, *Nature* **400**, 271 (1999).
16. E. Sucena, I. Delon, I. Jones, F. Payre, D. L. Stern, *Nature* **424**, 935 (2003).
17. H. Chanut-Delalande, I. Fernandes, F. Roch, F. Payre, S. Plaza, *PLoS Biol.* **4**, e290 (2006).
18. I. Fernandes *et al.*, *Dev. Cell* **18**, 64 (2010).
19. J. Andrews *et al.*, *Development* **127**, 881 (2000).
20. I. Delon, H. Chanut-Delalande, F. Payre, *Mech. Dev.* **120**, 747 (2003).
21. P. P. Amaral, M. E. Dinger, T. R. Mercer, J. S. Mattick, *Science* **319**, 1787 (2008).

22. We thank the Kyoto Drosophila Genetic Resource Center (DGRC); Bloomington *Drosophila* Stock Center for fly strains; the Indiana DGRC; G. Patterson, J. Lippincott-Schwartz, and C. Hill for plasmids; S. Takada and T. Okubo (NIBB) for technical advice; Y. Latapie and B. Ronsin (CBD) and J. D'Alayer (Institut Pasteur) for excellent technical assistance; and members of the Kobayashi laboratory for helpful comments and discussion. This work was supported by a Research Fellowship for Young Scientists from the Japan Society for the Promotion of Science; the JST PRESTO program; the Ministry of Education, Culture, Sports, Science and Technology KAKENHI (20370091); Agence Nationale de la Recherche (Programme Blanc "Netoshape"); Fondation pour la Recherche Médicale (Equipe 2005); and Association pour la Recherche sur le Cancer (1111).

Supporting Online Material

www.sciencemag.org/cgi/content/full/329/5989/336/DC1
Materials and Methods
Figs. S1 to S9
References

10 February 2010; accepted 20 May 2010
10.1126/science.1188158

Hedgehog Signaling Regulates Segment Formation in the Annelid *Platynereis*

Nicolas Dray,[1]*† Kristin Tessmar-Raible,[2,3]* Martine Le Gouar,[1]* Laura Vibert,[1] Foteini Christodoulou,[3] Katharina Schipany,[2] Aurélien Guillou,[4] Juliane Zantke,[2] Heidi Snyman,[3] Julien Béhague,[1,4] Michel Vervoort,[1,4] Detlev Arendt,[3] Guillaume Balavoine[1,4]‡

Annelids and arthropods share a similar segmented organization of the body whose evolutionary origin remains unclear. The Hedgehog signaling pathway, prominent in arthropod embryonic segment patterning, has not been shown to have a similar function outside arthropods. We show that the ligand Hedgehog, the receptor Patched, and the transcription factor Gli are all expressed in striped patterns before the morphological appearance of segments in the annelid *Platynereis dumerilii*. Treatments with small molecules antagonistic to Hedgehog signaling disrupt segment formation. *Platynereis* Hedgehog is not necessary to establish early segment patterns but is required to maintain them. The molecular similarity of segment patterning functions of the Hedgehog pathway in an annelid and in arthropods supports a common origin of segmentation in protostomes.

In the fruit fly, the axial patterning of each individual segment is controlled and maintained by two signaling pathways operating across the segment: Wnt/β-catenin and Hedgehog (*1*, *2*). The function of the Hedgehog (Hh) pathway in segment formation is conserved in other holometabolous insects (*3*) and probably also in noninsect arthropods (*4*, *5*). By contrast, mesodermal somites in vertebrates are patterned by nonhomologous segment polarity genes (*6*). Here, we investigated the role of the Hh pathway during segment formation in an annelid representative of the third great branch of Bilaterians, Spiralians (fig. S1). The nereidid *Platynereis dumerilii* presents two phases of segment formation: larval metamorphosis and juvenile posterior growth (fig. S2). Using degenerate polymerase chain reaction (PCR), we cloned four genes of the Hh pathway in *Platynereis* coding, respectively, for orthologs of the ligand Hedgehog (*Pdu-hh*), its receptor Patched *(Pdu-ptc)*, the transmembrane activator Smoothened (*Pdu-smo*),

Downloaded from www.sciencemag.org on July 15, 2010

and the transcription factor Cubitus interruptus (or Gli) (*Pdu-Gli*) (*7*) (predicted primary structures in fig. S3, phylogenetic trees in fig. S4). *Pdu-hh*, *Pdu-ptc*, and *Pdu-Gli* are expressed in segment polarity–like patterns strikingly reminiscent of their arthropod counterparts, i.e., in ectodermal segmental stripes, visible before the morphological appearance of segment anlagen, both during larval (Fig. 1, A, B, D, E, G, and H, and fig. S5, A to F) and posterior growth (Fig. 1, C, F, and I, and fig. S5, G to L) [detailed descriptions in supporting online material (SOM) text]. The thin stripes of *Pdu-hh* expression are located at the

[1]Centre de Génétique Moléculaire du CNRS, FRE 3144, Avenue de la Terrasse, 91189 Gif-sur-Yvette, France. [2]Max F. Perutz Laboratories, Universität Wien, Dr. Bohr-Gasse 9, 1030 Vienna, Austria. [3]Developmental Biology Unit, European Molecular Biology Laboratory, Heidelberg 69117, Germany. [4]Institut Jacques Monod, CNRS—Université Paris–Diderot, 15 rue Hélène Brion, 75205 Paris cedex 13, France.

*These authors contributed equally to this work.
†Present address: Department of Molecular, Cellular and Developmental Biology, Yale University, New Haven, CT 06520–8103, USA.
‡To whom correspondence should be addressed. E-mail: balavoine.guillaume@ijm.univ-paris-diderot.fr

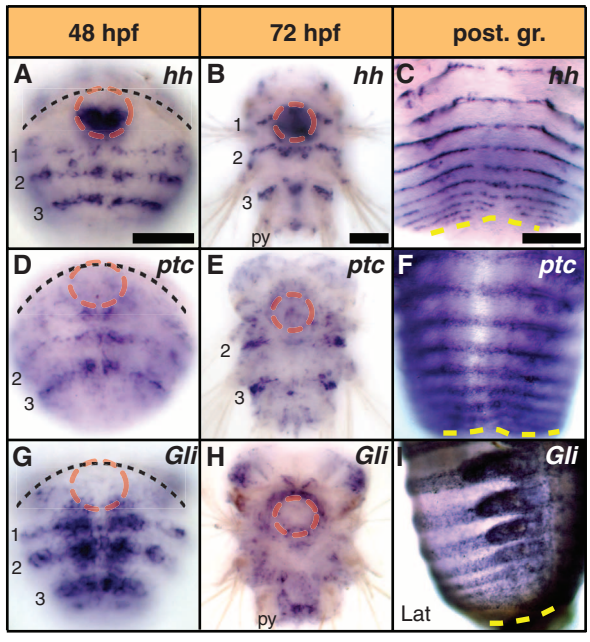

Fig. 1. Expression patterns of *hh* (**A** to **C**), *ptc* (**D** to **F**), and *Gli* (**G** to **I**) orthologs in *Platynereis* late trochophores (48 hpf), in early three-segmented larvae (72 hpf), and during posterior growth. All views are ventral except I, lateral right (Lat). Anterior or apical is up. Black dashed line, prototroch of larvae. The stomodeum is delimitated by a red dashed circle. Larval segment anlagen are numbered 1 to 3. Posterior growth panels [post. gr., (C), (F), and (I)] show patterns in posterior regenerates 1 week after caudal amputation, in front of the thin segment addition zone (yellow dashed line). Scale bars, 50 μm. py, pygidium.

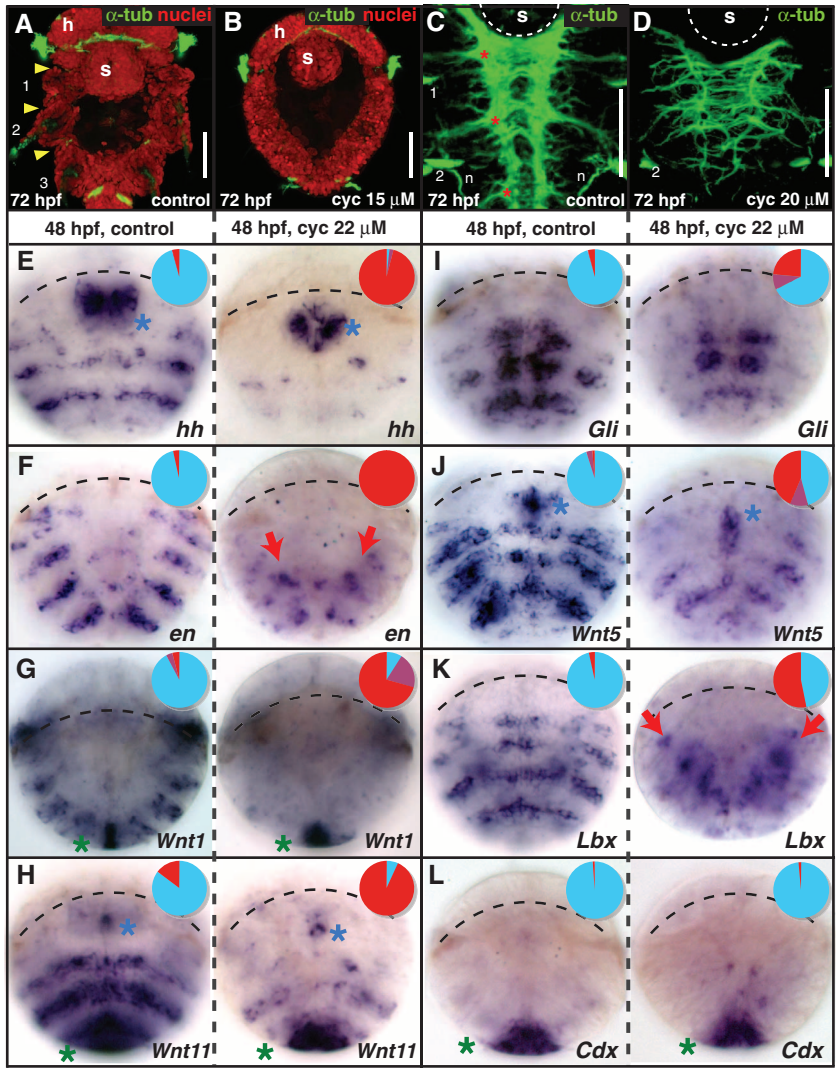

Fig. 2. Effects of mid-trochophore stage cyclopamine treatments on the development of *Platynereis* larvae. (**A** to **D**) Three-day larvae stained with an antibody against acetylated tubulin, which reveals the ciliary belts (trochae) (A) and (B) and the axonal scaffold of the nervous system (C) and (D). (A) and (B) are midbody frontal confocal sections of Hoechst 33342–stained larvae; (C) and (D) are ventral frontal confocal sections. Scale bars, 50 um. (**E** to **L**) Effects of cyclopamine treatment on the expressions of segment polarity–like genes and *Pdu-Cdx*, a pygidial ectoderm marker. The first and second columns show expression in untreated larvae and in the majority of treated larvae, respectively. Pie graphs show the frequencies of abnormal expressions with normal in blue, abnormal in red, and the maternal batch variability in violet where available. Small fractions of abnormal expressions in the untreated control reflect both a proportion of spontaneous abnormal development and the probe-dependent imperfect sensitiveness of the WMISH protocol. Prototroch, dashed black line and "p"; stomodeum, white dashed circle and "s"; 1, 2, 3, larval segments in (A) and (B), segmental trochae in (C) and (D); yellow arrows, segmental grooves; red asteriks, roots of the main lateral nerves; n, protonephridium; and h, head lobes. Red arrows, blue asterisks, and green asterisks: persistent mesodermal, stomodeal, or pygidial/proctodeal expressions, respectively.

Downloaded from www.sciencemag.org on July 15, 2010

anterior border of each segment (fig. S5, G and H), mostly in the same cells as two previously identified *Platynereis* segment polarity–like genes orthologous to *engrailed* (*8*) and *NK4*/*tinman* (*9*). The broader stripes of *Pdu-ptc* are centered on these *Pdu-hh*/*en*/*NK4* stripes spreading on each side of the segment border (fig. S5, I and J), whereas *Pdu-Gli* shows a complementary pattern in the middle of each future segment (fig. S5, K and L). *Pdu-smo* does not show distinctive patterns in whole-mount in situ hybridization (WMISH) until the three-segmented larva, when it is expressed predominantly in the pharyngeal area (fig. S6). Real-time PCR measurements, nevertheless, show that *Pdu-smo* is expressed at low, presumably ubiquitous, levels early in trochophore development and that maternal mRNAs are present in fertilized eggs (fig. S6), similar to the early embryos of the fruit fly and vertebrates (*10*–*12*).

These expression patterns suggest that the Hh pathway is involved in segmental patterning in *Platynereis*. However, striped expressions of Hh pathway genes appears distinctly later during trochophore development (fig. S5, A to F) than those of the previously identified *Platynereis* segment polarity–like genes *Pdu-en* (*8*), *Pdu-NK4*, and *Pdu-Lbx* (*9*). Thus the Hh pathway might play a late role in segment formation, in shaping the individual segments after the specification of the segmental pattern by other genes. To test this hypothesis, we used two small molecules, cyclopamine (*13*) and SANT-1 (*14*), known for antagonizing Hh signaling in vertebrates by binding to Smo proteins. We defined three time windows for treatments (*7*) (fig. S7): (i) an early trochophore window before any component of the Hh pathway is distinctly expressed in stripes [20 to 30 hours past fertilization (hpf)]; (ii) a mid-trochophore window when *Pdu-hh*, *Pdu-Gli*, and *Pdu-ptc* are all expressed in stripes (32 to 48 hpf); and (iii) a late trochophore window (54 hpf onward) when striped expression for *Pdu-ptc* and *Pdu-Gli* fade, but still a few hours before the larva starts to elongate and to form externally visible segments (*15*). Mid-trochophore treatments with increasing doses of cyclopamine or SANT-1 on mixed batches of trochophores coming from several females gave remarkably similar abnormal larvae (fig. S8, I and II). They fail to develop properly shaped segments at 3 days: They do not elongate properly, remaining ovoid in shape (Fig. 2, A and B, and fig. S8, II, A to C); segmental grooves do not appear (Fig. 2, A and B, yellow arrows), and segmental trochae (circular ciliary belts borne by larval segments) are reduced (fig. S8, II, D to F); and appendage outgrowths and chaetae do not appear (fig. S8, II, A to C). In addition, the axonal scaffolds of the ventral nerve cord and segmental peripheral nervous system (Fig. 2, C and D, and fig. S8, II, D to F) both appear underdeveloped and disorganized. In place of the metameric peripheral nerves (red asterisks), an asymmetric proliferation of axons projecting haphazardly to the periphery forms, which indicates that the segmental pattern of the nervous system is lost. The effects of two unrelated drugs and of different treatment time windows on embryos suggest that the phenotypes obtained are caused by blocking Hh signaling (fig. S8 and SOM text). In particular, the phenotypes cannot be due to a general toxicity of the drugs, because late trochophore treatments at a time of massive proliferation and morphogenesis cause few defects (fig. S8, II, G to K). We also tested the role of *Pdu-smo* on posterior segment addition by treating individuals with cyclopamine after caudal regeneration. One-half (12/24) of treated individuals showed regenerated posterior parts with fewer, abnormally shaped segment anlagen and reduced segmental grooves (fig. S12).

To analyze further the effects of cyclopamine on the segmental pattern, we looked at the expression patterns of the previously known segment polarity–like genes in cyclopamine-treated larvae (*7*). To take into account a strong maternal-effect polymorphism in the response to cyclopamine (SOM text and fig. S11A), we carefully selected only those batches of embryos that presented medium and strong morphological phenotypes (scored in 3-day larvae) for the gene expression study. Expression patterns for medium strength morphological phenotypes are presented in Fig. 2, E to L, and fig. S10. Complete results including one or two repeat experiments for each gene indicate that the effects of cyclopamine on gene expression correlate well with the strength of the phenotype in each same-female batch studied (fig. S11B). Early-trochophore cyclopamine treatment has no effect on the striped expressions of *Pdu-en*, *Pdu-NK4*, and *Pdu-Lbx* (figs. S10 and S11B) seen in 30 hpf larvae, showing that Smo does not act on the segmental pattern independently of the morphogen Hh and that the Hh pathway does not intervene in the initial laying of the segmental pattern. By contrast, mid-trochophore cyclopamine treatment at high dose leads to a complete or almost complete loss of striped expression for *Pdu-hh*, *Pdu-en*, and *Pdu-Wnt1* (Fig. 2, E, F, and G, respectively), showing that the segmental

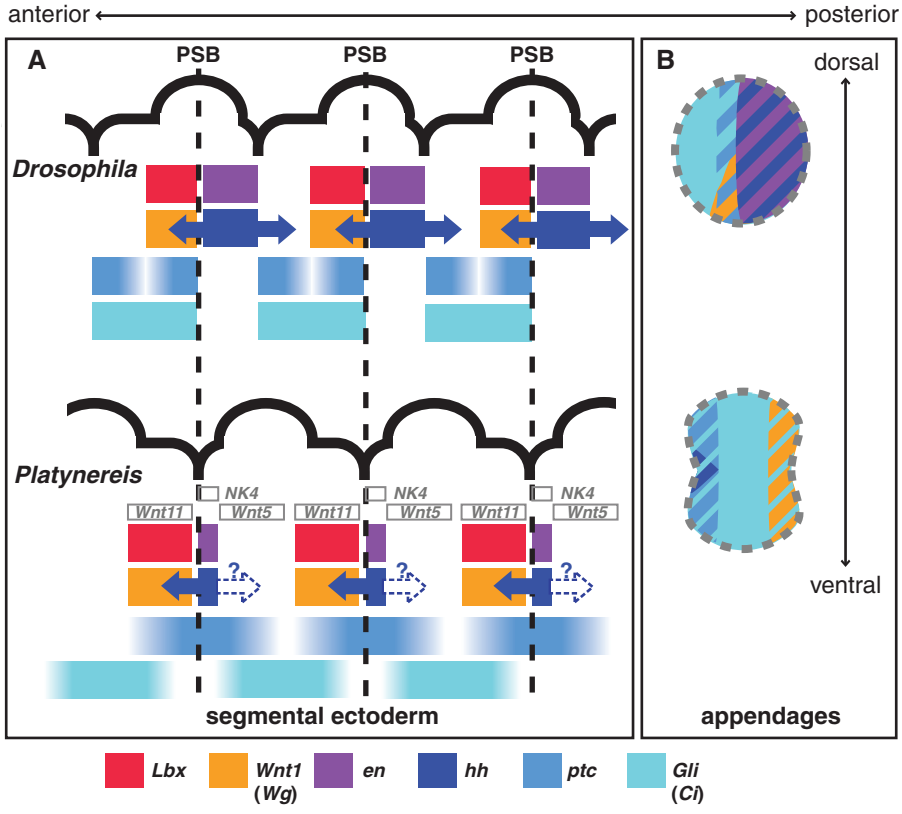

Fig. 3. (**A**) Comparison of the anteroposterior extension of striped expression patterns of proven and presumed segment polarity orthologous genes in *Platynereis* and *Drosophila*. Segment boundaries and limb anlagen positions are represented with a schematic body wall section in black. Orthologous genes are color-coded; segment polarity–like genes specific to *Platynereis* are represented by gray rectangles. The morphogenetic actions of the diffusible Hh proteins are represented with blue arrows. A white arrow with question mark indicates that Hh action on the anterior parts of annelid segments is not proven in this study. Unlike in fly, *Pdu-ptc* is expressed in *en*- and *hh*-positive cells, and *Pdu-Gli* expression does not abut *en*- and *hh*-positive cells in *Platynereis*. (**B**) Comparison of expression patterns of some of these segment polarity–like genes in the early stages of appendage formation. The homology of annelid segments with arthropod parasegments implies that annelid parapodia do not correspond in embryonic position with the arthropod appendages, which suggests that these appendages do not share a common origin in the protostome ancestor. PSB, parasegmental boundary.

Downloaded from www.sciencemag.org on July 15, 2010

pattern is largely affected well before metamorphosis. *Pdu-ptc* is also down-regulated (fig. S9), as it is observed in *hh*-mutant flies (*16*) and vertebrates lacking *shh* expression (*17*). *Pdu-Gli* (Fig. 2I) stripes are mostly persistent even at high doses of cyclopamine. The specificity of the effects of mid-trochophore cyclopamine treatment on the patterning of the segmental ectoderm is demonstrated by the persistence of gene expression in tissues other than segmental ectoderm. Hence the expression of *Pdu-en* and *Pdu-Lbx* in segmental mesoderm (Fig. 2, F and K, red arrows), the stomodeal expression of *Pdu-hh* and *Pdu-Wnt11* (Fig. 2, E and H, blue asterisks), and the pygidial expression of *Pdu-Wnt11* and *Pdu-Cdx* (Fig. 2, H and L, green asterisks) are maintained, whereas the proctodeal expression of *Pdu-Wnt1* is slightly enlarged (Fig. 2G, green asterisks).

The effect of cyclopamine on *Pdu-hh* stripes must be indirect, if we suppose that the direct targets of Hh signaling are only those cells expressing *Pdu-Gli*, away from segment borders. In *Drosophila* (Fig. 3), *wingless* (*wg*) expression is maintained by Hh signaling in the anterior compartment just anterior to the *en* stripe, whereas *wg* signaling is necessary to maintain *en* and *hh* striped expression in the posterior compartment (*18*). In *Platynereis*, *Pdu-Wnt1*, the ortholog of *Drosophila wingless* (*8*), is expressed just anterior to *Pdu-en* and *Pdu-hh* stripes on the other side of segmental grooves. Its strong down-regulation by cyclopamine (Fig. 2G) is consistent with a loop of regulation similar to the one known in *Drosophila*. *Ladybird*, the fly gene orthologous to *Pdu-Lbx*, is expressed in epidermal stripes overlapping *wingless* stripes in the anterior compartment of the epidermis and is positively regulated by *wingless* (*19*). By contrast, cyclopamine treatment in the annelid does not abolish completely *Pdu-Lbx* stripes in trochophores (Fig. 2K), which suggests that other factors are involved in its maintenance. Another difference between the annelid and the fly is that *Pdu-Wnt1* is not expressed in complete circular stripes in the trochophore (it is during posterior growth) but only in the lateral parapodial field (Fig. 2G). It was thus interesting to look at *Pdu-Smo* regulation of other *Wnt* genes potentially involved in segment formation. *Pdu-Wnt11* is expressed in thick stripes in the posterior halves of segments and is strongly down-regulated by cyclopamine (Fig. 2H). *Pdu-Wnt5* is expressed in the anterior halves of segments and is, in contrast, much more resistant to cyclopamine (Fig. 2J).

Our work demonstrates the involvement of the Hh pathway in segment formation outside of arthropods. It contrasts with earlier studies of *hh* orthologs in annelid species (*20*, *21*). The comparison of the effect of Hh signaling inhibition in *Platynereis* and in insects [i.e., the fruit fly and the coleopteran *Tribolium* (*3*)] reveals extensive similarities. As in insects, *Platynereis* Hh presumably diffuses anteriorly to maintain *Wnt* signaling anterior to the *hh*-expressing cells (Fig. 3), which may in turn be crucial to maintain segment boundary gene expressions, including *Pdu-hh*. As in insects, Hh is not necessary in the initial setting of the segmental pattern but is required to maintain this pattern before the morphological appearance of segments. The comparison of segment polarity gene patterns between *Platynereis* and arthropods (Fig. 3) reveals four independent players with remarkably similar expressions: *engrailed*, *Lbx/ladybird*, the Hh pathway, and *Wnt1/wingless* signaling. The most likely explanation of these similarities is that these genes were already playing similar roles in a metameric protostome ancestor. The alternative explanation would be a parallel recruitment of these genes for similar functions in annelids and arthropods. Because they are not known to be part of a conserved core regulatory network or "kernel" (*22*) that might have been coopted en bloc, each gene would have been recruited independently, which seems unlikely. Altogether, these four players are expressed in the same spatial relation across the annelid segment boundary as they are across the parasegmental boundary in arthropods (Fig. 3). This suggests that these two boundaries are homologous as was proposed earlier (*8*). Therefore, the segmented exoskeleton of the arthropods must have evolved out of frame with the ancestral protostome segmentation (fig. S13). This ancestral protostome segmentation is nowadays "recapitulated" as parasegmental patterning in the embryos of extant arthropods.

References and Notes

1. V. Hatini, S. DiNardo, *Trends Genet.* **17**, 574 (2001).
2. B. Sanson, *EMBO Rep.* **2**, 1083 (2001).
3. L. Farzana, S. J. Brown, *Dev. Genes Evol.* **218**, 181 (2008).
4. M. Pechmann, A. P. McGregor, E. E. Schwager, N. M. Feitosa, W. G. Damen, *Proc. Natl. Acad. Sci. U.S.A.* **106**, 1468 (2009).
5. F. Simonnet, J. Deutsch, E. Quéinnec, *Dev. Genes Evol.* **214**, 537 (2004).
6. S. A. Holley, *Dev. Dyn.* **236**, 1422 (2007).
7. Materials and methods are available as supporting material on *Science* Online.
8. B. Prud'homme *et al.*, *Curr. Biol.* **13**, 1876 (2003).
9. A. Saudemont *et al.*, *Dev. Biol.* **317**, 430 (2008).
10. M. van den Heuvel, P. W. Ingham, *Nature* **382**, 547 (1996).
11. J. Alcedo, M. Ayzenzon, T. Von Ohlen, M. Noll, J. E. Hooper, *Cell* **86**, 221 (1996).
12. W. Chen, S. Burgess, N. Hopkins, *Development* **128**, 2385 (2001).
13. J. K. Chen, J. Taipale, M. K. Cooper, P. A. Beachy, *Genes Dev.* **16**, 2743 (2002).
14. J. K. Chen, J. Taipale, K. E. Young, T. Maiti, P. A. Beachy, *Proc. Natl. Acad. Sci. U.S.A.* **99**, 14071 (2002).
15. P. R. Steinmetz, F. Zelada-Gonzáles, C. Burgtorf, J. Wittbrodt, D. Arendt, *Proc. Natl. Acad. Sci. U.S.A.* **104**, 2727 (2007).
16. A. Hidalgo, P. Ingham, *Development* **110**, 291 (1990).
17. J. P. Concordet *et al.*, *Development* **122**, 2835 (1996).
18. S. DiNardo, J. Heemskerk, S. Dougan, P. H. O'Farrell, *Curr. Opin. Genet. Dev.* **4**, 529 (1994).
19. K. Jagla *et al.*, *Development* **124**, 91 (1997).
20. D. Kang *et al.*, *Development* **130**, 1645 (2003).
21. E. C. Seaver, L. M. Kaneshige, *Dev. Biol.* **289**, 179 (2006).
22. E. H. Davidson, D. H. Erwin, *Science* **311**, 796 (2006).

23. We acknowledge the following agencies for funding: the CNRS, University Paris–Diderot and the Agence Nationale de la Recherche (France) (ANR grant BLAN-0294); the Max F. Perutz Laboratories (MFPL) funds and the Austrian Science Fund (FWF) START award (AY0041321), the French Research Ministry and the Fondation pour la recherche médicale (FRM) for fellowships (N.D.); the Boehringer Ingelheim Foundation and the Marie Curie Research Training Networks ZOONET (MRTN-CT-2004-005624) for fellowships (K.T.R.). We also thank the platform ImagoSeine staff for help in confocal imagery. GenBank accession numbers for the gene sequences newly identified in this study are HM179271 to HM179276.

Supporting Online Material

www.sciencemag.org/cgi/content/full/329/5989/339/DC1
Materials and Methods
SOM Text
Figs. S1 to S13
References

1 March 2010; accepted 24 May 2010
10.1126/science.1188913

Chemoattraction to Dimethylsulfoniopropionate Throughout the Marine Microbial Food Web

Justin R. Seymour,[1,2,3]* Rafel Simó,[4] Tanvir Ahmed,[1] Roman Stocker[1]

Phytoplankton-produced dimethylsulfoniopropionate (DMSP) provides underwater and atmospheric foraging cues for several species of marine invertebrates, fish, birds, and mammals. However, its role in the chemical ecology of marine planktonic microbes is largely unknown, and there is evidence for contradictory functions. By using microfluidics and image analysis of swimming behavior, we observed attraction toward microscale pulses of DMSP and related compounds among several motile strains of phytoplankton, heterotrophic bacteria, and bacterivore and herbivore microzooplankton. Because microbial DMSP cycling is the main natural source of cloud-forming sulfur aerosols, our results highlight how adaptations to microscale chemical seascapes shape planktonic food webs, while potentially influencing climate at the global scale.

Marine plankton inhabit heterogeneous microscale seascapes (*1*) where chemical cues allow motile organisms to exploit nutrient patches (*2*, *3*), locate mutualistic partners or hosts (*4*), and select or avoid prey (*5*). Dimethylsulfoniopropionate (DMSP) is a phytoplankton-produced solute, which can constitute up to 10% of total cell carbon (*6*). It is released into the water column via point source events, including exudation, grazing, and cell lysis (*6*). These events

Downloaded from www.sciencemag.org on July 15, 2010

generate submillimeter, diffusing DMSP pulses that may act as chemical hot spots for microbes that use DMSP as a source of carbon and sulfur (*7*, *8*). Although DMSP represents a potent direct or indirect [by transformation into dimethylsulfide (DMS)] foraging cue for sea urchins, coral-reef fish, procellariiform birds, penguins, and seals (*9*–*12*), its role as a chemical cue among marine microorganisms remains unclear. Some bacterioplankton exhibit attraction to DMSP (*4*, *13*), but it has also been suggested that this compound is involved in a grazing-deterrence mechanism in phytoplankton (*14*, *15*). These largely unresolved and apparently contradictory ecological functions of DMSP are likely to play important roles in global sulfur biogeochemistry. Oceanic cycling of DMSP into volatile DMS and the emission and subsequent oxidation of DMS in the atmosphere shape the atmospheric radiative balance by affecting the formation and albedo of clouds (*16*). Therefore, a potentially large and direct influence of the marine biosphere on climate is ultimately mediated by microbial interactions at the microscale.

We studied the chemotactic behavioral response of seven species of marine microbes by using a microfluidic system (fig. S1) (*17*, *18*) to create ephemeral, submillimeter diffusing patches of DMSP and related compounds, including DMS, dimethylsulfoxide (DMSO), and glycine betaine (GBT) (Fig. 1; Fig. 2, A to D; and fig. S2), all of which are ubiquitous in the pelagic ocean. The spatiotemporal scales of the chemical patches produced were congruent with release events in the ocean. DMS and DMSO are DMSP degradation products (*6*), whereas GBT is analogous to DMSP in chemical structure and physiological function (*19*). Strong chemotactic responses toward DMSP and GBT were displayed by five organisms, which is consistent with the structural analogy between the compounds and the fact that they share membrane transport systems in heterotrophic bacteria and some phytoplankton (*7*, *8*). Positive, albeit weaker, attraction to DMS and DMSO occurred, in line with the observation that these compounds are less biologically labile than DMSP (*6*, *7*). Positive responses were characterized by dense accumulations of cells within chemical micropatches, often occurring in less than 30 s (Fig. 2 and fig. S2). Although negligible chemotactic responses (Fig. 1 and fig. S2) or repulsion (e.g., Fig. 2D) were observed in some instances, positive chemotaxis was observed in 74% of tested cases, indicating that DMSP and related chemicals are potent chemoattractants across multiple trophic levels in the marine microbial food web. We measured the relative strength of the response using a chemotaxis index, I_C, that quantifies the magnitude of the accumulation of organisms within the chemical patch, and we estimated the increase in integrated chemical exposure due to chemotaxis with an exposure index, I_E (*18*) (fig. S3). Strong responses led to >65% enhancement in exposure to these compounds (Fig. 1), which, in the ocean, will confer a substantial advantage to chemotactic foragers.

DMSP is produced by many microalgal species, for which it plays multiple physiological roles (*6*). On the other hand, for non–DMSP-producing autotrophs, uptake and assimilation of DMSP may represent a source of reduced sulfur (*8*, *20*). We found that motile phytoplankton can use chemotaxis to actively seek out localized DMSP pulses. The chlorophyte *Dunaliella tertiolecta* [The Provasoli-Guillard National Center for Culture of Marine Plankton (CCMP)1320] and the prasinophyte *Micromonas pusilla* (CCMP2709) both exhibited substantial chemoattraction to DMSP, reaching I_C values of 1.94 and 4.96, respectively (Fig. 1; Fig. 2, B and D; and fig. S2, D and E). *D. tertiolecta* was also attracted to DMS (Fig. 1, Fig. 2D, and fig. S2E). In contrast, the motile cyanobacterium *Synechococcus* WH8102 did not exhibit chemotaxis to any tested compound ($I_C < 0$) (Fig. 1 and fig. S2C), despite its ability to take up DMSP (*20*). The *M. pusilla* strain used here actively assimilates DMSP sulfur into macromolecules (*18*) and utilizes chemotaxis to increase its exposure to DMSP by up to 41% (Fig. 1).

The strong response of *D. tertiolecta* is intriguing because [^{35}S]DMSP uptake experiments indicate that this strain does not take up or assimilate DMSP (*18*). Instead, it cleaves DMSP extracellularly to produce DMS (fig. S4). This, along with the strong attraction toward DMS, suggests an ecophysiological requirement for DMS. *Dunaliella* sp. have been shown to photooxidize DMS into DMSO (*21*), but in DMS-addition experiments with *D. tertiolecta* (CCMP1320), we did not observe any degradation or incorporation of DMS (fig. S5). Hence, in this case, an as-yet-undefined incentive other than sulfur incorporation drives chemotaxis to DMSP. Therefore, chemoattraction to DMSP by phytoplankton can be driven by divergent ecophysiological demands: Some phytoplankton use chemotaxis toward DMSP to assimilate it; others exhibit chemotaxis before extracellular transformation of the compound. Furthermore, because predators are also attracted to DMSP patches (e.g., Figs. 2C and 3) the ecological benefits of these responses must outweigh the potential cost of increased exposure to grazing.

DMSP produced by phytoplankton also supports a significant proportion of the carbon and sulfur requirements of marine heterotrophic bacteria (*7*, *22*). Between 30 and 90% of oceanic DMSP is metabolized by bacteria, which either demethylate DMSP to assimilate part of its sulfur as methanethiol (MeSH) or cleave DMSP to release DMS (*7*, *8*, *23*). We quantified the chemotactic response of the α-proteobacterium *Silicibacter* sp. (TM1040) and the γ-proteobacterium *Pseudoalteromonas haloplanktis* [American Type Culture Collection (ATCC) 700530]. Both *Silicibacter* sp. (TM1040) and some strains of *P. haloplanktis* demethylate DMSP (*24*, *25*). *P. haloplanktis*

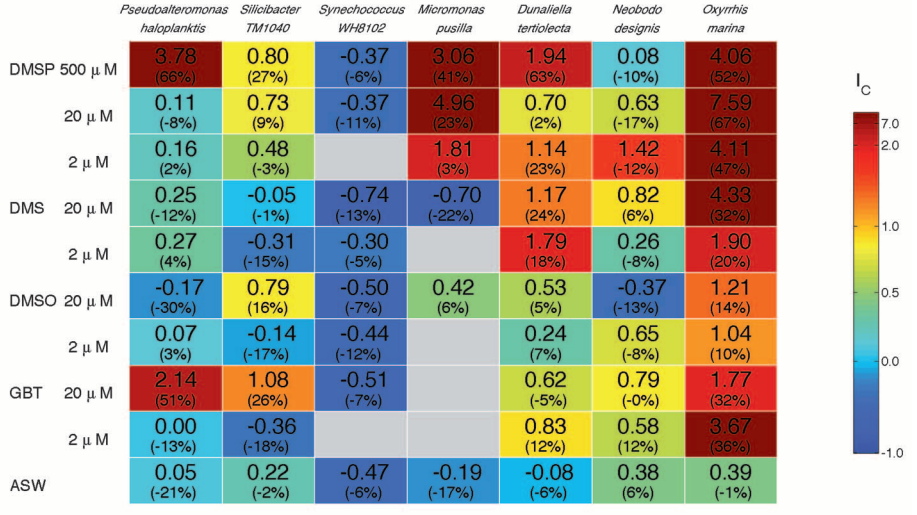

Fig. 1. The strength of the attraction to pulses of DMSP and related compounds, as illustrated by the chemotactic index (I_C), which is based on cell distributions, and the exposure index (I_E), which is based on response speed and substrate diffusion rates (*18*). Both I_C and I_E are population-averaged quantities. The color code and top number in each cell describe maximum I_C values observed during each experiment. Large positive I_C indicates strong chemotactic attraction, whereas $I_C \leq 0$ corresponds to lack of attraction. Numbers in parentheses correspond to the I_E averaged over time (1 to 6 min). Where I_C is large but I_E is small (e.g., *N. designis*), organisms respond strongly but not rapidly. ASW denotes the artificial-seawater-only control. Gray boxes are cases where no data were acquired.

[1]Ralph M. Parsons Laboratory, Department of Civil and Environmental Engineering, Massachusetts Institute of Technology, Cambridge, MA 02139, USA. [2]School of Biological Sciences, Flinders University, General Post Office Box 2100, Adelaide, South Australia, 5001, Australia. [3]Plant Functional Biology and Climate Change Cluster (C3), University of Technology, Sydney, Post Office Box 123 Broadway, New South Wales 2007, Australia. [4]Institut de Ciències del Mar (ICM), Consejo Superior de Investigaciones Científicas (CSIC) Passeig Maritim de la Barceloneta 37-49, 08003 Barcelona, Catalonia, Spain.

*To whom correspondence should be addressed. E-mail: Justin.Seymour@uts.edu.au

Downloaded from www.sciencemag.org on July 15, 2010

exhibited strong chemotaxis (I_C = 3.78) toward high (500 μM) DMSP concentrations (Figs. 1 and 2A), using highly directional swimming to migrate into the DMSP patch with a chemotactic velocity of up to 35 μm s^{-1}, or 44% of the mean swimming speed (80 μm s^{-1}). Bacterial chemotactic migration rates are typically <10% of swimming speed (*26*), indicating that DMSP represents a potent chemoattractant for this strain. In accordance with previous observations (*4*), TM1040 also exhibited positive, albeit weaker (I_C = 0.80), chemotaxis toward DMSP (20 and 500 μM) (Figs. 1 and 2D, and fig. S2B). The rapid response of these bacterial strains resulted in increased exposure to DMSP by up to 66% (Fig. 1). This will impart a significant advantage over nonmotile competitors in the environment. Such competitive interactions may also determine the balance of DMSP that is demethylated to MeSH or cleaved into DMS, influencing ocean-atmosphere sulfur flux (*7*, *16*).

For microzooplankton, DMSP may be both a resource and an infochemical. DMSP uptake has been shown to supply reduced sulfur to a dinoflagellate grazer via both prey ingestion and

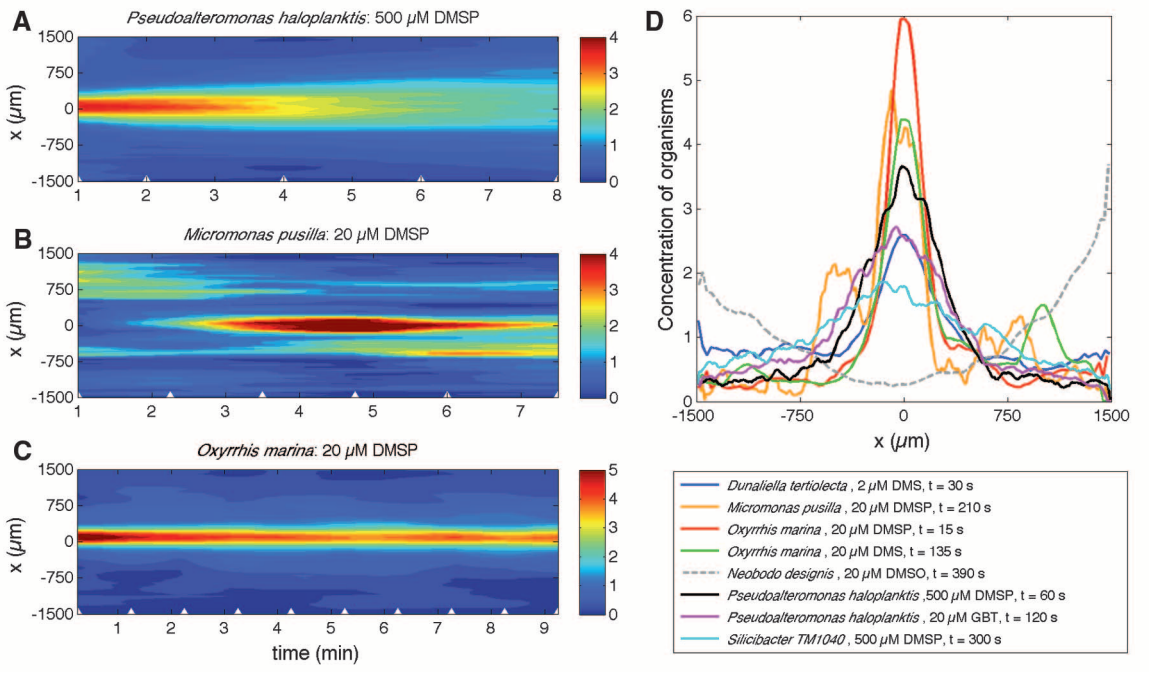

Fig. 2. Chemotactic responses to diffusing patches of DMSP and related compounds. Spatiotemporal distributions of (**A**) the bacterium *P. haloplanktis*, 500 μM DMSP, (**B**) the phytoplankter *M. pusilla*, 20 μM DMSP, and (**C**) the dinoflagellate *Oxyrrhis marina*, 20 μM DMSP. Colors denote cell concentration, normalized to a mean of 1. White triangles indicate times at which cell concentrations across the channel width (*x*) were measured. (**D**) Sample concentration profiles of organisms across the microchannel width, normalized to a mean of 1 (measurement times are given in the key). Although attraction was observed for many sulfur compounds (solid lines), repulsion also occurred (dashed line). For all cases, the pulse was released at time t = 0 at the center of the microchannel (x = 0) and had an initial width of 300 μm. The full set of spatiotemporal cell distributions is given in fig. S1.

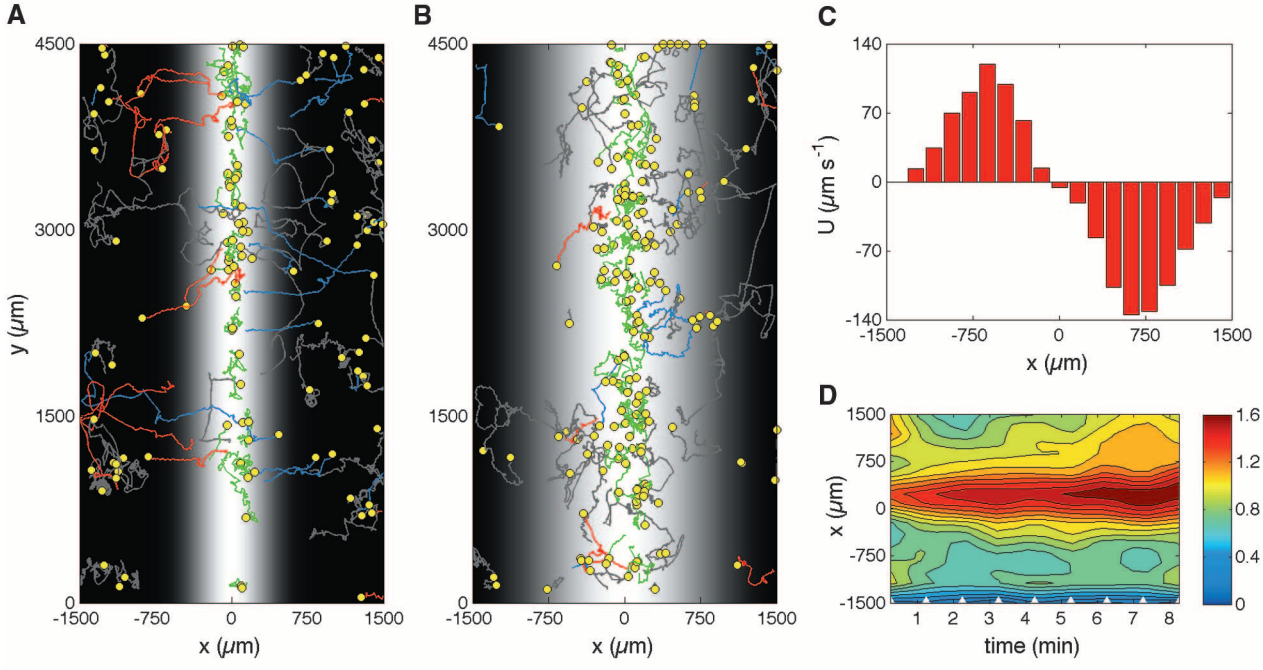

Fig. 3. Swimming behavior of *O. marina* in response to a 20 μM DMSP pulse. (**A** and **B**) Trajectories acquired (A) at t = 15 s and (B) t = 255 s, color-coded as follows: blue, swimming left at >85 μm s^{-1}; red, swimming right at >85 μm s^{-1}; green, trajectories fully within central 300 μm; and gray, all others. Yellow dots indicate starting points, and the gray background is the modeled DMSP concentration field. (**C**) Chemotactic velocity (i.e., inward speed), U, measured across the channel at t = 15 s. (**D**) Spatiotemporal distribution of the rate of change of direction relative to background value.

Downloaded from www.sciencemag.org on July 15, 2010

osmotrophic uptake (*27*). The chemical signature of DMSP produced by phytoplankton could also provide a prey cue for foragers, yet current evidence indicates that DMSP inhibits grazing by microzooplankton (*15*). To examine this apparent paradox, we measured the foraging response of the herbivorous dinoflagellate *Oxyrrhis marina* (ICM isolate) and the bacterivorous heterotrophic nanoflagellate *Neobodo designis* (CCAP1951/1) to DMSP micropatches. Both species exhibited positive chemotaxis. *N. designis* displayed the highest levels of chemoattraction (I_C = 1.40) to low concentrations (2 μM) of DMSP (Fig. 1 and fig. S2F), presumably because of the saturation of chemoreceptors at high DMSP concentrations. *O. marina* exhibited chemotaxis (I_C = 1.04 to 7.59) to all tested concentrations of DMSP, DMS, DMSO, and GBT (Fig. 1; Fig. 2, C and D; and fig. S2G), with its response to DMSP the strongest observed among all cases tested (I_C = 7.59). *O. marina* showed pronounced shifts in swimming behavior, migrating into DMSP patches with chemotactic velocities of up to 135 μm s^{-1}, or 35% of the mean swimming speed (330 μm s^{-1}) (Fig. 3, A to C), and doubling turning rates once inside the patch to retain position within it (Fig. 3D).

These chemotactic responses by *O. marina* are difficult to reconcile with the hypothesis that DMSP is used by phytoplankton in a chemical defense system against this species (*14*, *15*, *28*). This view was derived from observations that bulk additions of 20 μM DMSP reduced grazing rates of *O. marina* on the DMSP-producing phytoplankton *Emiliana huxleyi* (*15*). In light of the strong attractive responses observed here, we alternatively propose that *O. marina* might utilize DMSP as a prey cue. This is consistent with observations that viral infection of *E. huxleyi*, which will augment DMSP release, increases grazing rates by *O. marina* (*29*). We suggest that in previous grazing experiments (*15*), bulk additions of DMSP obscured the microscale chemical signature of individual phytoplankton cells by saturating the system with signal molecules, masking the position of cells, and reducing grazing rates.

Bulk seawater concentrations of DMSP are typically in the nanomolar range (*30*), whereas phytoplankton internal concentrations can exceed 100 mM (*6*). Thus, DMSP concentrations will be orders of magnitude higher than background within microzones surrounding individual phytoplankters that leak DMSP because of cell damage or lysis (Fig. 4, A and B). In our experiments, initial concentrations rapidly decreased as patches diffused (Fig. 4C), so that concentrations in the microchannel paralleled those expected around cells in the environment. Phagotrophic grazers responded to pulses with lower DMSP concentrations (2 μM) than were detected by heterotrophic bacteria (20 to 500 μM), potentially allowing grazers to respond from greater distances. A 0.1 μM sensitivity will allow a grazer to detect a stressed, or virus-infected (*29*), phytoplankton cell exuding DMSP from 50 μm away (Fig. 4B). At the chemotactic velocities observed here, *O. marina* can cover this distance in <0.5 s. In contrast, one-tenth the sensitivity (1 μM) will hardly allow bacteria to detect exuding phytoplankton (Fig. 4B). However, it enables them to detect the lysis of a DMSP-producing phytoplankton cell from >150 μm away and for a total time of >15 s (Fig. 4A), which permits uptake of the DMSP-rich cell lysis products. Therefore, the ecological role of chemotaxis toward DMSP may vary between microorganisms. Foraging microzooplankton could use DMSP chemotaxis as a searching tool to hone in on prey from tens of micrometers away, whereas bacteria might use it to maintain close associations with phytoplankton cells (*4*) or to exploit cell lysis events (*29*, *31*).

These findings imply that DMSP and related compounds are pervasive chemical cues that drive microbe-microbe interactions within the marine microbial food web and thus extend the importance of these infochemicals from macroorganisms (*9*–*12*) to microorganisms. In nature, the chemotactic responses demonstrated here may boost DMSP consumption rates by supporting algal-bacterial mutualism and could enhance DMS production by increasing both microbial exposure to DMSP pulses and grazing rates on DMSP-producing prey. These are key regulating processes for ocean-atmosphere DMS flux. This portends that microbial behaviors, played out over microscale chemical landscapes, shape planktonic food webs while potentially influencing climate at global scales.

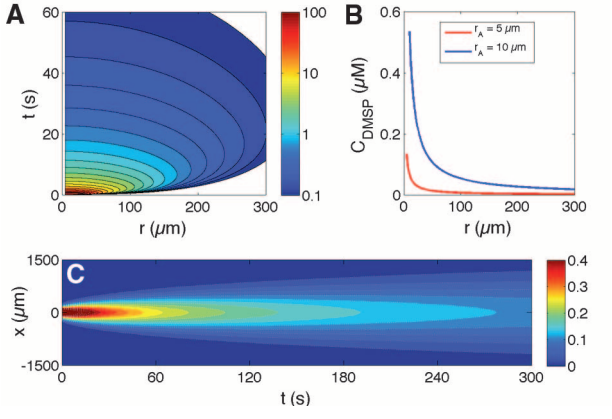

Fig. 4. Chemical micropatch diffusion dynamics. (**A**) Spatiotemporal variation of the DMSP concentration (μM) following the lysis of a 5-μm radius phytoplankton cell. Distance from the center of the cell is *r*, time elapsed since lysis is *t*. (**B**) Spatial variation of the DMSP concentration with distance from a stressed (*18*), DMSP-exuding phytoplankton cell, for two cell radii (5 and 10 μm). In (A) and (B), the intracellular DMSP concentration was 100 mM. (**C**) The initial DMSP concentration in the microfluidic pulses rapidly diffused to considerably lower values. Colors show the computed reduction factor (concentration normalized by the initial concentration in the patch), as a function of time *t* and distance *x* across the microchannel.

References and Notes

1. F. Azam, *Science* **280**, 694 (1998).
2. T. Fenchel, *Science* **296**, 1068 (2002).
3. R. Stocker, J. R. Seymour, A. Samadani, D. E. Hunt, M. F. Polz, *Proc. Natl. Acad. Sci. U.S.A.* **105**, 4209 (2008).
4. T. R. Miller, K. Hnilicka, A. Dziedzic, P. Desplats, R. Belas, *Appl. Environ. Microbiol.* **70**, 4692 (2004).
5. A. J. Hartz, B. F. Sherr, E. B. Sherr, *J. Eukaryot. Microbiol.* **55**, 18 (2008).
6. J. Stefels, M. Steinke, S. Turner, G. Malin, S. Belviso, *Biogeochemistry* **88**, 245 (2007).
7. R. P. Kiene, L. J. Linn, J. A. Bruton, *J. Sea Res.* **43**, 209 (2000).
8. M. Vila-Costa *et al.*, *Science* **314**, 652 (2006).
9. K. L. Van Alstyne, G. V. Wolfe, T. L. Freidenburg, A. Neill, C. Hicken, *Mar. Ecol. Prog. Ser.* **213**, 53 (2001).
10. J. L. DeBose, S. C. Lema, G. A. Nevitt, *Science* **319**, 1356 (2008).
11. G. A. Nevitt, *J. Exp. Biol.* **211**, 1706 (2008).
12. G. B. Cunningham, V. Strauss, P. G. Ryan, *J. Exp. Biol.* **211**, 3123 (2008).
13. R. K. Zimmer-Faust, M. P. de Souza, D. C. Yoch, *Limnol. Oceanogr.* **41**, 1330 (1996).
14. G. V. Wolfe, M. Steinke, G. O. Kirst, *Nature* **387**, 894 (1997).
15. S. Strom, G. V. Wolfe, A. Slajer, S. Lambert, J. Clough, *Limnol. Oceanogr.* **48**, 230 (2003).
16. R. Simó, *Trends Ecol. Evol.* **16**, 287 (2001).
17. J. R. Seymour, T. Ahmed, Marcos, R. Stocker, *Limnol. Oceanogr. Methods* **6**, 477 (2008).
18. Materials and methods are available as supporting material on *Science* Online.
19. D. T. Welsh, *FEMS Microbiol. Rev.* **24**, 263 (2000).
20. R. R. Malmstrom, R. P. Kiene, M. Vila, D. L. Kirchman, *Limnol. Oceanogr.* **50**, 192 (2005).
21. H. Fuse *et al.*, *Biosci. Biotechnol. Biochem.* **59**, 1773 (1995).
22. R. Simó *et al.*, *Aquat. Microb. Ecol.* **57**, 43 (2009).
23. E. C. Howard *et al.*, *Science* **314**, 649 (2006).
24. K. M. Ledyard, E. F. DeLong, J. W. H. Dacey, *Arch. Microbiol.* **160**, 312 (1993).
25. T. R. Miller, R. Belas, *Appl. Environ. Microbiol.* **70**, 3383 (2004).
26. H. C. Berg, D. A. Brown, *Nature* **239**, 500 (1972).
27. V. Saló, R. Simó, M. Vila-Costa, A. Calbet, *Environ. Microbiol.* **11**, 3063 (2009).
28. G. V. Wolfe, *Biol. Bull.* **198**, 225 (2000).
29. C. Evans, W. H. Wilson, *Limnol. Oceanogr.* **53**, 2035 (2008).
30. R. P. Kiene, D. Slezak, *Limnol. Oceanogr. Methods* **4**, 80 (2006).
31. N. Blackburn, T. Fenchel, J. G. Mitchell, *Science* **282**, 2254 (1998).

32. This research was funded by Australian Research Council grant DP0772186 to J.R.S., a Martin Fellowship for Sustainability to T.A., the Spanish Ministry of Science and Innovation project SUMMER to R.Si., funding from La Cambra de Barcelona to R.Si. and R.S., and support from the Hayashi Fund, a Doherty Professorship and NSF grant OCE-0744641-CAREER to R.S. We thank P. Jiménez and A. Calbet for growing and providing *O. marina*, W. M. Durham for preparing *M. pusilla*, Marcos for preparing *N. designis*, and R. Belas for providing *Silicibacter*. We thank S. Strom and J. G. Mitchell for comments on an earlier version of the manuscript.

Supporting Online Material

www.sciencemag.org/cgi/content/full/329/5989/342/DC1
Materials and Methods
Figs. S1 to S7

16 February 2010; accepted 10 June 2010
10.1126/science.1188418

Downloaded from www.sciencemag.org on July 15, 2010

NEW PRODUCTS FOCUS: MASS SPECTROMETRY

TRIPLE QUADRUPOLE GC-MS

The TSQ Quantum XLS is a triple quadrupole gas chromatography mass spectrometry (GC-MS) system designed to offer maximum precision, sensitivity, and laboratory productivity for quantitative analysis. It features the innovative Thermo Scientific DuraBrite IRIS high sensitivity ion source, which ensures high sensitivity in the low femtogram range, high quantitative precision at trace levels, and uninterrupted operation for increased productivity. Highly inert and exchangeable ion volumes allow for quick preventive maintenance within minutes without venting the vacuum system. The TSQ Quantum XLS is designed to improve laboratory efficiency and throughput by identifying and analyzing a very large number of compounds in a single analytical run.

Thermo Fisher Scientific

For info: 800-532-4752 | www.thermo.com/getready

MICROSCALE HPLC

The ExpressLC-Ultra is a microscale high performance liquid chromatography (HPLC) system that runs at column pressures up to 10,000 psi, allowing the use of sub-2-micron particle columns. Along with a new ultraviolet (UV) detection system, the instrument delivers all the advantages of microscale LC, including solvent savings, reduced sample requirements, and reduced frictional heating. The new system's charge-coupled device UV detector works with microfabricated flow cells to ensure ultrahigh sensitivity with no band broadening. The ExpressLC-Ultra's high UV sensitivity allows detection of impurities at levels as low as 0.05 percent, meeting the needs of researchers in drug discovery and many other applications. The system incorporates Eksigent's Microfluidic Flow Control technology to generate accurate and reproducible flow rates from 1 to 50 microliters per minute.

Eksigent

For info: 925-560-2600 | www.eksigent.com

FRACTIONATION KITS

A new line of cartridge kits is available for the Gelfree 8100 Fractionation System. The fractionation kits provide research scientists with the ability to perform molecular weight-based fractionation with liquid-phase recovery over various target mass ranges. The Low Mass Target Kit is tailored to provide maximum separation resolution of proteins with a molecular weight less than 60 kDa, which is useful in the area of top-down protein analysis using mass spectrometry. The Mid Mass Cartridge Kit provides separation across the mass range of 3.5 kDa to 150 kDa, which spans over 95 percent of the predicted proteome of most biological systems. The High Mass Cartridge Kit is designed for targeted enrichment of intact biotherapeutics, providing resolution in the mass range of 60 kDa to 300 kDa.

Protein Discovery

For info: 866-670-9038 | www.proteindiscovery.com

ULTRA HPLC

The Nexera ultrahigh-performance liquid chromatography (UHPLC) system, which delivers high-speed and high-resolution analysis without sacrificing basic performance parameters such as precision, near-zero carryover, linearity, stability, and ruggedness. These attributes enable Nexera to provide superior performance in various fields, covering high-resolution and high-speed separation as well as high-sensitivity detection. The system is optimized to enable analysis at pressures up to 130 MPa. The maximized pressure over a wide flow range enables various types of analyses, including micro LC to conventional LC, regular pressure LC to ultrahigh-pressure LC, and isocratic LC to ternary high-pressure gradient and multidimensional LC. The system is also suitable for LC-mass spectrometry applications.

Shimadzu

For info: 800-477-1227 | www.shimadzu.com

MASS SPECTROMETRY SYSTEM

The TripleTOF 5600 System is a fast and sensitive high-resolution mass spectrometer for high-performance qualitative and quantitative analysis. The instrument combines the quantitative capabilities typically associated with triple quadrupoles with the qualitative capabilities of a high-resolution, accurate-mass system. It is designed to enable new and better ways for scientists to conduct mass spectrometry experiments for a broad range of life science applications, such as discovering new drugs, detecting biomarkers, and aiding in food safety and environmental analysis. The system's innovations include the fast SmartSpeed 100 Hz Acquisition, the Accelerator TOF Analyzer for high-resolution data at high speed and sensitivity, and EasyMass Accuracy to achieve stable mass accuracy without continuous user calibration.

AB Sciex

For info: 800-327-3002 | www.absciex.com

Electronically submit your new product description or product literature information! Go to www.sciencemag.org/products/newproducts.dtl for more information.

Newly offered instrumentation, apparatus, and laboratory materials of interest to researchers in all disciplines in academic, industrial, and governmental organizations are featured in this space. Emphasis is given to purpose, chief characteristics, and availability of products and materials. Endorsement by *Science* or AAAS of any products or materials mentioned is not implied. Additional information may be obtained from the manufacturer or supplier.

Downloaded from www.sciencemag.org on July 15, 2010